UNIVERSITY OF READING

Department of Meteorology

Mechanisms of rainfall in Middle America

Armenia Franco Díaz

A thesis submitted for the degree of Doctor of Philosophy

September 2020

Declaration

I confirm that this is my own work and the use of all material from other sources has been properly and fully acknowledged.

Armenia Franco Díaz

Dedication/Dedicatoria

This thesis is dedicated to the families and teachers in Mexico's rural communities, and the migrants who have had to leave behind their loved homes due to extreme climate events, collective violence, or to pursue a better future.

Esta tesis está dedicada a las familias campesinas y a los maestros de las comunidades rurales de México, y a los migrantes que han tenido que dejar atrás sus amados hogares por condiciones climáticas extremas, violencia colectiva o por la búsqueda de un mejor futuro.

Abstract

Seasonal rainfall over Middle America is crucial for human and wildlife welfare, agriculture, industry, and hydroelectric infrastructure. The biophysical and social conditions in Middle America make this region particularly vulnerable to rainfall variability. Extreme events, such as tropical cyclones (TCs), can exacerbate seasonal variability of regional rainfall. This thesis aims to understand the causes of interannual variability of seasonal rainfall in Middle America, the TC contribution to the regional hydrological cycle, and the causes of interannual variability of seasonal TC-related rainfall.

Regions of coherent interannual variability of seasonal rainfall are identified using the objective Empirical Orthogonal Teleconnections (EOT) technique. El Niño-Southern Oscillation (ENSO) is responsible for the largest fraction of interannual variability of seasonal rainfall, with canonical ENSO events driving more variability than ENSO Modoki. The Atlantic Meridional Mode (AMM) and local land-atmosphere processes are secondary drivers of interannual rainfall variability.

TCs are important rainfall sources in Middle America during boreal summer, particularly on the Gulf coastal plain, the Mexican western coast and the southernmost states of Mexico. TCs contribute $\approx$ 10–30% of monthly accumulated rainfall (June-October) in those regions, with the most substantial contribution in Baja California Peninsula of up to 90% in September. TCs contribute 40–60% of extreme daily rainfall over Middle American coasts. TCs are a significant moisture source for the regional water budget; TC vertically integrated moisture flux (VIMF) convergence can turn regions of weak VIMF divergence by the mean circulation into regions of weak VIMF convergence.

Interannual variability of TC-related rainfall is mainly driven by ENSO, through variations in East Pacific and North Atlantic TC activity. The AMM is the secondary driver, through changes in North Atlantic TC activity. Changes in location and strength of the North Atlantic Subtropical High and the Caribbean Low-Level Jet are important circulation features that influence TC rainfall variability.

Acknowledgements

I want to express my deepest gratitude to my supervisors, Prof. Pier Luigi Vidale and Dr. Nicholas P. Klingaman, for their support, guidance, and encouragement during this Ph.D. project. Pier Luigi, thanks for your insightful ideas and comments, appreciable support, wisdom, and encouraging feedback; your objective perspective helped me to reflect on my strategic targets and to take my project forward in the right direction. Nick, thanks for your exceptional guidance, invaluable support and availability throughout my research project; I am extremely appreciative of your ideas and thorough feedback, which invariably helped me improve my research and pushed me to bring my work to a higher level. I also like to thank you both for welcoming me to the U.K. and for every conversation and meeting we had that made my Ph.D. more joyful.

I wish to thank my monitoring committee members, Dr. Oscar Martínez-Alvarado and Dr. Clare Watt, for evaluating my academic progress; I am grateful for your feedback and encouragement to analyse my research critically. I want to express my thanks to Dr. Marie-Estelle Demory for her guidance during this research project while she was my supervisor; I appreciate your continued interest in my academic progress and well-being. I wish to show my gratitude to Dr. Liang Guo and Dr. Kevin Hodges for their valuable input and help in the studies presented in this thesis.

I want to give my special regards to my loved family for their support and love: my parents Argelia and Carlos; my grandparents Enedina, Adela, Alfredo, and Carlos; my brother Carlos and sister in law Angélica. I wish to thank Lorenz for his invaluable encourage, care, and understanding during this journey; thank you for your advice and for helping me to maintain a positive attitude throughout.

I want to thank Clemente for his support, straightforward feedback on my work and for providing me with your rainfall datasets for the analysis presented in chapter 3 of this thesis. I am also indebted to my friends for their support when I needed it the most: María Luisa, Stella, Anita, James, Rohini, Lívia, Bei, Bryam, Lais, Pablo, and Carlo. I want to thank Dr. Ernesto Caetano, Dr. Rosmeri Porfirio Da Rocha, and Dr. Daniel Collins for their encouragement to study my Ph.D. at the University of Reading.

Finally, I want to profoundly thank Mexico for supporting my education during all these years and awarded me the scholarship for my Ph.D. studies at the University of Reading. This Ph.D. research project was funded by The National Council of Science and

Technology (CONACYT) Mexico, through the Sectoral Fund CONACYT-Secretariat of Energy-Energy Sustainability (CVU 489119).

Acronyms and Abbreviations

Acronym or Abbreviation	Definition
AEW	African easterly wave
AMM	Atlantic Meridional Mode
AMO	Atlantic Multidecadal Oscillation
AMOC	Atlantic Meridional Overturning Circulation
AWP	Atlantic Warm Pool
Chocó-jet	Chocó Low-Level Jet
CLLJ	Caribbean Low-Level Jet
DJF	December-January-February
ENSO	El Niño-Southern Oscillation
EOT	Empirical Orthogonal Teleconnection
EPWP	Eastern Pacific Warm Pool
ERA-In	ERA-Interim reanalysis
EW	Easterly wave
GCLLJ	Gulf of California low-level jet
GDP	Gross domestic product
GPLLJ	Great Plains Low-Level Jet
IAS	Intra Americas Sea region
ITCZ	Intertropical Convergence Zone
JJA	June-July-August
JRA-55	Japanese 55-year reanalysis
MAM	March-April-May
MCS	Mesoscale convective system
MDR	Main development region
MJO	Madden-Julian Oscillation

Acronym or Abbreviation	Definition
MSLP	Mean sea-level pressure
NAMS	North American Monsoon System
NAO	North Atlantic Oscillation
NASH	North Atlantic Subtropical High
OLR	Outgoing long-wave radiation
PDO	Pacific Decadal Oscillation
PNA	Pacific–North American pattern
SLP	Sea-level pressure
SON	September-October-November
SST	Sea surface temperature
TC	Tropical cyclone
TNI	Trans-Niño index
TS	Tropical storm
TRMM	Tropical Rainfall Measuring Mission
TMPA 3B42	TRMM Multi-satellite Precipitation Analysis
UEA	the University of East Anglia
UEA-CRU	UEA Climatic Research Unit
U.S.	United States of America
VIMF	Vertically integrated moisture flux
WWS	Wind-evaporation-SST feedback
WHWP	Western Hemisphere Warm Pool

Contents

Declaration i

Dedication iii

Abstract iv

Acknowledgements v

Acronyms and Abbreviations vii

Table of contents ix

1 Introduction 1

1.1 Climatology and interannual variability of rainfall in Middle America . . . 1

1.2 Synoptic-scale variability and extremes in Middle America 6

1.3 The objectives of this thesis 7

1.4 Outline of this thesis 9

2 Scientific background 11

2.1 The basic state of Middle America's climate: rainfall and moisture contributors 11

2.1.1 Relevant large-scale circulations 12

2.1.2 Relevant regional-scale circulations 14

2.1.3 The Western Hemisphere Warm Pool 19

2.1.4 The North American Monsoon System 20

2.2 Sources of Decadal and Multi-decadal Variability of Middle America's climate 21

2.2.1 The Pacific Decadal Oscillation 21

2.2.2 The Atlantic Multidecadal Oscillation 22

2.3 Sources of the Interannual Variability of Middle America's rainfall 23

2.3.1 El Niño-Southern Oscillation 23

2.3.2 The Atlantic Niño and the Atlantic Meridional Mode 33

2.3.3 The North Atlantic Oscillation 33

2.4 Sources of Intraseasonal Variability of Middle America's climate 34

2.4.1 The 10–30-day modes 34

2.4.2 The 30-90-day modes 35

2.5 Synoptic contributors to Middle America's rainfall and associated moisture transport 37

2.5.1 Tropical cyclones 37

2.5.2 Tropical easterly waves 46

3 Interannual Variability of Middle America's Rainfall 48

3.1 The purpose of the present study 48

3.2 Dataset and methods 52
3.2.1 Data 52
3.2.2 Empirical Orthogonal Teleconnections Analysis for interannual variability of rainfall 53
3.3 Drivers of interannual variability of seasonal rainfall in Middle America . 56
3.3.1 Summer 58
3.3.2 Winter 67
3.3.3 Spring 75
3.3.4 Autumn 82
3.4 Discussion and summary 91
3.5 Conclusions 95

4 Contribution of TCs to atmospheric branch of Middle America's hydrological cycle 97
4.1 Abstract 98
4.2 Introduction 99
4.3 Data and methods 101
4.3.1 Observations 101
4.3.2 Reanalysis datasets 101
4.3.3 TC feature tracking methodology 102
4.3.4 Quantifying the contribution of TCs to rainfall and moisture fluxes 103
4.4 Results 104
4.4.1 Contribution of Tropical Cyclones to the mean accumulated rainfall over Middle America 104
4.4.2 Contribution of Tropical Cyclones to the extreme rainfall over Middle America 110
4.4.3 Contribution of Tropical Cyclones to moisture transport over Middle America 115
4.5 Discussion 123
4.6 Conclusions 126

5 Interannual Variability of Rainfall Attributed to Tropical Cyclones in Middle America 128
5.1 The purpose of the present study 128
5.2 Datasets and methods 132
5.2.1 Data 132
5.2.2 Calculation of the rainfall associated with TCs 133
5.2.3 Empirical Orthogonal Teleconnections analysis for tropical-cyclone-related rainfall 134

5.3 Drivers of the inter-annual variability of TC-related rainfall over Middle America . . . 135
5.3.1 Summer . . . 136
5.3.2 Autumn . . . 147
5.4 Discussion . . . 159
5.5 Conclusions . . . 161

6 Conclusions **163**
6.1 Summary of key findings . . . 163
6.1.1 The large-scale and local drivers of interannual variability of rainfall in Middle America . . . 164
6.1.2 The TC's contribution to Middle Americas' hydrological cycle . . . 166
6.1.3 Main and secondary drivers of interannual variability of TC-related rainfall in Middle America . . . 167
6.2 Limitations and caveats . . . 168
6.3 Future work . . . 170

References **173**

Chapter 1:

Introduction

1.1 Climatology and interannual variability of rainfall in Middle America

Middle America is a region that comprises Mexico, northern Central America, and the southern United States (U.S.) (Fig. 1.1). This region encloses vast natural areas with varied physical landscapes and unique biodiversity, densely populated urban complexes, villages, hydroelectric infrastructure, and large agricultural areas that rely on water from seasonal rainfall for their subsistence. Rainfall is a crucial variable for Middle American climate, territory, society, and economy.

Middle America is located in a complex meteorological area that is characterised by hydrometeorological systems at different spatiotemporal scales, strongly linked with the Pacific and the Atlantic Oceans. This region is affected by tropical systems during summer and extratropical systems in winter. The transition seasons, spring and autumn, are characterised by the interplay of both tropical and extratropical rainfall regimes.

On the large-scale, Middle America's summer rainfall is strongly influenced by the northward migration of the Intertropical Convergence Zone (ITCZ; see sec. 2.1.1), the location of the Western Hemisphere Warm Pool (WHWP; see sec. 2.1.3), and trade winds. Synoptic to mesoscale meteorological systems that affect summer rainfall include tropical cyclones (TCs; see sec. 2.5.1) from both the eastern North Pacific and the North Atlantic basins, mesoscale convective systems (MCSs), and the North American Monsoon System (NAMS; see sec. 2.1.4). Regional summer rainfall also presents a pronounced diurnal cycle, characterised by complex land-sea-breeze effects (Yang and Slingo, 2001).

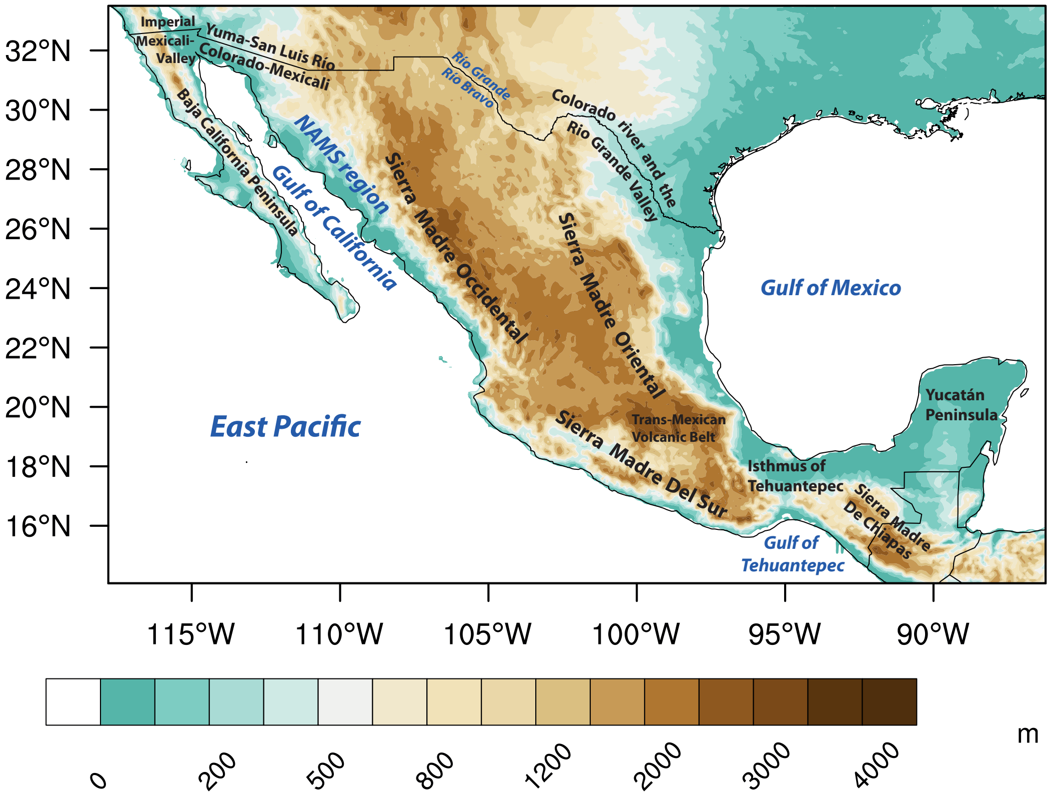

Figure 1.1: Elevation of Middle America domain, with areas of particular interest labeled. Data from TerrainBase, Global 5 Arc-minute Ocean Depth and Land Elevation from the US National Geophysical Data Center (NGDC, 1995).

Summer accounts for most of the annual rainfall in central-southern ($\approx 15-22°$ N, 106-86°W) and northwestern Middle America ($\approx 22-34°$ N, 110-105°W): the Isthmus of Tehuantepec has the highest rates of summer mean accumulated rainfall with around 1300 mm (JJA, Fig. 1.2b), followed by the core of the NAMS ($20-32°$ N, $110-105°$ W), which receives between 400 mm to 1000 mm of accumulated rainfall. The Baja California Peninsula presents the lowest mean accumulated rainfall in summer, with no more than 50 mm.

During boreal winter, Middle America is subject to extratropical meteorological systems, such as cold fronts (Henry, 1979), mid-latitude air outbreaks (known as 'nortes'; Hastenrath, 1988), which mainly affect the southeastern states of Mexico located on the Gulf Coastal Plain, such as Tamaulipas, Veracruz and Tabasco ($\approx 17-25°$ N, 97-90°W). Winter storms affect northernmost Middle America ($\approx 24-35°$ N, 118-86°W), which is an area that comprises the NAMS region, the northern states of Mexico (such as Baja

California, Sonora, Chihuahua, Coahuila and Nuevo León) and their adjacent USA territory. Upper-tropospheric circulations are dominated by the Pacific subtropical jet, with westerlies that extend through central-north Middle America ($\approx 24-35°$ N, $118-86°$ W). Seasonal accumulated rainfall in winter is considerably lower than that in summer. The highest mean accumulated rainfall in winter occurs on the northern side (which is also the windward side) of the Sierra Madre of Chiapas (see Fig. 1.1) with up to 600 mm, followed by northeastern Middle America ($\approx 28-34°$ N, 97-90°W) with up to 350 mm, and the NAMS region with up to 200 mm (DJF, Fig. 1.2d).

Spring is the transition between extratropical to tropical regimes of regional rainfall. This season is characterised by no or very little accumulated rainfall in most of western Middle America ($\approx 16-34°$ N, 119-100°W), while the eastern side ($\approx 15-34°$ N, 100-86°W) receives rainfall along the Gulf Coastal Plain and over the Sierra Madre of Chiapas (MAM, Fig. 1.2a).

Autumn is the transition between tropical to extratropical regimes of regional rainfall. It presents mean accumulated rainfall above 100 mm in most of Middle America. The highest rainfall is found in the southwest and southeast coast of Middle America, the Isthmus of Tehuantepec, and the Sierra Madre of Chiapas (SON, Fig. 1.2c).

The biophysical and social conditions in Middle America make this region particularly vulnerable to the effects of climate variability (e.g., Liverman, 1999; Ortega-Gaucin et al., 2018). Population and industrial growth in Middle America have increased the demand for food and water, which is associated with expanding urban areas and irrigated agriculture. The availability of water is particularly challenging in the drylands of Middle America, including the Mexico-U.S. border, where water use is governed by the 1944 Treaty for the "Utilization of Waters of the Colorado and Tijuana Rivers and the Rio Grande[1]". In recent decades, dry spells and shortages of water have raised conflicts over water allocations along that border (Endfield and Tejedo-Fernández, 2006; Mayorga, 2020). Water shortages are likely to be exacerbated by climate change, since most Middle America is projected to be warmer and drier under climate change scenarios (IPCC, 2013).

[1] Available in the International Boundary and Water Commission (USIBWC) website: `https://www.ibwc.gov/Files/1944Treaty.pdf`

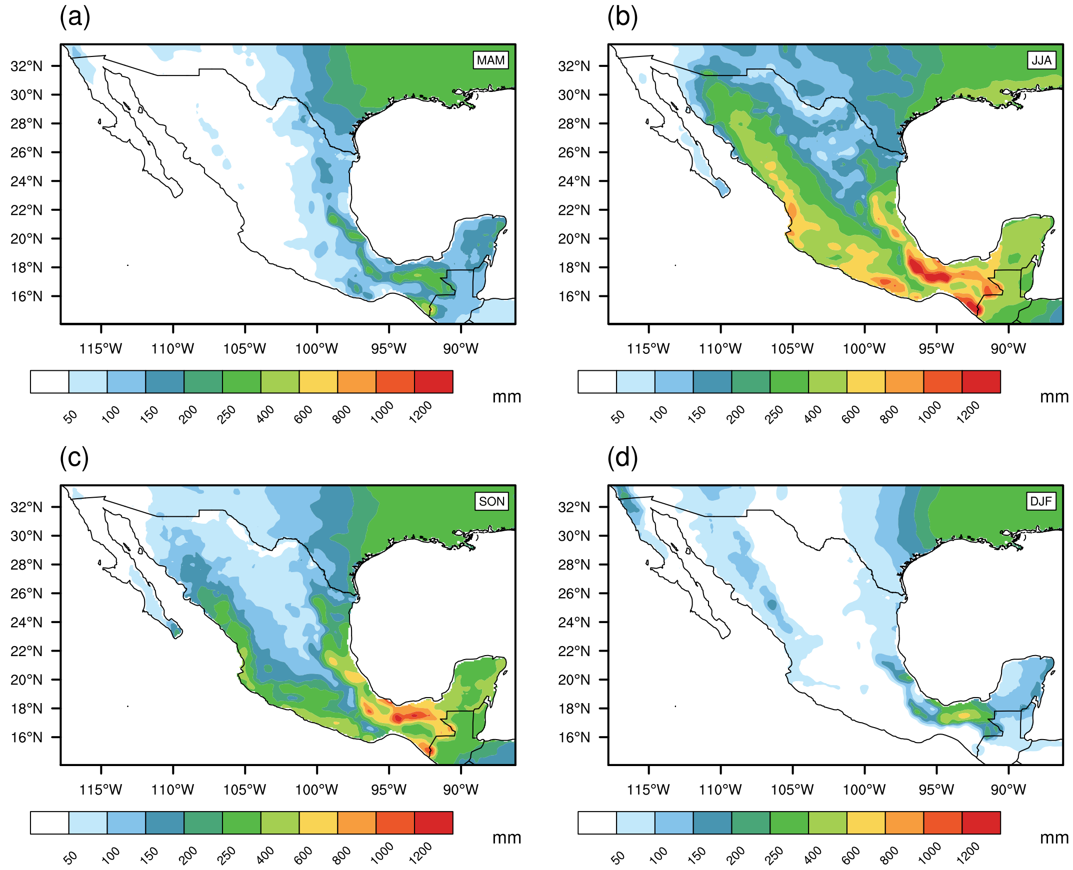

Figure 1.2: Climatology (1979-2011) of seasonal accumulated rainfall in Middle America (mm) for (a) March-April-May (MAM), (b) June-July-August (JJA), (c) September-October-November (SON), and (d) December-January-February (DJF), from daily precipitation data at 10 km×10 km horizontal resolution, fully described in López-Bravo (2015) and López-Bravo et al. (2018).

Much of the agriculture in northwestern Middle America is sensitive to the onset of the monsoon rainfall. The NAMS is a fundamental source of water for several managed river systems in northwestern Mexico and southern U.S., including the Río Bravo/Río Grande del Norte, which runs along the eastern part of the Mexico-U.S. border (see Fig. 1.1). The NAMS is the main source of the Colorado River[2], which supplies water to the border's population in fourteen city pairs and to the agricultural areas of the Imperial-Mexicali and the Colorado River valleys (together centred at ≈ 33° N, 115°W). Agriculture consumes about 81% of total water resources in the Mexicali Valley (CONAGUA, 2018).

[2]With a length of 2230 m, the Colorado River starts in the Rocky Mountains of Colorado, flows across the Colorado Plateau and the Grand Canyon. In the Arizona-Nevada border, the Colorado River turns southwards the international border, delimiting te the border between Baja California and Sonora states in México to finally reach the Gulf of California.

The region influenced by the NAMS also encounters protected national parks, wildlife refuges and biosphere reserves, alongside one of the most productive agriculture districts in northern Middle America. The three major irrigated agricultural areas that depend on the Colorado river are the Río Grande Valley (the Río Grande region that crosses New Mexico/Texas/Chihuahua/Coahuila/Nuevo León/Tamaulipas, centred at $\approx 29°$ N, 103.2°W), Yuma–San Luis Río Colorado–Mexicali (Arizona–Sonora–Baja California; centred at $\approx 32.5°$ N, 115°W), and Imperial Valley Coachella (California; centred at $\approx 32.7°$ N, 114.9°W) (Wilder et al., 2013).

Climate variability is an important factor for human migration in Middle America. Hunter et al. (2013) found associations between rainfall variability patterns and U.S. migration from rural Mexican households. The authors linked seasonal severe rainfall deficits in rural areas of Mexico with a considerable rise of emigration, roughly two years after a bad harvest. On the other hand, conditions of above-average rainfall seem to decrease emigration of rural Mexican households, when greater agricultural production potential requires less livelihood migration.

Middle America's rainfall experiences considerable interannual variance (e.g., Liverman, 1999), which is controlled primarily, but far from exclusively, by the El Niño-Southern Oscillation (ENSO; see sec. 2.3.1) phenomenon (Ropelewski and Halpert, 1987). Many meteorological phenomena that dominate the eastern Pacific, the Caribbean Sea and the Gulf of Mexico also influence Middle America's climate. On the interannual timescale, ENSO affects rainfall, atmospheric moisture, and surface temperature anomalies in these regions (e.g., Bell et al., 1999; Kim and Alexander, 2015; Serra et al., 2016). Most El Niño events (warm equatorial Pacific ocean surface temperatures; see section 2.3.1) bring wetter-than-normal conditions in northern Middle America during winter, and drier-than-normal conditions in southern Middle America in summer (e.g., CPC, 2005). Opposite-signed patterns are observed during La Niña (cold equatorial Pacific ocean surface temperatures) in winter.

Although the effects of ENSO on the regional interannual climate variability are widely documented (e.g., Hastenrath, 1978; Ropelewski and Halpert, 1987; Taylor et al., 2002), there are gaps in the understanding of how variations in intensity, position, and lifecycle phase (growing/decaying) affect teleconnections to Middle America. Even more, there is a lack of understanding about the role of secondary large-scale modes of interannual variability, and how these influence seasonal rainfall variability for Middle America's complex and contrasting hydroclimate. The drivers of Middle America's rainfall variability have only been partially explained. It is necessary to expand the current knowledge on the causes of seasonal rainfall variability to understand better their impacts on society, ecosystems, and regional economy.

1.2 Synoptic-scale variability and extremes in Middle America

TCs are synoptic-scale contributors to rainfall in Middle America. Larson et al. (2005) suggested that up to 15-20% of the mean accumulated rainfall in southwest and northeast Middle America is associated with TCs during September. Usually, TCs making landfall or tracking close to the continent bring strong wind gusts, heavy rainfall, and storm surges that bring flash floods and deadly landslides (e.g., Antinao and Farfán, 2016). Flooding is the cause of most of the socioeconomic losses in Mexico during TC events (e.g., CENAPRED, 2001, 2015). In 2013 Category 1 Hurricane Manuel (13-20 September) and Category 1 Hurricane Ingrid (12-17 September) made landfall within 24 hours on the east coast and west coast of Mexico, respectively. On 14 September, Tropical Storm (TS) Manuel tracked north-northestward, slowing down in response to the proximity of land and Hurricane Ingrid in the Gulf of Mexico, before making landfall in Michoacán on 15 September. Even as the circulation weakened in both TCs, the TC-related rainfall persisted for several hours resulting in deadly flash floods and landslides. Hurricane Manuel produced a maximum accumulated rainfall of 1107 mm in San Isidro, Guerrero, and Hurricane Ingrid a maximum of 367 mm in La Pesca, Tamaulipas (Pasch et al., 2014; Beven II, 2014). At least 192 people were killed or listed missing; extensive damage was reported across more than two-thirds of Mexico estimated at MXN75 billion (USD5.7 billion) (Jakubowski et al., 2014).

TCs contribute to the regional rainfall (e.g., Larson et al., 2005; Prat and Nelson, 2013a), extreme rainfall (e.g., Prat and Nelson, 2016), and moisture transport (e.g., Xu et al., 2017). A deeper understanding is required of their role and significance in the seasonal hydroclimate variability of Middle America under current and future climates.

TCs are subject to interannual variability. The influence of ENSO on Atlantic TCs variability has been studied (e.g., Gray, 1984; Camargo et al., 2007; Patricola et al., 2014; Lim et al., 2016), in which El Niño and La Niña phases are associated with decreased and increased TC frequency, respectively. ENSO also influences the eastern Pacific by reducing vertical wind shear over the eastern North Pacific, which favours TC activity in this basin (Laing and Evans, 2016). In contrast, relatively few studies have examined the mechanisms of interannual variability TC-related in the context of regional hydroclimates (e.g., Larson et al., 2005; Bregy et al., 2020).

Interannual TC-rainfall variability might have a substantial effect on Middle America's hydroclimate since rainfall associated with TCs is not confined to the coasts only (e.g., Xu et al., 2017). In some cases, TC remnants bring heavy rainfall and transport moisture further inland, resulting in a reversed sign of negative anomalies of seasonal rainfall, which influence water availability in the region and serve an essential ecological role (Prat and Nelson, 2013b; Knapp et al., 2016). For example, in 1997, six East Pacific TCs tracked close and/or making landfall in Mexico, reversing the existing signal of below-normal rainfall associated with the strong El Niño 1997-1998 episode (Bell et al., 1999).

Overall, the variability of rainfall in Middle America has far-reaching social, economic, and ecological impacts that affect millions of people in one of the most biodiverse regions in the world, in which the economy strongly depends on water availability. Climatic information and studies on rainfall variability in Middle America are essential to understand, anticipate, and cope with the year-to-year water availability. This information could be useful for improved forecasting to support decision making, which could help to improve the human and wildlife welfare, environment, and socioeconomic activities (e.g., WMO, 2007; Emanuel et al., 2012). Advanced knowledge of the impacts of the large-scale drivers of interannual variability of rainfall could aid seasonal rainfall predictions since, at these lead times, numerical models have good skill for predicting variability associated with large-scale atmospheric systems but poor skill for local or regional rainfall (e.g., Webster, 1995; Kim et al., 2012).

Population growth and economic development will increase pressure on water resources; climate studies and improved seasonal forecasts will be crucial to mitigate the impacts of rainfall variability to protect human wellbeing and safeguard ecosystems and socioeconomic activities. Advances in this understanding may create opportunities to improve climate risk management and adaptation to climate change.

1.3 The objectives of this thesis

Interannual variability of seasonal rainfall influences Middle America's society, natural areas, and economic activities. Previous studies have documented the effects of ENSO on regional anomalies of seasonal rainfall, mainly during summer and winter (e.g., Ropelewski and Halpert, 1987; Magaña et al., 2003). In contrast, the effect of ENSO on the transition seasons (autumn and spring) has not been studied as extensively neither fully understood. Even more, no study has addressed the causes of variability across Middle America in all seasons using a consistent method. Recent studies have addressed the effects of the Modoki ENSO in the global context (e.g., Ashok et al., 2007; Weng et al., 2007, 2009, see sec. 2.3.1). The effect of these events on the interannual variability of rainfall in Middle America is still a matter of study. Further, it is unclear what role secondary modes of interannual variability play in rainfall variability in Middle America. To address this gap in understanding the causes of seasonal rainfall variability, chapter 3 of this thesis aims to (a) objectively identify regions in Middle America that show coherent interannual variability of rainfall for all seasons, (b) to associate these regions with their main and secondary mechanisms of variability, and (c) to describe physical local mechanisms that create conditions for anomalous seasonal rainfall over the region.

Secondly, the study of the contribution of the multiple meteorological systems that impact Middle America's seasonal rainfall is key to understanding the regional hydrological cycle and its interannual variability. TCs making landfall or tracking close to Middle America are of particular interest, since they bring heavy rainfall and transport moisture into the region. TCs are also associated with extreme rainfall, floods and damage that deeply affect the society, ecosystems and economy. Some studies have evaluated the contribution of TCs to rainfall (e.g., Larson et al., 2005; Prat and Nelson, 2013b) and moisture transport (e.g., Xu et al., 2017) over particular portions of Middle America. This thesis aims to complement these studies by using a novel approach to quantify TCs contribution to rainfall through the use of trajectories identified from observations and two stat-of-the-art reanalyses, which allows to make a robust analysis of this contribution when including the pre- and post-stages of the TC. Chapter 4 aims to presents the contribution of TCs to (a) monthly rainfall, (b) monthly extreme rainfall and (c) atmospheric moisture transport over Middle America.

Lastly, several studies have linked East Pacific and North Atlantic TC activity with interannual modes of variability (e.g., Gray, 1984; Camargo et al., 2007; Patricola et al., 2014; Lim et al., 2016). However, only a few studies have linked TCs rainfall activity in certain regions of Middle America to large-scale modes of variability (e.g., Larson et al., 2005; Bregy et al., 2020). The causes of the interannual variability of TC-related rainfall over the region is still a matter of study. Chapter 5 of this dissertation aims

(a) to identify regions in Middle America that show coherent interannual variability of seasonal TC-related rainfall; and (b) to identify large-scale climate phenomena that drive the interannual variability of TC-related rainfall over Middle America. These objectives and those of chapter 3 are connected by the hypothesis that interannual variability of seasonal TC-related rainfall and total rainfall are driven by different mechanisms.

1.4 Outline of this thesis

Chapter 2 provides an overview of the foundations of Middle America's climate, particularly the large-scale, synoptic, and mesoscale contributors to rainfall and moisture, such as the ITCZ, the NAMS, and TCs. An overview of the regional climate will provide the reader with the background to understand the large-scale and local systems that influence the regional climate. This chapter also summarises past research concerning the decadal (sec. 2.2), interannual (sec. 2.3), and intraseasonal (sec. 2.4) modes of climate variability that affect Middle America's climate. Section 2.5 reviews tropical weather systems that contribute to the regional rainfall, in which TCs are examined thoroughly (sec. 2.5.1).

Chapter 3 is dedicated to the study of the interannual variability of seasonal rainfall in Middle America. Through the implementation of the Empirical Orthogonal Teleconnection (EOT) method (described in sec. 3.2.2), coherent spatial patterns that represent most of the interannual variance of Middle America's rainfall are identified and analysed. Regression analysis is used to identify large-scale modes of variability and the plausible physical mechanisms linked to anomalous seasonal rainfall over the region. This chapter also provides insights into the contribution of TCs to the interannual variability of seasonal rainfall in Middle America.

Chapter 4 is dedicated to the study of TC contributions to the atmospheric branch of the hydrological cycle over Middle America. Contributions of TCs to monthly rainfall, extreme rainfall, and atmospheric moisture are presented. TC contributions to rainfall are quantified using TC tracks derived from three sources: the International Best Track Archive for Climate Stewardship (IBTrACS), and tracks from an objective feature tracking method applied to the Japanese 55-year and ERA-Interim reanalyses. The strengths and weaknesses of each source of TC tracks are described. Chapter 4 has been published as Franco-Díaz et al. (2019).

Chapter 5 is dedicated to the study of the interannual variability of seasonal rainfall associated with TCs in Middle America. The EOT method is implemented to identify coherent spatial patterns representing most of the interannual variance of Middle America's TC-related rainfall. Regression and composite analyses are used to identify phenomena and mechanisms associated with the interannual variability of regional TC-related rainfall, connected to variability of TC genesis and tracks in the East Pacific and the North Atlantic basins.

Chapter 6 contains a summary of the key conclusions of this thesis (sec. 6.1), describes known limitations (sec. 6.2), and details several potential lines of future inquiry (sec. 6.3).

Chapter 2:

Scientific background

This chapter provides an overview of the mean state and sources of rainfall variability of Middle America. Section 2.1 sets out the mechanisms for rainfall and moisture in the Intra Americas Sea region (IAS; Fig. 2.1), a region that includes both the Gulf of Mexico and the Caribbean Sea extending from the tropical East Pacific to the western tropical North Atlantic, entirely north of the equator (Amador, 2009; Serra et al., 2016). The importance of the IAS in the context of mean state, and in decadal, interannual, and intraseasonal variability of Middle America's climate is emphasised. Sections 2.2, 2.3 and 2.4 describe previous research into mechanisms of multidecadal, interannual, and intraseasonal variability of Middle America's rainfall, respectively. Since this thesis investigates the contribution of TCs to the regional rainfall and its interannual variability, section 2.5 explains the current understanding of TC physics and sources of variability of TC activity in the IAS.

2.1 The basic state of Middle America's climate: rainfall and moisture contributors

Middle America is a complex region affected by the interaction of diverse meteorological systems at different temporal scales. Its climate has a strong dynamic and thermodynamic connection with the western tropical Pacific, interacting with the IAS. On the large-scale, the East Pacific ITCZ, the Atlantic ITCZ, and the westernmost branch of the North Atlantic Subtropical High (NASH) are the three main circulations associated with the location of the main core of rainfall and the distribution of moisture for precipitation in the IAS (e.g., Martinez et al., 2019). The spatial extent of this moisture is modified by the Atlantic Warm Pool and the Caribbean Low-Level Jet (CLLJ).

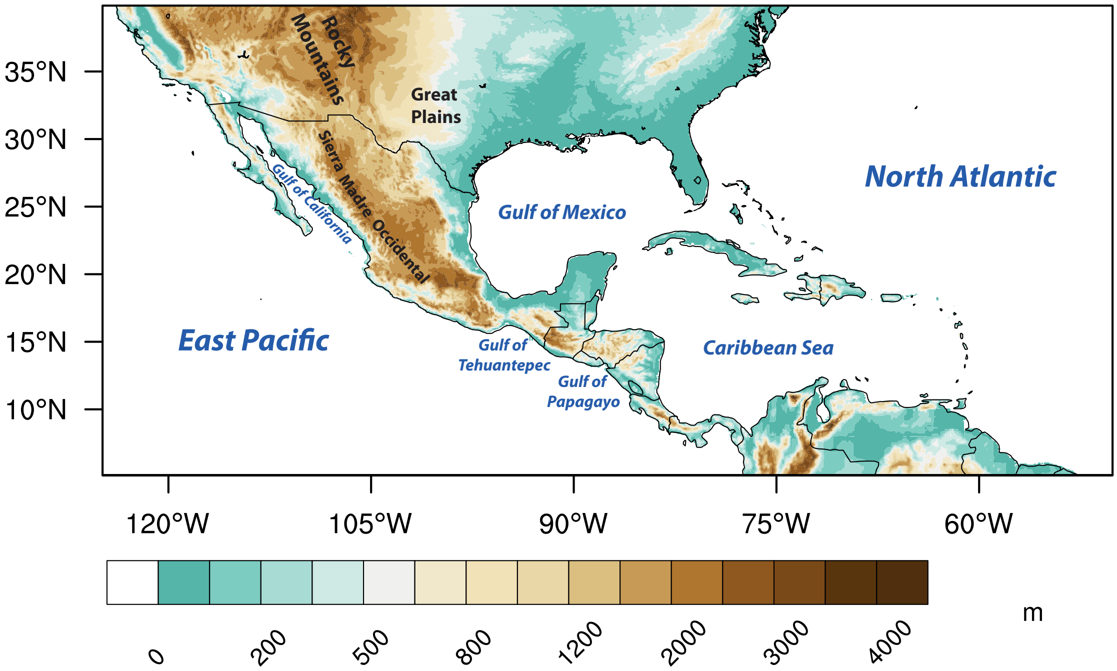

Figure 2.1: Elevation of Middle America, northern South America, the southern U.S. and the Caribbean islands, with areas of particular interest labeled. The oceanic portion represents the Intra Americas Sea region. Data from TerrainBase, Global 5 Arc-minute Ocean Depth and Land Elevation from the US National Geophysical Data Center (NGDC, 1995).

2.1.1 Relevant large-scale circulations

The Intertropical Convergence Zone

The annual cycle of Middle America's climate is largely influenced by large-scale circulations in the Pacific and Atlantic Oceans, such as the Hadley circulation and the Walker circulation. The main core of rainfall over Middle America in the tropics is collocated with the ITCZ (Durán-Quesada et al., 2012), which migrates with the seasonal cycle of insolation (Fig. 2.3). The ITCZ is a permanent low pressure zone that constitutes the ascending branch of the Hadley circulation, which on average lies 6° north of the equator (Waliser and Gautier, 1993).

The ITCZ is characterised by low-level northeast and southeast trade winds, coupled with surface evaporation, which converge into a band of strong atmospheric convection (Xie et al., 2005). The seasonal cycle of the two branches of the ITCZ in the East Pacific and Atlantic are characterised by a meridional seasonal migration of convection and rainfall, lagging the solar peak by one to two months over the ocean (Mitchell and

Wallace, 1992; Toma and Webster, 2010a). The seasonal migration of the ITCZ over the continent, the eastern Pacific and the Atlantic ocean is an important modulator of Middle America's rainfall.

Throughout the year, the East Pacific and Atlantic ITCZ remain in the Northern Hemisphere (Fig. 2.2), where its southernmost location occurs in boreal spring (March-April) and the northernmost in boreal autumn (September) (Waliser and Gautier, 1993). Figure 2.3 shows the climatological satellite-based estimations of accumulated rainfall per season, over both the ocean and continent. These estimations show that in the Northern Hemisphere summer rainfall (JJA; Fig. 2.3b), the deepest East Pacific ITCZ convection is found over $\approx 5^{\circ} - 20^{\circ}$ N with the eastern edge trimmed by the Mexican and Central American coasts (Toma and Webster, 2010a). Similar to Figure 1.2 in Chapter 1 (which is based on *in situ* observations over continent), Figure 2.3b shows the Middle American maximum accumulated rainfall during JJA. This maximum of precipitation in the Middle American Plateau is highly dependent on the northward migration of the ITCZ over continent.

In autumn, the Atlantic ITCZ is at its most intense (Fig. 2.3c), concurrent with the strongest Hadley circulation, and the peak of the regional sea surface temperatures (SSTs) (Fig. 2.2).

The Pacific Subtropical Jet

The Pacific subtropical jet is an important feature of Middle America's climate, particularly for its northern region during winter, since it is a means of transport for extratropical weather systems. In winter, the jet is located at the poleward edge of the Hadley cell at $\approx 30^{\circ}$ N in the tropical-subtropical upper troposphere at ≈ 200 hPa (Krishnamurti, 1961). The Pacific subtropical jet is the result of the ascending air flowing poleward in the Hadley cell. In this process, the air increases its speed as it moves to higher latitudes to conserve angular momentum. The jet has a westerly component with wind speeds of 75-100 $\text{m}\cdot\text{s}^{-1}$.

The Northern Hemispheric mean latitudinal position of the Pacific Subtropical jet is more equatorwards in April and more polewards in August ($\approx 27^{\circ}$ N and $\approx 42^{\circ}$ N, respectively; see Fig. 7 in Maher et al. (2020) for reference). The Pacific subtropical jet stream also varies its meridional location with the seasons and in accordance with the horizontal temperature fields across the globe, which depends on the annual march of the sun. The subtropical jet follows the contours of low and high atmospheric pressure areas, corresponding with atmospheric Rossby waves troughs and ridges, respectively.

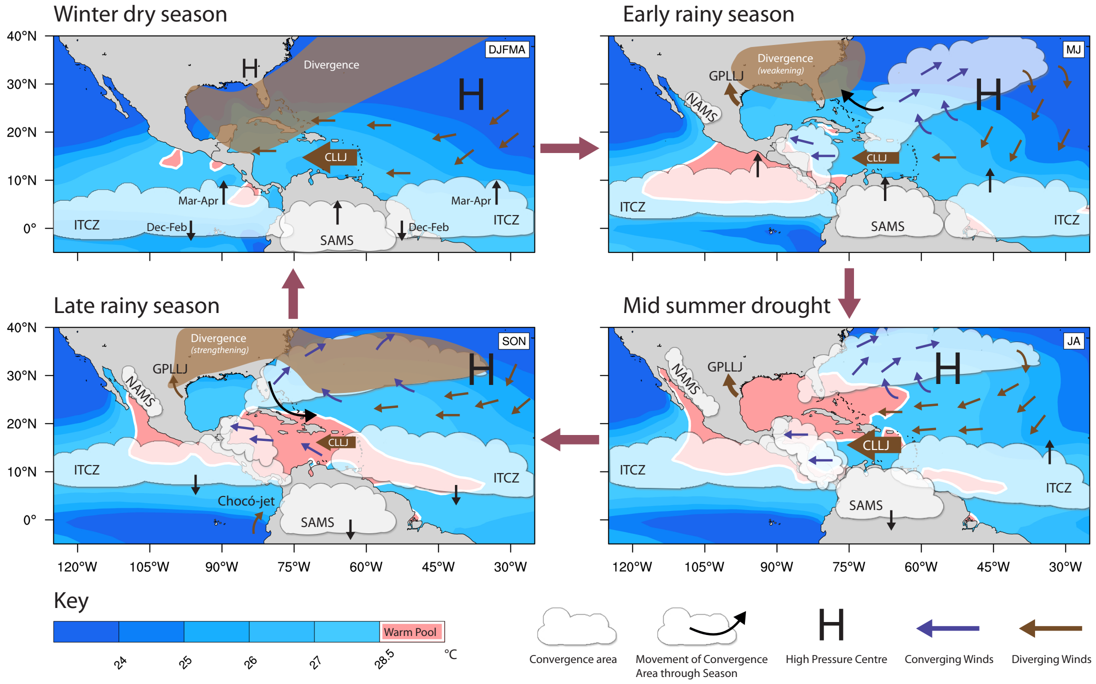

Figure 2.2: Schematic that shows the features associated with the seasonal cycle of rainfall over Middle America and the IAS. Areas shaded in white are the convergence bands. Areas shaded in brown denote transient divergence. Black arrows denote convergence bands movement during a given season. Shaded blue and brown arrows denote convergent and divergent wind vectors, respectively. The "NAMS" convergence denotes the location of the North American Monsoon System. The "CLLJ" and "GPLLJ" arrows indicate the location of the peak winds of the Caribbean Low-Level Jet and the Great Plain Low-Level Jet, respectively. The large "H" denotes the North Atlantic Subtropical High. The small "H" denotes the U.S. continental High. The warm pool denotes SSTs greater than 28.5 °C, highlighted in pink. Adapted from Martinez et al. (2019).

.

2.1.2 Relevant regional-scale circulations

The North Atlantic Subtropical High

Another relevant circulation for Middle America's climate is the NASH, which is a prominent low-level atmospheric circulation feature of the North Atlantic formed as a consequence of the Northern Hemisphere Hadley Cell, the land-ocean distribution and land-ocean contrast (Fig. 2.4). The NASH is dominated by two spatial modes: a summer pattern that presents high pressure dominating over the Atlantic, and the winter pattern that consists of anticyclones over North America and northwestern Africa (Davis et al., 1997).

The NASH is stronger when located farther west, generally during May and the end of July (Fig. 2.4). In May, the western flank of the NASH expands west while strengthening and interacting with the northward migrating eastern Pacific ITCZ (Martinez et al., 2019).

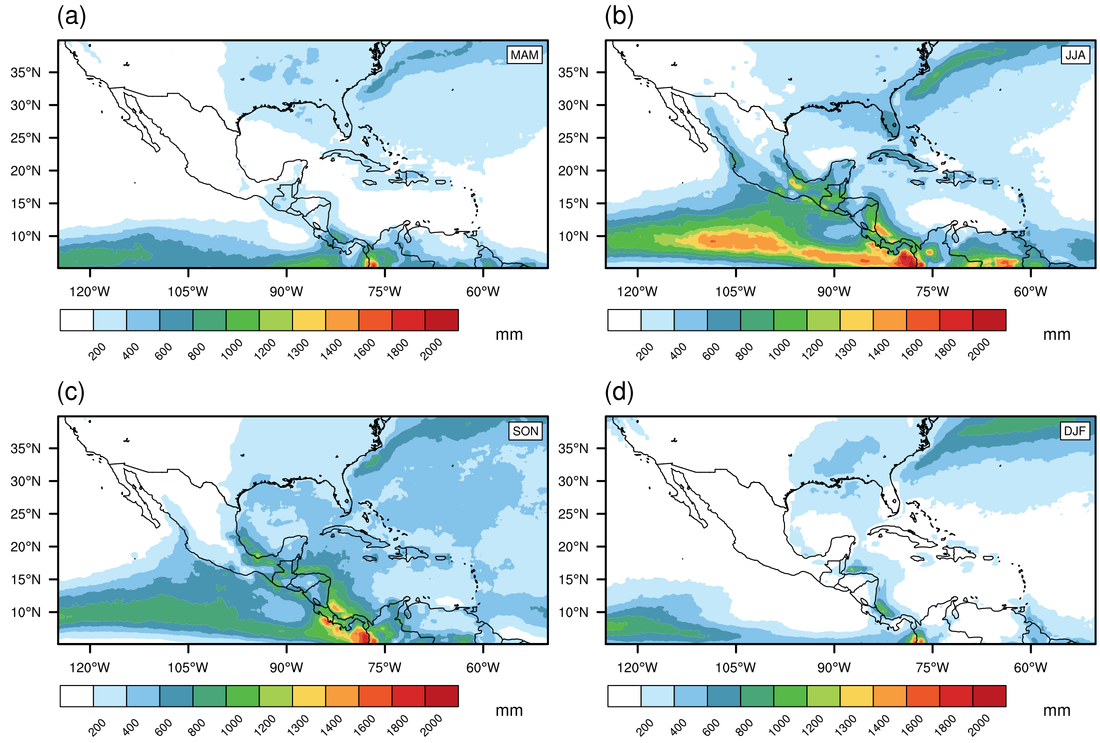

Figure 2.3: Climatology (1998-2016) of seasonal accumulated rainfall (*mm*) for (a) MAM, (b) JJA, (c) SON, and (d) DJF. Data from the Tropical Rainfall Measuring Mission (TRMM) Multi-satellite Precipitation Analysis (TMPA 3B42) (Huffman and Bolvin, 2015).

Under this configuration, the NASH transports moisture from southeast to northwest and advects warm air from the tropical Atlantic and the Gulf of Mexico towards the eastern half of North America (Fig. 2.2). By July, the anticyclone shifts northwards and occupies most of the Atlantic basin, with a single maximum centred around 30° N, 40° W. The trade winds along the southern flank of the NASH inhibit moisture transport in the Caribbean and Middle America; moisture divergence prevails in the Caribbean.

In early August, the NASH moves eastwards and weakens, which continues through autumn (Fig. 2.4c). In September, the NASH western flank migrates southeast and mid-latitude systems shift southward. This weakens the convergence on the western flank of the NASH and inhibits interactions with the eastern Pacific ITCZ. The NASH continues to contract until the wintertime North American high emerges, resulting in the dissipation of its western flank. In early January, the oceanic centre of the NASH reaches its farthest point in the East, presenting two anticyclonic centres over the southeastern U.S. and west of Morocco (Davis et al., 1997). The NASH connects with the continental North American high, providing subsidence and divergent trade winds to the Caribbean, the Gulf of Mexico and Central America.

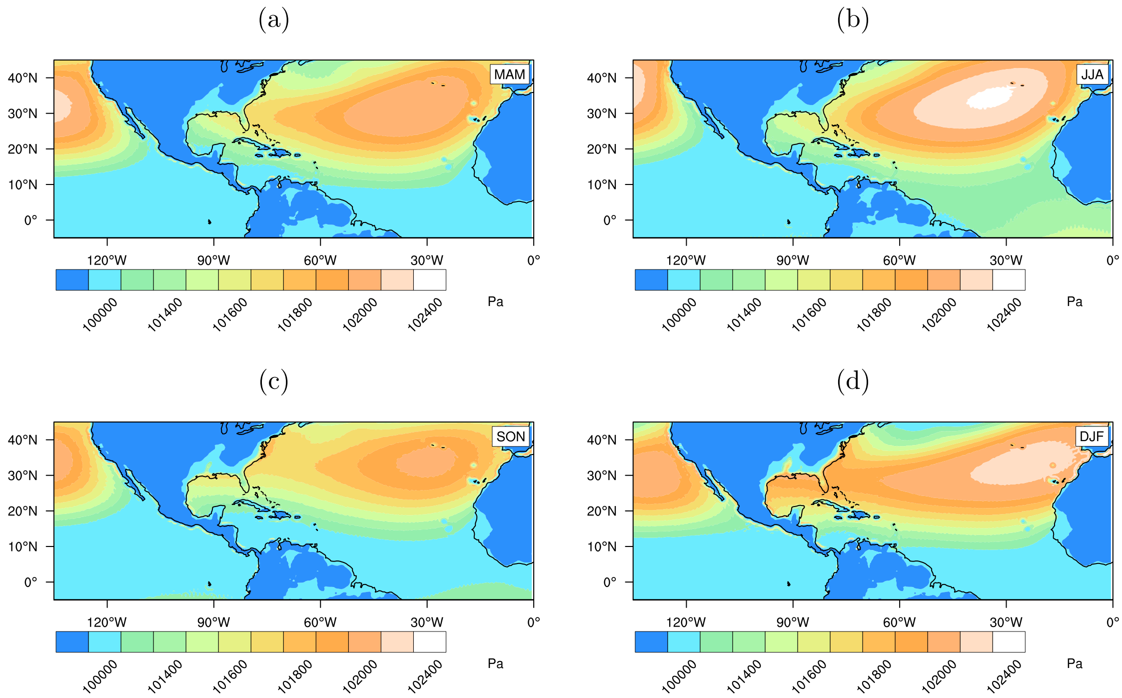

Figure 2.4: Climatology (1979-2016) of surface pressure for (a) MAM, (b) JJA, (c) SON, and (d) DJF. Data from the Japanese 55-year reanalysis (Kobayashi et al., 2015).

Low-level jets

The low-level jets influence the distribution of moisture in continental tropical America (Amador, 2009). They result from spatial temperature gradients across the topography or the ocean at lower altitudes, which lead to pressure gradients and, as a result of the Coriolis force, flow of air perpendicular to the thermal gradient.

The Caribbean Sea presents a low-level jet (CLJJ) in the trade wind regime, characterised by strong easterly wind, with a peak at 925 hPa over the Caribbean Sea at approximately 12.5° N-17.5° N, 80° W-70° W (Wang, 2007), with an extension into the east Pacific known as the Papagayo jet (Fig. 2.5). Its annual cycle presents two peaks of intensity throughout the year in July and February.

The source of momentum for intensification of the CLLJ is still a matter of scientific debate (Maldonado et al., 2017). Some studies have linked the genesis of the CLLJ with variations of sea level pressure in the Atlantic, suggesting that the CLLJ is an extension of the NASH (Wang, 2007; Cook and Vizy, 2010) and that its northeasterly Atlantic trades are amplified by thermal and orographic influences in the Caribbean region (Muñoz et al., 2008). Conversely, Herrera et al. (2015) suggest that the meridional amplification of the NASH over the Caribbean might respond via geostrophic adjustment to the intensification of the CLLJ.

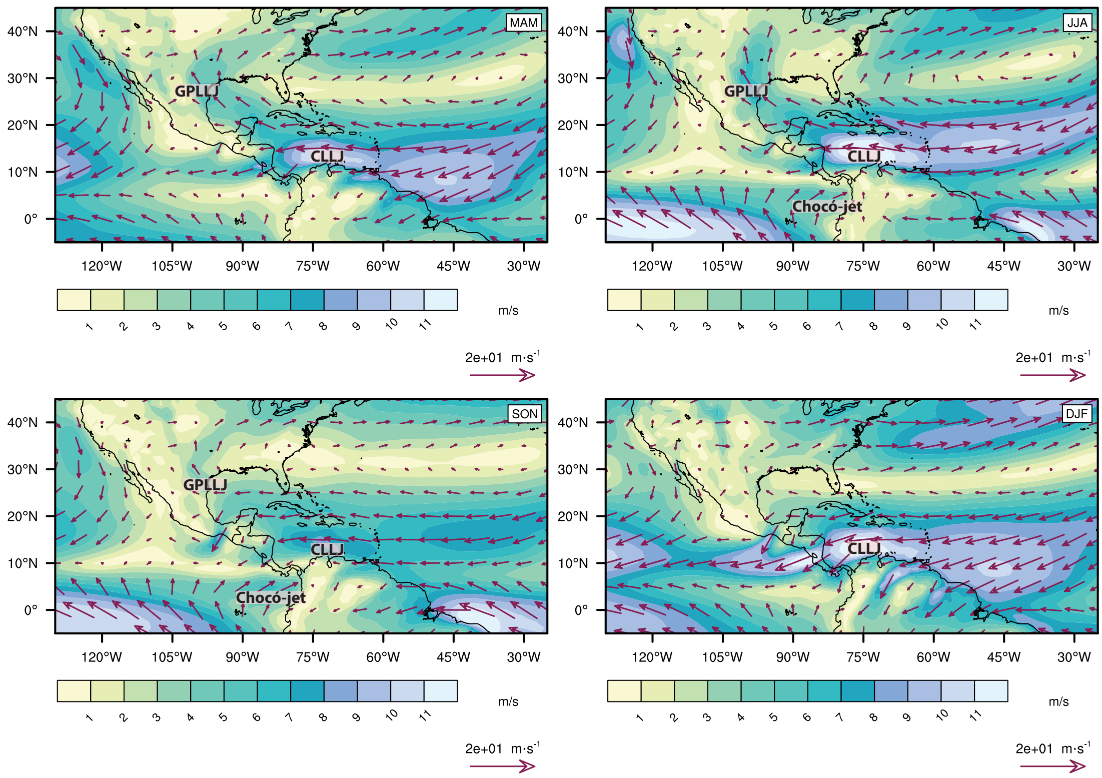

Figure 2.5: Climatology (1979-2016) of the wind magnitude (shaded) and vector (arrows) at 925 hPa for MAM, JJA, SON, and DJF. The "CLLJ", "GPLLJ", and Chocó-arrows indicate the location of the peak winds of the Caribbean Low-Level Jet, the Great Plain Low-Level Jet, and the Chocó Jet, respectively. Data from the Japanese 55-year reanalysis (Kobayashi et al., 2015).

.

The CLLJ strength is anticorrelated with seasonal rainfall in the Caribbean, southern Mexico and Central America, while it is positively correlated with rainfall in the Great Plains of the U.S. (Cook and Vizy, 2010). For Central America, the Caribbean Sea is a primary source of moisture and the CLLJ is the principal moisture transport mechanism (Durán-Quesada et al., 2010; Vigaud and Robertson, 2017). During May–September the CLLJ distributes moisture mainly in two directions or branches: one crossing Central America to the eastern Pacific, and the other to the Gulf of Mexico and northeastern Middle America (Wang, 2007; Durán-Quesada et al., 2010). In the first branch, the CLLJ flows westwards and crosses central America with an orographically induced southward component (at $\approx 10°$ N, 85° W), to finally reach the Pacific basin (as a single branch) and to become the Papagayo Jet. The second branch flows into the Gulf of Mexico to connect with the Great Plains low-level jet (GPLLJ; Cook and Vizy, 2010).

The southerly GPLLJ is present from April to September (Fig. 2.5), confined to the boundary layer with maximum wind speeds typically at 500–1000 m above northwestern Mexico and the Great Plains of the U.S. (Jiang et al., 2007). The GPLLJ plays an important role in supplying warm, moist air to developing of mesoscale convective complexes over the region (Cotton et al., 1989). The GPLLJ develops in response to a pressure gradient associated with increasing elevation from east to west, towards the Rocky Mountains. This jet exhibits a strong diurnal oscillation, characterised by strong nocturnal wind speeds. It has been suggested that this jet modulates the diurnal cycle of summertime rainfall in northeastern Middle America and the Great Plains, where the deep convection exhibits a midnight/early morning maximum (Jiang et al., 2007). Byerle and Paegle (2003) suggested that the GPLLJ is generated by the interaction between the ambient flow and the Rockies, where strong (weak) upper level winds upstream of the Rockies create strong (weak) GPLLJs and more (less) rainfall over the Great Plains.

During spring, lower tropospheric to mid-tropospheric air frequently originates over the warm, dry northern Middle America and is advected eastwards, following a developing cyclonic circulation to the lee of the Rocky Mountains. This dry air encounters warm moist air from the Gulf of Mexico advected by the GPLLJ, creating horizontal moisture contrast that triggers severe weather in northeastern Middle America (Cotton et al., 2010).

Another low-level jet formed in the region is the Chocó Low-Level Jet (Chocó-jet) characterised by westerly flow over the eastern Pacific (Fig. 2.5), which is an extension of the southwesterly cross-equatorial flow with a peak at 925 hPa over the eastern Pacific, at approximately $0° - 5°$ N, 80° W (Yepes et al., 2019). This jet is an important source of moisture for Central America, particularly from September to November, when the winds in the core of the jet are stronger.

The convection associated with the Chocó-Jet over northern South America and Central America is very sensitive to the combined effects of the topography of the Andes and the Coriolis force, which allows moisture from the eastern Pacific to be transported towards the continent (Durán-Quesada et al., 2010).

2.1.3 The Western Hemisphere Warm Pool

The WHWP is a region of SSTs greater than 28.5°C encompassed by the IAS (Wang and Enfield, 2003). Middle America's landmass divides the WHWP into two ocean regions: the Atlantic warm pool (AWP) in the East, and the eastern North Pacific warm pool (EPWP) in the West.

The EPWP is found north of 8° N off Middle America's coasts, and east of 120° W in May-June (Fig. 2.2). This is a region of deep convection, which corresponds to a northward extension of the Eastern Pacific ITCZ (Mitchell and Wallace, 1992; Wang et al., 2008). The region of deep atmospheric convection, rainfall and tropical cyclone activity is generally confined to the north of the equator.

The AWP contributes to the large-scale Hadley-type overturning circulation centred over the tropical western Atlantic Ocean (Wang et al., 2010); it is also a region of strong tropical cyclone activity.

The annual cycle of the WHWP is associated with changes in tropospheric moisture, heat and stability (Wang and Enfield, 2001). The EPWP develops first through surface heat fluxes[1]. By April and May, strong northerly winds from the Gulf of Mexico over the Gulf of Tehuantepec (located at $\approx$ 15° N, 94°W; see Fig. 2.5) create wind stress accompanied by Ekman pumping and downwelling in the Gulf of Tehuantepec (Santiago-García et al., 2019). There is a local minimum of latent and sensible flux in May due to reduced wind speeds associated with the meridional migration of the ITCZ (Wang and Enfield, 2001). These conditions warm the East Pacific SSTs to 28.5°C by May (Fig. 2.2). Simultaneously, the basin experiences a reduction in sea level pressure, warming and moistening of the troposphere, and the weakening of both easterly trade winds and vertical wind shear (e.g., Knaff, 1997). The expansion of the WHWP and the increased convective activity of the East Pacific ITCZ trigger the onset of the rainy season in Middle America.

[1] The surface net heat flux is composed of shortwave and longwave radiation, and sensible and latent heat flux

Southern Middle America presents a maximum of convective activity at the beginning of the rainy season (mid-May), when EPWP SSTs reach ≈ 29°C.

By June, the SST warming expands to the Gulf of Mexico (the AWP), enhancing the moisture convergence provided by both the eastern Pacific ITCZ and the western flank of NASH, while the EPWP decays (Misra et al., 2016). In July, the Gulf of Mexico reaches the 28.5°C while the EPWP continues cooling (Fig. 2.2) due to a greater cloud cover (Wang and Enfield, 2001). The consequent deep convection decreases regional incoming solar radiation (simultaneously with the enhancement of the easterly wind flow), which cools SSTs by ≈ 1°C during July-August. This negative air-sea feedback process is accompanied by reduction of rainfall over southern Middle America, which corresponds to the period of the midsummer drought, a relative minimum of rainfall during July and August (Magaña et al., 1999). By August, the Gulf of Mexico SSTs reach 29.5°C and extend towards the Caribbean Sea by September, when the AWP reaches its maximum size. By October the AWP only persists in the Caribbean and the western tropical Atlantic (Wang and Enfield, 2003).

2.1.4 The North American Monsoon System

The NAMS is a significant climatic feature of Middle America during boreal summer (Figs. 2.2 and 2.3). Nearly 60-80% of the annual rainfall in northwestern Middle America is linked to the NAMS (Stensrud et al., 1995).

The NAMS circulation has a characteristic upper-level anticyclone/low-level heat low over the Sierra Madre Occidental of northwestern Middle America. The strengthening and northward movement of the anticyclone during the summer is a sign of the development of the NAMS. The NAMS onset is characterised by the northward extension of rainfall from central to the northwestern Middle America in early June, which persists through September. As the NAMS extends northward during the monsoon season, the diurnal rainfall cycle becomes more intense over high topography, where the surface heating over the region plays an important role for the development and maintenance of the monsoon.

The NAMS circulation is characterised by ascent over the ocean and subsidence on the continent, which corresponds to a Sverdrup-type balance between advection of planetary vorticity and the vorticity source associated with diabatically-forced vertical motion (e.g., Chen, 2003). This balance creates a positive feedback with low-level poleward motion advecting warm moist air into the convective regions (Mechoso et al., 2004). Baroclinic Rossby waves set up the planetary vorticity of the NAMS, through induced subsidence to the west of the monsoon heating that interacts with the ITCZ (Mechoso et al., 2004).

The NAMS interacts with northwesterly winds over Baja California from the subtropical Pacific high, with the Gulf of California low-level jet (GCLLJ) (Mechoso et al., 2004; Anderson et al., 2000b,a), and with the Rockies and the GPLLJ in the East (e.g., Rodwell and Hoskins, 2001; Mo and Berbery, 2004). There is controversy surrounding the relative importance of moisture sources for NAMS precipitation, such as the mean flow (Schmitz and Mullen, 1996) and synoptic transients. Rodwell and Hoskins (2001) suggest that the NAMS precipitation is mostly dominated by the Gulf of Mexico moisture source with secondary contributors from a Pacific source.

2.2 Sources of Decadal and Multi-decadal Variability of Middle America's climate

2.2.1 The Pacific Decadal Oscillation

The Pacific Decadal Oscillation (PDO) is a dominant pattern of North Pacific SST anomalies, which exhibits variability on interannual as well as decadal scales. The PDO is likely the sum of several different mechanisms. At the interannual scales, the ENSO-induced fluctuations in the strength of the Aleutian low (via surface heat flux forcing) are important in determining PDO variability. At decadal scales, contributions to determine PDO variability are the tropical Pacific atmospheric bridge to the North Pacific, changes in the North Pacific oceanic gyre circulation, and stochastic heat flux forcing (Alexander, 2010).

The positive phase of the PDO is characterised by negative SST anomalies in the central Pacific and positive anomalies along the coast of North America, which are accompanied by a deeper Aleutian Low. During this phase, negative sea level pressure anomalies prevail over the North Pacific and warm surface air temperature prevails over western North America. The positive phase is associated with enhanced precipitation over Alaska and northern Middle America, and reduced precipitation across the northern U.S./southern Canada (Deser et al., 2004; Alexander, 2010).

During the negative phase of the PDO, the CLLJ weakens and easterly wave activity increases, leading to more convection over southern Middle America and less moisture flux into northern Middle America (Méndez and Magaña, 2010).

2.2.2 The Atlantic Multidecadal Oscillation

The Atlantic Multidecadal Oscillation (AMO) is a mode of natural decadal variability of the North Atlantic Ocean, with a period of 60-80 years (Trenberth et al., 2019). The traditional AMO index is based on a 10-year running mean of the average SST in the entire North Atlantic basin and linearly detrended to isolate the natural variability (Enfield et al., 2001). However, since the aforementioned detrending does not separate the multidecadal variability from the nonlinear global-scale signal, other methods have been proposed to remove the nonlinear global-scale signal (e.g., Trenberth and Shea, 2006; Ting et al., 2009; Sutton et al., 2018).

Different physical mechanisms for the generation of the AMO have been explored. Many studies have initially attributed the Atlantic Meridional Overturning Circulation (AMOC) as the main driver of the AMO (e.g., Delworth et al., 1993; Knight et al., 2005; Trenberth and Shea, 2006; Zhang et al., 2019). More recently, Clement et al. (2015, 2016) suggested that the mid-latitude atmospheric circulation is the main driver of the AMO and the thermal coupling playing a role in tropical regions. Murphy et al. (2017) highlighted the role of external radiative forcing for the definition of the magnitude, the multidecadal frequency and timing of the AMO variability. However, these new views have been questioned (O'Reilly et al., 2016; Zhang et al., 2016, 2019).

The AMO is associated with cross-equatorial SST anomaly gradients in the Atlantic basin, and with the meridional shift of the ITCZ. The AMO is also strongly linked to decadal variability in Atlantic tropical cyclone activity (Goldenberg et al., 2001; Molinari and Mestas-Nuñez, 2003; Trenberth and Shea, 2006). The warm phase of the AMO, characterised by a warmer North Atlantic Ocean, is related with a doubling of the tropical storms that evolve into severe hurricanes, relative to the cold phase. Since the AMO switched to its warm phase in 1995, more severe hurricanes have formed in the Atlantic basin (Trenberth and Shea, 2006). The AWP links the AMO and Atlantic TC activity, where SST warming in the low latitudes of the AWP region can decrease the tropospheric vertical wind shear in the Atlantic main development region (MDR; Landsea et al., 1999; Enfield et al., 2001; Nigam and Guan, 2011), constrained to 6°-18°N and 20°-60°W.

The occurrence of major droughts in North America, such as the 1930s Dust Bowl, have occurred during the positive phase of the AMO (Nigam et al., 2011). During these episodes northern Middle America experiences prolonged periods of below-normal rainfall and moisture flux (Méndez and Magaña, 2010; Ting et al., 2014). The AMO also influences the extra tropics by shifting the subtropical ridges and jet streams.

The role of anthropogenic aerosol cooling in the decadal variability of the North Atlantic SSTs and the AMO has been widely discussed. Mann and Emanuel (2006) argued that long-term trends for August–October MDR SST are mainly driven by a combination of regionally enhanced anthropogenic aerosol cooling over the North Atlantic and large-scale SST increase. Trenberth and Shea (2006) found the large-scale anthropogenic warming drives the tropical Atlantic SST trends.

2.3 Sources of the Interannual Variability of Middle America's rainfall

2.3.1 El Niño-Southern Oscillation

The ENSO is a natural mode of interannual variability in the Pacific basin. As first recognised by Bjerknes (1969), ENSO is a recurrent atmosphere-ocean coupled phenomenon linked with the redistribution of atmospheric momentum and heat in the equatorial Pacific. ENSO period roughly is three to seven years, with ENSO events lasting between nine months to three years (McPhaden et al., 2006).

Each ENSO event is characterised by a particular developing and decaying stage, magnitude, duration, and location of the maximum SST anomaly. For example, some events develop mainly in the Eastern Pacific "attached" to the coast of South America, known as canonical ENSO events (e.g., Deser et al., 2010), while others are constrained to the central equatorial Pacific, known as 'Modoki'[2] events (e.g., Ashok et al., 2007). Modoki mode timescales are longer than the canonical modes, having an interannual periodicity of four to twelve years.

The extreme oceanic components of ENSO are termed El Niño and La Niña. El Niño is characterised by anomalously warm SSTs in the central-eastern Pacific and simultaneous anomalously cold SSTs in the Western Pacific; La Niña can be considered as the opposite of El Niño. In general, El Niño events last for nine to fifteen months, while La Niña events last between one to three years; there may be neutral years in between events.

El Niño is usually followed by La Niña but rarely follows La Niña; the period of transition between an episode El Niño and La Niña takes about a year (Larkin and Harrison, 2002). This transition occurs around March-April, in periods when the atmosphere-ocean coupling is weak, characterised by weak near-surface winds and a less pronounced east-

[2] Ashok et al. (2007) defines the meaning of the classical Japanese word 'Modoki' as "similar but different thing".

west equatorial Pacific SST gradient (e.g., Webster and Yang, 1992; Lee et al., 1998).

There are different indices used to define El Niño and La Niña events, based on tropical Pacific SST anomalies averaged across a given region. In this thesis the following indices are employed, which are based on Trenberth (2020):

- Niño 1+2 (0°-10°S, 90°W-80°W), which corresponds with the region of coastal South America;
- Niño 3 (5°N-5°S, 150°W-90°W);
- Niño 3.4 (5°N-5°S, 170°W-120°W), which is used to define El Niño or La Niña events when SST anomalies exceed ± 0.4°C for six months or more;
- Niño 4 (5°N-5°S, 160°E-150°W), which captures SST anomalies in the central equatorial Pacific;
- Trans-Niño index (TNI), which defines the difference in normalised SST anomalies between the Niño 1+2 and Niño 4 regions (Trenberth and Stepaniak, 2001). Large TNI values indicate ENSO "Modoki" events.

When the SST gradient is particularly large (say, due to positive anomalies in the Niño 4 region and negative anomalies in the Niño 1+2 region), some researchers classify the event as a "central Pacific El Niño " or "El Niño Modoki".

The Southern Oscillation (SO) is the atmospheric component of ENSO, which is characterised by a see-saw atmospheric pressure pattern in the Pacific Ocean, often referred to the difference between Darwin, Australia and Tahiti. El Niño and La Niña are dynamically linked with the SO, meaning that changes in the SSTs influence changes in the atmospheric pressure, although pressure does not directly influence SSTs.

The ENSO Dynamics

ENSO perturbs the Walker Circulation through induced wind changes in the equatorial Pacific (Fig. 2.6b). The Walker circulation is a thermally driven zonal circulation located in the tropical Pacific Ocean, which occurs simultaneously with the distribution of tropical surface heating. The Pacific Walker circulation influences the cloud cover, short-wave and long-wave radiation, latent heat flux, precipitation and atmospheric moisture (Bayr et al., 2018). The Walker circulation plays a fundamental role in the distribution of convection in the Pacific Ocean. Under normal conditions, the Walker circulation is easterly in the surface and westerly in the upper-troposphere, while cold water is pushed west by the surface wind, forming an SST gradient along the Pacific (Fig. 2.6a) and the cold upwelling ocean water in the east. This circulation is possible because the surface winds drive ocean currents; the ocean currents distribute surface thermal gradients. The wind-SST feedback is also caused by a zonal shift in atmospheric deep convection which is linked to the rising branch of the Walker circulation (Bayr et al., 2018). The positive feedback described above is known as the Bjerknes feedback mechanism, which is the dominant positive feedback that leads to the development of an ENSO event.

The ENSO development is caused by an initial westerly stress anomaly in the central Pacific, triggering downwelling equatorial oceanic Kelvin waves that propagate eastwards with a wave speed of 2-3 $m{\cdot}s^{-1}$ taking about three months to cross the Pacific. As a consequence of the Kelvin wave propagation, the upwelling is reduced and the thermocline deepens in the East Pacific and shoaled in the West Pacific (Fig. 2.7b). During canonical El Niño, the easterly near-surface winds weaken, which allows Pacific warm subsurface water to migrate eastwards through downwelling equatorial oceanic Kelvin waves (Fig. 2.7b). An east-propagating oceanic Kelvin wave reaching the eastern South American coast is reflected as an upwelling Rossby wave. This Rossby wave spreads along the coast both sides of the equator within 10° latitude and returns to the Western Pacific in about 8 months following a westward propagation (Laing and Evans, 2016). This delayed negative feedback shoals the thermocline and inverts the sign of the SST anomalies in the Eastern Pacific (Wang, 2018), starting La Niña events.

During El Niño events, the zonal sea-level pressure (SLP) gradient and the Walker circulation weaken (McPhaden, 2003). Convection associated with rising branches of the anomalous Walker Circulation shift east along with the warmer central Pacific SSTs. Convection is also enhanced over tropical Africa and suppressed over the Caribbean (Fig. 2.6b).

Canonical La Niña enhances the Walker circulation and its associated near-surface easterly trade winds that blow from the colder Southeastern Pacific (where the atmospheric pressure is higher) towards a region of lower pressure in the warmer West Pacific (Fig. 2.6c). The combined effects of the enhanced easterly winds and the Coriolis force strengthen the climatological equatorial Ekman upwelling into the East Pacific. As a result, the sea level rises in the West Pacific and drops in the East Pacific (Chu, 2004) (Fig. 2.7a). Convection is enhanced in the Maritime continent and the Caribbean, and suppressed in tropical Africa (Fig. 2.6c).

(a)

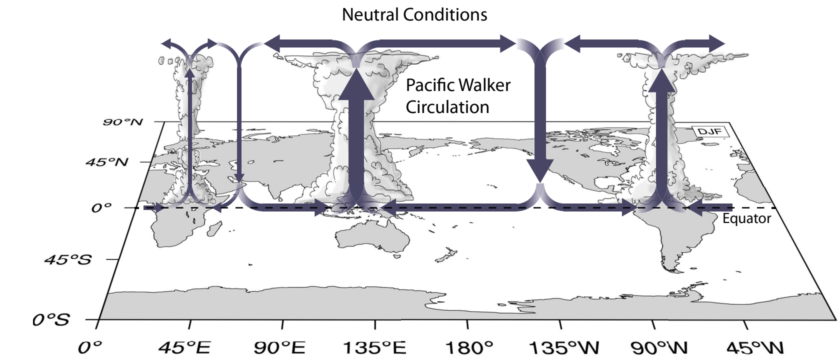

(b)

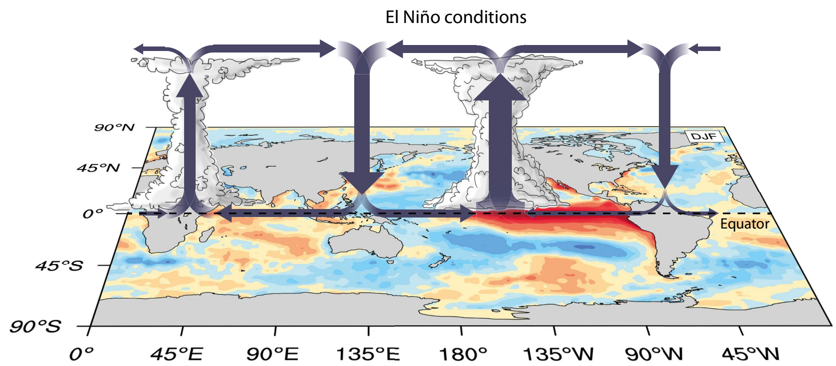

(c)

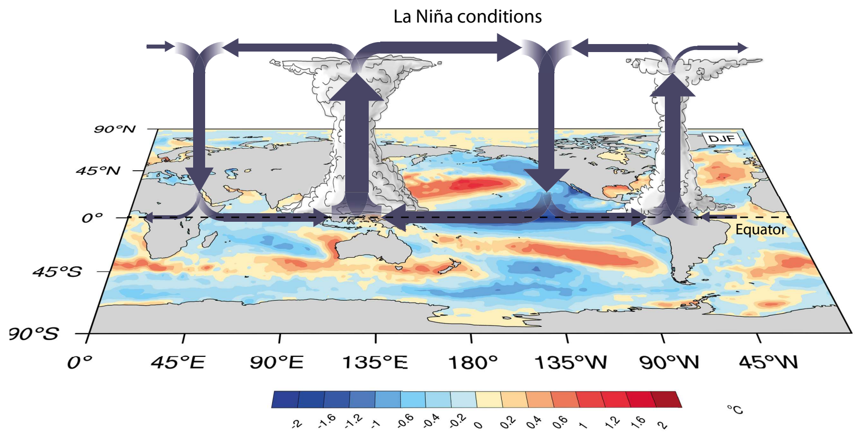

Figure 2.6: Generalized Walker Circulation during DJF (a) ENSO-neutral, (b) El Niño, and (c) La Niña conditions. During (a) ENSO neutral, convection associated with rising branches of the Walker Circulation is found over the Maritime continent, northern South America, and eastern Africa. Schematics adapted from NOAA Climate.gov. SST anomalies calculated from the NOAA Optimum Interpolation Monthly SST (OISST; Reynolds et al., 2002).

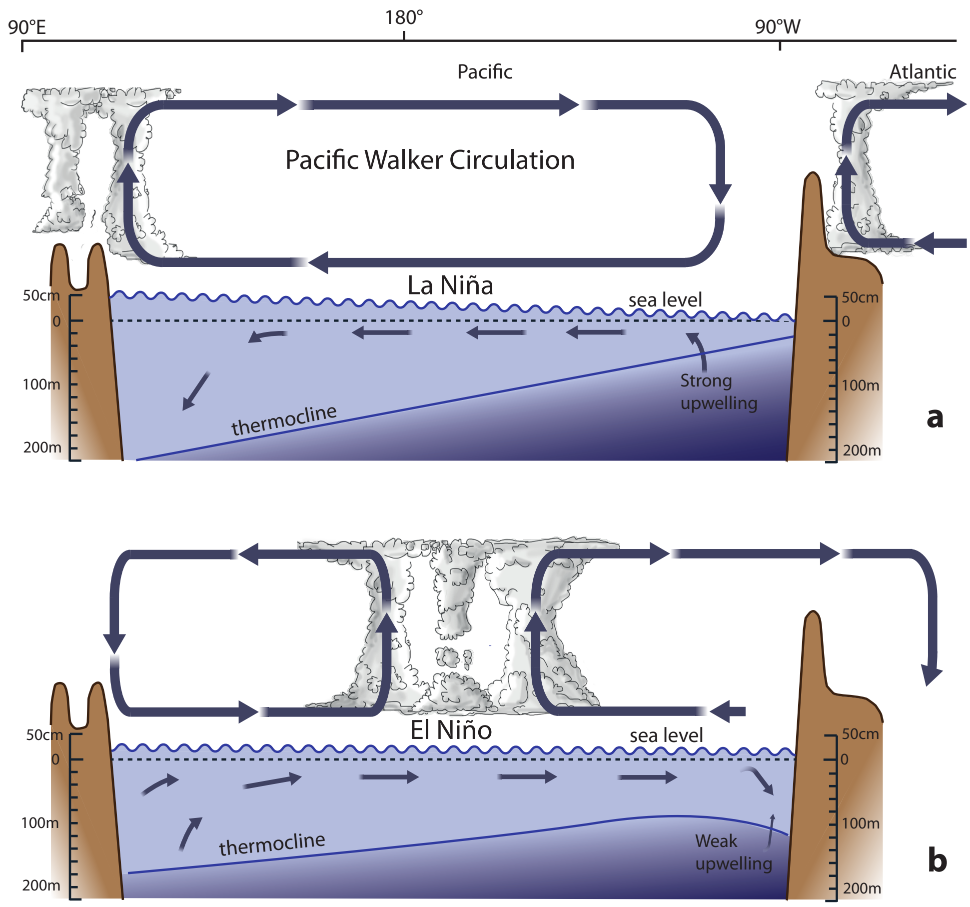

Figure 2.7: Schematics showing the near-equatorial atmosphere and ocean circulations in the Pacific and western Atlantic associated with (a) La Niña and (b) El Niño conditions. Adapted from Chu (2004).

Two major components of negative feedback that lead to an ENSO event to decay come from the surface net heat flux feedback (Guilyardi et al., 2009): (1) the cloud-SST feedback, which influences the incoming shortwave radiation at the surface due to changes in cloudiness. This feedback is more relevant over the western equatorial Pacific since the largest changes in deep convection occur there. (2) The evaporation-SST feedback, which is more relevant in the eastern equatorial Pacific where the change of SSTs are largest (Bayr et al., 2018). A third negative feedback that is related to the adjustment of the equatorial Pacific thermocline to the wind field is also important. This last one is related with the time delay that conducts to the decay of an event (Deser et al., 2010).

Two paradigms have been postulated to explain ENSO dynamics. One paradigm proposes ENSO as a system of self-sustained regular oscillations, which is represented in conceptual models such as as the Delayed Oscillator or Recharge Oscillator Theory (Suarez and Schopf, 1988; Battisti and Hirst, 1989), the Recharge/discharge Theory (Jin, 1997), the Advective-Reflective Oscillator (Picaut et al., 1997), the Western-Pacific Oscillator (Weisberg and Wang, 1997), and the Unified Oscillator Theory, which tries to combine the previous oscillation mechanisms (Wang and Enfield, 2001).

A second paradigm suggests the stochastic forcing theory where ENSO is considered a damped stable mode interacting with high-frequency forcing that provides the energy required to mantain the oscillation. This hypothesis considers the Madden-Julian Oscillation (MJO, see sec. 2.4.2) and westerly wind bursts as energetic weather systems that act as the stochastic forcing in the atmosphere (e.g., Penland and Sardeshmukh, 1995; Moore and Kleeman, 1999) while high frequency variability associated to tropical oceanic waves acts as oceanic stochastic forcing (An, 2008).

Ashok et al. (2007) suggests that the two aforementioned paradigms for canonical ENSO might also apply to Modoki ENSO modes as well since the equatorial easterly (westerly) wind anomalies are always located to the east (west) of the anomalously warm SSTs (Wang, 2018). Jadhav et al. (2015) identified strength of the aforementioned zonal winds and oceanic condition as the ones that determine the canonical and Modoki events of ENSO.

ENSO teleconnections

ENSO is accompanied by changes in deep tropical convection through changes in the global atmospheric circulation. The location of the anomalously warm SSTs during a particular El Niño determines the global climate impacts. During a canonical El Niño boreal winter (DJF), the Walker circulation shifts its rising branch to the east side of

180°longitude. This shift substitutes the usual rising branches in the southern Mexico, Central America, Caribbean Sea and the Maritime continent for strong sinking branches, which are accompanied by anomalous strong divergence in the low-levels of the atmosphere (Fig. 2.6b) and to below-average rainfall in those regions.

The East Pacific ITCZ normally remains in the Northern Hemisphere throughout the year, except during El Niño episodes, where the ITCZ anomalously shifts equatorwards (Toma and Webster, 2010a) as surface waters warms (McPhaden, 2003). In boreal spring the eastern Pacific ITCZ splits due to the weakening of the southeast trade winds, which weaken the equatorial coastal upwelling. This leads to the anomalous warming of the SSTs south to the equator (Waliser and Gautier, 1993). On the contrary, the eastern Pacific ITCZ anomalously shifts northwards during La Niña.

The interannual variability of the Chocó-jet is driven by gradients of SSTs from region Niño 1+2 and the Colombian Pacific (Poveda and Mesa, 1999), with La Niña (El Niño) strengthening (weakening) the jet. Arias et al. (2015) found that anomalies of rainfall in northern South America depend on the combined effects of the CLLJ and the Chocó-jet variability associated with the ENSO. For example, El Niño Modoki leads to above-average rainfall in southern Mexico and some parts of Central America during summer, and below-average temperatures in Colombia, Venezuela, and some regions of Mexico (Ashok et al., 2007).

Changes in the location of deep tropical convection in the equatorial Pacific during ENSO are also accompanied by anomalous low-level convergence, upper-level divergence and anomalous tropospheric heating that generates teleconnections. The ENSO teleconnections refer to the effect of ENSO outside the tropical Pacific, which are stronger for the extratropics in winter. For example, the anomalous tropospheric heating during El Niño is accompanied by anomalous upper-level atmospheric vorticity, in which its horizontal component forces large-scale atmospheric Rossby waves that propagate into the extratropics to excite the Pacific North American Pattern (PNA) (Hoskins and Karoly, 1981). Canonical El Niño teleconnections also involve anomalous surface heat fluxes and Ekman transport that create positive SST anomalies along the west coast of North America (Alexander and Scott, 2002).

An "atmospheric bridge" (Alexander and Scott, 2002) between the tropical and North Pacific, during both canonical and Modoki El Niño, is linked to an enhanced Aleutian low (Kim and Alexander, 2015) and anomalous low pressure over the northeastern Middle America. This configuration of anomalous pressure enhances moisture transport from the subtropical Pacific into the western U.S. and northern Middle America. El Niño Modoki is associated with an equatorward shift of the enhanced Aleutian low over the North Pacific relative to the canonical El Niño, which increases moisture transport towards central and northern Middle America. Canonical El Niño is related with anomalous southerly advecting warm moist air along the west coast of North America (Deser et al., 2010). Moisture transport increases from the northward shifted ITCZ to northern Middle America during El Niño Modoki (Weng et al., 2007).

ENSO influences the strength and location of the subtropical highs and subtropical jet streams. El Niño promotes the eastward extension of the North Pacific subtropical jet to the extreme eastern Pacific, as well as a southward shift and strengthening. This southward shift in the storm track brings above-normal precipitation in the north of Middle America during boreal winter. In contrast, La Niña reduces convective activity in the East Pacific and deep tropospheric heating in the West Pacific. This anomalous tropospheric heating contracts the Pacific subtropical ridge to West of the date line and reduces the meridional gradient of temperature in the subtropical eastern Pacific (CPC, 2005). Similar anomalies are observed in the subtropical jet in the southern hemisphere.

The North Atlantic responds to the ENSO-related heating sources through an atmospheric bridge; this bridge occurs through anomalies in the Hadley and Walker cells, Rossby waves, and interactions between the quasi-stationary flow and storm tracks. Figure 2.8 illustrates the tropical Atlantic response to canonical El Niño, which is a result of the weakening of the Pacific Walker circulation, the Western Pacific Hadley circulation and the Atlantic Hadley circulation, as well as the concurrent strengthening of the eastern Pacific Hadley circulation (Wang, 2004). Simultaneously, the NASH weakens and surface pressure reduces over the equatorial Atlantic. These anomalies lead to anomalously warm SSTs to the North of the equator, approximately three to six months following the peak of the ENSO-related SST anomalies in boreal spring (Covey and Hastenrath, 1978; Enfield and Mayer, 1997). Through this mechanism ENSO influences the interannual variability of the WHWP, inducing and anomalously warming of the Atlantic warm pool during decaying El Niño.

The global ENSO-TC connections make it possible to forecast seasonal TC activity. Through changes in large-scale environmental conditions and its teleconnections, ENSO modulates global TC activity, such as genesis, tracks, landfall location, and intensity (Camargo et al., 2007; Aiyyer and Thorncroft, 2011; Zheng et al., 2015; Fu et al., 2017). For example, during developing El Niño years, western North Pacific (WNP) TCs tend to track closer to the international date line (Bell et al., 2014). Additionally, the WNP TCs are long-lived and larger in size during these episodes (Chan and Yip, 2003). On the other hand, TCs drop in frequency in this basin during decaying El Niño years (Chan, 1985).

Developing El Niño also influences the central and eastern North Pacific TC activity by shifting it towards the dateline (Fu et al., 2017) and increasing their life-time (Chu, 2004; Bell et al., 2014; Toma and Webster, 2010a).

The influence of ENSO on the North Atlantic TC activity has been widely discussed in the literature. Firstly addressed by Gray (1984), during developing El Niño (La Niña) years there is a reduction (increase) in the number of North Atlantic TCs. Many studies have confirmed the suppressive effect of El Niño on the North Atlantic TC activity (Patricola et al., 2014). Section 2.5.1.5 of this thesis offers an extended literature review on the ENSO effect over TC activity in both the North eastern Pacific and the Atlantic Ocean.

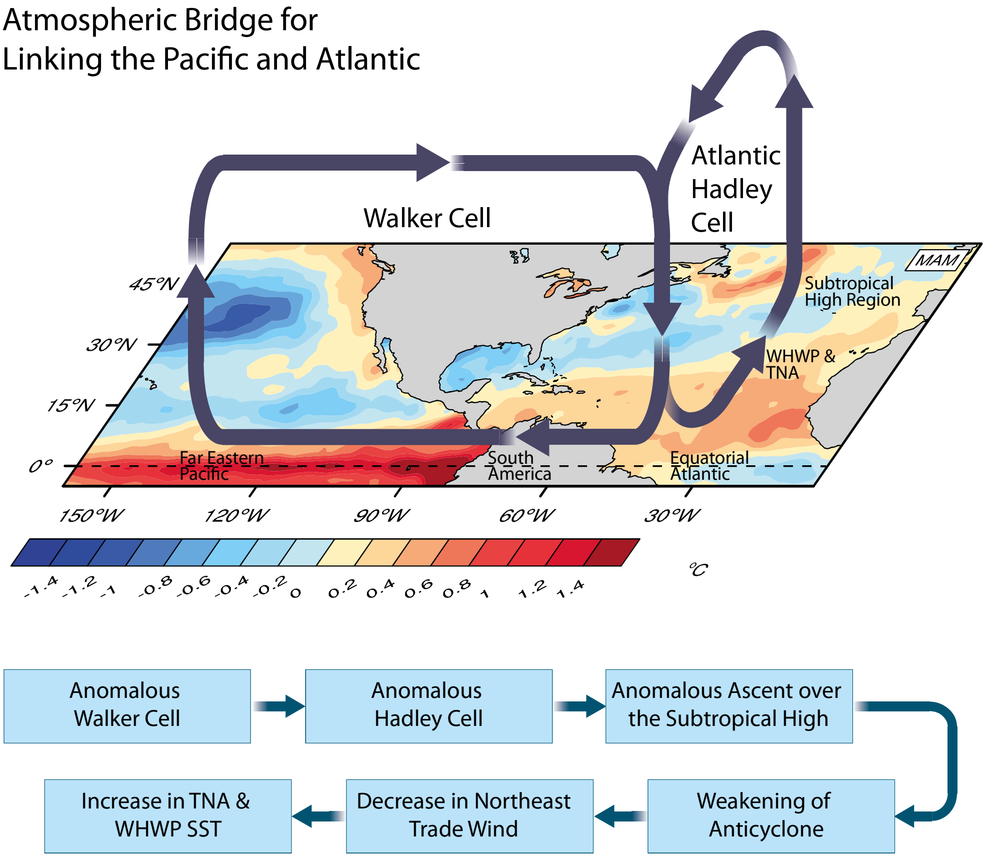

Figure 2.8: Schematic diagram showing linkage of the Pacific El Niño with the tropical North Atlantic and the Western Hemisphere warm pool by the Walker and Hadley circulations. Adapted from Wang (2004).

2.3.2 The Atlantic Niño and the Atlantic Meridional Mode

The tropical Atlantic variability is characterised by a period of two to three years with two principal oceanic modes of interannual variability: the Atlantic 'Niño' (Zebiak, 1993), which is the Atlantic equatorial mode similar to the Pacific El Niño (Deser et al., 2010), and the Atlantic Meridional Mode (AMM; Chiang and Vimont, 2004).

The Atlantic Niño is characterised by SST anomalies in the central and eastern equatorial Atlantic, peaking in May-July, with an amplitude usually smaller than +1°C. This mode of variability is associated with significant shifts in the Atlantic Walker and Hadley Circulations (Wang, 2004). The Atlantic Niño ocean-atmospheric interactions follow the Bjerknes positive feedback. During the warm phase, anomalously warm SSTs are found in the central equatorial Atlantic, accompanied by anomalous westerlies in the western Atlantic, which oppose the climatological easterlies. The Atlantic Niño significantly affects rainfall over South America and Africa, resulting from low-level anomalous convergence of the Atlantic ITCZ moving towards the warmer side of the SSTs.

The AMM is a coupled ocean-atmosphere mode of interannual variability characterised by cross-equatorial SST anomaly gradients in the Atlantic, with subtropical SST anomalies ≈ 0.5°C, peaking in boreal spring (MAM). The AMM is also characterised by boundary layer winds flowing towards the anomalously warmer SST, which, influenced by the Coriolis force, turn right in the northern hemisphere, and left in the southern hemisphere (Vimont and Kossin, 2007). The wind-evaporation-SST (WES; Xie and Philander, 1994) feedback is the primary driver of the evolution of the AMM (e.g., Amaya et al., 2017). The WES is characterised by weaker winds over the warmer hemisphere, whereas the colder hemisphere experiences stronger winds by the Coriolis effect. This mechanisms reinforces the cross equatorial SST gradient through opposite-signed changes in surface evaporation between the two hemispheres.

Positive AMM is linked to a negative SLP anomaly over the western tropical Atlantic, positive SST anomalies over the subtropical North Atlantic and reduced vertical wind shear (Smirnov and Vimont, 2011). The AMM affects North Atlantic hurricanes through its influence on SST in the MDR (Kossin and Vimont, 2007; Vimont and Kossin, 2007).

2.3.3 The North Atlantic Oscillation

The North Atlantic Oscillation (NAO) is an Atlantic mode of intraseasonal to interannual variability expressed as redistribution of atmospheric mass in the North Atlantic:

anomalous mean sea-level pressure (MSLP) in the subtropical Atlantic and the northern Atlantic, linked to the NASH and the Icelandic low, respectively. The NAO influences boreal winter rainfall over North America and Europe through changes in the location and intensity of the North Atlantic jet stream.

The NAO positive phase is characterised by strong low-level westerly winds between an enhanced Icelandic low and an enhanced NASH, particularly in winter. The prevailing conditions during the positive phases are above-normal geopotential height and surface pressure over the central North Atlantic, western Europe and the eastern U.S.. Fewer winter storms and cold-air outbreaks over eastern North America occur during these episodes. Opposite-signed patterns occur during the negative NAO.

During boreal summer, the NAO influences the North Atlantic TC tracks through changes in the strength and location of the NASH. More TCs make landfall over the eastern U.S. coast during positive NAO, whereas the Gulf Coastal Plain is more susceptible to TCs making landfall during negative NAO (Elsner, 2003). Wang (2007) suggested that the NAO varies in phase with the CLLJ: the positive (negative) NAO is related with a stronger (weaker) NASH and CLLJ.

2.4 Sources of Intraseasonal Variability of Middle America's climate

2.4.1 The 10–30-day modes

During the boreal summer, vigorous convection appears over the eastern Pacific and Middle America, which exhibits variability on 10–30-day scales. A first dominant mode of rainfall (east-west mode) is characterised by trans-Pacific Rossby wave train, extending from the western North Pacific to the East Pacific/North America along a large-scale circular path (Jiang and Lau, 2008). This is the primary mode of intraseasonal variability that affects the NAMS, with the MJO being a secondary mode of variability (Mo, 2000). The rainfall associated with this mode first emerges near the eastern Pacific at about $20°N$ and the Gulf of Mexico. Afterwards, the rainfall moves to the southwestern U.S. along the slope of the Sierra Madre Occidental (Jiang and Waliser, 2008).

The intraseasonal variability of the NAM and the rainfall events over the Great Plains are also dominated by a second 10–30-day mode (west-east mode). This mode is linked with heavy rainfall events in the western Atlantic, Caribbean, Gulf of Mexico, and East Pacific. This mode is characterised by a westward propagation of convection from Africa along 15°N (Wen et al., 2011).

A third mode, known as the north-south mode, propagates eastward from the western Pacific and then northward into North America (Wen et al., 2011). This mode has a periodicity of about 18 days and it is detected in the rainfall field over the eastern Pacific ITCZ. This mode is not associated with a trans-Pacific Rossby wave train (Jiang and Waliser, 2008, 2009).

2.4.2 The 30-90-day modes

The MJO (Madden and Julian, 1971, 1972) is the dominant mode of intraseasonal variability in tropical convection. This oscillation is characterised by eastward moving organised convection, rainfall, pressure, and winds near the equator with a period of approximately 30 to 90 days, mostly starting in the western or central Indian Ocean. The MJO tends to propagate at $\approx 5-7$ m·s^{-1} (Roundy and Kiladis, 2006). The MJO signal is not always present but it has been observed in all seasons, with stronger events occurring in boreal winter and spring; it is more frequent in the Pacific during El Niño, and in the Indian Ocean during La Niña.

The atmospheric structure associated with the MJO is baroclinic, characterised by enhanced and suppressed equatorial convection and upper-level divergence, formed by super cloud clusters (SCCs). As the convection approaches, easterly (westerly) trade winds are enhanced at the Equator at low levels (aloft). This flow creates counter-rotating vortices north and south of the Equator. Convergence and ascent are located with MJO convection, and westerly winds follow convection. The convective signal of the MJO is strongest over the Indian and Pacific Oceans. For scientific purposes, the location of the MJO enhanced convection is grouped into 8 (broad) regions, also known as MJO phases (Wheeler and Hendon, 2004).

The MJO affects subtropical and extratropical flow patterns at intraseasonal time-scales through waves that communicate the MJO forcing to the remote circulation (e.g., Moore et al., 2010). The MJO can influence changes in jet streams and adjustments in the precipitation patterns in the eastern tropical Pacific, with increased precipitation over the warm pool to the west of Middle America in boreal summer (Higgins and Shi, 2001): during the convectively active phase of the MJO in the East Pacific (e.g., phases 1 and 8), the trade winds weaken in the eastern tropical Pacific, and favour the formation of an anomalous cyclonic circulation over western Middle America. Moisture is transported from the eastern tropical Pacific to Middle America, where it converges into the ITCZ.

Conversely, the convectively inactive phases of the MJO (e.g., phases 2 and 3) are characterised by enhanced trade winds over the eastern tropical Pacific, accompanied by an anomalous anticyclonic circulation to the west of Middle America. During these phases anomalous moisture is transported from Middle America to the eastern tropical Pacific, accompanied by decreased rainfall over southwestern and western Middle America. This directly influences the intraseasonal variability of the North American Monsoon (Higgins and Shi, 2001; Lorenz and Hartmann, 2006). Higgins and Shi (2001) suggest that the propagation of an MJO active event from the eastern tropical Pacific to the Atlantic, increases rainfall over the Gulf of Mexico and portions of the southeastern Middle America.

The MJO also influences TC activity globally (Klotzbach, 2014; Camargo et al., 2009). Its impact in the IAS TC activity has been widely documented (Maloney and Hartmann, 2000a,b; Aiyyer and Molinari, 2008). The convective phase of the MJO promotes significant barotropic energy conversions from the mean state to the eddies, which modulates tropical cyclogenesis (Hartmann and Maloney, 2001). Maloney and Hartmann (2000a) showed the influence of the MJO in the East Pacific and the Gulf of Mexico, defining active and inactive MJO phases over the East Pacific. These phases correspond to an anomalous westerly jet at around 10° N in the East Pacific and cyclonic circulation at 850 hPa to the North over the eastern Pacific and the Gulf of Mexico. Particularly, the active (inactive) phase of the MJO has been linked with more (fewer) frequency of tropical cyclones in the eastern North Pacific and the Gulf of Mexico (e.g., Maloney and Hartmann, 2000a; Aiyyer and Molinari, 2008). Yu et al. (2011) found evidence of MJO signals propagating to the Atlantic across Central America and the Caribbean Sea during boreal winter and spring, suggesting that MJO influences intraseasonal variability in the tropical and subtropical Atlantic.

The tropical eastern North Pacific also experiences intraseasonal variability on 30–90-day timescales that is linked with the variability of ITCZ rainfall (Jiang and Waliser, 2009). This mode has a maximum amplitude during boreal summer and a structure similar to the MJO, but it has been suggested to be a mode independent from the MJO (Rydbeck et al., 2013): since the MJO emits eastward-propagating dry Kelvin waves, they can link with the east Pacific, which provides a possible phase locking mechanism between the two hemispheres.

2.5 Synoptic contributors to Middle America's rainfall and associated moisture transport

2.5.1 Tropical cyclones

Variability in Middle America's hydrological cycle is linked to the occurrence of extreme hydrometeorological events, such as TCs from the East Pacific and the North Atlantic basin. In the East Pacific, the TC season usually starts in June over an area close to the west coast of Mexico at about 10-20° N. Atlantic TCs are most likely to develop during August-October. The MDR for TCs in the tropical North Atlantic extends from the west coast of Africa to the tropical Atlantic between 6°N and 18°N, and 20°W and 60°W (Mann and Emanuel, 2006).

TCs are non-frontal atmospheric disturbances that develop over the tropical ocean (25°S to 25°N); they are characterised by a structure that consists of a warm-core with low atmospheric pressure, with persistent, organised convection, and a well-organised, cyclonic, near-surface wind circulation (Frank, 1977). According to the World Meteorological Organization (WMO; Neumann, 2017), TCs are classified by intensity using the 10-metre wind speeds, with peaks sustained for 1, 3, or 10 minute, depending on the TC-basin. In the Eastern Pacific and North Atlantic basins, tropical cyclones are classified based on 1-minute average winds, as follows:

• Tropical depressions, which have maximum sustained surface winds (10 minute averaged wind speed) less than 17.5 m·s^{-1} (34 kt).

• Tropical storms, which have maximum sustained surface wind speeds 17.5-33 m·s^{-1} (34-64 kt).

• Hurricanes (in the Atlantic or East Pacific Oceans) have maximum sustained surface winds in excess of 33 m·s^{-1} (64 kt). They are also known as typhoons in the northern West Pacific, or severe cyclonic storms in the North Indian Ocean and southern hemisphere.

2.5.1.1 Large-Scale Conditions Necessary for Tropical Cyclone Formation

According to the original definition of Gray (1968), TCs develop over the tropical oceans under at least six necessary but not sufficient conditions for tropical cyclogenesis:

(1) Low vertical wind shear between the surface and the upper troposphere (less than 10 m·s^{-1}): large vertical wind shear can prevent TC genesis or weaken or destroy a TC

by interrupting the organisation of deep convection around the TC centre.

(2) A minimum distance from the equator (of at least 5° in latitude): this condition provides the necessary planetary vorticity for TC development. TCs typically form in the tropics, between $5°-20°$ latitude. At higher latitudes TCs usually dissipate or undergo extratropical transition.

(3) A pre-existing disturbance with sufficient vorticity and near-surface convergence: some tropical disturbances (e.g., easterly tropical waves) develop into TCs.

(4) Warm ocean waters of at least 26.5°C, over a relatively large depth ($\approx$ 50 m): the necessary heat energy and moisture for TC development comes from ocean-atmosphere latent heat flux.

(5) Conditional instability near the mid-troposphere: This promotes the development of deep, moist convection in the vicinity of a tropical disturbance.

(6) Moist lower to middle troposphere: Deep layers with large relative humidity decrease the likelihood of potentially destructive convective downdrafts on the lower-tropospheric circulation of the initial disturbance.

Nowadays, and in particular under climate change, threshold SSTs Gray (1968) are no longer considered a criteria for the occurrence of TCs (Tory and Dare, 2015). Besides, there also exists much regional variability (Defforge and Merlis, 2017). More recent discussions focus on other variables that are not based on thresholds, for instance potential intensity (Emanuel, 1995) and relative SST (Dare and McBride, 2011; Tory and Dare, 2015).

2.5.1.2 Structure of a tropical cyclone

TCs extend through the troposphere to the lower stratosphere, reaching heights of about 15-18 km. On the horizontal plane, TCs size are about 5 degrees radius although they can vary considerably (e.g., Xu et al., 2017). The TC circulation is in gradient wind balance, which means the pressure gradient force opposes the Coriolis and centripetal forces. This balance exists above 2 km of the surface. In the first 2 km the surface friction is an important source of TC kinetic energy as it breaks the gradient balance. The TC air spirals due to the existent vorticity, and accelerates toward the TC centre. This air spirals upward to the eye wall or into the spiral rain bands, to finally spiral outward aloft below the tropopause (Laing and Evans, 2016).

The low-level convergence forces convection, for example, under the eyewall, where a frontal mechanism prevails. Also, thermal instability can drive strong upward motion near the centre of the storm, producing convection in the eyewall. This results in cirrus shields that may extend 2 horizontal degrees from the centre of the TC.

Due to the thermal wind relationship of a rotating fluid, the temperature of the TC decreases outward proportionally to the rate at which the vertical wind decreases upward (Emanuel, 2005). The relative humidity increases with the air flowing towards the TC centre. Usually, a mature TC has its strongest winds around the eyewall, decreasing outwards from the centre of the TC, where the gale winds may extend horizontally 5°. In the vertical, the strongest winds are found in the lower troposphere, weakening with height. The more intense winds and rainfall are found in the eyewall (within 100 km of the TC centre).

2.5.1.3 Processes of development of a tropical cyclone

The TC development requires the aforementioned prevailing conditions (sec. 2.5.1.1). Besides these, a sequence of different thermodynamic and dynamic processes might lead a TC to weaken or strengthen:

Genesis of a tropical cyclone. For an initial perturbation to become a TC depends primarily on the environmental conditions to trigger deep, moist convection, and on the Rossby radius of deformation of the lower-tropospheric convergence associated to the perturbation. The first stage of TC genesis occurs over a period of 12 to 24 hours, characterised by convection growing upscale to form a mesoscale convective system (MCS; Zehr, 1992). Stratiform rainfall associated with the MCS results in diabatic warming in the mid-troposphere and diabatic cooling in the low-troposphere. This process amplifies cyclonic vorticity generation and stretching (developing a mid-tropospheric mesoscale convective vortex), as a result of the concentration of ascent in the lower troposphere.

A common mechanism for the TC genesis is the interaction of a tropical wave (equatorial wave or an easterly wave; see sec. 2.5.2) with the tropical upper-tropospheric trough that will locally enhance low-level convergence and thus moist convection, providing a favourable environment for TC genesis.

Dunkerton et al. (2009) introduced the marsupial paradigm, which is a conceptual framework to describe the transition sequence from synoptic-scale easterly wave to tropical depression. This framework describes how a hybrid diabatic Rossby wave or a vortex (that exists in a wave critical layer), could become a tropical depression and, therefore, evolve into a TC (e.g. Montgomery et al., 2010). Such paradigm introduced a sequence of three hypothetic physical mechanisms that involve the following: (a) a vortical organisation of the critical layer at scale meso-α, (b) moisture supply to the proto-vortex and protection from dry or dusty air outside (”pouch” mechanism), and (c) a mutually beneficial interaction of wave and vortex.

The tropical cyclone vortex and warm core development. The presence of the mid-tropospheric mesoscale convective vortex and the deep, moist convection, plays a key role in the development of a lower tropospheric vortex. Later, the latent and sensible heat fluxes from the ocean to the atmosphere increase boundary-layer equivalent potential temperature via warming and moistening. Eventually, the weak vertical wind shear of the lower- and middle-tropospheric vortices align vertically. The intensification of mesoscale convective vortex decreases dry air infiltration into the centre of the disturbance. During TC development, the latent heat flux and convection must sufficiently warm and moisten the boundary layer to support deep, moist convection to subsequently renew thunderstorm development. At this stage, the mid-troposphere shows significantly higher moisture compared to the first stage of TC genesis; as a consequence, the downdraft activity driven by evaporation is largely suppressed, enhancing convection.

Strengthening and weakening of a tropical cyclone. The main sources of energy (latent heat flux from evaporation and sensible heat flux) and moisture of a TC come from the warm, tropical oceans. The continuous release of latent heat by condensation in the warm core maintains the TC baroclinic structure and generates available potential energy, which is converted into kinetic energy (Anthes, 1974). High water vapour in the Ekman boundary layer is necessary for moisture convergence and strong condensational heating in a TC. The influx of vapour water into a TC across its lateral boundaries and from surface evaporation must be at least equal to the precipitation (Anthes, 1974).

A TC weakens when there are not enough sources of energy and moisture to feed the clouds that drive it: when a TC makes landfall, it weakens due to the lack of the moisture source from the ocean, which eventually weakens the convection. TCs passing overland will also weaken due to greater surface friction.

2.5.1.4 Climatology of tropical cyclones activity in the eastern North Pacific and the North Atlantic

The eastern North Pacific TC season usually starts in June and extends to November (e.g., Prat and Nelson, 2013a). In this basin TC genesis mainly occurs over the EPWP and can be triggered by tropical easterly waves initiated by local instabilities (e.g Serra et al., 2008; Toma and Webster, 2010a) or by cross-isthmus propagation (Raymond et al., 2006). During boreal summer, South Pacific southeast trades crossing the equator prevail and turn northwestwards in the eastern North Pacific; TCs generally track to the NE and gradually weaken over cooler SSTs; however, some TCs track northeastwards and make landfall over Middle America. Seasonally, JJA is the peak TC activity in the eastern Pacific basin (Fig. 2.9).

In the Atlantic basin, which includes Atlantic Ocean, Caribbean Sea, and the Gulf of Mexico, TC activity peaks mostly between June and November (Fig. 2.9); more than 80% of TCs form in August, September and October (Chu, 2004). On the synoptic time scale, African easterly waves (Thorncroft et al., 2008; Patricola et al., 2018) are some of the disturbances that originate Atlantic TCs.

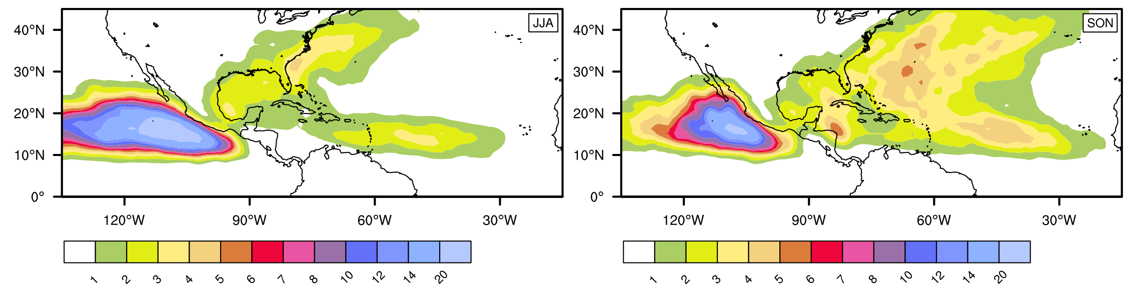

Figure 2.9: Seasonal climatology of TC track densities for JJA and SON calculated with 1979-2015 TC tracks from the The International Best Track Archive for Climate Stewardship (IBTrACS; Knapp et al., 2010).

2.5.1.5 Variability of tropical cyclone activity of eastern North Pacific and North Atlantic

Modes of variability at different temporal scales can influence key climate factors for TC activity (genesis, intensity, frequency), as well as their individual trajectories. The dependence of the interannual variability of TC activity on large-scale modes of variability has been extensively studied. TC variability has been related to large-scale modes of subseasonal, interannual, and decadal variability, such as the MJO (Molinari et al., 1997; Maloney and Hartmann, 2000a,b; Aiyyer and Molinari, 2008; Camargo et al., 2009; Kossin et al., 2010), the ENSO (Gray, 1984; Camargo et al., 2007; Kossin et al., 2010; Patricola et al., 2014; Lim et al., 2016), the AMM (Vimont and Kossin, 2007; Kossin and Vimont, 2007; Kossin et al., 2010; Colbert and Soden, 2012), the NAO (Kossin et al., 2010), the AMO (Goldenberg et al., 2001; Kossin and Vimont, 2007) and the PDO (e.g., Méndez and Magaña, 2010).

Decadal SST variability in the Pacific and the Atlantic (e.g., Shapiro and Goldenberg, 1998; Wang et al., 2011) influence TC activity. For example, Méndez and Magaña (2010) found that the negative PDO is anticorrelated with the CLLJ. They suggest that a weakened CLLJ enhances tropical easterly wave (EW) activity in the Caribbean Sea, which promotes convection over southern Middle America and Central America and reduces moisture flux into Middle America. In consequence, this also promotes TC activity in the Caribbean (e.g., Wang, 2007). The AMO is strongly linked with multidecadal Atlantic TC variability (Goldenberg et al., 2001): the positive AMO (warmer Atlantic SSTs) favours more intense Atlantic TCs.

ENSO has been suggested as one the most predictable factors that influences interannual variability of TC genesis in different oceanic basins (Camargo et al., 2007). ENSO influences Atlantic TC activity through induced positive (negative) anomalies of tropospheric vertical wind shear, reduction (enhancement) of relative humidity, and subsidence (convergence) (Gray, 1984; Goldenberg and Shapiro, 1996; Chu, 2004) during El Niño (La Niña).

The interannual variability of Caribbean TC genesis and the CLLJ are linked through changes in the vertical wind shear during ENSO events (Wang, 2007): the CLLJ strengthens during El Niño as a consequence of a weakened Walker circulation, increasing the vertical wind shear and inhibiting the Caribbean TC genesis. Oppositely, La Niña weakens the CLLJ and reduces of wind shear, which favours the TC genesis in the Caribbean Sea.

ENSO impacts on Caribbean TC activity are not symmetric: El Niño has a stronger influence on the north, and a weaker influence on the east and the west; whereas La Niña is linked to a basin-wide increase in TC activity (Laing and Evans, 2016). In the eastern North Pacific, El Niño increases TC frequency on the western side of the eastern North Pacific and reduces TC frequency on the eastern side nearshore Middle America, whereas La Niña typically brings opposite conditions (Fu et al., 2017).

In the Atlantic basin, the NAO influences TC genesis and trajectories (Rodwell and Hoskins, 2001). During the negative phase of the May-June NAO, the NASH weakens, allowing Atlantic TCs with genesis in the MDR to follow a more northeastern track (Kossin et al., 2010). Atlantic TC trajectories are steered by the surrounding large-scale flow through the depth of the troposphere (850 – 200 hPa, approx.). The location and strength of the NASH influences Atlantic TC trajectories: easterly flow prevails on the equatorward side of the NASH, and westerlies on the poleward side of the NASH. When the NASH is strong, the associated steering flow of its anticyclonic circulation results in TCs remaining close to the equator and displacing westwards. The opposite occurs when the NASH is weak, allowing TCs to turn northward and, later, eastward by following the poleward steering flow.

The AMM modulates Atlantic TC activity through its influence on tropical Atlantic SSTs (Kossin et al., 2010; Patricola et al., 2014; Lim et al., 2016), particularly in the Atlantic MDR (Vimont and Kossin, 2007). The positive phase of the AMM is related with equatorial Atlantic warm SSTs and reduced vertical wind shear in the subtropical North Atlantic, which enhance TC activity (Smirnov and Vimont, 2011).

The MJO is the dominant control on variability in the intraseasonal TC activity. Klotzbach and Oliver (2014) showed a positive correlation between the MJO enhanced convection over the western Indian Ocean and Africa (e.g., MJO phases 1 and 2) and TC activity in the North Atlantic. When combined with favourable phases of the MJO, La Niña or positive AMO could lead to enhanced North Atlantic TC activity. El Niño or negative phases of the AMO combined with favourable phases of the MJO do not further enhance North Atlantic TC activity.

Maloney and Hartmann (2000a) linked the westerly phases of the MJO with favourable conditions for TC genesis in the eastern Pacific near the Mexican west coast through decreased vertical wind shear, and the enhancement of low-level convergence and cyclonic vorticity. Maloney and Hartmann (2000b) also found that during the westerly phases of the MJO, TC genesis in the Gulf of Mexico and the western Caribbean is up to four times greater than during the easterly phases.

On intraseasonal scales, the influence of convectively-coupled atmospheric Kelvin waves on TC genesis has been analysed in recent studies (e.g., Ventrice et al., 2012). These synoptic-scale waves have wavelengths of 3000–7000 km, with eastward phase speeds of 10–20 $m \cdot s^{-1}$. The strongest Kelvin waves are often embedded within the MJO, which allows them to persist longer and they may enhance the 850 hPa cyclonic vorticity for the storm (Fang and Zhang, 2016).

2.5.1.6 Rainfall and moisture transport associated with tropical cyclone activity

Rainfall associated with individual TCs is conditioned to the maintenance of the deep convection surrounding its core, which is related to atmospheric and land surface forcings. Cerveny and Newman (2000) suggest that rainfall associated with the TC inner core represents most TC-related rainfall, being ≈ 35% of the total rainfall for the weakest TCs and strong Hurricanes, compared with less than 25% of the weakest hurricanes.

In general terms, TCs and their related rainfall weaken when making landfall since the TC inner core is isolated from oceanic moisture, latent heat flux from evaporation. However, TCs may continue creating rainfall further inland in post-landfall while interacting with local topography (e.g., Matyas, 2007; Brun and Barros, 2014) and/or other synoptic systems (e.g., Dare et al., 2012). Matyas (2007) suggests that TC-associated rainfall and moisture depends on the intensity of the storm, the distance inland over which the storm moves and the orientation of elevated topography encountered by the TC. In that study, strong hurricanes (associated to faster winds) are shown to advect moisture almost completely around their centers (an arc-lenght ≈ 349°), whereas weaker TCs have a more limited rain shield (an arc-lenght ≈ 171°).

TC-related rainfall and moisture is influenced by TC size (Xu et al., 2017), that might be influenced by their location basin (e.g., Jiang and Zipser, 2010). For example, Atlantic TCs are typically smaller than those in the Indian Ocean, the South Pacific or the northwest Pacific. TC rainfall for individual storms is also conditioned to dynamical mechanisms, such as vertical wind shear, TC translation and proximity to the continent. Thermodynamic effects such as differential temperature and radiation effects over land and ocean, and microphysical processes also might determine the amount of TC-associated rainfall (Yu and Wang, 2018). Hence, this topic is still a matter of research.

Many studies have quantified the rainfall associated with TC activity at a regional (e.g., Larson et al., 2005; Kunkel et al., 2010; Ritchie et al., 2011; Barlow, 2011; Lau and Zhou, 2012; Gutzler et al., 2013; Prat and Nelson, 2013b; Wood and Ritchie, 2013; Prat and Nelson, 2016; Guo et al., 2017; Touma et al., 2019) or global scale (Jiang and Zipser, 2010; Prat and Nelson, 2013a).

Some other studies have also quantified the TC contribution to moisture transport at a regional scale (e.g., Xu et al., 2017). Different approaches and techniques have been applied to quantify TC influence in rainfall and moisture, such as reanalysis, observations or satellite estimations of rainfall, the TC's radius of influence, and the source of the TC tracks (e.g., inclusion/exclusion of pre- and post-stage of a TC). Each technique has its advantages and weaknesses.

For example, to attribute an area influenced by a particular TC and to give an objective definition of the TC size is a challenging task. A fixed 500 km (≈ 5 longitudinal degree) radius is a common choice in TC-related studies (e.g., Larson et al., 2005; Jiang and Zipser, 2010; Guo et al., 2017) since this criteria captures the primary wind circulation domain of the TC, which is usually found between 80-400 km from the TC centre and the TC cloud shield, commonly found at 550-600 km (Prat and Nelson, 2013a). However, it has been suggested that fixed radius might not capture the full extent of the TC influence or to include the influence from other weather systems, leading to uncertainties in the TC attributions of rainfall and moisture flux (Ren et al., 2007; Xu et al., 2017).

The amount of TC-related rainfall varies considerably from storm to storm (Corbosiero et al., 2009) and depends on their location (e.g., Khouakhi et al., 2017), and time of the year (Larson et al., 2005; Guo et al., 2017). For example, Corbosiero et al. (2009) showed that TC contribution to rainfall in northwestern Middle America. depends on the genesis location and the time of the year, as September tends to favour TC landfall over the region. In the same study it is shown that East Pacific TCs cause considerable rainfall over north western Middle America even without making landfall or during TC post-stages. Ritchie et al. (2011) quantified that up to 30% of the annual precipitation in the southwestern U.S. is associated with remnants of eastern North Pacific TCs. Kunkel et al. (2010) found that North Atlantic TCs account for 6% of the annual total rainfall.

In terms of extreme rainfall, Khouakhi et al. (2017) found that in North America the highest TC contribution to annual rainfall maxima ($\approx$ 10-30%) can be found at rain gauges located within $\approx$ 400 km of the shore. In some regions with different climatic areas with arid or tropical characteristics, TCs contribute to more than 25% and up to 61% of the annual precipitation budget (Prat and Nelson, 2013a). Barlow (2011) quantified that 50% and more than two-thirds of all extreme events in stations at the Mexican west coast and northeast U.S. are linked to hurricane-related activity, respectively. Kunkel et al. (2010) quantified that North Atlantic TCs are associated with 30% of extreme events in some stations located in the south and southeast U.S..

North Atlantic and northeast Pacific trends and relationships between TC-intensity of TC-related rainfall have been analysed. Lau and Zhou (2012) suggested that there is an approximate linear relationship between Saffir-Simpson storm intensity classification, and the TC-related rainfall (calculated with the accumulated total rainfall along storm tracks). Touma et al. (2019) found larger contributions of TC-related rainfall from TCs after they have weakened to tropical storms. The authors also found that there is a trend of heavier rainfall associated with major hurricanes in the recent six decades, compared with the earlier six decades of their study.

2.5.2 Tropical easterly waves

Tropical EWs are important synoptic features of the ITCZ in the eastern Pacific and the Atlantic ocean. They appear during boreal summer and autumn, following a similar timeframe as the TCs.

The EWs are important modulators of convection in the IAS and Middle America. During boreal summer, there are about 6–8 EWs per month (Toma and Webster, 2010a) and their origin varies in accordance with the basin. For example, African EWs (AEWs) are synoptic-scale disturbances induced by the mid-tropospheric sub-Saharan jet, also known as the African easterly jet, during the West African Monsoon season (e.g., Burpee, 1972), which normally occurs from June to October. Thorncroft and Hoskins (1994) found that AEWs are formed from a joint barotropic–baroclinic instability of the African easterly jet. AEWs modulate daily rainfall over West Africa (Reed et al., 1977) while propagating westwards between 600-850 hPa (e.g., Thorncroft and Hodges, 2001). Some of these waves propagate through the equatorial North Atlantic and reach the Caribbean Sea and Middle America, inducing instability and producing heavy rainfall.

Different interpretations exist to explain the origin of eastern Pacific EWs: some studies consider that these EWs are originally formed in the Atlantic and propagated towards the eastern Pacific across Central America (Frank, 1970; Raymond et al., 2006). Other studies suggest that disturbances from the Atlantic Ocean interacting with the Sierra Madre (e.g., Sierra Madre Occidental, Trans-Mexican Volcanic Belt, and Sierra Madre del Sur) lead to barotropic instablility and EW genesis (Zehnder and Reeder, 1997; Zehnder et al., 1999).

The early study by Ferreira and Schubert (1997) proposed the origin of eastern Pacific EWs as barotropic instability of the eastern Pacific ITCZ, leading to the generation of a series of eddies. More recently Serra et al. (2008) suggested that the genesis and the character of the Pacific EWs are quite different from Atlantic EWs, where only 4–8% of the latter reach the eastern Pacific basin. Toma and Webster (2010a) suggest that the development of EWs *in situ* are directly linked to ITCZ instabilities, particularly in regions of strong cross-equatorial pressure gradient. Thus, local instabilities are a major source of EWs in the eastern Pacific Ocean.

EWs are important precursors of TCs (Serra et al., 2008; Thorncroft et al., 2008; Toma and Webster, 2010a,b; Belanger et al., 2016): more than a half of all the Atlantic TCs and approximately 85% of the major hurricanes in the basin originate from AEWs (Agudelo et al., 2011).

CLLJ activity influences eastern Pacific low-level winds, low-level vorticity, moisture and convection, which are important factors for EW growth and tropical cyclogenesis in the IAS. Strong easterly flow is associated with more frequent and stronger eastern Pacific EWs (e.g., Molinari et al., 1997; Serra et al., 2008). According to Méndez and Magaña (2010), a relatively weak CLLJ (≈ 10 m$\cdot$s^{-1}) favours more AEWs activity in the IAS and, consequently, more rainfall in the Caribbean, Central America and southern Mexico. Many studies suggest that the AEWs and TCs strongly influence seasonal cycle of Caribbean and Middle America rainfall (e.g., Taylor et al., 2002; Larson et al., 2005; Méndez and Magaña, 2010; Herrera et al., 2015); in contrast Martinez et al. (2019) found marginal influences on the Caribbean rainfall cycle.

Chapter 3:

Interannual Variability of Middle America's Rainfall

3.1 The purpose of the present study

This study addresses the first set of objectives of the thesis, stated in 1.3: (a) to objectively identify regions in Middle America that show coherent interannual variability of rainfall at all season; (b) to identify the large-scale climate phenomena responsible for rainfall interannual variability over Middle America, and (c) to describe physical mechanisms by which these large-scale climate phenomena create conditions for anomalous rainfall over the region.

Rainfall is a crucial factor for Middle American society, natural areas, infrastructure, and economic activities such as agriculture and hydroelectric power generation. As an example, crop cultivation is the main activity in the primary production sector in most of Mexico; more than 79% of this activity is rainfed (INEGI, 2019). Cattle ranching, which also belongs to the Mexican economy primary sector, depends on the climatic conditions and the availability of local water, which is directly linked with variability in seasonal rainfall. Agriculture represented $\approx 3.3\%$ of the Mexican gross domestic product (GDP) in the first quarter of 2020 (INEGI, 2020). Mexico has 182 protected natural areas, which comprise 21,886,691 ha and represent 11.14% of the land area of continental Mexico (CONANP, 2019); these areas are particularly vulnerable to climate variability, in variables such as precipitation rates and moisture availability.

ENSO plays the leading role in driving interannual variability of Middle America's climate in winter and summer (Giannini et al., 2001); its direct influence on regional rainfall anomalies has been widely documented (e.g., Hastenrath, 1978; Ropelewski and

Halpert, 1987; Taylor et al., 2002). Middle America's rainfall varies with the ENSO phases (see sec. 2.3.1), in which La Niña shows the opposite of all El Niño patterns of rainfall. Canonical El Niño is often associated with drought over Middle America in summer. El Niño is accompanied by the anomalous eastward shift of the Walker Circulation, whose descending branch is then closer to Middle America and the Caribbean Sea. El Niño winters are characterised by colder and wetter conditions over northern Middle America, linked to an equatorward shift of the eastern Pacific subtropical jet. This leads to stronger winds at $\approx 200\ hPa$ crossing the region and to an amplified storm track over northern Middle America (CPC, 2005).

Higgins et al. (1999) and Higgins and Shi (2001) found that SSTs in the eastern Pacific are linked with interannual variability of the NAMS (see sec. 2.1.4), via an anomalous Hadley circulation. During El Niño, the ITCZ shifts equatorwards and the eastern Pacific Hadley circulation intensifies, which reduces rainfall over Middle America. NAMS variability has been linked with rainfall anomalies in the previous boreal winter: wet (dry) conditions over the monsoon region are often followed by an enhanced (weaker) NAMS, which suggests an influence of ENSO on the interannual variability of the NAMS (Mechoso et al., 2004).

The CLLJ strengthens during El Niño summers, inhibiting both the Caribbean's cyclogenesis and the propagation of AEWs into the Caribbean Sea (Amador, 2008). Increased rainfall in the western Caribbean and Central America and reduced rainfall in the central IAS are observed during El Niño.

El Niño events enhance central and eastern North Pacific TC frequency, except in the area close to the Middle American western coast; opposite TC frequency patterns in this basin occur during La Niña (Chu, 2004; Fu et al., 2017). Also, there is a shift of the location of TC activity to the central North Pacific (i.e. westwards) during developing El Niño (Camargo et al., 2008; Bell et al., 2014; Wood and Ritchie, 2013; Fu et al., 2017). However, the impact of the SSTs do not have a major influence on TC activity at central and eastern North Pacific TC activity during El Niño, since the warming signal is mostly confined along the equator (Jin et al., 2014; Murakami et al., 2017). The increase in TC activity is mainly attributed to changes in vertical wind shear, and an increase in vorticity (Chu, 2004), which promotes the westward shift of both TC tracks and genesis region (Wu and Chu, 2007; Camargo et al., 2008).

ENSO influences Atlantic TC activity through induced changes in tropospheric vertical wind shear (Gray, 1984; Goldenberg and Shapiro, 1996; Patricola et al., 2014), and the upper-tropospheric temperature (Tang and Neelin, 2004), where an enhancement of Atlantic TC activity occurs during La Niña and suppression during El Niño.

The strength of the teleconnection between ENSO and Middle America's rainfall has varied with time. Méndez and Magaña (2010) found that prolonged dry conditions in central-south Mexico occur during El Niño events in the positive phase of the PDO, while prolonged wet conditions prevail during La Niña events in the negative phase of the PDO.

The effects of ENSO in the transition seasons and the differentiation of canonical El Niño climate impacts from those of El Niño Modoki over Middle America have received little attention. Even more, the regional climate effects of secondary oceanic and atmospheric modes of interannual variability, such as the AMM (Chiang and Vimont, 2004; Kossin and Vimont, 2007) and the NAO have been less thoroughly explored.

Some studies have addressed the responses in rainfall and moisture transport over North America in canonical El Niño and El Niño Modoki years: Mo (2010) found that during El Niño Modoki winters the storm track shifts more south relative to canonical El Niño events. El Niño Modoki response to the extratropical wave train resembles a Pacific–North American pattern (PNA; Barnston and Livezey, 1987), while canonical El Niño response is more similar to a tropical Northern Hemisphere pattern (Barnston et al., 1991). Kim and Alexander (2015) suggests that during peak El Niño Modoki, the southwards shift of the Aleutian low may transport more moisture into Middle America compared with peak canonical El Niño. This is possible due to higher atmospheric moisture in the lower latitudes, even though the winter Aleutian low strengths less in El Niño Modoki than in canonical El Niño.

There are studies that have examined point correlations between Middle America's rainfall and its individual drivers (e.g., Magaña et al., 2003). However, only a few have linked coherent spatial patterns of seasonal rainfall variability across some portions of Middle America with their particular driving mechanisms (e.g., Higgins et al., 1998; Cavazos, 1999).

In this study, coherent patterns of rainfall that represent most of the interannual variance of seasonal rainfall over Middle America are obtained by implementing a consistent and objective method, the Empirical Orthogonal Teleconnection (EOT; van den Dool et al., 2000) analysis. The EOT analysis is applied to the 1982–2016 rainfall over Middle America. This technique has been applied successfully in previous studies on interannual and decadal variability of rainfall: Smith (2004) examines long-term trends and interannual variability in Australian rainfall, identifying that interannual rainfall totals can be attributed to the first two EOT patterns that cover much of central-western Australia and central-eastern Australia. The author found that 60% of the variability of annual rainfall is strongly linked with the SOI. Klingaman et al. (2013) proved that the EOT technique was useful in separating Queensland rainfall into regional patterns of variability, identifying ENSO as the phenomenon responsible for the most significant rainfall variance in Queensland in spring, summer and winter. In contrast, autumn rainfall variations are controlled by the late-season strength of the Australian monsoon. The authors also identified TCs approaching the Queensland coast as secondary drivers of the interannual rainfall variability in summer. Stephan et al. (2018a) identified that ENSO mainly drives interannual variability of rainfall in large areas of eastern China during winter, spring, and summer. The authors also found that the interannual variability of rainfall in China's southeast coast is linked to anomalous convection in the tropical eastern Atlantic, interacting through a zonal wavenumber-three Rossby wave.

In this chapter, the influence of the leading and secondary modes of climate variability in the amount and location of rainfall in Middle America are explored. This study finds the relationship between interannual rainfall variability over Middle America and particular climate forcings for specific seasons by linearly regressing the EOT time-series onto observations and reanalysis data. The corresponding large-scale phenomena and mechanisms, meteorological systems, and climatic conditions associated with interannual variability of rainfall in Middle America are explained. This new knowledge is potentially valuable for future studies regarding predictions of seasonal rainfall, as often numerical models have good skill at predicting large-scale atmospheric circulations at seasonal scales.

This study examines some of the most relevant atmospheric and oceanic variables, which are linked to modes of interannual variability that influence Middle America's climate. Modes of variability such as ENSO, the AMM, and the AMO (among others studied in chapter 2 of this thesis) modulate large-scale environmental conditions, including SSTs, rainfall, wind fields, vertically integrated moisture flux and its divergence, outgoing long wave radiation, and atmospheric surface pressure. The analysis of these conditions in relationship with the modes of variability help to explain the mechanisms through which Middle America's climate variability occurs.

As studied in Section 2.5.1.4, Middle America's rainfall is influenced by the North East Pacific and the North Atlantic TC activity. TC attributes (e.g. genesis, track and landfall locations) are widely controlled by large-scale environmental conditions that can be modulated by ENSO, the AMM and other modes of variability. Modulations in the atmosphere include vertical wind shear, moisture, and the strength and location of subtropical highs. In addition, the ocean influences TC activity through SST changes.

3.2 Dataset and methods

3.2.1 Data

For the period 1982–2016, seasonal means of accumulated rainfall are computed using the University of East Anglia Climatic Research Unit (UEA-CRU) global monthly precipitation dataset for global land areas, at $0.5°\times0.5°$ spatial resolution (Mitchell and Jones, 2005).

Seasonal winds on pressure levels, atmospheric surface pressure, and vertically integrated moisture fluxes (VIMF) from the Japanese 55-year reanalysis (JRA-55; Kobayashi et al., 2015, all at the original resolution of TL319, $\approx$ 55 km) are used in this study. Harada et al. (2016) assessed the representation of the global atmospheric circulation and climate variability in the JRA-55 reanalysis. The authors found consistency in the zonal mean field when compared with different reanalyses. Compared with its predecesor, the Japanese 25-year reanalysis (Onogi et al., 2007, JRA-25;) the authors found improvements in the representation of the atmospheric flow and phenomena, such as equatorial waves, and transient eddies in the storm track regions. Among other reanalysis datasets, JRA-55 has one of the best estimates of seasonal and annual variabilities of surface wind speeds over the Northern Hemisphere (e.g., Miao et al., 2020). However, compared with other reanalyses, JRA-55 present a weaker amplitude of equatorial waves and the MJO and shows an unrealistic strong cooling in South America and Australia (Harada et al., 2016).

The divergence of JRA-55 vertically integrated moisture fluxes fields is computed using spherical harmonics with truncation T64, employing the windspharm Python package (Dawson, 2016). Wind shear is defined as the magnitude of the difference between the horizontal wind fields at 850 hPa and 200 hPa, which has been widely used for empirical studies of TC activity (e.g., Camargo et al., 2007; Wang et al., 2011).

JRA-55 reanalysis represents around 95% of the 6-hourly global TC frequencies observed for the period from the 1950s to the 1980s and gradually decreases to 85–90 % in the 2000s (Kobayashi et al., 2015). This reflects an artificial weakening trend of JRA-55 to detect TCs that goes against the effect of increasing observations. Despite this, JRA-55 helps representing TCs in the correct location (e.g., Hodges et al., 2017).

In this chapter seasonal statistics of TC track densities and TC genesis densities are used, which are computed with the objective TC tracking method based on Hodges (1994, 1995, 1999), and applied to the JRA-55 reanalysis dataset, for the period 1979–2016. The methodology employed for the calculation of the TC tracks and their statistics is fully described in Hodges et al. (2017). The objective TC tracking method identifies tropical disturbances through relative vorticity fields, vertically averaged from 850 to 600 hPa pressure levels. Tropical systems with wavenumbers between 6 to 63 are retained after applying the spectral filter of Sardeshmukh and Hoskins (1984). The TC is identified using a threshold criterion of vertically decreasing vorticity is applied to the filtered vorticity fields (across 850-250 hPa) to detect the typical warm core vertical structure of a TC. A vorticity maximum at the different levels is found applying the B-spline interpolation, with the maximum at the previous pressure level as a starting point.

The NOAA Optimum Interpolation Monthly SST (OISST; Reynolds et al., 2002) Analysis dataset at a horizontal resolution of $1^\circ \times 1^\circ$ is used to compute SST means. Seasonal values of outgoing long-wave radiation (OLR) are calculated from NOAA Climate Diagnostics Center (CDC) OLR dataset at $2.5^\circ \times 2.5^\circ$ horizontal resolution (Liebmann and Smith, 1996).

Monthly mean indices corresponding to the regions Niño 1+2, 3, 3.4, 4 and Trans-Niño index are retrieved from `https://climatedataguide.ucar.edu/climate-data/` (Trenberth, 2020). The monthly mean AMM index dataset is provided by `http://www.aos.wisc.edu/~dvimont/MModes/Data.html`. The monthly mean NAO index dataset is retrieved from `https://www.cpc.ncep.noaa.gov/products/precip/CWlink/pna/nao.shtml`. The monthly mean CLLJ index dataset is provided by `https://iridl.ldeo.columbia.edu/maproom/ACToday/Colombia/CLLJI.html`.

3.2.2 Empirical Orthogonal Teleconnections Analysis for interannual variability of rainfall

A modified version of the original EOT method (van den Dool et al., 2000), following Smith (2004), is implemented to identify the large-scale climate phenomena associated with interannual rainfall variability over Middle America. Both the original EOT and the modified EOT version allow objectively identifying regions that show strong coherent interannual variability in seasonal rainfall, with the difference that in the EOT modified version the regions are identified by the explained variance of the domain area-averaged rainfall, rather than by the sum of the explained space-time variance over all points.

In the original EOT method proposed by van den Dool et al. (2000), the use of global variance biases the results to areas of the domain of higher rainfall totals. Smith (2004) argues that the temporal variance of the spatially averaged rainfall is a less-biased descriptor than the space–time variance, particularly over domains where rainfall variance is concentrated in particular areas (e.g., coastal Australia, southern and eastern China). Smith (2004) methodology implies that all-grid points contribute to the temporal variance calculation on an equal basis, thereby removing the bias towards regions of high rainfall. Therefore, this version of the EOT methodology is suitable for studies of rainfall in Middle America, since this region presents a considerable concentration of rainfall in a small part of the domain.

The EOT analysis offers a novel approach to the analysis of interannual rainfall variability in Middle America. This technique emphasises regions of strong coherent temporal variability, maximising variance only in one dimension (time in this study), different from classical algorithms that seek eigenvectors that maximise space-time variance. The modified EOT method is explained in detail in the following paragraphs.

In this thesis, the modified EOT method is implemented for seasonal accumulated rainfall, denoted $f(e,t)$, which varies in space ($1 \leq e \leq ne$) and time ($1 \leq t \leq nt$), where ne represents all the grid points in the domain of study, and nt represents all the time steps within the period of analysis. $f(e,t)$ is analysed for each of the following seasons: March-April-May (MAM), June-July-August (JJA), September-October-November (SON), and December-January-February (DJF; where January and February correspond to the following year).

The modified EOT method consists of searching for the base point (denoted eb_1) among all e in $f(e,t)$ that explains the most temporal variance of the area-average rainfall in the domain. In other words, the first EOT or eb_1 is the point with the highest correlation with the area-average of seasonal rainfall in Middle America. This first base point eb_1 has an associated time series β_1 (also called EOT1 time-series), corresponding to the time series of the original data, $f(e,t)$, at point eb_1.

The next most important point in space (the one that explains most of the variance of the original area-average rainfall) is searched using the procedure explained before, except that the reduction starts with the $f(e,t)$ after the effect of the previous EOT removed (eq. 3.2). The effect of the base point $f(eb_1,t)$ is removed from the original seasonal accumulated rainfall, $f(e,t)$, by linear regression. This process requires the calculation of the regressed coefficients (denoted R) between $f(eb_1,t)$ and f at all other points e. Each regressed coefficient $R(e)$ is later multiplied by its corresponding time series β_1:

$$f_{effect}(e,t) = \beta_1 R_1(e) \qquad \text{for} \quad \text{all} \quad e \quad \text{and} \quad t. \tag{3.1}$$

The f_{effect} coefficient is removed from the original dataset, yielding in a new seasonal rainfall dataset with the effect of the first EOT removed:

$$f_{new}(e,t) = f(e,t) - f_{effect}(e,t) \qquad \text{for} \quad \text{all} \quad e \quad \text{and} \quad t. \tag{3.2}$$

Ultimately, a set of functions orthogonal in time (EOTs, result from a 'covariance-based' calculation) that emphasise regions of strong coherent variability is obtained. The EOTs explain successive non-overlapping fragments of the variance. The orthogonality of the EOTs in the time domain (in which the correlation and standard deviation are calculated) implies that

$$\sum_t \beta_m(t)\beta_n(t) = 0 \qquad \text{for} \quad \text{n} \neq \text{m}, \tag{3.3}$$

where $\beta_m(t) = f_{new}(eb_m,t)$, eb_m is the m^{th} base point, f_{new} is f after $m-1$ reductions.

To obtain patterns of coherent variability within the domain of study (referred as EOT patterns), the corresponding leading EOT, $f(eb_m,t)$, is correlated with all the points of the domain for the variable $f(e,t)$ of the corresponding m iteration.

In a following step, the EOT is linearly regressed onto relevant atmospheric and oceanic variables associated with modes of variability (as discussed in Sec. 3.1). Through these linear regressions, the EOT analysis aids in the identification and understanding of the associated local and large-scale atmospheric and coupled air-sea processes that drive the variability (e.g., Smith, 2004; Rotstayn et al., 2010; Klingaman et al., 2013; Stephan et al., 2018a).

This study analyses the three leading EOTs of rainfall for each season that also represent a threshold of more than 88% of accumulated explained variance. Individually, each EOT is connected with local and large-scale phenomena by linear regression applied to oceanic and atmospheric fields (such as SSTs, atmospheric pressure, wind fields, OLR, VIMF, VIMF divergence, among others) onto time-series corresponding to each EOT rainfall pattern.

3.3 Drivers of interannual variability of seasonal rainfall in Middle America

In this section, the three leading seasonal rainfall EOTs for each season MAM, JJA, SON, and DJF are analysed. Table 3.1 summarises the three leading EOTS for JJA and SON and their Pearson correlation coefficient with the most significant interannual climate indices, related with candidate modes of variability of the interannual variability of seasonal rainfall in Middle America. For these correlations, monthly mean indices were used to calculate the seasonal Niño SST, AMM, NAO, and CLLJ indices.

EOT	Expl. variance (%)	σ_{bp} (mm)	Niño 3.4	3-mo lag Niño 3.4	TNI	Niño 4	Niño 1+2	AMM	NAO	CLLJ
MAM										
EOT1	58.18	31.44	**0.45*** **	0.30**	-0.25*	**0.44*** **	0.16	0.05	0.17	0.06
EOT2	20.67	39.84	-0.29**	**-0.40*** **	-0.14	-0.10	-0.29**	-0.06	0.12	**0.57*** **
EOT3	11.17	118.25	0.05	-0.07	0.20	0.05	0.18	**-0.36** **	0.16	0.14
JJA										
EOT1	71.29	210.04	**-0.70*** **	-0.30**	0.10	**-0.65*** **	**-0.35** **	0.31**	0.02	**-0.58*** **
EOT2	15.72	71.80	-0.03	0.03	-0.10	0.00	-0.03	0.00	0.05	-0.02
EOT3	5.28	110.42	-0.11	**-0.41*** **	-0.10	-0.10	-0.15	-0.18	-0.10	0.10
SON										
EOT1	71.05	58.97	0.05	0.03	-0.07	0.16	0.10	0.13	0.06	**0.50*** **
EOT2	11.85	107.69	0.19	0.14	0.10	0.10	0.25*	-0.23	0.02	0.27*
EOT3	5.47	18.62	-0.13	-0.20	**0.37*** **	-0.27*	-0.00	0.26*	0.11	**-0.34** **
DJF										
EOT1	70.94	114.42	**0.52*** **	**0.43*** **	-0.06	**0.40*** **	**0.47*** **	-0.23	-0.00	0.16
EOT2	16.36	30.11	0.26*	0.15	**-0.27** **	0.26*	0.05	-0.20	0.00	-0.05
EOT3	5.60	82.81	0.19	0.18	-0.10	0.18	0.12	-0.11	0.26*	0.06

Table 3.1: For the three leading EOTs of seasonal Middle America's rainfall: the percentage of variance of the area-averaged rainfall explained; the seasonal standard deviation of rainfall of the base point of the EOT (σ_{bp}; the correlation between the EOT time series and Niño 3.4, the 3-month lagged Niño 3.4, the Trans-Niño Index (TNI), Niño 4, Niño 1+2, the SST Atlantic Meridional Mode, the North Atlantic Oscillation index, and the Caribbean Low Level Jet index. A *, ** , and *** indicate correlations that are statistically significant at the 12%, 6%, and 1% level, respectively.

Even though the relationship between the leading EOTs with other climate indices, such as the ones mentioned in Chapter 2 (e.g. Atlantic Niño, AMO, PDO, MJO), was considered, these relationships were not statistically significant and are not shown in table 3.1.

To understand the drivers of the interannual variability of seasonal rainfall in Middle America, regressions analyses of climate variables are calculated for each EOT. Table 3.2 summarises the results of this EOT analysis, for the reader's reference throughout this section.

EOT	**Expl. variance (%)**	**Region affected**	**Likely driving mechanism**
MAM			
EOT1	58.18	Northeastern Middle America	Developing canonical El Niño
EOT2	20.67	Southern Middle America	Decaying canonical La Niña
EOT3	11.17	Northeastern Middle America	Negative phase of the AMM
JJA			
EOT1	71.29	Southern and eastern Middle America	Developing canonical La Niña, positive phase of the AMM
EOT2	15.72	Northeastern Middle America	Regional land-atmosphere interactions
EOT3	5.28	Northwestern Middle America	Lagged peak and decaying canonical La Niña
SON			
EOT1	71.05	Central and eastern Middle America	CLLJ variability
EOT2	11.85	Northern and central-eastern Middle America	Developing canonical El Niño and TC activity
EOT3	5.47	Southern/southwestern Middle America	Developing La Niña 'Modoki' and TC activity
DJF			
EOT1	70.94	Northern Middle America	Peaking canonical El Niño
EOT2	16.36	Western/north-central Middle America	Peaking El Niño 'Modoki'
EOT3	5.60	Southern/central Middle America	Unclear, but association with the positive phase of the NAO

Table 3.2: Summary of the EOT analysis, showing each EOT percentage of variance explained in area-average seasonal rainfall, the region of Middle America encompassed by the pattern, and the likely driving mechanism.

3.3.1 Summer

JJA EOT1

EOT1 for JJA presents a base point that explains 71% of the temporal variance of the area-average rainfall. The base point is located in the state of Chiapas, Mexico (Fig. 3.1a); this EOT is highly correlated with a large area of southern and eastern Middle America.

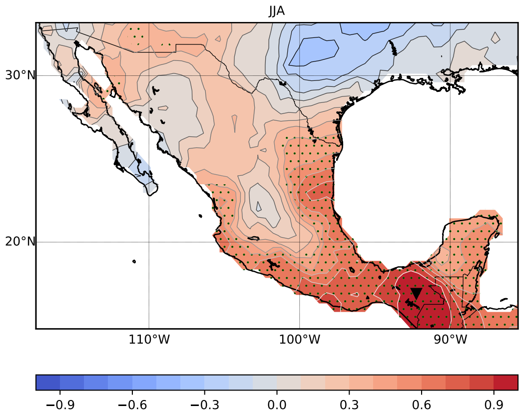

(a)

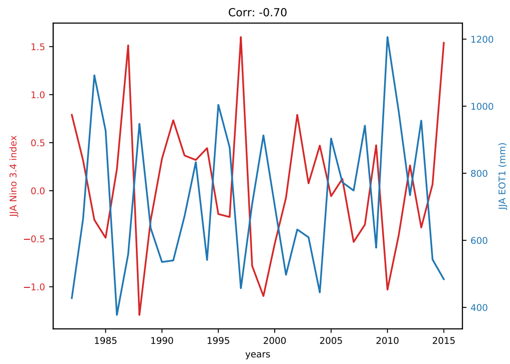

(b)

Figure 3.1: (a) Correlation of JJA EOT1 base point with the JJA rainfall at each point of the domain; the EOT base point is marked with a black inverted triangle (stippling indicates correlations that are significant at the 5% level). (b) Seasonal time-series of JJA EOT1 rainfall (blue line) and the JJA Niño 3.4 (red line), with a correlation coefficient of -0.70 for the period 1982-2015.

JJA EOT1 is anticorrelated with the concurrent Niño 3.4 ($r = -0.70$, Fig. 3.1b). Figure 3.2a shows a strong relationship between anomalous Pacific SSTs and JJA EOT1: the corresponding pattern of linear SST regressions onto JJA EOT1 resembles La Niña, when equatorial western Pacific SSTs show anomalous warming, and central/eastern Pacific SSTs show anomalous cooling. It is important to mention that the linear regressions between the EOT and the atmospheric and oceanic variables are calculated for the period 1982-2015. Therefore, the linear regression coefficient patterns shown in Figure 3.2a are multiplied by the standard deviation of the corresponding EOT. This pattern can be interpreted as an anomalous condition of the independent variable in respect to the mean seasonal rainfall of the corresponding EOT (for the period 1982-2015).

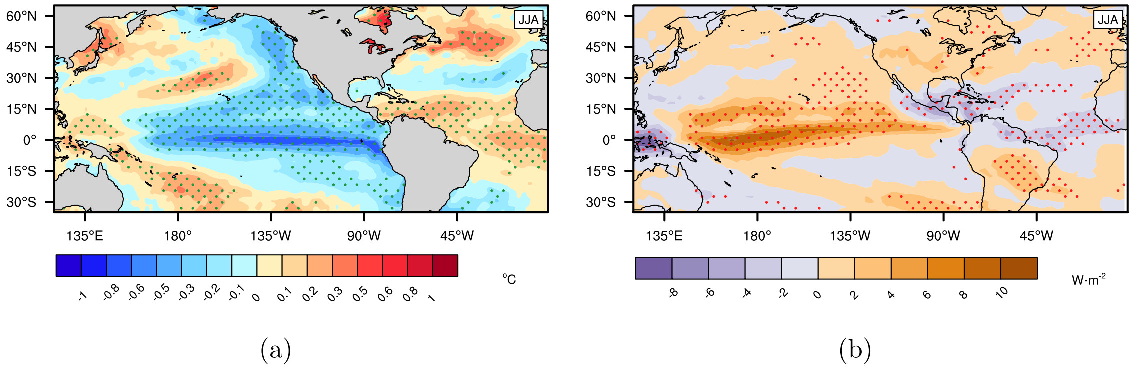

Figure 3.2: Linear regression coefficient of JJA (a) SSTs and (b) OLR, onto the normalised JJA EOT1. Shading shows the regression slopes in (a) $°C$ and (b) $W{\cdot}m^{-2}$ per standard deviation of seasonal rainfall (mm). Stippling indicates correlations that are significant at the 10% level. Period 1982-2015.

The relationship between La Niña and JJA EOT1 also appears in regressed OLR, where the OLR is used as a proxy for convection: Figure 3.2b shows negative anomalies (enhanced convection) over the western equatorial Pacific, southern Middle America, the Caribbean and the tropical Atlantic Ocean. It also shows significant positive anomalies (suppressed convection) over the central Pacific.

Anomalous positive atmospheric surface pressure over the equatorial central Pacific is associated with positive JJA EOT1 (Fig. 3.3a), consistent with La Niña. The linear regression coefficient of winds at 850 hPa show an anomalous Walker circulation (Fig. 3.3a): strengthened easterly winds in the equatorial western Pacific and anomalous westerlies in the eastern Pacific are associated with increased rainfall in southern Middle America. The anomalous low-level westerly winds extend from the eastern Pacific to the Atlantic Ocean, opposing the climatological winds in the Caribbean and weakening the CLLJ.

During positive JJA EOT1, positive anomalies of VIMF convergence occur in the eastern Pacific and southern Middle America, consistent with La Niña's anomalous northward shift of the eastern Pacific ITCZ. The low-level winds of the anomalous Walker circulation promote anomalous eastward moisture transport from the central/eastern Pacific to Middle America and the Caribbean (Fig. 3.3b). This anomalous circulation also favours convection and rainfall over southern Middle America and the IAS during JJA EOT1.

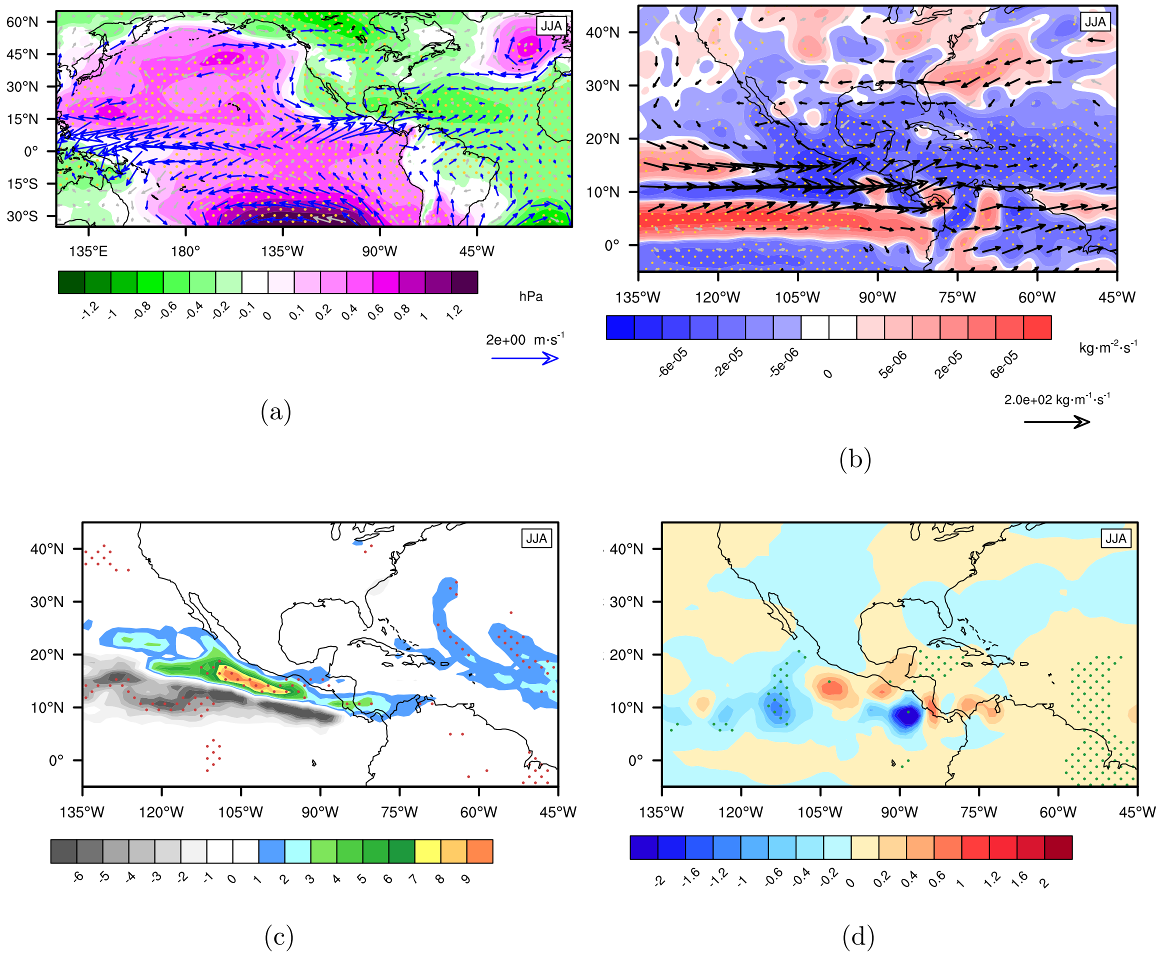

Figure 3.3: (a) Linear regression coefficient of JJA surface pressure (shaded, hPa) and wind fields at 850 hPa (arrows, $m{\cdot}\mathrm{s}^{-1}$) onto the normalised JJA EOT1, per standard unit of seasonal rainfall (mm); wind vectors are drawn in blue when at least one component of the vector is significant at the 10% level. (b) Linear regression coefficient of JJA VIMF (arrows, $kg \cdot \mathrm{m}^{-1}{\cdot}\mathrm{s}^{-1}$) and VIMF divergence (shaded, $kg \cdot \mathrm{m}^{-2}{\cdot}\mathrm{s}^{-1}$) onto the normalised JJA EOT1, per standard unit of seasonal rainfall (mm); VIMF vectors are drawn in black when at least one component of the vector is significant at the 10% level. (c) Linear regression coefficient of JJA TC track density scaled to number density per unit area ($\approx 10^6 km^2$) per season onto the normalised JJA EOT1, per standard unit of seasonal rainfall (mm). (d) Linear regression coefficient of JJA TC genesis density per unit area ($\sim 10^6 km^2$) per season onto the normalised JJA EOT1, per standard unit of seasonal rainfall (mm). Stippling indicates correlations of (a) surface pressure, (b) VIMF divergence, (c) TC track density, and (d) TC track genesis that are significant at the 10% level.

Regression analyses show a significant anticorrelation between JJA EOT1 and surface pressure in the tropical Atlantic (Fig. 3.3a), as well as a positive correlation between JJA EOT1 and previous MAM (not shown) and simultaneous JJA tropical Atlantic SSTs (Fig. 3.2a). This regression pattern resembles the AMM warm phase (e.g., Kossin and Vimont, 2007), where SSTs are anomalously warm in the tropical eastern Atlantic and trade winds in the equatorial western Atlantic are weaker than normal (Fig. 3.3a). An additional correlation analysis confirms that JJA EOT1 is positively correlated with the AMM SST index ($r = 0.31$) for the period 1982-2015.

Reduced atmospheric surface pressure and warm SSTs over the Caribbean and Gulf of Mexico are associated with high JJA EOT1 rainfall. Anomalously warm Atlantic SSTs in late spring and early summer can be explained by changes in the surface winds associated with meridional shifts in the ITCZ. Regression analysis of previous MAM OLR and SSTs onto JJA EOT1 suggest a northward shift of the North Atlantic ITCZ, characteristic of the AMM development by the WES process (Xie and Philander, 1994), fully described in sec. 2.3.2. This analysis suggests that the Atlantic warming associated with JJA EOT1 is linked to AMM variability.

Linear regression coefficient of JJA TC track densities onto JJA EOT1 indicate significant positive anomalies of the Eastern Pacific TC activity, particularly in Middle America's eastern nearshore area, and a decrease of TC activity in the western portion of the East Pacific. Negative anomalies of OLR (Fig. 3.2b) and VIMF divergence (Fig. 3.3b) suggest an increased convective activity in the EPWP, which might be linked with positive anomalous TC activity near Middle America's east coast. During JJA EOT1, TC genesis density increases over the Tehuantepec Gulf and decreases in the western portion of the eastern Pacific and the Papagayo Gulf. Positive anomalies of TC genesis close to the Gulf of Tehuantepec might be favoured by the decrease in the Central American Gap Winds, which produce low-level cyclonic relative vorticity anomalies and favour cyclogenesis (Fu et al., 2017).

JJA EOT2

The second EOT for JJA has a base point that explains 15% of the temporal variance of the area-average rainfall, located in south Texas (Fig. 3.4a). Regressed SSTs and surface pressure fields onto JJA EOT2 show no significant correlations with any large-scale driver, such as ENSO (Fig. 3.4b) or the AMM (not shown). This may be explained by the prior removal of the influence of JJA EOT1, which is highly correlated with developing canonical ENSO and the AMM.

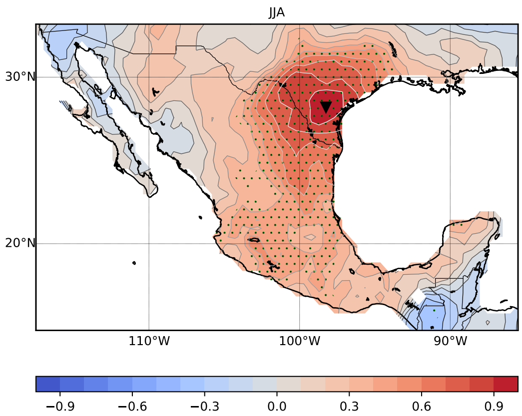

(a)

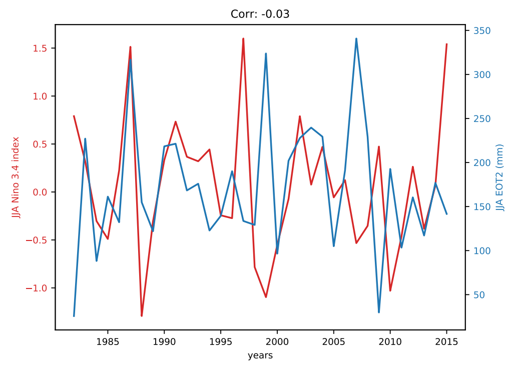

(b)

Figure 3.4: (a) Correlation of JJA EOT2 base point with the JJA rainfall at each point of the domain; the EOT base point is marked with a black inverted triangle (stippling indicates correlations that are significant at the 5% level). (b) Seasonal time-series of JJA EOT2 rainfall (blue line) and the JJA Niño 3.4 (red line), with a correlation coefficient of -0.03 for the period 1982-2015.

Positive JJA EOT2 is related to anomalous, continental high surface pressure over the eastern U.S. (Fig. 3.5c). Linear regression of winds at 850 hPa onto JJA EOT2 show anomalous southeasterly winds converging over northeastern Middle America (Fig. 3.5a). This significant anomalous wind convergence at 850 hPa over the northeastern High Plains of Middle America (Fig. 3.5a) is consistent with a region of significant anomalous VIMF convergence in the region of JJA EOT2 (Fig. 3.5b).

Regression coefficient of OLR onto JJA EOT2 shows a significant positive correlation, indicating enhanced convective activity over northeastern Middle America (Fig. 3.5d). Simultaneously, regressed VIMF shows some anomalous moisture transported from the northern High Plains of Middle America to the region of JJA EOT2 (Fig. 3.5b); however, the significance of this transport is little.

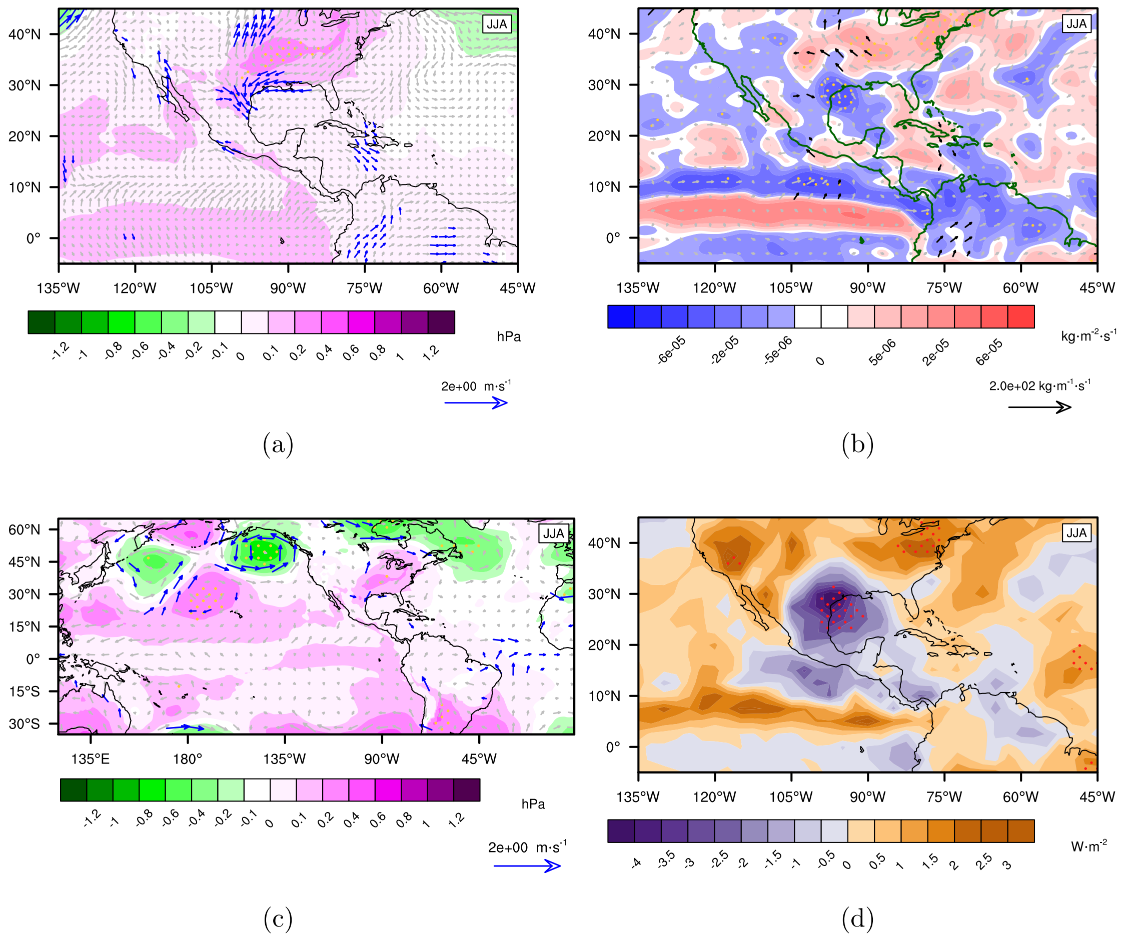

Figure 3.5: (a, c) Linear regression coefficient of JJA surface pressure (shaded, hPa) and wind fields at 850 hPa (arrows, $m{\cdot}s^{-1}$) onto the normalised JJA EOT2, per standard unit of seasonal rainfall (mm); wind vectors are drawn in blue when at least one component of the vector is significant at the 10% level. (b) Linear regression coefficient of JJA VIMF (arrows, $kg{\cdot}m^{-1}{\cdot}s^{-1}$) and VIMF divergence (shaded, $kg{\cdot}m^{-2}{\cdot}s^{-1}$) onto the normalised JJA EOT2, per standard unit of seasonal rainfall (mm); VIMF vectors are drawn in black when at least one component of the vector is significant at the 10% level. (d) Regressed JJA OLR ($W{\cdot}m^{-2}$) onto the normalised JJA EOT2, per standard unit of seasonal rainfall (mm). Stippling indicates correlations of (a, c) surface pressure, (b) VIMF divergence, and (d) OLR that are significant at the 10% level.

JJA EOT3

JJA EOT 3 describes areas in northwestern Middle America influenced by the occurrence of the NAMS and explains 5% of the total variance of the area-average rainfall (Fig. 3.6a). This EOT is anticorrelated with previous MAM Niño 3.4 index ($r = -0.41$, Fig. 3.6b).

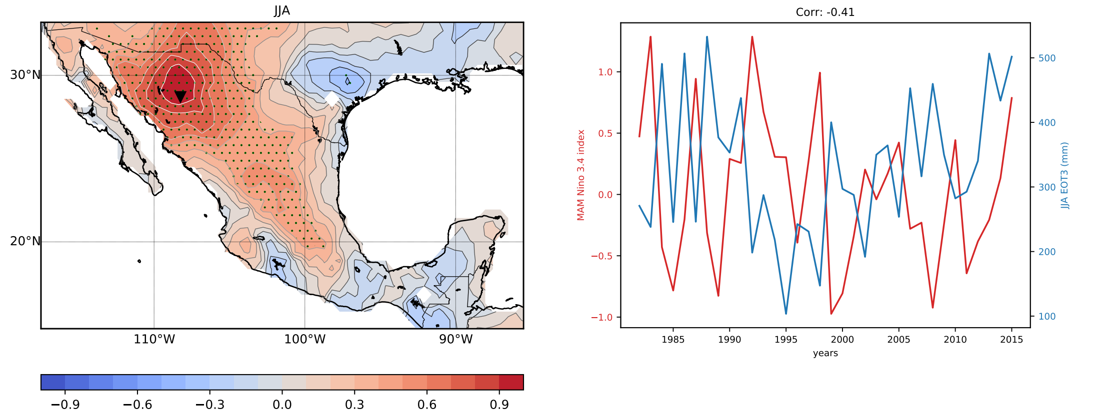

(a) (b)

Figure 3.6: (a) Correlation of JJA EOT3 base point with the JJA rainfall at each point of the domain; the EOT base point is marked with a black inverted triangle (stippling indicates correlations that are significant at the 5% level). (b) Seasonal time-series of JJA EOT3 rainfall (blue line) and the Niño 3.4 index for previous MAM (red line), with a correlation coefficient of -0.41 for the period 1982-2015.

JJA EOT3 is anticorrelated with previous DJF (not shown) and MAM SSTs (Fig. 3.7a), as well as with JJA SSTs (Fig. 3.7b) in the equatorial eastern Pacific, corresponding with peak and decaying stages of La Niña, respectively. Higgins et al. (1998) also found that strong monsoons in southwest Middle America tend to follow La Niña events. La Niña winters and their following springs are associated with a dry and warm northern Middle America; these conditions exacerbate the land-sea temperature contrast during the following summer when the continent is warm (NOAA, 2004). A reinforced NAM circulation is, in part, enhanced by the impact of local negative SST anomalies on the land-sea thermal contrast (Higgins et al., 1999). This circulation enhances moisture transport from the Gulf of California and the subtropical eastern Pacific towards northwestern Middle America. JJA EOT3 is highly correlated with VIMF convergence over the region (Fig. 3.8a) and with negative anomalies of OLR (Fig. 3.8b), which indicate enhanced convective activity.

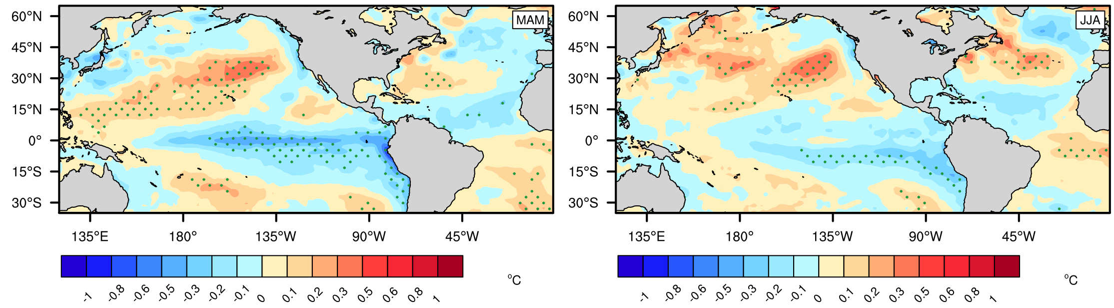

(a) (b)

Figure 3.7: Linear regression coefficient of (a) previous MAM and (b) simultaneous JJA SSTs onto the normalised JJA EOT3. Units: $^{\circ}C$ per standard deviation of seasonal rainfall in mm. Stippling indicates correlations that are significant at the 10% level.

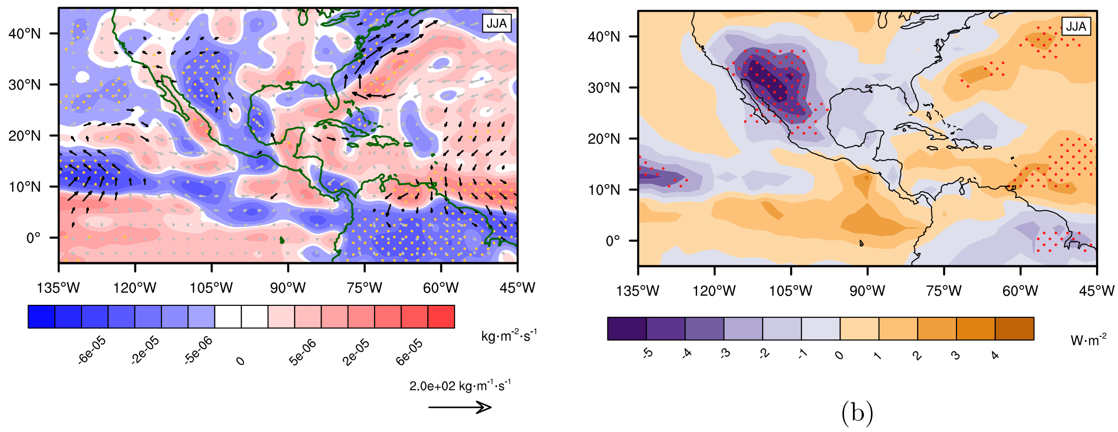

(b)

(a)

Figure 3.8: (a) Linear regression coefficient of JJA VIMF (arrows, $kg{\cdot}m^{-1}{\cdot}s^{-1}$) and VIMF divergence (shaded, $kg{\cdot}m^{-2}{\cdot}s^{-1}$) onto the normalised JJA EOT3, per standard unit of seasonal rainfall (mm); VIMF vectors are drawn in black when at least one component of the vector is significant at the 10% level. (b) Regressed JJA OLR ($W{\cdot}m^{-2}$) onto the normalised JJA EOT3, per standard unit of seasonal rainfall (mm). Stippling indicates correlations of (a) VIMF divergence and (b) OLR that are significant at the 10% level.

An additional regression analysis of winds at 200 hPa helps to identify an anomalous weakening of the upper-tropospheric winds (Fig. 3.9a). Figure 3.9b shows regressions of 850 hPa wind fields with a significant wind advected from the Rocky Mountains towards western Middle America.

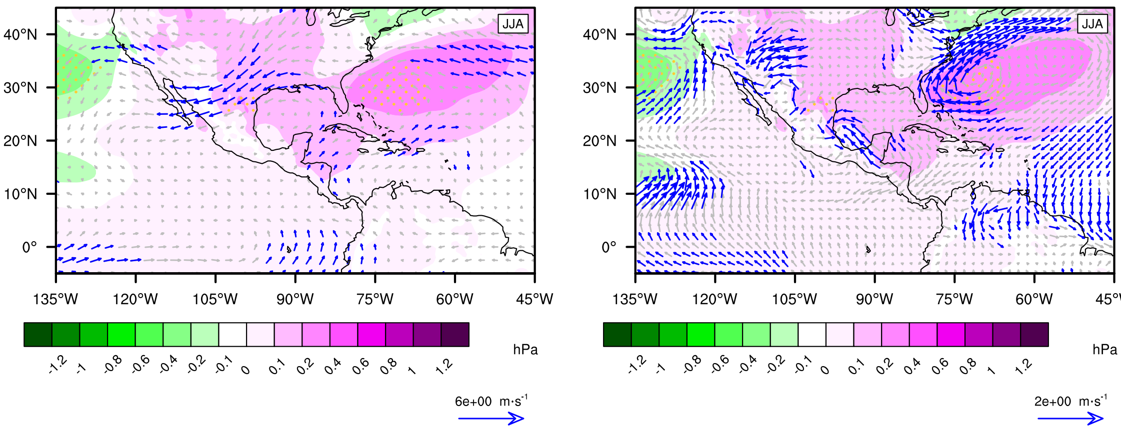

(a) (b)

Figure 3.9: Linear regression coefficient of JJA winds at (a) 200 hPa and (b) 850 hPa (arrows, $m{\cdot}s^{-1}$), and surface pressure (shaded, hPa) onto the normalised JJA EOT3, per standard deviation of seasonal rainfall (mm). Wind vectors are drawn in blue when at least one component of the vector is significant at the 10% level. Yellow stippling indicates surface pressure significant at the 10% level.

3.3.2 Winter

DJF EOT1

EOT1 for DJF seasonal means shows a base point that explains 70% of the temporal variance of the area-average rainfall. The base point is located in a region of high mean winter rainfall in Texas and is correlated with much of northern and northwestern Middle America's rainfall (Fig. 3.10a).

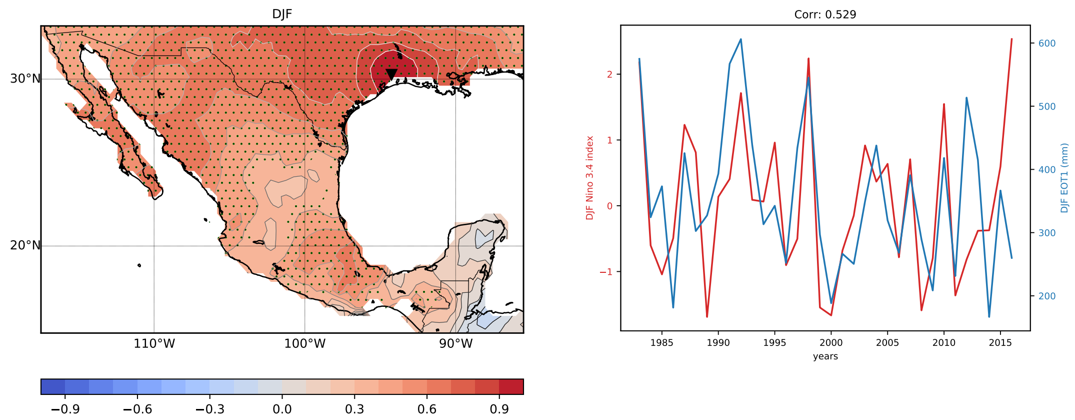

(a) (b)

Figure 3.10: (a) Correlation of DJF EOT1 base point with the DJF rainfall at each point of the domain; the EOT base point is marked with a black inverted triangle (stippling indicates correlations that are significant at the 5% level). (b) Seasonal time-series of DJF EOT1 rainfall (blue line) and the DJF Niño 3.4 (red line), with a correlation coefficient of 0.52 for the period 1983-2016.

DJF EOT1 has a correlation coefficient of 0.52 with DJF Niño 3.4 (Fig. 3.10b). Regression patterns for DJF SSTs resemble canonical El Niño (Fig. 3.11a). The mature phase of El Niño occurs during DJF, showing maximum anomalous warming in the equatorial eastern Pacific and cold SST anomalies over the off-equatorial western Pacific and the central North Pacific (e.g., Deser et al., 2010). These results are consistent with wet conditions over the northern Middle America observed in winter during strong El Niño episodes (e.g., Ropelewski and Halpert, 1987; Magaña et al., 2003)

OLR regressions mostly agree with the corresponding SST patterns over the central Pacific Ocean, with the opposite sign (Figs. 3.11b and 3.11a, respectively). Simultaneously, regression maps show negative OLR anomalies over most Middle America and the Gulf of Mexico, directly related to positive DJF EOT1.

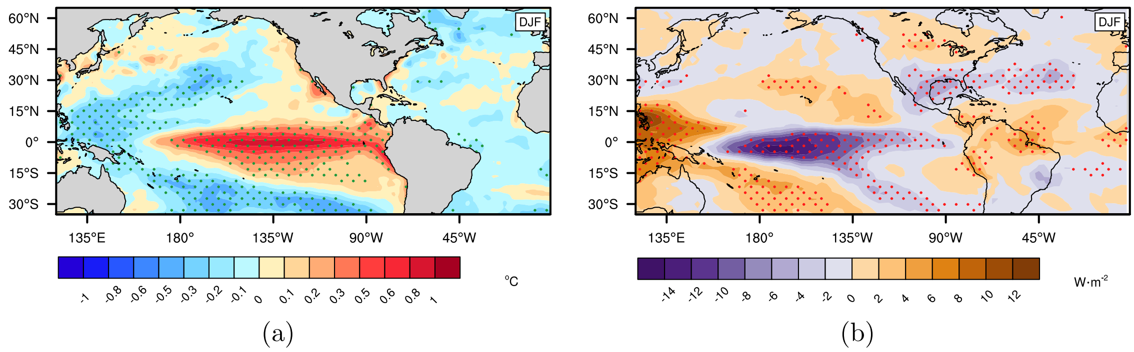

Figure 3.11: Linear regression coefficient of DJF (a) SSTs ($^{\circ}C$) and (b) OLR ($W{\cdot}m^{-2}$), onto the normalised DJF EOT1, per standard deviation of seasonal rainfall (mm). Stippling indicates correlations that are significant at the 10% level.

Positive DJF EOT1 is associated with reduced surface pressure in the tropical eastern Pacific and enhanced surface pressure in the tropical western Pacific (Fig. 3.12a). DJF EOT1 is also correlated with 850 hPa westerly wind anomalies, associated with the mature stage of canonical Pacific El Niño, extending from the equatorial western Pacific to the equatorial central Pacific (Fig. 3.12a). The patterns mentioned above are characteristic of a typical weakened Walker circulation during El Niño.

During DJF EOT1, the Aleutian Low and its associated low-level winds are reinforced (Fig. 3.12a). Regressed wind fields at 200 hPa onto DJF EOT1 show the canonical upper-tropospheric response to equatorial convective diabatic heating as in shallow-water models (Matsuno, 1966; Gill, 1980). Figure 3.12a represents the lower-tropospheric convergence and Figure 3.12b shows upper-tropospheric divergence linked to two anticyclonic circulations in the equatorial Pacific. This response reinforces the subtropical Pacific jet westerly winds and shifts the storm track towards northern Middle America, increasing the rainfall over these regions.

Under these conditions, significant anomalous VIMF convergence occurs over northern Middle America (Fig. 3.12c). Also, additional moisture is transported to DJF EOT1 from a region of anomalous VIMF divergence along the eastern Pacific.

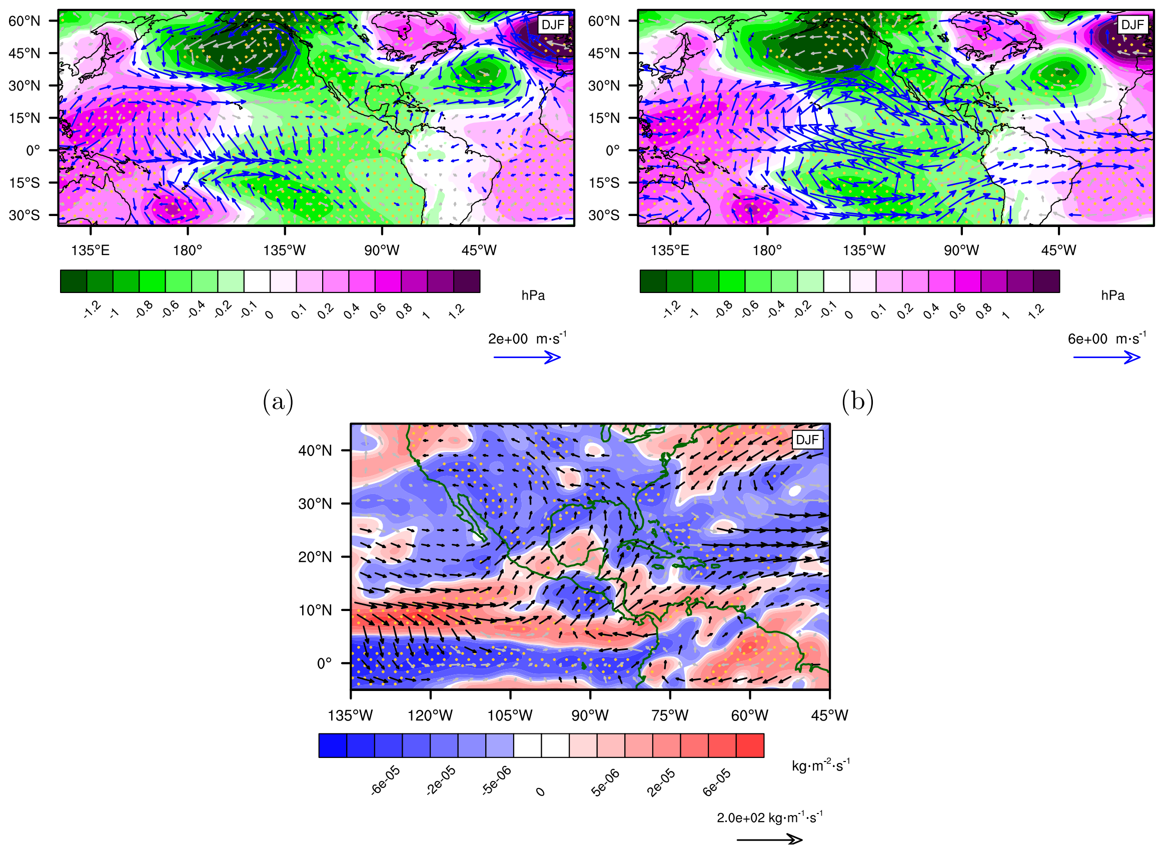

(a) (b)

(c)

Figure 3.12: (a, b) Linear regression coefficient of DJF surface pressure (shaded, hPa) and wind fields (arrows, $m{\cdot}s^{-1}$) at (a) 925 hPa and (b) 200 hPa onto the normalised DJF EOT1, per standard unit of seasonal rainfall (mm); wind vectors are drawn in blue when at least one component of the vector is significant at the 10% level. (c) Linear regression coefficient of DJF VIMF (arrows, $kg{\cdot}m^{-1}{\cdot}s^{-1}$) and VIMF divergence (shaded, $kg{\cdot}m^{-2}{\cdot}s^{-1}$) onto the normalised DJF EOT1, per standard unit of seasonal rainfall (mm); VIMF vectors are drawn in black when at least one component of the vector is significant at the 10% level. Stippling indicates correlations of (a, b) surface pressure and (c) VIMF divergence that are significant at the 10% level.

Figure 3.12a shows a weakened subtropical anticyclone in the North Atlantic Ocean, which might be related to a dynamic mechanism in the troposphere that transfers the effects of the Pacific ENSO to the Atlantic, where ENSO directly influences the zonal pressure gradient between the Pacific and the Atlantic (Enfield and Mayer, 1997; Wang et al., 2010). During El Niño, an anomalous Walker Cell weakens the Atlantic Hadley Cell (Wang, 2004), accompanied by anomalous ascent over the subtropical high, weakening the anticyclonic circulation. Consequently, the tropospheric northeast trade winds slacken, surface fluxes reduce, and, eventually, the upward latent heat flux also reduces. This mechanism leads to ocean surface warming delayed about a season relative to a mature ENSO episode (Alexander and Scott, 2002; Giannini et al., 2001).

DJF EOT2

DJF EOT2 describes a large area in western-to-northern Mexico and explains 16% of the total space–time variance (Fig. 3.13a). This EOT is anticorrelated with the TNI ($r = -0.27$, Fig. 3.13b), and correlated with Niño 4 ($r = 0.26$).

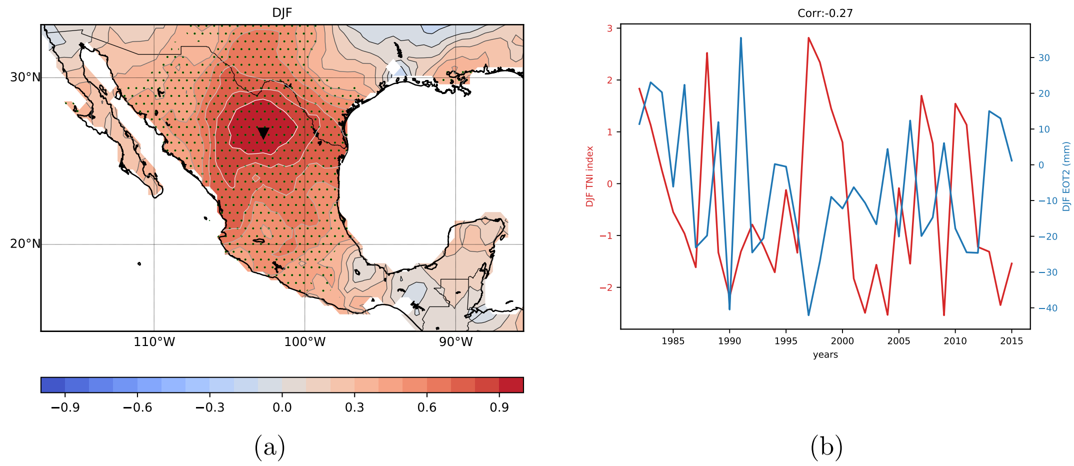

Figure 3.13: (a) Correlation of DJF EOT2 base point with the DJF rainfall at each point of the domain; the EOT base point is marked with a black inverted triangle (stippling indicates correlations that are significant at the 5% level). (b) Seasonal time-series of DJF EOT2 rainfall (blue line) and the DJF TNI (red line), with a correlation coefficient of -0.27 for the period 1983-2016.

Figure 3.14a shows that DJF EOT2 anomalies are associated with anomalous warm SSTs over the equatorial west-central Pacific, which resemble El Niño Modoki (e.g., Ashok et al., 2007; Taschetto et al., 2010). During peak Modoki, SSTs anomalies in the west-central tropical Pacific are warmer than those in the eastern tropical Pacific. El Niño Modoki events drive an anomalous Walker circulation in which the eastern subsiding branch lies over the eastern tropical Pacific, creating VIMF divergence over the eastern tropical Pacific (Fig. 3.15c). This anomalous circulation shifts the eastern Pacific ITCZ northwards (Fig. 3.14b). Additional moisture is transported from the eastern tropical Pacific (where the subsiding branch of the Walker circulation lies) to continental Middle America(Fig. 3.15c). Our results are consistent with Weng et al. (2009), which found that the northward shift of the ITCZ during the El Niño Modoki brings additional moisture from the tropical Pacific to northwestern Middle America. This additional moisture might be accomplished through higher specific humidity rather than stronger wind.

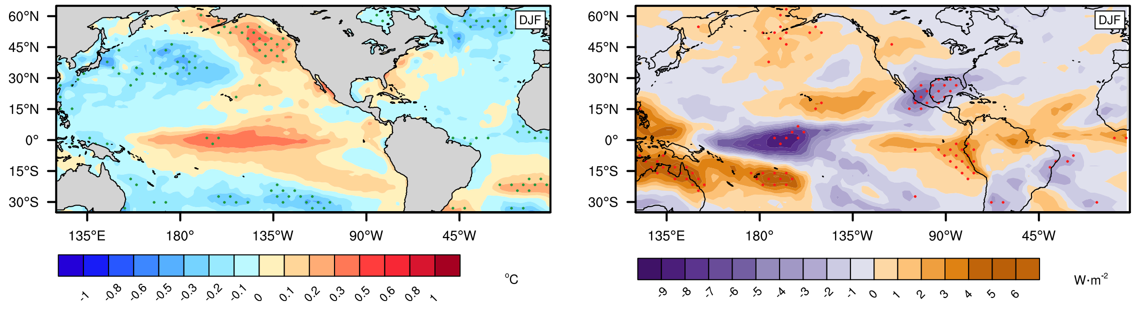

(a) (b)

Figure 3.14: Linear regression coefficient of DJF (a) SSTs ($^{\circ}C$) and (b) OLR ($W{\cdot}m^{-2}$), onto the normalised DJF EOT2, per standard deviation of seasonal rainfall (mm). Stippling indicates correlations that are significant at the 10% level.

During DJF EOT2, the Aleutian Low is stronger and shifted southwards, and its associated low-level and upper-tropospheric cyclonic circulations are both reinforced (Fig. 3.15a). Our results are consistent with Kim and Alexander (2015), who found that during central Pacific El Niño (Modoki) events, an anomalous southward shift of the cyclonic flow around a deeper Aleutian low allows VIMF anomalies from the subtropical Pacific into southwestern Middle America. Figure 3.15c shows additional moisture transported from the tropical eastern Pacific into Middle America, and VIMF convergence over most northern Middle America, which is highly associated with DJF EOT2.

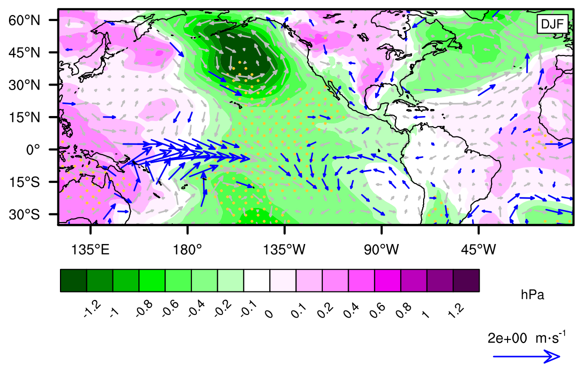

(a)

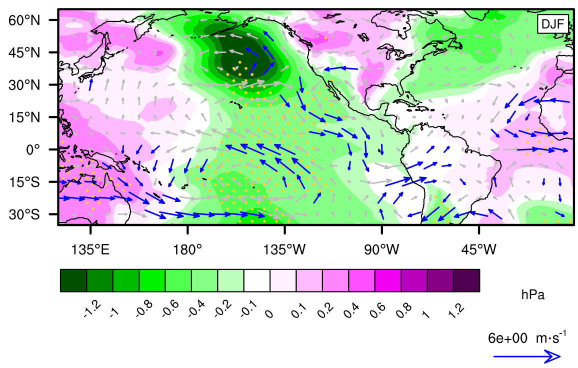

(b)

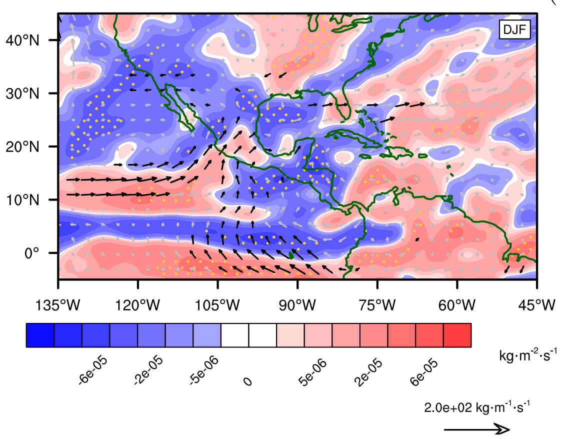

(c)

Figure 3.15: (a, b) Linear regression coefficient of DJF surface pressure (shaded, hPa) and wind fields (arrows, $m{\cdot}s^{-1}$) at (a) 925 hPa and (b) 200 hPa onto the normalised DJF EOT2, per standard unit of seasonal rainfall (mm); wind vectors are drawn in blue when at least one component of the vector is significant at the 10% level. (c) Linear regression coefficient of DJF VIMF (arrows, $kg{\cdot}m^{-1}{\cdot}s^{-1}$) and VIMF divergence (shaded, $kg{\cdot}m^{-2}{\cdot}s^{-1}$) onto the normalised DJF EOT2, per standard unit of seasonal rainfall (mm); VIMF vectors are drawn in black when at least one component of the vector is significant at the 10% level. Stippling indicates correlations of (a, b) surface pressure and (c) VIMF divergence that are significant at the 10% level.

DJF EOT3

DJF EOT3 presents a base point that explains 5% of the temporal variance of the area-average rainfall, which is highly correlated with Central America and the Yucatan Peninsula (Fig. 3.16a).

DJF EOT3 is linked to surface pressure anomalies over the North Atlantic basin: regressed surface pressure shows a reinforcement of the the Icelandic low and regressed winds at 925 hPa show an anomalous anticyclonic circulation associated with an enhanced NASH (Fig. 3.17a). These anomalies drive moisture flux from an area of strong VIMF divergence over the tropical North Atlantic, which is transported to the Caribbean through the westernmost flank of the NASH. However, there is no a clear significance between this DJF EOT3 and this moisture transport.

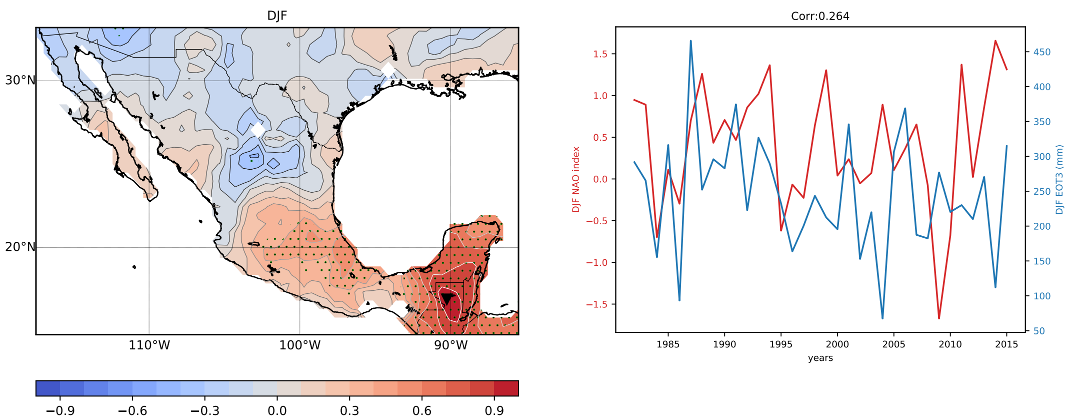

(a) (b)

Figure 3.16: (a) Correlation of DJF EOT3 base point with the DJF rainfall at each point of the domain; the EOT base point is marked with a black inverted triangle (stippling indicates correlations that are significant at the 5% level). (b) Seasonal time-series of DJF EOT3 rainfall (blue line) and the DJF NAO index (red line), with a correlation coefficient of 0.26 for the period 1983-2016.

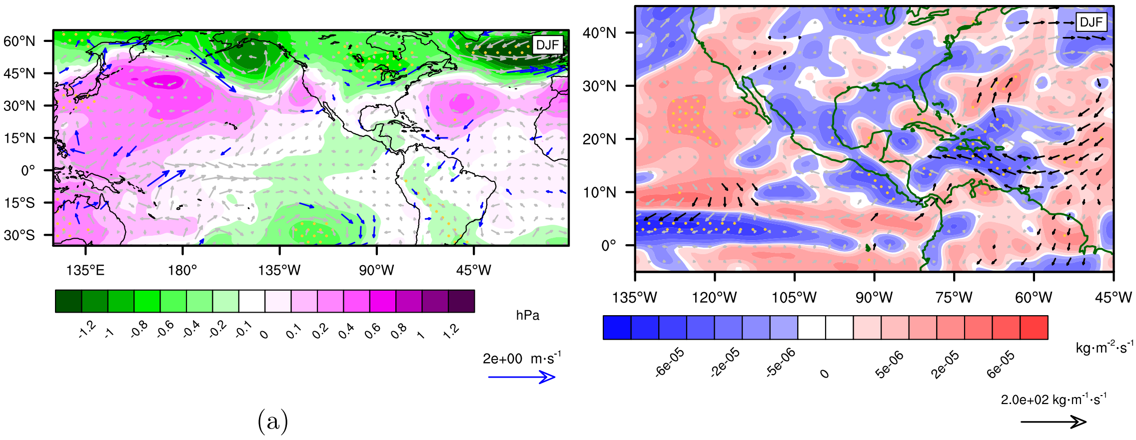

(a)

(b)

Figure 3.17: (a) Linear regression coefficient of DJF surface pressure (shaded, hPa) and wind fields (arrows, $m{\cdot}s^{-1}$) at 925 hPa onto the normalised DJF EOT3, per standard unit of seasonal rainfall (mm); wind vectors are drawn in blue when at least one component of the vector is significant at the 10% level. (b) Linear regression coefficient of DJF VIMF (arrows, $kg{\cdot}m^{-1}{\cdot}s^{-1}$) and VIMF divergence (shaded, $kg{\cdot}m^{-2}{\cdot}s^{-1}$) onto the normalised DJF EOT3, per standard unit of seasonal rainfall (mm); VIMF vectors are drawn in black when at least one component of the vector is significant at the 10% level. Stippling indicates correlations of (a) surface pressure and (b) VIMF divergence that are significant at the 10% level.

3.3.3 Spring

MAM EOT1

The EOT analysis for MAM shows a base point that explains 58% of the temporal variance of the area-average rainfall. The base point in northeast Mexico is highly correlated with a wide area of the Gulf coastal plain and northern Middle America (Fig. 3.18a). MAM EOT1 is correlated with Niño 3.4 ($r = 0.45$, Fig. 3.18b).

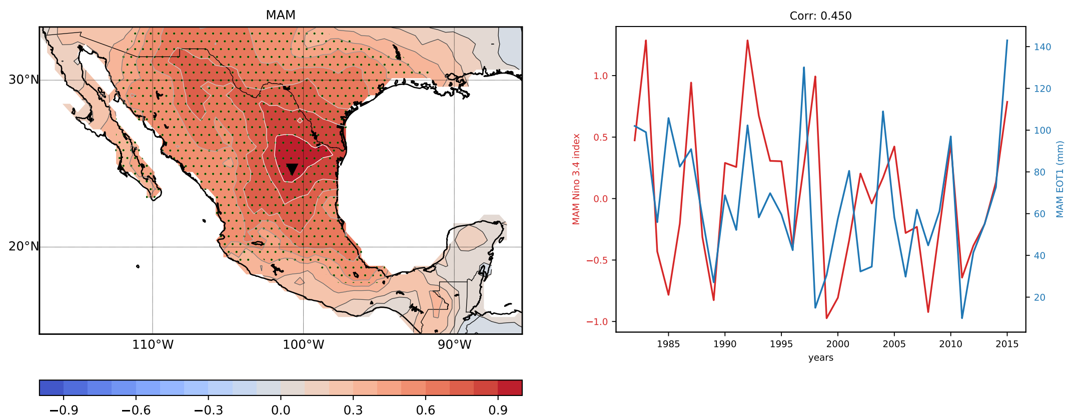

(a) (b)

Figure 3.18: (a) Correlation of MAM EOT1 base point with MAM rainfall at each point of the domain; the EOT base point is marked with a black inverted triangle (stippling indicates correlations that are significant at the 5% level). (b) Seasonal time-series of MAM EOT1 rainfall (blue line) and the MAM Niño 3.4 (red line), with a correlation coefficient of 0.45 for the period 1982-2015.

Regression analysis shows that strong MAM EOT1 is associated with warmer MAM SSTs in the central Pacific (Fig. 3.19), and with anomalous low-level westerlies over the western Pacific (Fig. 3.20b). Regressed SSTs (simultaneous and time-lagged) onto MAM EOT1 (Fig. 3.19) show patterns linked to the seasonal evolution of canonical El Niño events (e.g., Deser et al., 2010) over four seasons, starting with MAM, and followed by JJA, SON, and DJF.

Additional regression analysis onto MAM EOT1 reveals anticorrelations with OLR over the western Pacific (Fig. 3.20a) and positive correlations with anomalous westerly moisture flux (not shown), similar to the ones observed during developing El Niño (e.g., Deser et al., 2010), which may be enhanced by westerly wind anomalies over the equatorial western-central Pacific (Fig. 3.20b).

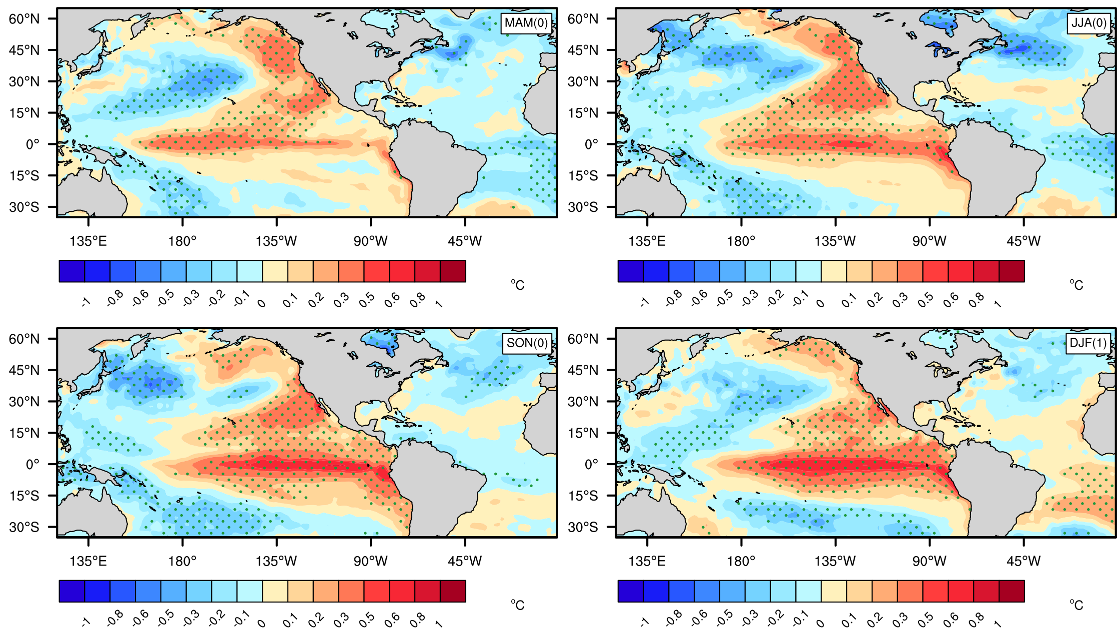

Figure 3.19: Linear regression coefficient of simultaneous MAM and following JJA, SON and DJF SSTs onto the normalised MAM EOT1 for 1982-2015. Units: $^{\circ}C$ per standard deviation of seasonal rainfall in mm. Stippling indicates correlations that are significant at the 10% level.

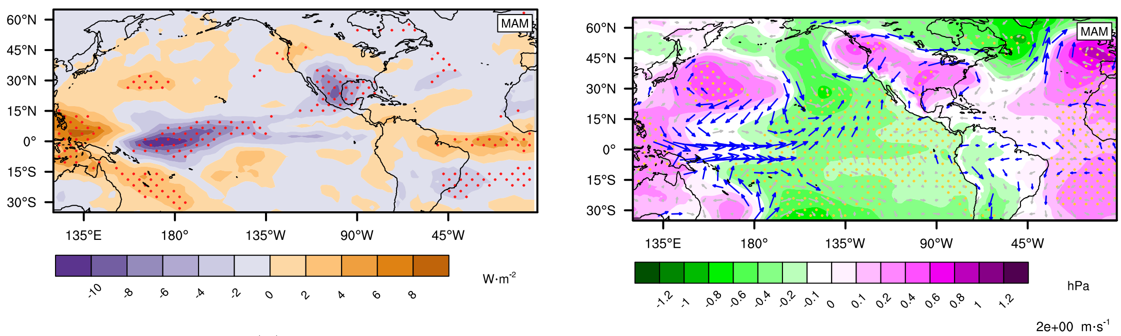

(a)

(b)

Figure 3.20: (a) Linear regression coefficient of MAM OLR ($W{\cdot}m^{-2}$), onto the normalised MAM EOT1, per standard deviation of seasonal rainfall (mm). (b) Linear regression coefficient of MAM surface pressure (shaded, hPa) and wind fields at 850 hPa (arrows, $m{\cdot}s^{-1}$) onto the normalised MAM EOT1, per standard unit of seasonal rainfall (mm); wind vectors are drawn in blue when at least one component of the vector is significant at the 10% level. Stippling indicates correlations of (a) OLR and (b) surface pressure that are significant at the 10% level.

Regression analysis also suggests a strong teleconnection between developing El Niño and negative OLR anomalies over Middle America. (Fig. 3.20a). Concurrently, significant enhanced VIMF convergence over eastern Middle America and the Gulf of Mexico favours high MAM EOT1 (Fig. 3.21c).

Significant additional moisture from the subtropical eastern Pacific is transported to MAM EOT1 along with an enhanced westerly circulation in the eastern Pacific (around 20°N, see Fig. 3.21c). The ENSO teleconnection also suggests a weakening of the North Pacific High during canonical El Niño in MAM (Fig. 3.20b). During these episodes, anomalous northeasterly low-level winds are advected towards eastern Middle America, (Fig. 3.21a), following the circulation of an enhanced semipermanent continental high in eastern Middle America and the Gulf coastal plain.

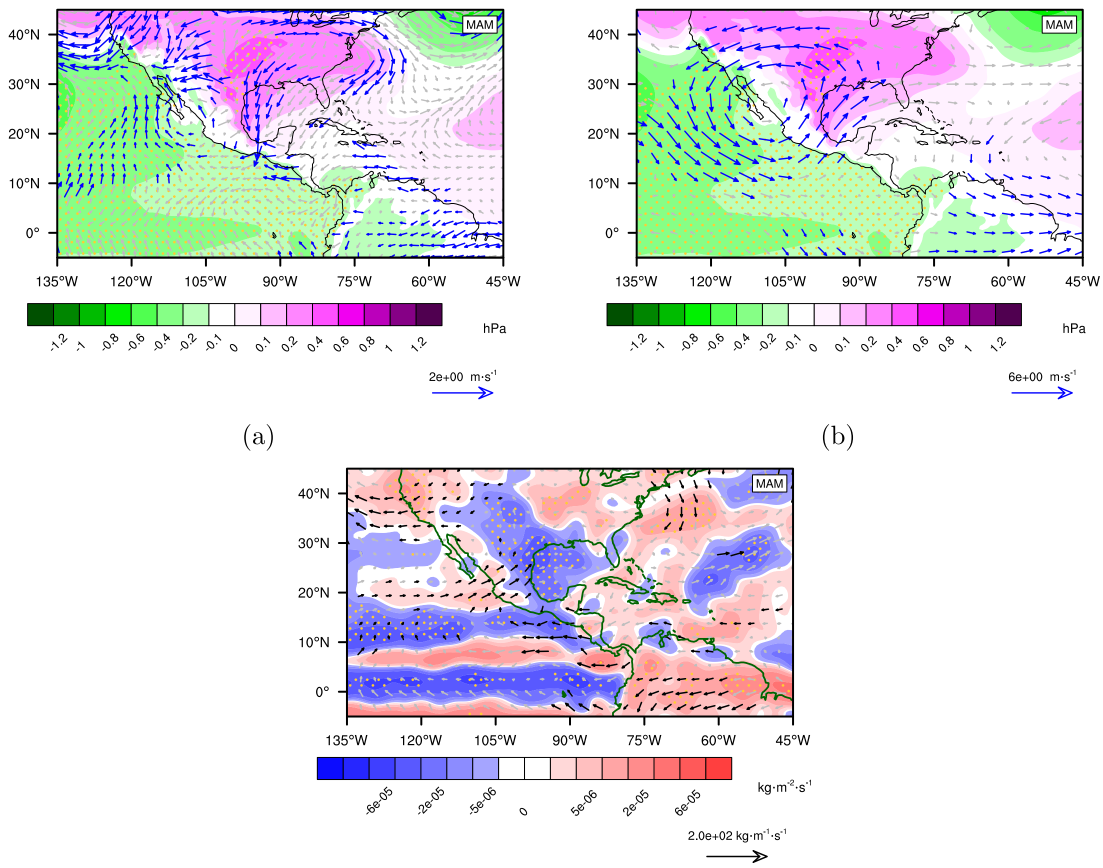

(a) (b)

(c)

Figure 3.21: (a,b) Linear regression coefficient of MAM surface pressure (shaded, hPa) and wind fields (arrows, $m{\cdot}s^{-1}$) at (a) 850 hPa and (b) 200 hPa onto the normalised MAM EOT1, per standard unit of seasonal rainfall (mm); wind vectors are drawn in blue when at least one component of the vector is significant at the 10% level. (c) Linear regression coefficient of MAM VIMF (arrows, $kg{\cdot}m^{-1}{\cdot}s^{-1}$) and VIMF divergence (shaded, $kg{\cdot}m^{-2}{\cdot}s^{-1}$) onto the normalised MAM EOT1, per standard unit of seasonal rainfall (mm); VIMF vectors are drawn in black when at least one component of the vector is significant at the 10% level. Stippling indicates correlations of (a,b) surface pressure and (c) VIMF divergence that are significant at the 10% level.

MAM EOT2

MAM EOT2 is located over the Mexican state of Guerrero and explains 20% of the temporal variance of the area-average rainfall (Fig. 3.22a). This EOT is highly correlated with a substantial area of central Middle America.

MAM EOT2 is anticorrelated with previous DJF Niño 3.4 ($r = -0.40$, Fig. 3.22b), and positively correlated with both simultaneous MAM Niño 3.4 and Niño 1+2 (both with $r = 0.29$, see Table 3.1). Regressed SSTs suggest that decaying La Niña strongly influences MAM EOT2 (Fig. 3.23d). This regression analysis also show an anomalous warm Gulf of Mexico linked with positive MAM EOT2 (Fig. 3.23d).

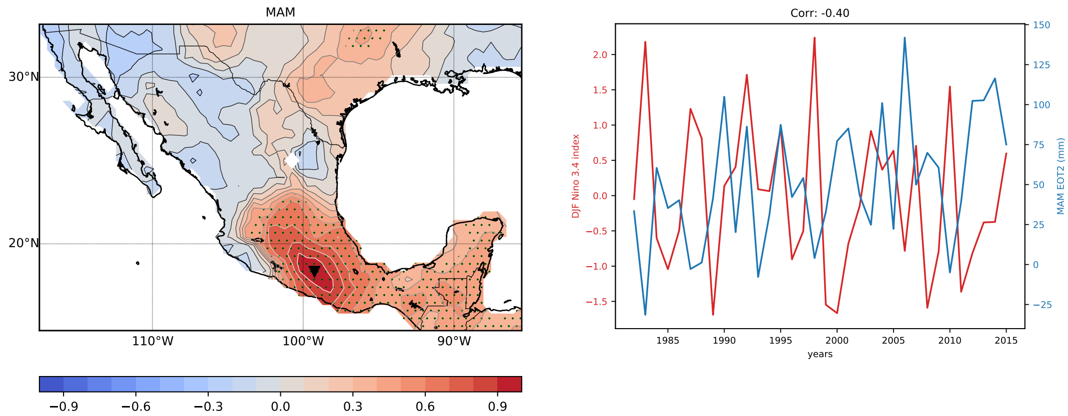

(a) (b)

Figure 3.22: (a) Correlation of MAM EOT2 base point with the MAM rainfall at each point of the domain; the EOT base point is marked with a black inverted triangle (stippling indicates correlations that are significant at the 5% level). (b) Seasonal time-series of MAM EOT2 rainfall (blue line) and the previous DJF Niño 3.4 (red line), with a correlation coefficient of -0.40 for the period 1982-2015.

Regression analysis of surface pressure and 925 hPa wind fields shows a typical La Niña associated weakening of the Aleutian Low (Fig. 3.23c). Anomalously high pressure in the eastern Middle America., the Gulf of Mexico, and the Caribbean Sea is linked with the enhanced CLLJ. MAM EOT2 is positively correlated with the CLLJ index ($r = 0.57$). The anomalous low-level circulations in the Atlantic may facilitate the variability of moisture transport and convergence in the Caribbean and southern/central Middle America (Fig. 3.23a).

Regressed OLR onto MAM EOT2 suggests that positive anomalies of OLR in the subtropical North Atlantic, the Caribbean and the Gulf of Mexico are associated with regional VIMF divergence (Fig. 3.23b). Anomalous positive OLR over the equatorial central/eastern Pacific suggests an anomalous northward shift of the location of the Pacific

ITCZ, which may enhance local convective activity over the eastern Pacific warm pool and the Mexican southwest coast (Fig. 3.23b). In this sense, regression analysis shows a strong correlation between VIMF convergence (associated with the variability of the Pacific ITCZ) and MAM EOT2 (Fig. 3.23a).

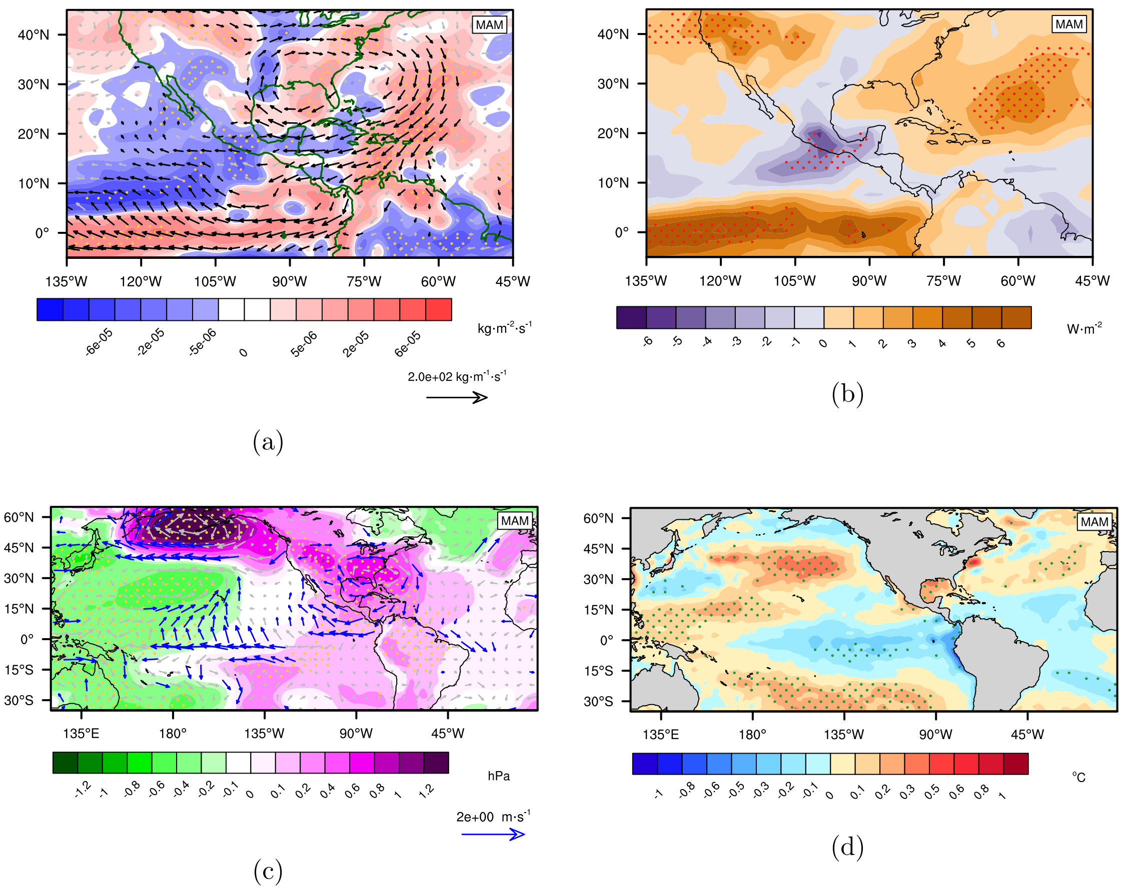

Figure 3.23: (a) Linear regression coefficient of MAM VIMF (arrows, $kg{\cdot}m^{-1}{\cdot}s^{-1}$) and VIMF divergence (shaded, $kg{\cdot}m^{-2}{\cdot}s^{-1}$) onto the normalised MAM EOT2, per standard unit of seasonal rainfall (mm); VIMF vectors are drawn in black when at least one component of the vector is significant at the 10% level. (b) MAM OLR ($W{\cdot}m^{-2}$), onto the normalised MAM EOT2, per standard deviation of seasonal rainfall (mm). (c) Linear regression coefficient of MAM surface pressure (shaded, hPa) and wind fields at 925 hPa (arrows, $m{\cdot}s^{-1}$) onto the normalised MAM EOT2, per standard unit of seasonal rainfall (mm); wind vectors are drawn in blue when at least one component of the vector is significant at the 10% level. (d) Linear regression coefficient of MAM SSTs ($^{\circ}C$) onto the normalised MAM EOT2, per standard unit of seasonal rainfall (mm). Stippling indicates correlations of (a) VIMF divergence, (b) OLR, (c) surface pressure, and (d) SSTs that are significant at the 10% level.

MAM EOT3

MAM EOT3 is centred in northeastern Middle America and explains 11% of the variance of area-averaged rainfall (Fig. 3.24a). This EOT is significantly correlated with eastern Middle America and the Baja California Peninsula, and significantly anticorrelated with central-eastern Middle America. MAM EOT3 is anticorrelated with the simultaneous AMM index ($r = -0.36$).

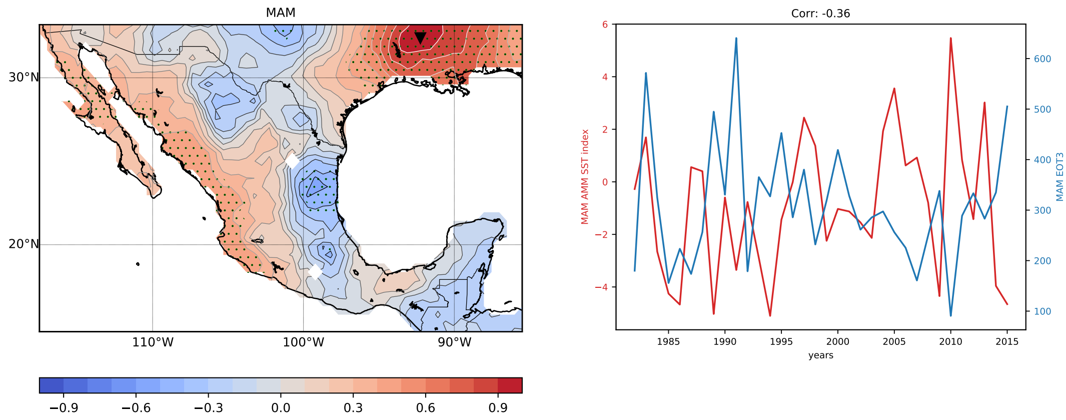

(a) (b)

Figure 3.24: (a) Correlation of MAM EOT3 base point with MAM rainfall at each point of the domain; the EOT base point is marked with a black inverted triangle (stippling indicates correlations that are significant at the 5% level). (b) Seasonal time-series of MAM EOT3 rainfall (blue line) and the SST AMM index for MAM (red line), with a correlation coefficient of -0.36 for the period 1982-2015.

MAM EOT3 is anticorrelated with SSTs in the North Atlantic. Regressed SSTs onto MAM EOT3 show the characteristic pattern the negative phase of the AMM (Fig. 3.25a). Regressed OLR shows negative anomalies over the southeastern U.S. and positive anomalies over the tropical North Atlantic and the Caribbean Sea, at approximately 20°N (Fig. 3.25b).

During positive MAM EOT3, a strong NASH prevails over the tropical North Atlantic and the Caribbean Sea (Fig. 3.26a). A reinforced low-level anticyclonic circulation over the subtropical Atlantic favour VIMF divergence in the Caribbean (Fig. 3.26b). An enhanced NASH promotes the transport of additional moisture towards northeastern Middle America but inhibits the moisture convergence in east-central Middle America.

The negative AMM, favours the southward migration of the ITCZ, which is linked with anomalous subsidence in Central America and south-eastern Middle America. These conditions strongly inhibit convection and rainfall in MAM EOT3.

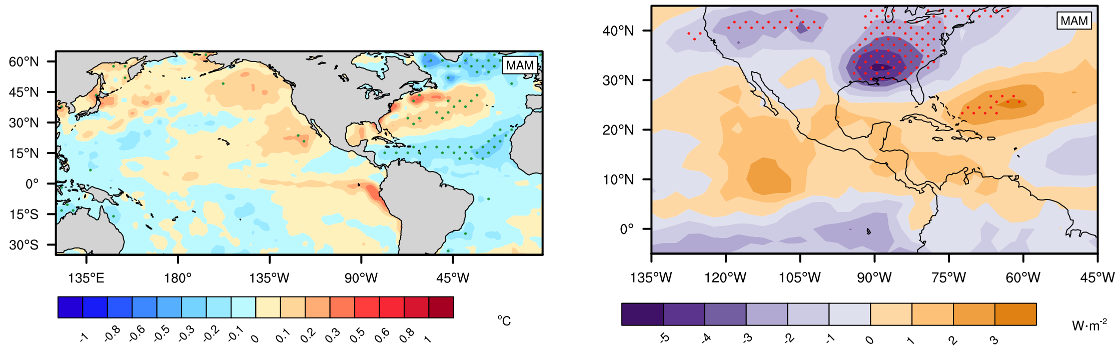

(a) (b)

Figure 3.25: Linear regression coefficient of MAM (a) SSTs ($°C$) and (b) OLR ($W{\cdot}m^{-2}$), onto the normalised MAM EOT3, per standard deviation of seasonal rainfall (mm). Stippling indicates correlations that are significant at the 10% level.

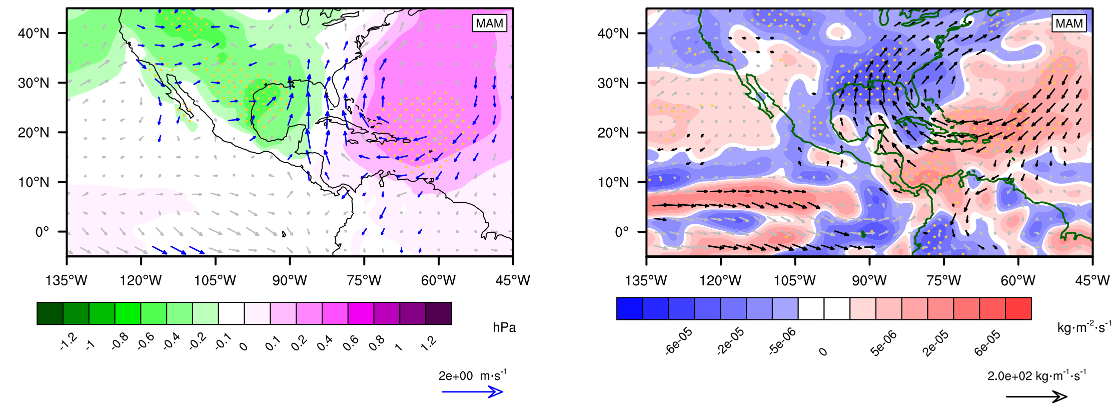

(a) (b)

Figure 3.26: (a) Linear regression coefficient of MAM surface pressure (shaded, hPa) and wind fields (arrows, $m{\cdot}s^{-1}$) at 925 hPa onto the normalised MAM EOT3, per standard unit of seasonal rainfall (mm); wind vectors are drawn in blue when at least one component of the vector is significant at the 10% level. (b) Linear regression coefficient of MAM VIMF (arrows, $kg{\cdot}m^{-1}{\cdot}s^{-1}$) and VIMF divergence (shaded, $kg{\cdot}m^{-2}{\cdot}s^{-1}$) onto the normalised MAM EOT3, per standard unit of seasonal rainfall (mm); VIMF vectors are drawn in black when at least one component of the vector is significant at the 10% level. Stippling indicates correlations of (a) surface pressure and (b) VIMF divergence that are significant at the 10% level.

3.3.4 Autumn

SON EOT1

The first EOT for SON shows a base point over central Middle America that explains 71% of the temporal variance of area-averaged rainfall. This EOT has a strong across central and eastern Middle America (Fig. 3.27a).

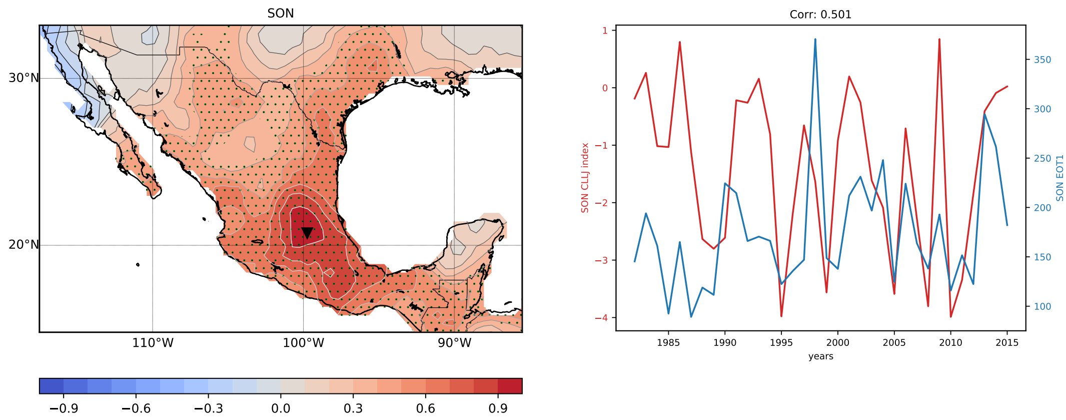

(a) (b)

Figure 3.27: (a) SON EOT1 base point correlated with the SON rainfall at each point of the domain; the EOT base point is marked with a black inverted triangle (stippling indicates correlations that are significant at the 5% level). (b) Seasonal time-series of SON EOT1 rainfall (blue line) and the SON CLLJ index (red line), with a correlation coefficient of 0.50 for the period 1982-2015.

Linear regression coefficient of SSTs onto SON EOT1 do not show a significant connection with simultaneous SON equatorial Pacific SSTs, but show positive correlations with previous DJF, MAM, and JJA, similar to those observed during peak and decaying canonical El Niño events(Fig. 3.28).

Regression analysis also shows positive correlations with simultaneous SST anomalies in the North Atlantic Ocean and the Gulf of Mexico (SON, Fig. 3.28). SON EOT1 is also associated with strong VIMF and VIMF divergence in the Caribbean Sea, near the CLLJ core (15°N, 75°W, Fig. 3.29c). The SON CLLJ index is positively correlated with SON EOT1 (r = 0.50, Fig. 3.27b), which suggests that CLLJ variability is a potential modulator of the regional moisture convergence and transport for SON EOT1.

Figure 3.29c shows easterly moisture flux from the Caribbean turns north-easterly near Central America and toward the Gulf of Mexico and the Gulf Coast Plain, which reinforces the mean seasonal pattern of moisture transport over the region. This moisture transport is strongly linked with low-tropospheric winds and with surface pressure anomalies that prevail in the IAS (Fig. 3.29d) during positive SON EOT1.

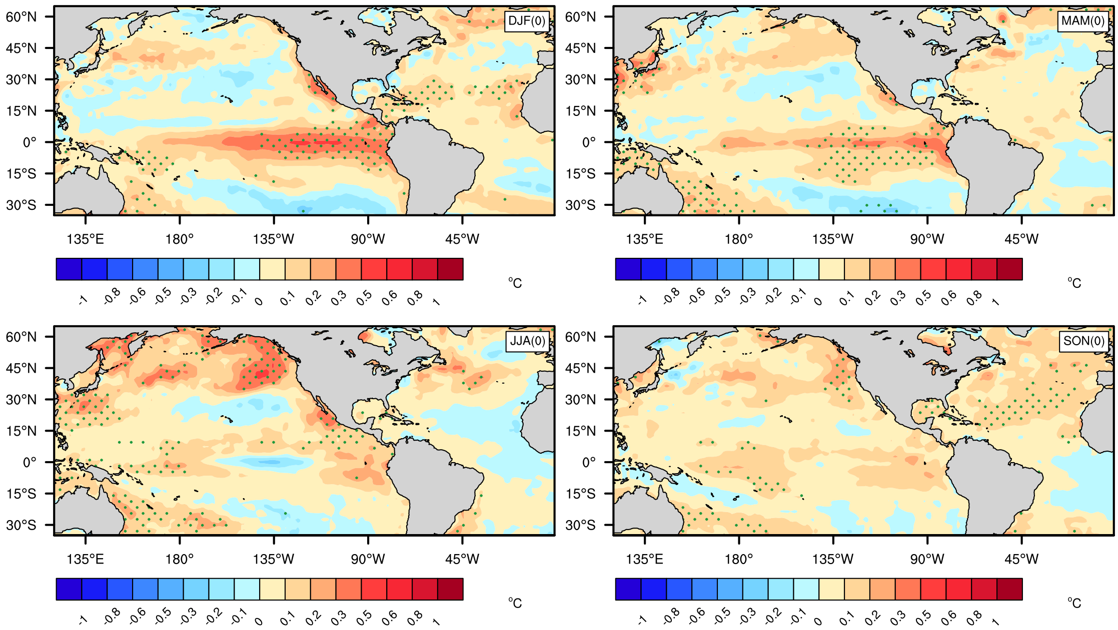

Figure 3.28: Linear regression coefficient of previous DJF(0), MAM(0), and JJA(0) and simultaneous SON(0) SSTs onto the normalised SON EOT1 for 1982-2015. Units: $°C$ per standard deviation of seasonal rainfall in mm. Stippling indicates correlations that are significant at the 10% level.

VIMF convergence anomalies in both continental Middle America and the IAS promote high SON EOT1 (Fig. 3.29c). Anomalies of OLR are anticorrelated with SON EOT1; regressed OLR indicates significantly increased convective activity over central Middle America during enhanced SON EOT1. Regression analysis of TC track densities suggests that this anomalous convection is linked to enhanced TCs activity in both the Gulf of Mexico and the eastern Pacific (Fig. 3.29b). Figure 3.29d shows westerly equatorial 850hPa wind anomalies accompanied by enhanced convection (Fig. 3.29a) and by positive anomalies of TC activity over the eastern Pacific (Fig. 3.29b), which may favour positive SON EOT1.

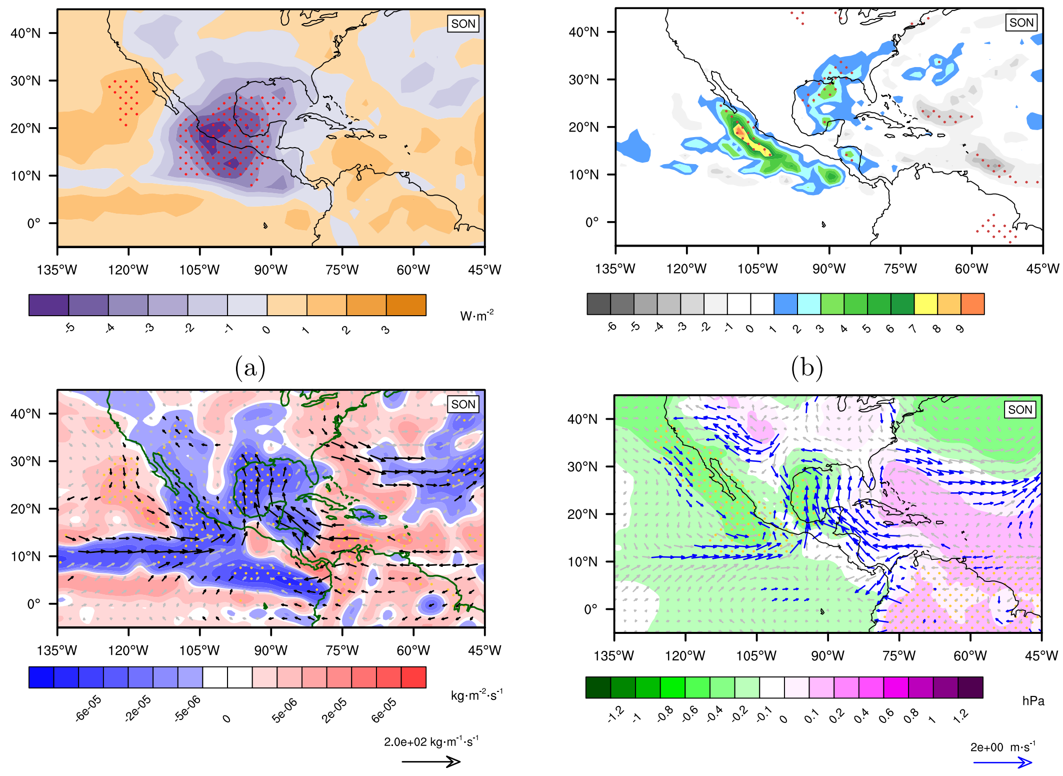

(a) (b) (c) (d)

Figure 3.29: (a) Linear regression coefficient of SON OLR ($W{\cdot}m^{-2}$) onto the normalised SON EOT1, per standard deviation of seasonal rainfall (mm). (b) Linear regression coefficient of SON TC track density scaled to number density per unit area ($\sim 10^6 km^2$) per season onto the normalised SON EOT1, per standard unit of seasonal rainfall (mm). (c) Linear regression coefficient of SON VIMF (arrows, $kg{\cdot}m^{-1}{\cdot}s^{-1}$) and VIMF divergence (shaded, $kg{\cdot}m^{-2}{\cdot}s^{-1}$) onto the normalised SON EOT1, per standard unit of seasonal rainfall (mm); VIMF vectors are drawn in black when at least one component of the vector is significant at the 10% level. (d) Linear regression coefficient of SON surface pressure (shaded, hPa) and wind fields at 850 hPa (arrows, $m{\cdot}s^{-1}$) onto the normalised SON EOT1, per standard unit of seasonal rainfall (mm); wind vectors are drawn in blue when at least one component of the vector is significant at the 10% level. Stippling indicates correlations of (a) OLR, (b) TC track density, (c) VIMF divergence, and (d) surface pressure that are significant at the 10% level.

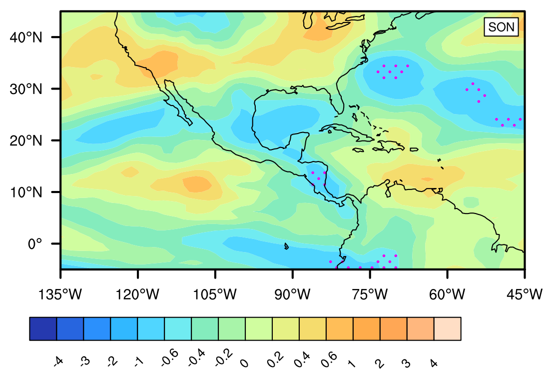

Figure 3.30: Linear regression coefficient of SON vertical wind shear ($m{\cdot}s^{-1}$) onto the normalised SON EOT1, per standard unit of seasonal rainfall (mm). Stippling indicates significance at the 10% level.

SON EOT2

Located over northeastern Middle America, SON EOT2 explains 11% of the variance of the area-averaged rainfall in the season (Fig. 3.31a). This EOT is significantly correlated with a region of central-western Middle America and anticorrelated with a region of the central-eastern Middle America.

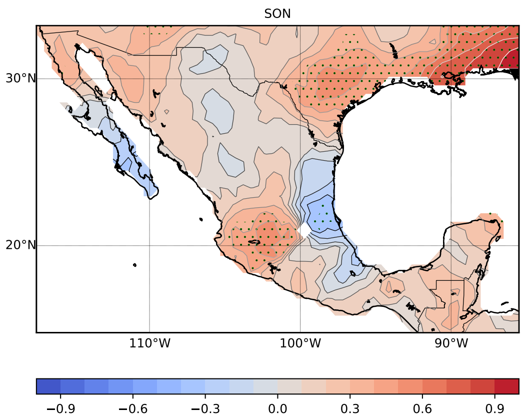

(a)

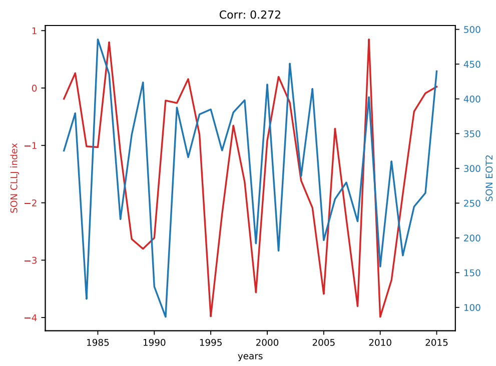

(b)

Figure 3.31: (a) Correlation of SON EOT2 base point with the SON rainfall at each point of the domain; the EOT base point is marked with a black inverted triangle (stippling indicates correlations that are significant at the 5% level). (b) Seasonal time-series of SON EOT2 rainfall (blue line) and the SON CLJJ index (red line), with a correlation coefficient of 0.27 for the period 1982-2015.

SON EOT2 is positively correlated with central Pacific SSTs, which resemble a developing canonical El Niño (Fig. 3.32c). Canonical El Niño promotes subsidence and inhibits convection over the Caribbean Sea, as part of an anomalous Walker circulation (e.g., Alexander and Scott, 2002; Wang, 2004). Consequently, this mechanism weakens the Atlantic Hadley circulation and favours higher surface pressures in the tropical North Atlantic and lower pressures in the subtropical Atlantic, similar to those in regressions of atmospheric pressure and winds on SON EOT2 (Figure 3.32). Enhanced low-tropospheric easterly winds strengthen the CLLJ (Fig. 3.32b) and favour moisture transport from the Caribbean to northeast Middle America (Fig. 3.33a).

Regression analysis shows enhanced OLR and VIMF divergence over the Caribbean (Figs. 3.33c and 3.33a, respectively) during positive SON EOT2. Additional moisture from the Caribbean Sea is transported to the Gulf of Mexico (Fig. 3.33c) following an eastward shifted low-level flow (Fig. 3.33b), mechanically forced by the subsidence prevailing in the tropical North Atlantic.

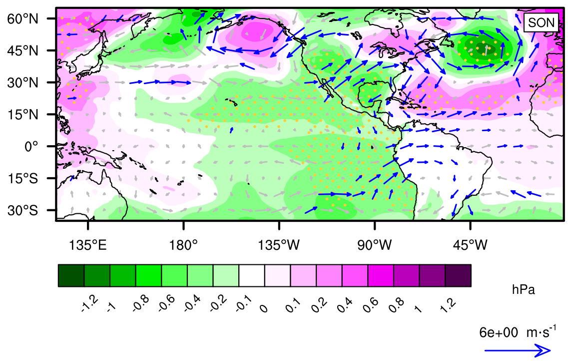

(a)

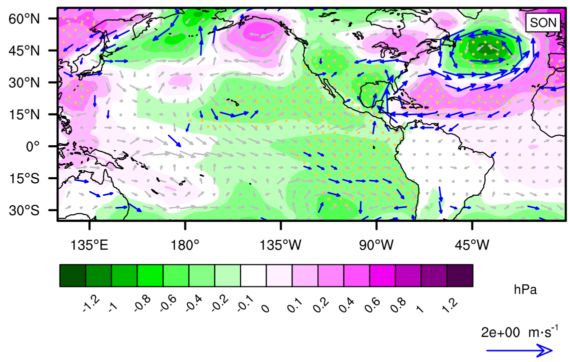

(b)

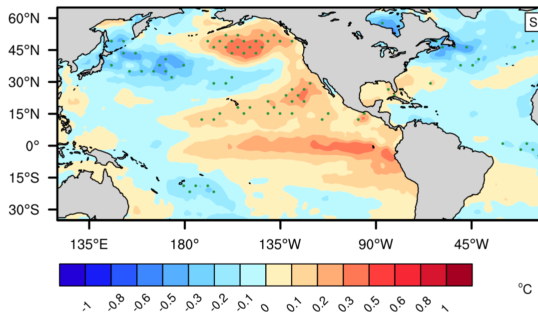

(c)

Figure 3.32: (a, b) Linear regression coefficient of SON surface pressure (shaded, hPa) and wind fields (arrows, $m{\cdot}s^{-1}$) at (a) 200 hPa and (b) 925 hPa onto the normalised SON EOT2, per standard unit of seasonal rainfall (mm); wind vectors are drawn in blue when at least one component of the vector is significant at the 10% level. (c) Linear regression coefficient of SON SSTs ($^{\circ}C$) onto the normalised SON EOT2, per standard unit of seasonal rainfall (mm). Stippling indicates correlations of (a, b) surface pressure and (c) SSTs that are significant at the 10% level.

Reduced OLR (Fig. 3.33c) and increased VIMF convergence (Fig. 3.33a) over northeastern Middle America occur during enhanced SON EOT2. These anomalies are linked with a higher TC activity in the region (Fig. 3.34a). Regression analysis reveals a significant relation between high SON EOT2 and reduced wind shear over the Gulf of Mexico (Fig. 3.34b), which favours TC activity in the region (Fig. 3.34a). An enhanced NASH promotes more TCs from the Gulf of Mexico to track towards northeastern Middle America, decreasing the number of TCs making landfall in central-eastern Middle America.

During canonical El Niño events, TC activity is enhanced by warmer SSTs, decreased wind shear, and enhanced VIMF convergence in the eastern Pacific. These conditions favour TCs making landfall in northeastern Middle America, bringing positive anomalies of rainfall in the area.

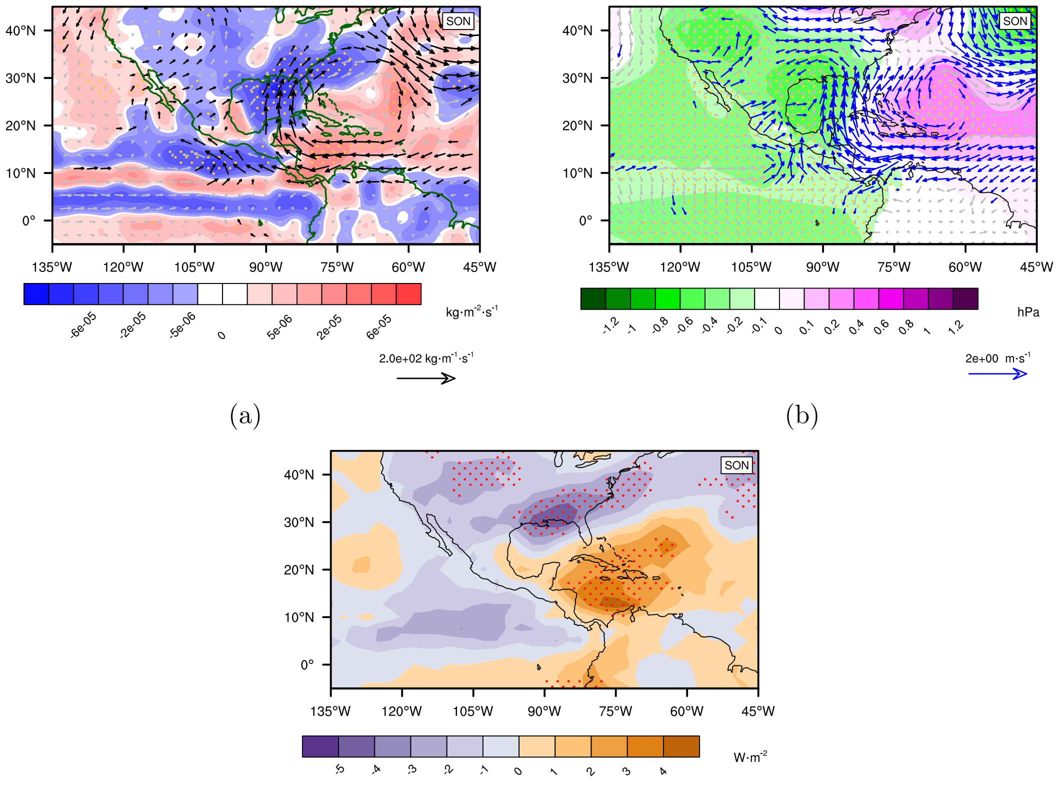

(a) (b) (c)

Figure 3.33: (a) Linear regression coefficient of SON VIMF (arrows, $kg{\cdot}m^{-1}{\cdot}s^{-1}$) and VIMF divergence (shaded, $kg{\cdot}m^{-2}{\cdot}s^{-1}$) onto the normalised SON EOT2, per standard unit of seasonal rainfall (mm); VIMF vectors are drawn in black when at least one component of the vector is significant at the 10% level. (b) Linear regression coefficient of SON surface pressure (shaded, hPa) and wind fields at 850 hPa (arrows, $m{\cdot}s^{-1}$) onto the normalised SON EOT2, per standard unit of seasonal rainfall (mm); wind vectors are drawn in blue when at least one component of the vector is significant at the 10% level. (c) Linear regression coefficient of OLR ($W{\cdot}m^{-2}$), onto the normalised SON EOT2, per standard deviation of seasonal rainfall (mm). Stippling indicates correlations of (a) VIMF divergence, (b) surface pressure, and (c) OLR that are significant at the 10% level.

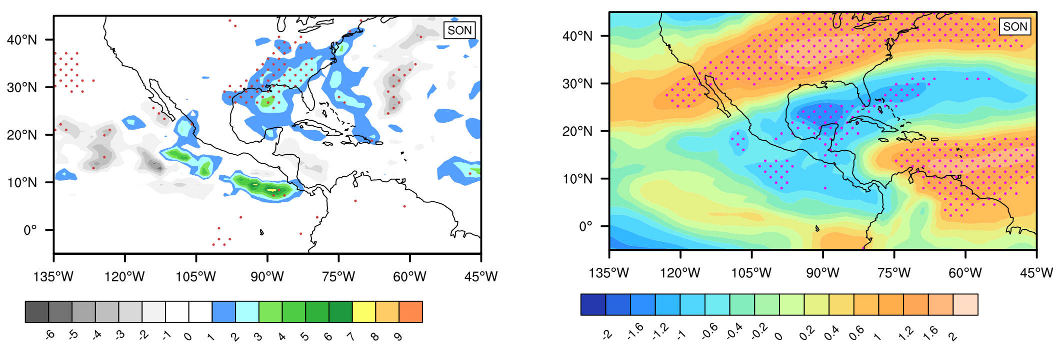

(a) (b)

Figure 3.34: Linear regression coefficient of SON (a) TC track density scaled to number density per unit area ($\sim 10^6 km^2$) per season and (b) vertical wind shear ($m{\cdot}s^{-1}$), onto the normalised SON EOT2, per standard deviation of seasonal rainfall (mm). Stippling indicates correlations that are significant at the 10% level.

SON EOT3

Located in southern Middle America, SON EOT3 explains 5% of the temporal variance of the area-averaged rainfall (Fig. 3.35a). This EOT is positively correlated with simultaneous TNI ($r = 0.37$, Fig. 3.35b).

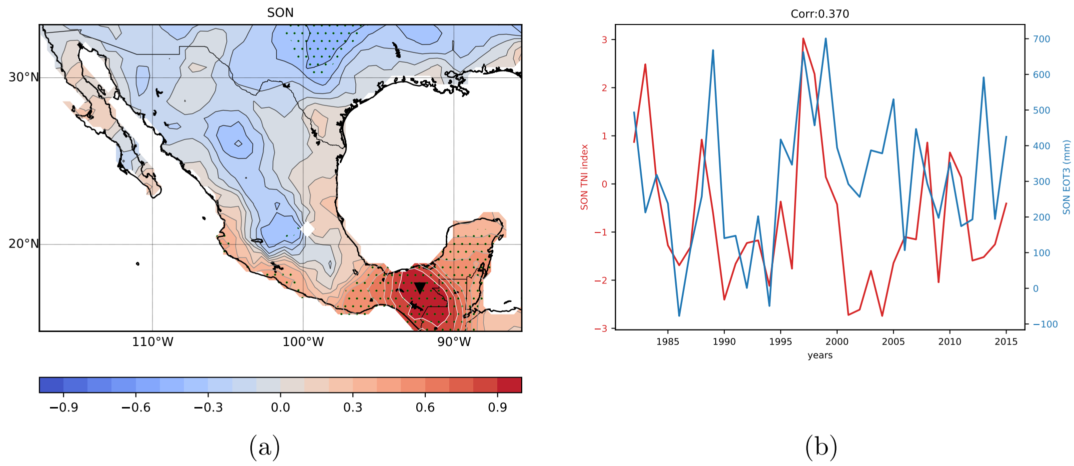

Figure 3.35: (a) Correlation of SON EOT3 base point with the SON rainfall at each point of the domain; the EOT base point is marked with a black inverted triangle (stippling indicates correlations that are significant at the 5% level). (b) Seasonal time-series of SON EOT3 rainfall (blue line) and the SON TNI (red line), with a correlation coefficient of 0.37 for the period 1982-2015.

SON EOT3 is negatively correlated with central Pacific SSTs, which resemble a developing La Niña Modoki (Fig. 3.36a). Positive surface pressure anomalies in the tropical North Atlantic are correlated with SON EOT3, indicating a weakening of the NASH that extends to the Caribbean and the Gulf of Mexico (Fig. 3.36c).

Linear regression coefficient of winds onto SON EOT3 at 925 hPa show a significant weakening of the mean flow over the tropical eastern Pacific and the Caribbean, where the latter is related with a weaker CLLJ (Fig. 3.36c). An additional analysis shows that SON EOT3 is significantly anticorrelated with the CLLJ ($r = -0.34$).

Enhanced VIMF convergence (Fig. 3.37b) and OLR (Fig. 3.37c) prevail over most southern Middle America, the Gulf of Mexico, and the Caribbean, which indicate anomalous enhanced convective activity over the region that is related with anomalous TC activity. Regressed analysis of TC track densities shows significant positive anomalies in the Caribbean and the Gulf of Mexico and negative anomalies over the eastern Pacific (Fig. 3.38a).

Significant anomalous westerly winds at 850 hPa extend over the eastern Pacific to the Caribbean, following a cyclonic circulation over the Gulf of Mexico (Fig. 3.37), which favours high SON EOT3 and higher TC activity in the Gulf of Mexico. These anomalous circulations are associated with reduced wind shear in the Caribbean Sea (Fig. 3.38b), which, under conditions of significant warmer SSTs in the basin (Fig. 3.6a), and positive anomalies of atmospheric moisture (Fig. 3.37b), favours TC activity in the Caribbean and the Gulf of Mexico.

On the other hand, significant colder SSTs (Fig. 3.36a) and higher wind shear (Fig. 3.38) in the eastern Pacific reduce TC activity in the EPWP.

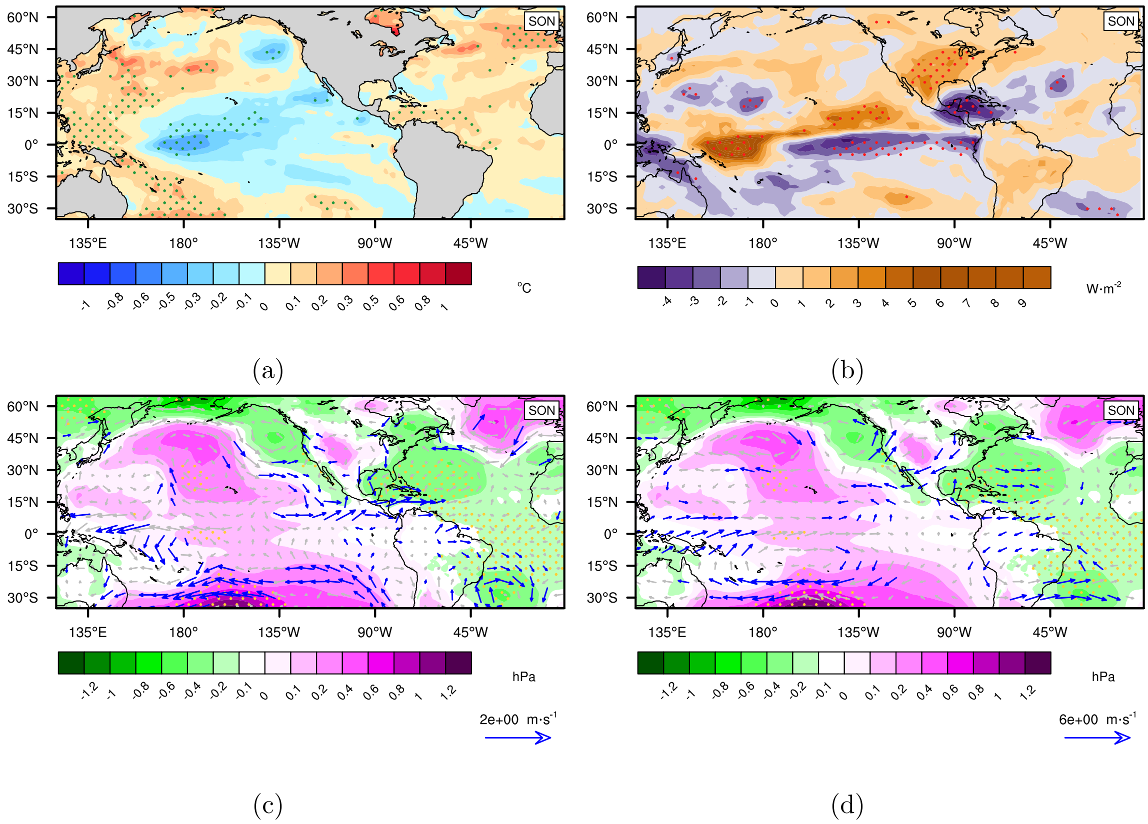

Figure 3.36: (a) Linear regression coefficient of SON SSTs ($°C$) onto the normalised SON EOT3, per standard unit of seasonal rainfall (mm). (b) OLR ($W{\cdot}m^{-2}$), onto the normalised SON EOT3, per standard deviation of seasonal rainfall (mm). (c, d) Linear regression coefficient of SON surface pressure (shaded, hPa) and wind fields (arrows, $m{\cdot}s^{-1}$) at (a) 925 hPa and (b) 200 hPa onto the normalised SON EOT3, per standard unit of seasonal rainfall (mm); wind vectors are drawn in blue when at least one component of the vector is significant at the 10% level. Stippling indicates correlations of (a) SSTs, (b) OLR and (c, d) surface pressure that are significant at the 10% level.

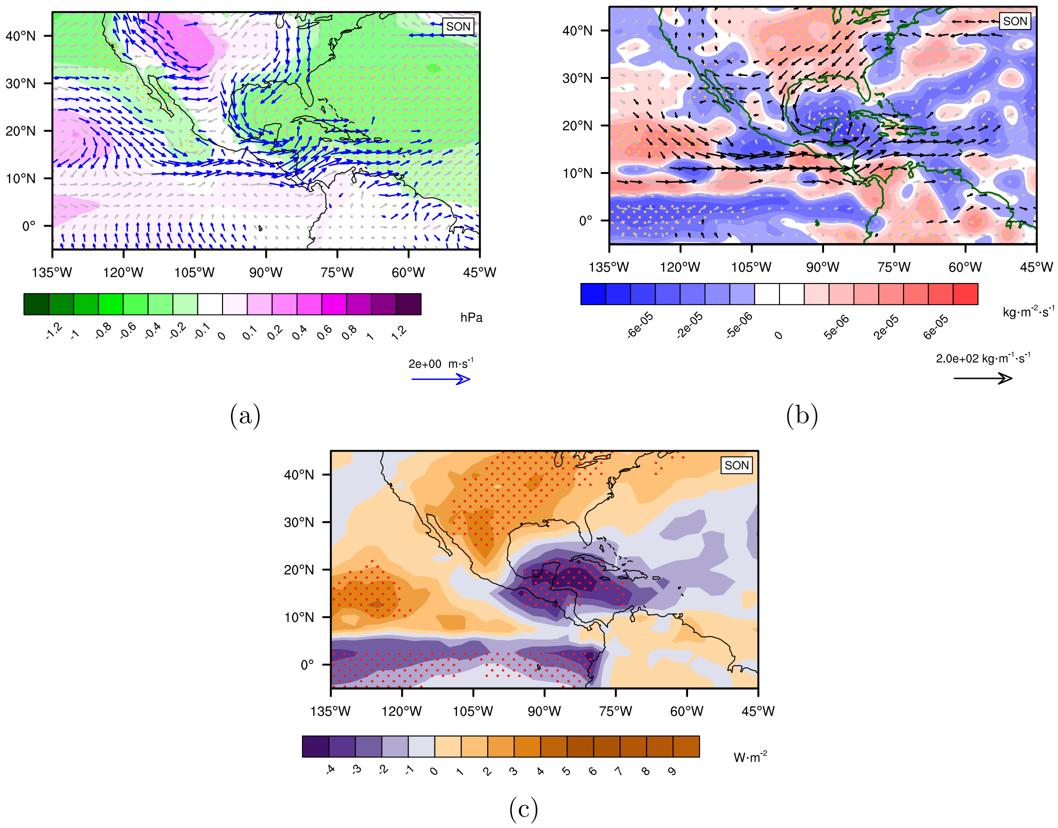

Figure 3.37: (a) Linear regression coefficient of SON surface pressure (shaded, hPa) and wind fields at 850 hPa (arrows, $m{\cdot}s^{-1}$) onto the normalised SON EOT3, per standard unit of seasonal rainfall (mm); wind vectors are drawn in blue when at least one component of the vector is significant at the 10% level. (b) Linear regression coefficient of SON VIMF (arrows, $kg{\cdot}m^{-1}{\cdot}s^{-1}$) and VIMF divergence (shaded, $kg{\cdot}m^{-2}{\cdot}s^{-1}$) onto the normalised SON EOT3, per standard unit of seasonal rainfall (mm); VIMF vectors are drawn in black when at least one component of the vector is significant at the 10% level. (c) Linear regression coefficient of OLR ($W{\cdot}m^{-2}$), onto the normalised SON EOT3, per standard deviation of seasonal rainfall (mm). Stippling indicates correlations of (a) surface pressure, (b) VIMF divergence, and (c) OLR that are significant at the 10% level.

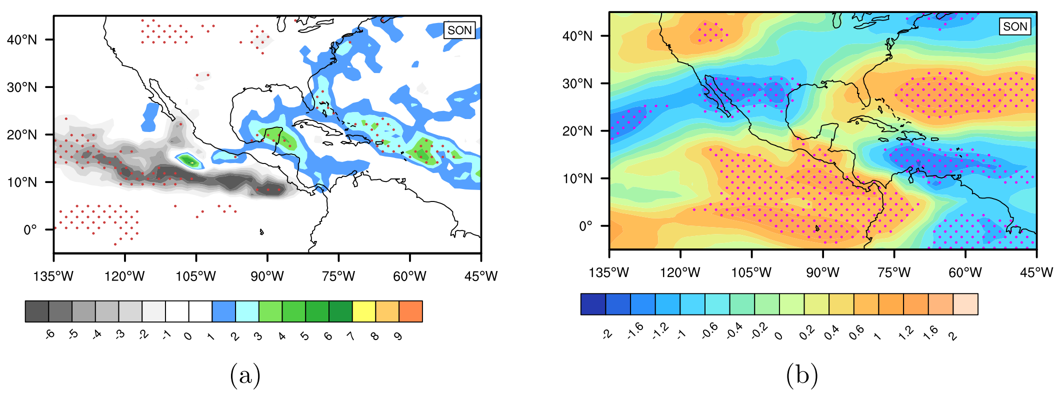

Figure 3.38: Linear regression coefficient of SON (a) TC track density scaled to number density per unit area ($\sim 10^6 km^2$) per season and (b) vertical wind shear ($m{\cdot}s^{-1}$), onto the normalised SON EOT3, per standard deviation of seasonal rainfall (mm). Stippling indicates correlations that are significant at the 10% level.

3.4 Discussion and summary

The leading EOT (EOT1) explains the most interannual variance of the domain-average rainfall. The locations of the EOT1 base points for each season and the corresponding areas of highest correlations resemble the climatological seasonal cycle of precipitation over Middle America: JJA (boreal summer) rainfall is mostly affected by the northward migration of the ITCZ, the NAMS (at northwestern Middle America), and tropical weather system activity such as TCs (Fig. 3.1a). DJF (boreal winter) rainfall is influenced by mid-latitude weather systems, mostly over the north of Middle America (Fig. 3.10a). MAM represents the transition season from winter to summer (Fig. 3.18a), and SON the transition season from summer to winter (Fig. 3.27a).

The regression analysis onto the individual EOTs has identified potential mechanisms that drive regional interannual variability of rainfall. This analysis has reproduced the documented effects of canonical El Niño and La Niña on winter (DJF) and summer (JJA) rainfall variability over Middle America (e.g., Ropelewski and Halpert, 1987), and to identify El Niño Modoki as a secondary mode of variability in Middle America's winter rainfall and La Niña Modoki in autumn. Even though there is a scientific debate over whether there are two different El Niño or just a continuum warm state of El Niño events (e.g., Ashok et al., 2007; Weng et al., 2007; Johnson, 2013), the EOT method identifies that seasonal rainfall over Middle America responds to interannual shifts in the location of the Pacific SST anomalies.

Canonical El Niño is the most important mode of variability of rainfall in Middle America during winter (DJF EOT1) (Fig. 3.11a), followed by El Niño Modoki in the same season (DJF EOT2; Fig. 3.14a). In both canonical El Niño and El Niño Modoki, significant additional moisture from the tropical eastern Pacific is transported to northern Middle America, following a stronger cyclonic circulation from a stronger Aleutian low (Figs. 3.12 and 3.15, respectively). During El Niño Modoki the North Pacific subtropical jet shifts even further southward, increasing moisture transport to northwestern Middle America.

Hence, the strength and location of the Aleutian low and the anomalous subtropical jet over Middle America are key to regional rainfall anomalies in winter. This study agrees with others that explore rainfall and moisture transport differences between canonical El Niño and El Niño Modoki in North America (e.g., Mo, 2010; Kim and Alexander, 2015).

The influence of the Atlantic Ocean and the Gulf of Mexico in the seasonal rainfall variability of Middle America is stronger during canonical El Niño than during the El Niño Modoki: in the former, there is a more significant weakening of the NASH, which suggests that the coupling (feedback) between the Pacific with the Atlantic Ocean is stronger (e.g., Alexander and Scott, 2002; Wang, 2004).

This study identifies patterns of coherent rainfall variability during transitional seasons that have not been analysed in previous studies. The EOT analysis shows that the influence of ENSO in Middle America's rainfall variability depends on the stage of the development of the ENSO phenomena: 58% and 20% of the variance of the MAM area-averaged rainfall is explained by developing canonical El Niño and by decaying canonical La Niña, respectively. These results show that for cases in which the ENSO event was strong and long-lasting, the effects of developing and decaying canonical ENSO are significant in Middle America.

The interannual variability of rainfall in summer (JJA), which is the rainiest season in Middle America, is mainly influenced by two flavours of ENSO. Developing canonical La Niña and the positive AMM are associated with enhanced rainfall over most central and south Middle America (Fig. 3.2a). Canonical La Niña favours strong regional convection through the northward shift of the eastern Pacific ITCZ and the strength of the Walker circulation. This mechanism reduces the easterly mean flow in the eastern Pacific and the Central American gap winds, decreasing the wind shear. These anomalies lead to favourable conditions for TC genesis in the nearshore eastern Pacific, particularly in the Gulf of Tehuantepec. Even though canonical La Niña also weakens the CLLJ, the tropical eastern Pacific supplies a significant anomalous amount of moisture to southern Middle America, where VIMF convergence prevails (Fig. 3.3b).

Positive anomalies of SSTs, enhanced VIMF convergence, and reduced vertical wind shear in the Caribbean Sea favour enhanced Caribbean TC activity. These conditions are linked to positive anomalies of rainfall over southern Middle America and the Caribbean during canonical La Niña. This study also shows that canonical La Niña is correlated with enhanced TC activity in the north Atlantic basin eastward of $75°W$ (Fig. 3.3c).

This study shows that Middle America's rainfall variability in summer also responds to the North Atlantic warming due to the ENSO atmospheric bridge (Alexander and Scott, 2002; Wang, 2004) when a canonical El Niño precedes canonical La Niña. In late spring and early summer, anomalously warm SSTs in the Caribbean Sea, accompanied by a reduction of the atmospheric surface pressure and an enhanced Atlantic ITCZ, favour moisture convergence in the Caribbean Sea and southern Middle America.

Both the positive AMM and the North Atlantic warming due to the ENSO are characterised by anomalously warm SSTs in the tropical North Atlantic. However, the regression analysis presented here does not allow to determine the relative weight of each driver for the seasonal anomalies of rainfall in EOT1, representing a limitation of the technique.

This study suggests that decaying canonical La Niña (Fig. 3.7) enhances the NAMS: La Niña winters and springs are characterised by drier and warmer conditions in northwestern Middle America, which exacerbate the sea-land contrast in the following summer and strengthen the NAMS. These results agree with studies that have explored the relationship between ENSO and the NAMS (e.g., Higgins et al., 1998, 1999). In a later study, Higgins and Shi (2001) suggested that ENSO-related impacts on the NAMS are also linked to meridional adjustments of the ITCZ. Conversely, the present study does not show a significant correlation between JJA EOT3 and the simultaneous anomalies of the ITCZ location due to ENSO.

Unlike JJA EOT1 and JJA EOT3, which are patterns of interannual variability driven by large-scale modes of variability, JJA EOT2 strongly varies with locally driven convective variations in northeastern Middle America. These results could be linked with other studies that suggest that northeastern Middle America is a region of strong land-atmosphere coupling during JJA (Koster et al., 2004; Cotton et al., 2010). Koster et al. (2004) suggested that the atmosphere in northeastern Middle America can trigger moist convection through boundary-layer moisture. The authors also suggested that evaporation in the region is sensitive to soil moisture; hence, soil moisture influences rainfall in that region. A further study on land-atmosphere coupled mechanisms in this region in relation to interannual variability of rainfall would require the analysis of variables such as soil moisture and evaporation; an approach of Global Circulation Model (GCM) experiments would help the understanding of the land-atmosphere mechanisms that influence interannual variability of rainfall in Middle America.

The effect of La Niña Modoki in Middle America is strong during autumn, when anomalous westerly flow from the eastern Pacific weakens the CLLJ and the local wind shear, which favours TC activity in the Caribbean and the Gulf of Mexico and increased rainfall in southernmost Middle America. The environmental conditions that favour TC activity in La Niña Modoki during autumn (SON EOT3; Fig. 3.38) resemble those corresponding canonical La Niña during summer (JJA EOT1; Fig. 3.3). However, the effect of La Niña Modoki on enhanced TC activity is higher in the Gulf of Mexico and lower in the eastern Pacific, compared with canonical La Niña.

The AMM is a secondary large-scale mode of interannual variability for Middle America's rainfall in summer (JJA EOT1) and spring (MAM EOT3). Increased rainfall in JJA EOT1 occurs during the positive phase of the AMM, where the Atlantic ITCZ is anomalously shifted northwards, enhancing VIMF convergence and rainfall in southern Middle America. These conditions promote TC activity, positive anomalous convection, and rainfall in the Caribbean and Middle America. The Atlantic warming response to ENSO is also likely to be an important driver of the rainfall variability during JJA EOT1.

In MAM EOT3, the negative AMM (Fig. 3.25a) favours a stronger NASH and forces additional moisture transport in the U.S. Gulf Coastal Plain. The associated AMM southward migration of the Atlantic ITCZ creates anomalous VIMF divergence in southeastern Middle America and strongly inhibits rainfall in these regions (Fig. 3.24a). This study suggests that the effect of anomalous local VIMF divergence. and the location and strength of the NASH at specific seasons strongly determines rainfall variability in Middle America.

Autumn (SON) is the only season in this study that does not show ENSO as its first mode of rainfall variability. Most of Autumn's rainfall variability is linked to SST anomalies in the North Atlantic and the Gulf of Mexico (SON in Fig. 3.28), the strength of the CLLJ (Fig. 3.27b), and TC activity in the eastern Pacific, the Caribbean Sea, and the Gulf of Mexico (Fig. 3.29b). Once the effect of the leading EOT is removed, developing canonical El Niño drives the variability of rainfall for SON EOT2 (Fig. 3.32c). La Niña Modoki is a mechanism of interannual variability of rainfall for SON EOT3 (Fig. 3.36a), which is related to positive anomalies of TC activity in the Gulf of Mexico (Fig. 3.38a).

As it commonly happens with decomposition techniques, it was not possible to link all of the EOTs with a particular driver; the causes of DJF EOT3 rainfall variability in south-central Middle America remain unclear. However, this study shows that the NAO is associated with an enhanced NASH extending eastwards during DJF EOT3 (Fig. 3.17a). This mechanism allows additional moisture transport from the Caribbean, but it does not seem clear what the connexion is between the NAO and DJF EOT3.

A major limitation of the EOT analysis presented here is the use of correlations and regression to identify the drivers of interannual variability of seasonal rainfall. The correlations may not necessarily show a causal relationship, and the identified "drivers" and plausible mechanisms might not be a cause of rainfall variability.

The EOT analysis assumes that the relationship between drivers and interannual variability of seasonal rainfall is stationary. This represents a limitation of the EOT method since the climate is non-stationary, and future changes in the regional rainfall response to their respective drivers might be expected.

The EOT analysis presented here can be used as the basis to assess the performance of GCMs to simulate circulation features that are key for interannual variability of seasonal rainfall in Middle America. Rotstayn et al. (2010) and Stephan et al. (2018c) showed that EOT analysis is useful for assessing regional climate variability in GCMs by using the study of the leading patterns of annual rainfall in Australia and seasonal rainfall in China, respectively. Sensitivity experiments with GCMs is a proposed way to understand the response of rainfall variability to changes in SST, under current and future climates.

Further studies could also refer this study to understand the influence of interannual variability of the rainfall in Middle America on regional human migration (e.g., Hunter et al., 2013), wildfires (e.g., Westerling et al., 2006), harvesting, dry spells, water shortages, floods, and diseases such as dengue (e.g., Lozano-Fuentes et al., 2012), malaria, chikungunya, and Valley Fever (e.g., Weaver and Kolivras, 2018), considering the regions of coherent variability identified with the EOT method and their drivers. Meteorological variables such as atmospheric temperature, soil moisture, and evaporation could be added to future EOT analysis.

3.5 Conclusions

The EOT method has been implemented to separate Middle American rainfall into regional patterns of coherent variability and has helped to identify atmospheric and coupled atmosphere-ocean drivers of that variability. This study shows that ENSO is the leading driver of Middle America's rainfall variability in winter, summer, and spring. The ENSO – Middle America's rainfall teleconnection is stronger in summer and winter, and weaker in the transitional season of autumn. The interannual variability of Middle America's rainfall responds to the shift in the location of SST anomalies, identified in this study as canonical and Modoki states of ENSO.

This study support previous studies that identified canonical ENSO as the lead driver of interannual variability of seasonal rainfall in Middle America (e.g., Ropelewski and Halpert, 1987; Curtis, 2002; Magaña et al., 2003; Maloney et al., 2014), and identifies ENSO Modoki as a secondary mode of interannual variability of seasonal rainfall in the region. This study contributes to the physical understanding of the response of Middle America's rainfall to distinct "flavours" of ENSO.

The AMM and the Atlantic warming response to ENSO have been identified as secondary modes of interannual variability. Concurrent with La Niña, the anomalous warm SSTs over the Atlantic are an essential source of variability of summer rainfall in Middle America, though their influence is weaker than canonical La Niña.

Autumn rainfall variability is strongly linked with modes of variability in the Atlantic Ocean, and with moisture transport from the eastern Pacific to continental Middle America and the Caribbean Sea. Unlike the other three seasons analysed, the ENSO influence over autumn is found only for the second and third EOT. The variability of TC activity is strongly linked with Middle America's variability of rainfall in this season.

The NAO influences rainfall and moisture transport in the Caribbean during winter by enhancing the NASH and regional anomalous VIMF convergence. This study shows that the Pacific and Atlantic ITCZ, the NASH, and the CLLJ are key modulators of VIMF and VIMF divergence and rainfall variability in Middle America and the IAS.

The use of the EOT method for the analysis of GCM simulations would be useful to assess the skill to simulate Middle America's rainfall variability and the mechanisms that drive its variability.

Chapter 4:

Contribution of TCs to atmospheric branch of Middle America's hydrological cycle

This chapter is dedicated to the study of the contributions of TCs to the atmospheric branch of the hydrological cycle over Middle America. As stated in section 1.3, this chapter aims to characterise the contribution of TCs to monthly (a) mean rainfall, (b) extreme rainfall, and (c) atmospheric moisture transport in Middle America.

TC contributions to rainfall are quantified using TC tracks derived from three sources: IBTrACS, and trajectories from an objective feature tracking method (Hodges, 1994, 1995, 1999) applied to the Japanese 55-year and ERA-Interim reanalyses. The use of trajectories identified from two state-of-the-art reanalyses is a novel approach that allows for a robust analysis of the TC contribution to rainfall and atmospheric moisture, throughout the TC lifecycle including the pre- and post-stages of the TCs. This study advances the work of Larson et al. (2005), Prat and Nelson (2013a), and Prat and Nelson (2016) on the characterisation of the mean rainfall and extreme rainfall associated with TCs over North America.

The methodology used in this chapter to quantify rainfall associated with TCs is also implemented in chapter 5 to study of the variability of rainfall related to TCs in Middle America. Thus, this chapter's results are used to guide the application of TC track datasets to describe TC rainfall in the region.

The text and figures that follow have been published in Climate Dynamics (Franco-Díaz et al., 2019).

Franco-Díaz, A., N. P. Klingaman, P. L. Vidale, L. Guo, and M.-E. Demory, 2019: The contribution of tropical cyclones to the atmospheric branch of Middle America's hydrological cycle using observed and reanalysis tracks. *Clim. Dyn.*, 53, 6145–6158, doi:10.1007/s00382-019-04920-z

The article is presented as published; its content has not been modified. A. Franco Díaz's contribution to this paper is 94%. A.Franco Díaz carried out the analysis based on the methodology previously developed by L. Guo. A.Franco Díaz led the writing of the paper, with input from N.P. Klingaman, P.L. Vidale., L. Guo, and M.-E. Demory, and valuable contributions from reviewers.

4.1 Abstract

Middle America is affected by tropical cyclones (TCs) from the Eastern Pacific and the North Atlantic Oceans. We characterize the regional climatology (1998-2016) of the TC contributions to the atmospheric branch of the hydrological cycle, from May to December. TC contributions to rainfall are quantified using Tropical Rainfall Measuring Mission (TRMM) Multi-satellite Precipitation Analysis (TMPA) product 3B42 and TC tracks derived from three sources: the International Best Track Archive for Climate Stewardship (IBTrACS), and an objective feature tracking method applied to the Japanese 55-year and ERA-Interim reanalyses. From July to October, TCs contribute 10-30% of rainfall over the west and east coast of Mexico and central Mexico, with the largest monthly contribution during September over the Baja California Peninsula (up to 90%). TCs are associated with 40-60% of daily extreme rainfall (above the 95th percentile) over the coasts of Mexico. IBTrACS and reanalyses agree on TC contributions over the Atlantic Ocean but disagree over the Eastern Pacific Ocean and continent; differences over the continent are mainly attributed to discrepancies in TC tracks in proximity to the coast and TC lifetime. Reanalysis estimates of TC moisture transports show that TCs are an important moisture source for the regional water budget. TC vertically integrated moisture flux (VIMF) convergence can turn regions of weak VIMF divergence by the mean circulation into regions of weak VIMF convergence. We discuss deficiencies in the observed and reanalysis TC tracks, which limit our ability to quantify robustly the

contribution of TCs to the regional hydrological cycle.

4.2 Introduction

Middle America, a continental region that includes Mexico and Central America, is influenced by various precipitating weather systems that drive the regional hydrology. During the warm season, this region is subject to landfalling tropical cyclones (TCs), which include tropical depressions, tropical storms and hurricanes from the Eastern Pacific and the North Atlantic basins. During September 2013, TCs Ingrid and Manuel simultaneously made landfall in the western coast of Mexico and eastern Mexico, respectively, bringing very heavy rains to a large portion of Mexico and causing deadly mudslides and flash flooding (LeComte, 2014). During summer, other weather systems also contribute to rainfall, including isolated thunderstorms, synoptic and mesoscale convective systems associated with the activity of easterly waves (EWs) (Serra et al., 2016; Vigaud and Robertson, 2017). Tropical EWs are synoptic-scale precursors of TCs in both the Northeast Pacific and North Atlantic (Belanger et al., 2016). Eastern Pacific and North Atlantic vertical wind shear and sea surface temperatures (SSTs) favour cyclogenesis during boreal summer and early autumn (Molinari et al., 2000).

The influence of TCs on the hydrological cycle has been examined by many studies (e.g. Larson et al., 2005; Jiang and Zipser, 2010; Prat and Nelson, 2013b,a, 2016; Guo et al., 2017; Xu et al., 2017). Prat and Nelson (2013b) found that 8-12% of rainfall are attributable to TCs in the Southeastern United States (US) for inland areas located between 150 and 300 km from the coast and 15-20% along the coast. TCs account for 50-70% of daily accumulations above 100 mm day^{-1} ($\sim$ 4 in day^{-1}) along the U.S. Atlantic coast from Florida to New England (Prat and Nelson, 2016). Over the coastal region of Eastern Asia, TCs contribute 10-30% of the monthly total rainfall, and around 50% of the occurrence of extreme daily rainfall [above the 95th percentile] (Guo et al., 2017). TCs contribute approximately 10% of the total moisture transport to the East Asia coast (Guo et al., 2017), and 14% to the North American coast (Xu et al., 2017). Positive global trends in TC-associated rainfall are expected (Kossin, 2018). Only a few studies have evaluated the contribution of TCs to the atmospheric branch of Middle America's hydrological cycle: Larson et al. (2005) found summer TC-related rainfall contributions exceeding 20% along the southwest coast of Mexico, using rain gauge observations. Jiang and Zipser (2010) found that TCs contribute about 55% of yearly rainfall over Baja California, Mexico. Prat and Nelson (2013a) found that near 15% of yearly rainfall over

Mexico's Pacific Coast is related to TCs; later, Prat and Nelson (2016) quantified that up to 32% of the precipitation is associated with TCs along the Gulf of Mexico and 50% in southern Baja California; TCs accounted for almost all daily accumulations above 100 mm day^{-1} over Baja California. Over semiarid regions of Mexico TCs may contribute up to 50% of the seasonal rainfall (Domínguez and Magaña, 2018). To complement these previous studies, we analyse the monthly climatology of the contribution of TCs over Middle America, including the effect of TCs on extreme rainfall.

TC contributions to the atmospheric moisture transport and their role in the Middle America's moisture budget have received little attention. In view of such a gap, we develop a climatology of the monthly contribution of TCs to the atmospheric moisture transport over Middle America. Several methodologies for quantifying the contribution of TCs to rainfall (Prat and Nelson, 2016; Guo et al., 2017) and moisture transport (Prat and Nelson, 2013b, 2016; Guo et al., 2017; Xu et al., 2017) employing an Eulerian framework have been developed, which require a set of TC tracks. A variety of TC track datasets are available, including those based on observations, as well as those obtained from objective feature tracking methods applied to reanalysis data.

All sources of TC track data involve uncertainties. For observed tracks, there are uncertainties related to location and intensity, superimposed on operational differences between agencies in TC identification. These uncertainties are greatest for the weakest storms, as well as during the pre-TC and post-TC stages for all storms (Hodges and Emerton, 2015). To fill this gap, TC tracks from reanalyses can complement the observations, providing added value information on earlier and later stages of the TCs life cycle (Hodges et al., 2017). Hodges et al. (2017) applied their objective tracking method to reanalysis and found that the largest uncertainties in TC identification come from the representation of TC intensities and structure. Differences between reanalyses are expected due to variations in dynamical core and physical parameterizations, the data assimilation methods, as well as their model grid resolution (Hodges et al., 2017). Previous studies typically have quantified the TC contribution to the hydrological cycle using either observed or reanalysis tracks. To investigate the uncertainty due to the source of TC track data, we quantify TC contributions to precipitation using observed tracks and tracks from two state-of-the-art reanalyses.

In this paper, we characterize the regional climatology of the TCs contribution to the atmospheric branch of the hydrological cycle over Middle America, from May to December, also exploiting the advantages and considering the uncertainties associated with the representation of TCs identified in observations and reanalyses. To achieve this purpose, we quantify the mean monthly rainfall (Section 4.4.1) and extreme daily rainfall associated with TCs (Section 4.4.2), employing and comparing trajectories identified from observations and two reanalyses. We also quantify monthly moisture flux and moisture divergence associated with TCs for these two reanalyses (Section 4.4.3).

4.3 Data and methods

4.3.1 Observations

Monthly contributions of TCs at regional scale are computed using satellite rainfall estimates from the Tropical Rainfall Measuring Mission (TRMM) Multi-satellite Precipitation Analysis (TMPA 3B42) for 1998-2016. Version 7 TMPA 3B42 provides estimates of rainfall for $50°S-50°N$, at $0.25°\times0.25°$ spatial resolution and 3-hourly temporal resolution (Huffman and Bolvin, 2015). Historical records of TCs from various official meteorological agencies worldwide, obtained from the International Best Track Archive for Climate Stewardship (IBTrACS) dataset (Knapp et al., 2010), are used to identify observed TCs. The IBTrACS dataset is a global repository of TC best-track data from Regional Specialized Meteorological Centers (RSMCs) and other agencies around the world, which provides 6-hourly information for each tropical storm such as its location intensity, central pressure, among others. The primary data source in the North Atlantic and the East Pacific basins is the Atlantic Hurricane Database (HURDAT; Landsea and Franklin, 2013) from RSMC Miami. The HURDAT dataset is already a best-track dataset for the Atlantic basin. TC-related rainfall quantified by using IBTrACS are compared to that quantified by using TC tracks from an objective tracking method (described in section 2.3) applied to two recent global atmospheric reanalysis datasets, (a) the European Centre for Medium-Range Weather Forecasts (ECMWF) interim reanalysis (ERA-Interim; Dee et al., 2011) and (b) the Japanese 55-year reanalysis (JRA-55; Kobayashi et al., 2015), described below.

4.3.2 Reanalysis datasets

ERA-Interim and JRA-55 reanalyses datasets are used for TC trajectory identification and moisture transport calculations. Six-hourly (0000, 0600, 1200, and 1800 UTC)

ERA-Interim variables used in this study include temperature, winds, vorticity (native resolution of T255, $\sim$ 60 km), specific humidity on pressure levels, and vertically integrated moisture fluxes and their divergence (regular grid with a resolution of $0.78° \times 0.78°$). Six-hourly JRA-55 reanalysis variables of vorticity and temperature, winds on pressure levels, and vertically integrated moisture fluxes (all at the original resolution of TL319, $\sim$ 55 km) are used in this study; the divergence of JRA-55 vertically integrated moisture fluxes fields are computed using spherical harmonics with truncation T64, employing the windspharm Python package (Dawson, 2016). An important feature of the JRA-55 is the assimilation of tropical wind retrievals to improve the representation of TC intensity. The wind profile surrounding and over each observed TC centre is retrieved from historical data during the processing and assimilation, in a way that observations are used to simulate data from a dropsonde (Hatsushika et al., 2006; Hodges et al., 2017).

4.3.3 TC feature tracking methodology

The objective TC tracking method based on Hodges (1994, 1995, 1999) is applied separately to each reanalysis dataset. The method (fully described in Hodges et al. (2017)) consists on firstly identifying the tropical disturbances using relative vorticity fields, vertically averaged from 850 to 600 hPa; through the use of a spectral filter (Sardeshmukh and Hoskins, 1984), tropical systems with wavenumbers between 6 to 63 are retained. A second step consists of applying a direct space- and time- matching criterion between the identified tropical systems tracks from the reanalysis and the observed IBTrACS tracks. This criterion allows matching both tracks when the distance between them is no more than 4 geodesic degrees, at the same time that they overlap in time. Hodges et al. (2017) found that, under this criterion, the probabilities of detection for the Northern Hemisphere for TCs obtained from JRA-55 and ERA-Interim reanalyses that match with IBTrACS and/or hurricanes category 1 to 5, are 0.95 and 0.81, respectively. Afterwards, for the detection of a TC, a threshold criterion of vertically decreasing vorticity is applied to the filtered vorticity fields (across 850-250 hPa) to detect the typical warm core vertical structure of a TC. With this objective TC tracking method it is possible to detect the precursor and post-extratropical transition stages of the TC, which results in an extended description of the life cycle of the TC compared to observed tracks from IBTrACS (Hodges et al., 2017).

4.3.4 Quantifying the contribution of TCs to rainfall and moisture fluxes

A total of 19 TC seasons (from 1998 to 2016) of the Pacific and the Atlantic oceans have been analysed to quantify the contribution of TCs to rainfall. To study the spatial distribution of the rainfall attributed to TCs, the TC season is subdivided into eight months, from May to December. To investigate the contribution of TCs to rainfall over Middle America, 3-hourly TMPA 3B42 rainfall within 5 geodesic degrees radius centred over the TC location is identified as TC associated rainfall (e.g. Larson et al., 2005; Jiang and Zipser, 2010; Guo et al., 2017); the rest of the rainfall is masked as non-TC-related rainfall. The 5 geodesic degrees radius criterion captures the primary wind circulation domain of the TC, commonly located between 80-400 km from the TC centre, as well as part of the TC cloud shield, commonly found at 550-600 km (Prat and Nelson, 2013b). Although the aforementioned TC fixed radius is commonly chosen in TC-related rainfall and moisture transport studies, in some cases this assumption does not capture the full extent of the TC (e.g. Xu et al., 2017). Since the temporal interval of the TC position for all the track datasets is 6 hr, two consecutive 3 hr steps of TMPA 3B42 rainfall are applied to the same TC-associated mask. To investigate the contribution of TCs to extreme rainfall, we first compute the extreme daily rainfall, defined as the frequency of daily events that exceed the 95th percentile of the TMPA 3B42 daily accumulated rainfall for each month and grid point during 1998-2016. A 5 geodesic degrees radius mask centred over the TC location is then applied to the daily rainfall to further obtain the fraction amount (intensity) and fraction count (frequency) of daily extreme events related to TCs.

Following the methodology of Guo et al. (2017), we analyse the contribution of TCs to the regional monthly moisture transport over Middle America for a total of 38 TC seasons (from 1979 to 2016), employing the horizontal wind (v) and the specific humidity (q) fields of the 6-hourly ERA-Interim and JRA-55 reanalyses. Time means of v and q refer to monthly climatologies of horizontal wind ($\bar{v}$) and specific humidity ($\bar{q}$), respectively, over 1979-2016. Moisture flux fields (derived from v and q) are decomposed into time-mean and eddy (deviation from the time-mean) terms, following the equation:

$$\begin{aligned} vq &= \left(\bar{v} + v'\right)\left(\bar{q} + q'\right) \\ vq &= \left(\bar{v} + v'_{TC} + v'_{non-TC}\right)\left(\bar{q} + q'_{TC} + q'_{non-TC}\right) \end{aligned} \tag{4.1}$$

where vq represents the total moisture flux field. The deviations from the time-mean values (eddies) of the wind field and the specific humidity are represented by the terms $v' = v - \bar{v}$ and $q' = q - \bar{q}$, respectively. The eddy component terms related to TCs of eq. 4.1, v'_{TC} and q'_{TC}, are obtained using the criterion of 5 geodesic degrees radius mask centred over the TC location, applied to the 6-hourly eddy wind field (v') and to the eddy specific humidity field (q'), respectively. The total moisture flux (vq) at each pressure level is subdivided into the transport of mean moisture by the mean horizontal wind ($\bar{v}\bar{q}$), the moisture transport by non-TC eddies $\left((vq)'_{non-TC}\right)$, and the moisture transport by TC eddies ($(vq)'_{TC}$), the latter represented by the equation:

$$(vq)'_{TC} = \bar{v}q'_{TC} + v'_{TC}\bar{q} + v'_{TC}q'_{TC} \tag{4.2}$$

where the first term of the right-hand side of eq. 4.2 represents the transport of TC eddy moisture by the mean horizontal wind ($\bar{v}q'_{TC}$), the second term represents the transport of mean moisture by the TC eddy horizontal wind ($v'_{TC}\bar{q}$), and the third term represents the transport of TC eddy moisture by the TC eddy horizontal wind ($v'_{TC}q'_{TC}$). A subsequent analysis of the contribution of TC on the water balance for the region uses vertically integrated moisture flux (hereafter VIMF) divergence fields from ERA-Interim and JRA-55 reanalyses, integrated throughout the atmospheric column. The VIMF divergence field relates the mean balance of evaporation ($\bar{E}$) and precipitation ($\bar{P}$): divergence means that, in the long term, evaporation exceeds precipitation ($\bar{E} - \bar{P} > 0$), indicating a source of water vapour to the atmosphere from the region. The sinks of atmospheric water vapour are identified as regions of VIMF convergence where precipitation exceeds evaporation ($\bar{E} - \bar{P} < 0$).

4.4 Results

4.4.1 Contribution of Tropical Cyclones to the mean accumulated rainfall over Middle America

From the observed tracks (IBTrACS), the contribution of the TCs to the monthly mean rainfall over the continent is more noticeable during June, and August to October (Fig. 4.1), being larger over the southeast coast of the US, and the Mexican west and east coasts during September, followed by the central/southern Mexico and Central America during October. From mid-August to late October, the Eastern Pacific Ocean and the

North Atlantic (Gulf of Mexico and the Caribbean) show a peak in TC activity (Gilford et al., 2017; NHC, 2018) and with more frequent landfalls than in other stages of the hurricane season (e.g. Prat and Nelson, 2013b). The simultaneous increase in TC activity in both basins affects a wide portion of the south and centre of Mexico, mainly during October, when North Atlantic and Eastern Pacific TCs together contribute about 10-20% of the monthly-accumulated rainfall (Fig. 4.2).

The largest climatological contributions of TCs to the accumulated rainfall over the Gulf of Mexico, the east coast of Mexico, and the US southeast coast are found during September, with about 10-20% of the monthly rainfall (Fig. 4.2). The effect of TCs on the regional rainfall extends along the Gulf Coastal Plain, which reaches from eastern to northeastern Mexico through the Yucatan Peninsula, continues along Tabasco and Veracruz to Tamaulipas, and extends around the Gulf of Mexico in the Southern US. Our results suggest that the effect of the Atlantic TCs on precipitation is in part constrained by the orographic features of the region, with the largest contribution over the Gulf Coastal Plain. During the majority of the months analysed, the contributions of TCs to the rainfall over the southern portion of Mexico's coastline are between 10% and 20% of the total precipitation, covering almost the entire Yucatan Peninsula. Throughout July, August and September, rainfall associated with the Atlantic TCs extends further north within the domain of Middle America, having a noticeable effect inland, contributing 10% of rainfall over the northeast of Mexico in the states of Tamaulipas and Nuevo Leon (beyond 200 km inland), especially over portions of land below 1,500 m altitude.

In climatological terms, the eastern North Pacific is the most active ocean basin for the genesis of TCs, per unit area and time (Molinari et al., 2000). East Pacific TCs have an important effect on the summer rainfall of continental Middle America. The TC-related rainfall over the west coast of Mexico is strongly influenced by the presence of the Sierra Madre Occidental, Mexico's longest mountain range, which stretches 1,100 km through North-western and Western Mexico. The results show a pattern of TC-related rainfall that extends along the coast next to the Gulf of California and the Gulf of Tehuantepec. Over this large continental area, the largest contribution of TCs to climatological rainfall occurs during the last three months of the TC season. TCs account for between 10% and 50% of the rainfall along the Northwest coast of Mexico, and can contribute as much as 10% to the seasonal rainfall in the western interior locations in the states of Sonora, Chihuahua, Durango and Sinaloa, particularly during September and October, coincident with the end retreat of the North American Monsoon. TC contributions to the monthly rainfall maximise during September, over the west coast of Mexico, the centre of Mexico and the Baja California Peninsula, contributing to the latter to more than 60% of the total monthly rainfall, the largest fractional contribution of TCs over the entire domain. The high percentage contribution over Baja California is exaggerated by the low mean rainfall in the region, which is generally less during boreal summer than winter, and very low compared with other continental areas of the domain of study. In cases like Hurricane Jimena in 2009, the contribution can be more than 90% of the monthly rainfall over a large portion of the peninsula. The large-scale flow pattern necessary to turn the storms northward toward Northwest Mexico is much more likely at the end of the TC season in boreal autumn (Corbosiero et al., 2009). Another factor that favours development of TCs

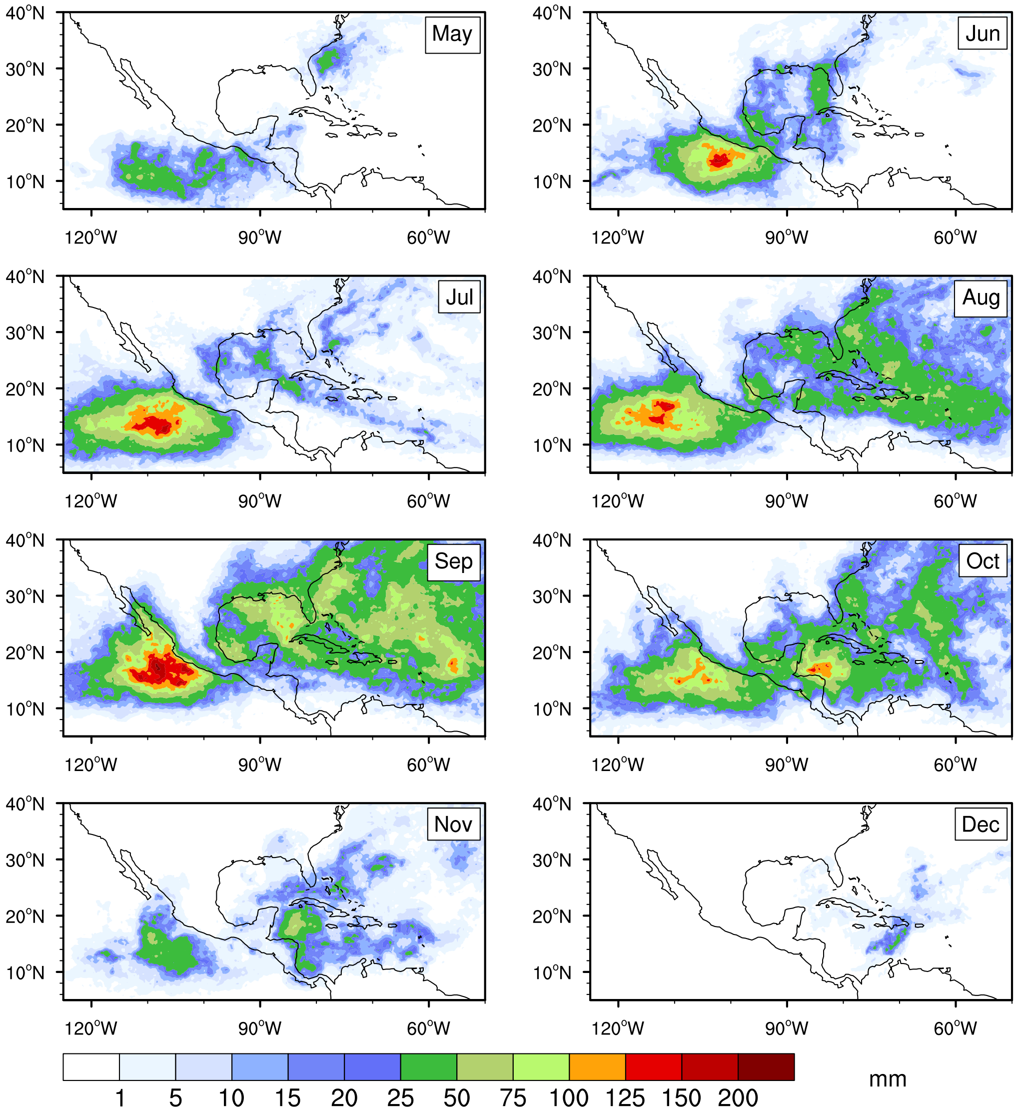

Figure 4.1: Contribution of TCs to the mean monthly-accumulated rainfall (*mm*) from May to December, quantified with observed TCs trajectories from IBTrACS and TMPA 3B42 estimates of rainfall. Climatology for 1998-2016.

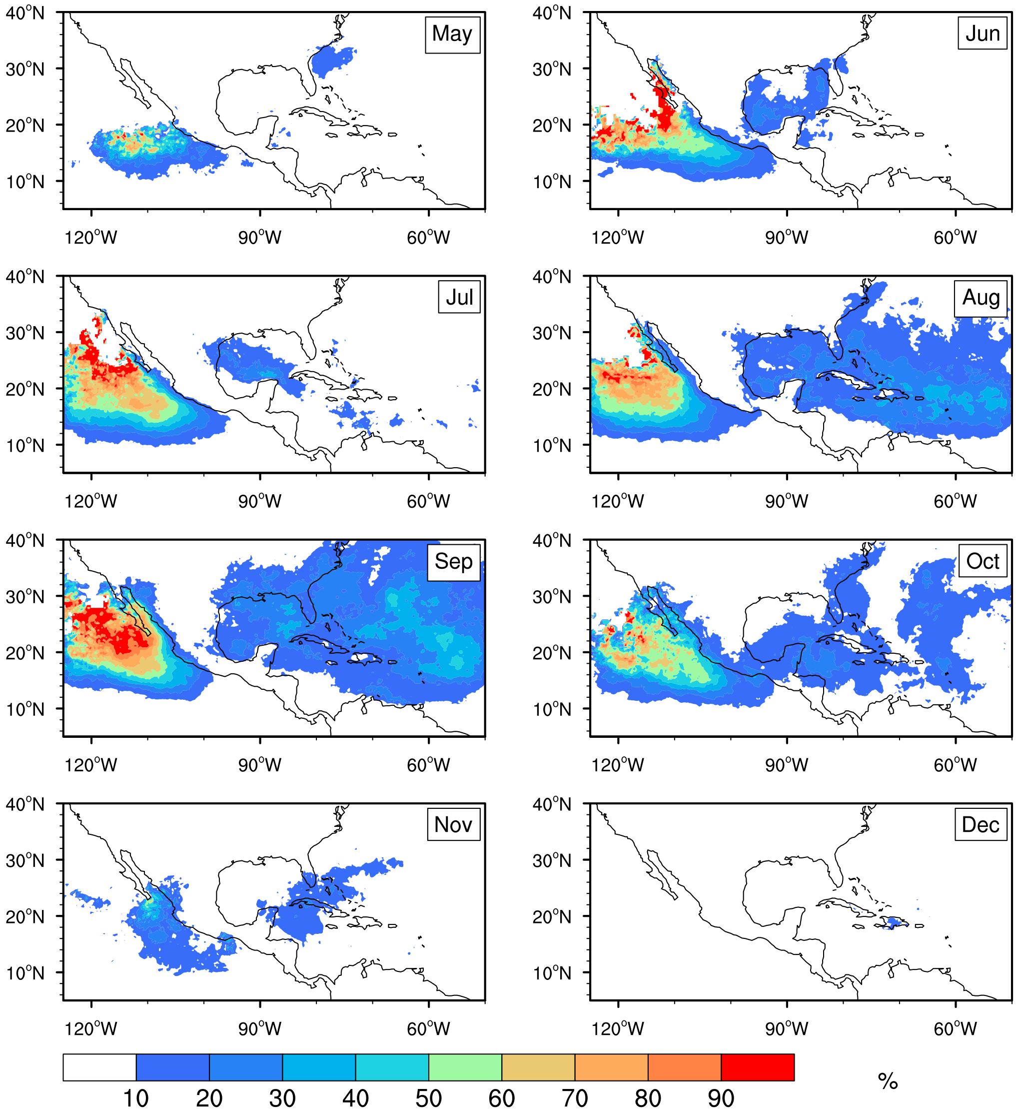

Figure 4.2: Contribution of TCs to the mean monthly-accumulated rainfall (%) from May to December, quantified with observed TCs trajectories from IBTrACS and TMPA 3B42 estimates of rainfall. Climatology for 1998-2016.

is the increase of the monthly mean SST to above 27°C over the Gulf of California from July to October (e.g. Hall and Tippett, 2017).

Differences between TC associated monthly rainfall calculated with IBTrACS and ERA-Interm/JRA-55 reanalyses. After estimating the contribution of TCs to precipitation using IBTrACS tracks, we now consider the same quantity by using TC tracks from the objective TC tracking method applied to ERA-Interim and JRA-55 data (described in section 4.3.3). Figure 3 shows the differences between the monthly climatology for 1998-2016 of TC-accumulated rainfall (mm) calculated from TMPA 3B42 data, using (a) ERA-Interim and IBTrACS tracks, and (b) JRA-55 and IBTrACS tracks.

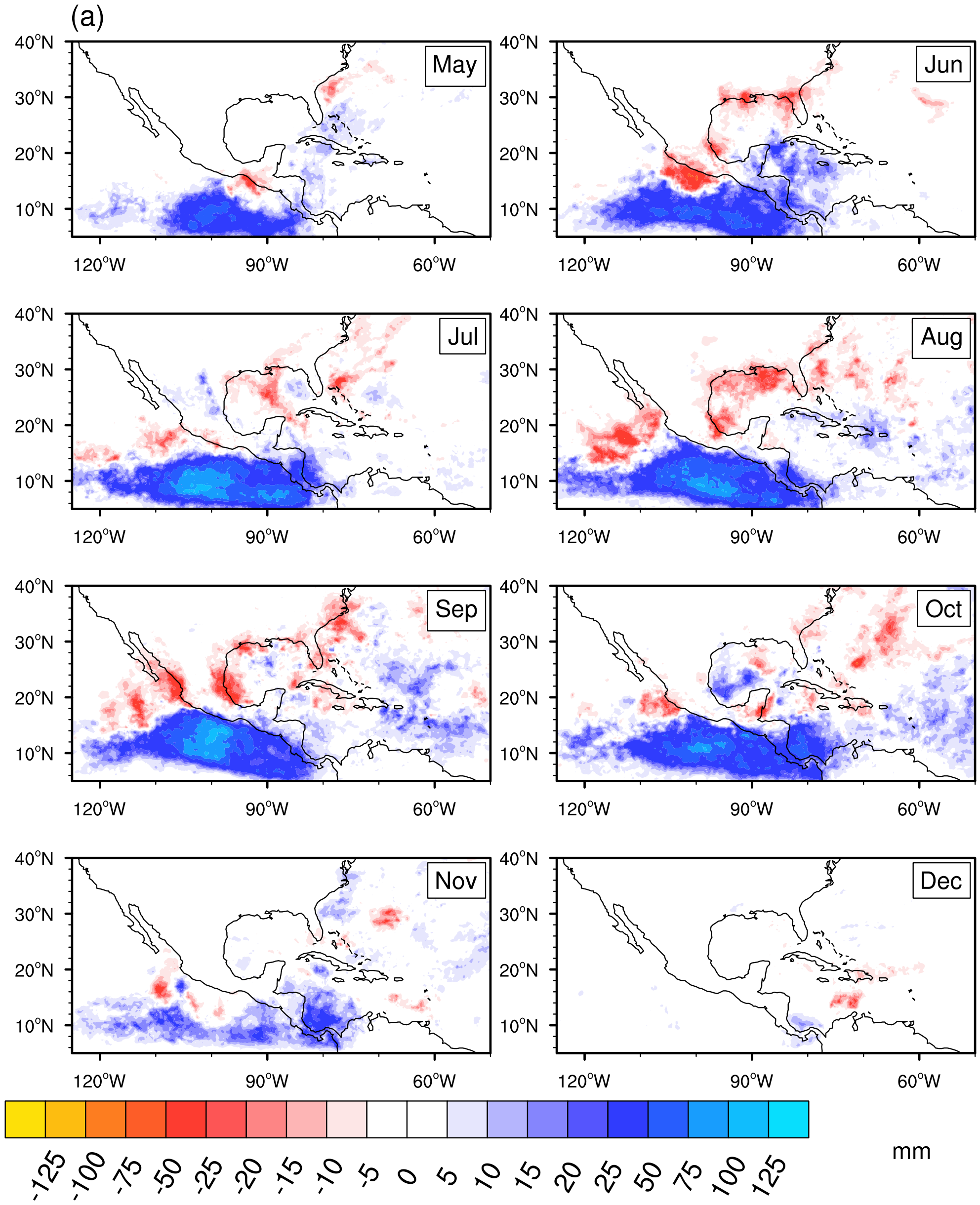

Figure 4.3: Differences between the contributions of TCs to the mean monthly-accumulated rainfall (*mm*) quantified with TMPA 3B42 estimates of rainfall and with TC trajectories based on (a) ERA-Interim reanalysis and IBTrACS, and on (b) JRA-55 reanalysis and IBTrACS, from May to December (1998-2016) *(continued on next page)*.

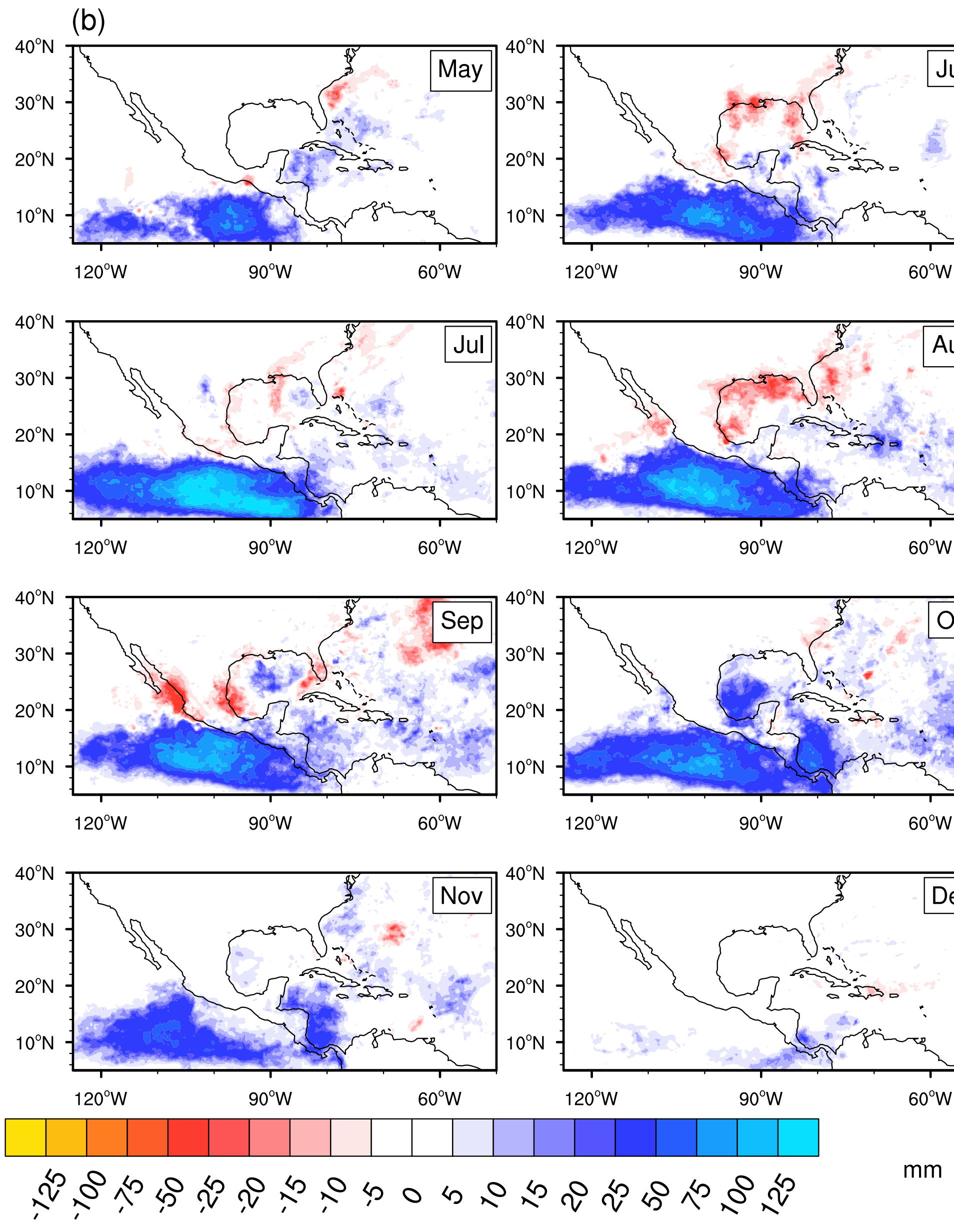

Figure 4.3: *(continued).*

Some agreement between the TC-associated rainfall calculated with ERA-Interim and IBTrACS tracks is found over the North Atlantic at the beginning of the TC season. The differences get larger as the season progresses, reaching monthly differences ($\pm$ 50 mm) over the Caribbean Sea and the Gulf of Mexico. Throughout the season, a dipole of differences develops over the Eastern Pacific basin and Central America, with larger values in ERA-Interim in the south of the domain (with up to 100 mm per month), and larger values in IBTrACS further north in the basin (mainly up to 50 mm per month, located northwards 10°N). Most of the negative differences are found over land, varying in location and rate each month, being larger over the west and east Mexican coasts by September. Slight reductions of TC-related rainfall (about 15 mm per month) using JRA-55 tracks relative to IBTrACS are found over the Caribbean Sea throughout the TC season. The largest positive differences (25-150 mm) are found over Central America and the Eastern Pacific next to the southwest Mexican coast, collocated with the Eastern Pacific warm pool. Important reductions in JRA-55 relative to IBTrACS are found each month throughout the TC season over Middle America and the Southeast of the US., being more noticeable during September in the west and east coast of Mexico. The reductions are up to 50 mm and are widespread from the coast to inland, especially in Central Mexico, along the Gulf of Tehuantepec and the Gulf of Mexico. However, the two estimates largely agree over the North Atlantic Ocean basin, where the differences during May and August are within $\pm$15 mm, with a minimum along the US southeast and the western Mexico coasts during June and September, respectively, and a maximum during October over the Gulf of Mexico and Central America. In general, the TC-associated rainfall calculated with JRA-55 tracks agrees more closely with IBTrACS than that calculated with ERA-Interim tracks; in both cases, the climatology obtained with the reanalyses tracks show lower TC contributions to rainfall over the continent, especially over the coasts and Central Mexico. These differences are discussed in section 4.5.

4.4.2 Contribution of Tropical Cyclones to the extreme rainfall over Middle America

TCs are related to episodes of heavy rainfall, causing severe damages and losses. We examine the seasonal contributions of TCs to amounts and frequency of extreme rainfall (Fig. 4.4) over Middle America during July, August, September, and October (JASO), based on TC tracks from IBTrACS and on the 95th percentile of daily rainfall of each month during 1998-2016, calculated from TMPA 3B42 rainfall estimations. The percentage of amount of TC extreme rainfall represents the daily TC accumulated extreme rainfall relative to the total accumulated rainfall of all the extreme events; the percentage of frequency of TC extreme rainfall represents the events of extreme rainfall related to TCs relative to all the extreme rainfall events.

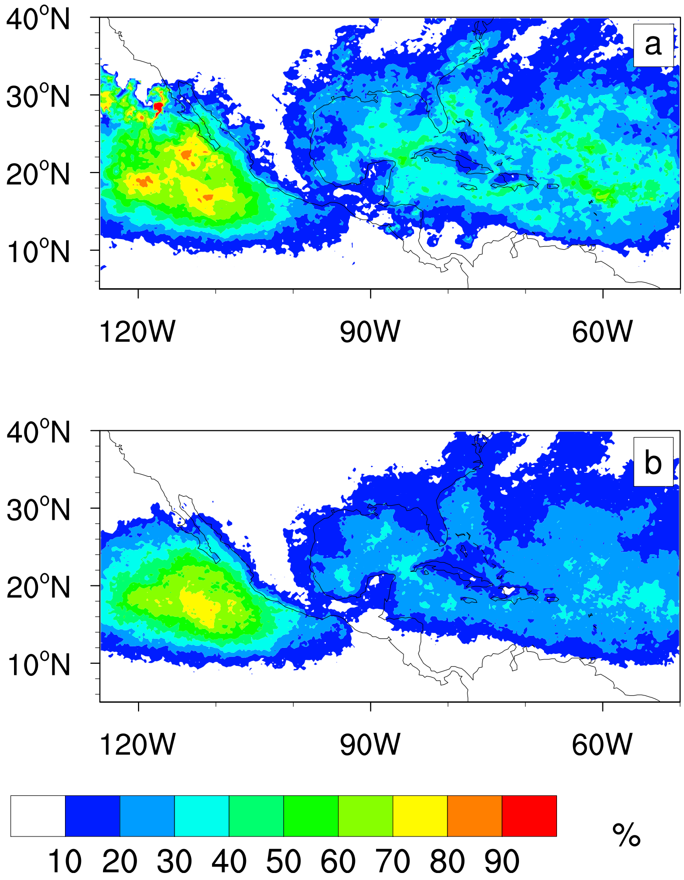

Figure 4.4: Mean contribution of TCs to the extreme rainfall (a) amount (%) and (b) frequency (%) during JASO, employing TCs tracks from IBTrACS. Climatology for 1998-2016.

During JASO, the highest contributions of TCs to the extreme rainfall amounts and frequencies over the continent are found over a large area of the Baja California Peninsula, followed by the west coast of Mexico, and much of the Gulf Coastal Plain. The relative values of the contributions of TCs to extreme rainfall amount and frequency define regions where the TC-related extreme rainfall is heavier than extreme rainfall from systems unrelated to TCs: larger values of amount than frequency indicate that TC-related extreme rainfall, per event, is heavier than non-TC extreme rainfall, per event. For example, this occurs over the Baja California Peninsula, part of the northwest of Mexico, and along the Gulf Coast of the United States, where the amount TC-related extreme rainfall exceeds the frequency by more than 10%.

To further examine the seasonal cycle of the TC contribution to the regional extreme rainfall, we examine the monthly contributions of TCs to extreme rainfall amounts and frequency of extreme rainfall (Figs. 4.5 and 4.6, respectively) during July, August, September and October, based on the 95th percentile of daily rainfall of each month during 1998-2016, calculated from TMPA 3B42 rainfall estimations. Observations and reanalyses show that the highest contribution of TCs to extreme rainfall occurs on the east coast of Mexico during September and October, with extreme rainfall amounts mainly between 20% and 50% of the total extreme rainfall amount (Fig. 4.5). The largest inland contribution of TCs to extreme rainfall amount occurs during September over the Baja California Peninsula and the Gulf Coast of the US, with up to 60% and 50% of the extreme rainfall amount, respectively, followed by northwestern Mexico (encompassing an area that includes the states of Tamaulipas, Nuevo Leon and Coahuila) with up to 50% during July. The amount of TC-related extreme rainfall exceeds the frequency by more than 10% over much of the northeast of Mexico during July, over the Baja California Peninsula from August to October, and throughout the season over some portions of the Gulf Coast of the US, Central and Southern Mexico, Nicaragua, Honduras, and the Caribbean.

Most of the agreement between the contribution of TCs to the monthly extreme rainfall using IBTrACS and reanalysis tracks is found over the Atlantic Ocean and over the Middle America landmass, whereas some differences are found over the Pacific Ocean. The contribution of TCs to extreme rainfall amounts and frequency obtained from the reanalysis tracks is more than that obtained from IBTrACS over the some portions of the Eastern Pacific Ocean between 5°N-10°N.

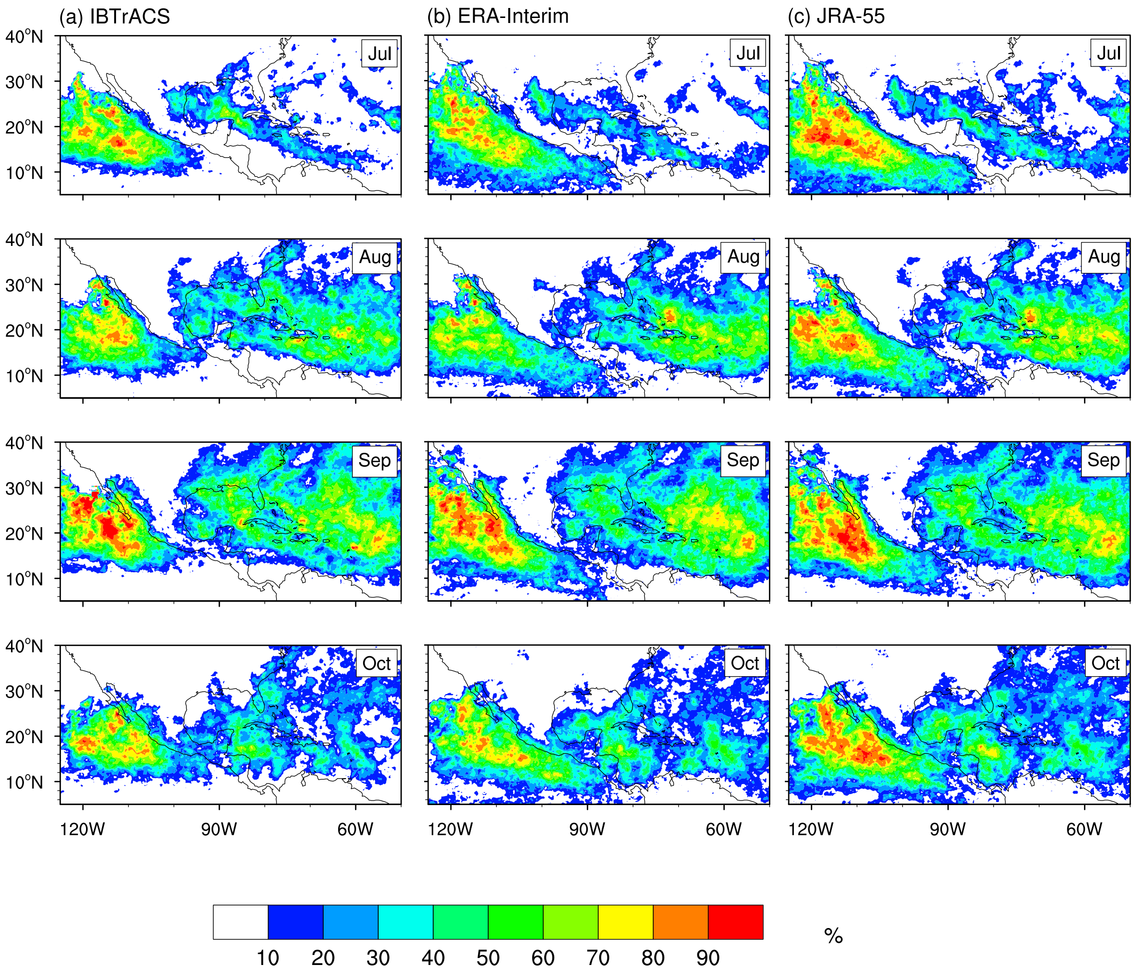

Figure 4.5: Monthly contributions of TCs to the extreme rainfall amount (%) from July to October, employing TCs tracks from (a) IBTrACS, (b) ERA-Interim, and (c) JRA-55. Climatology for 1998-2016.

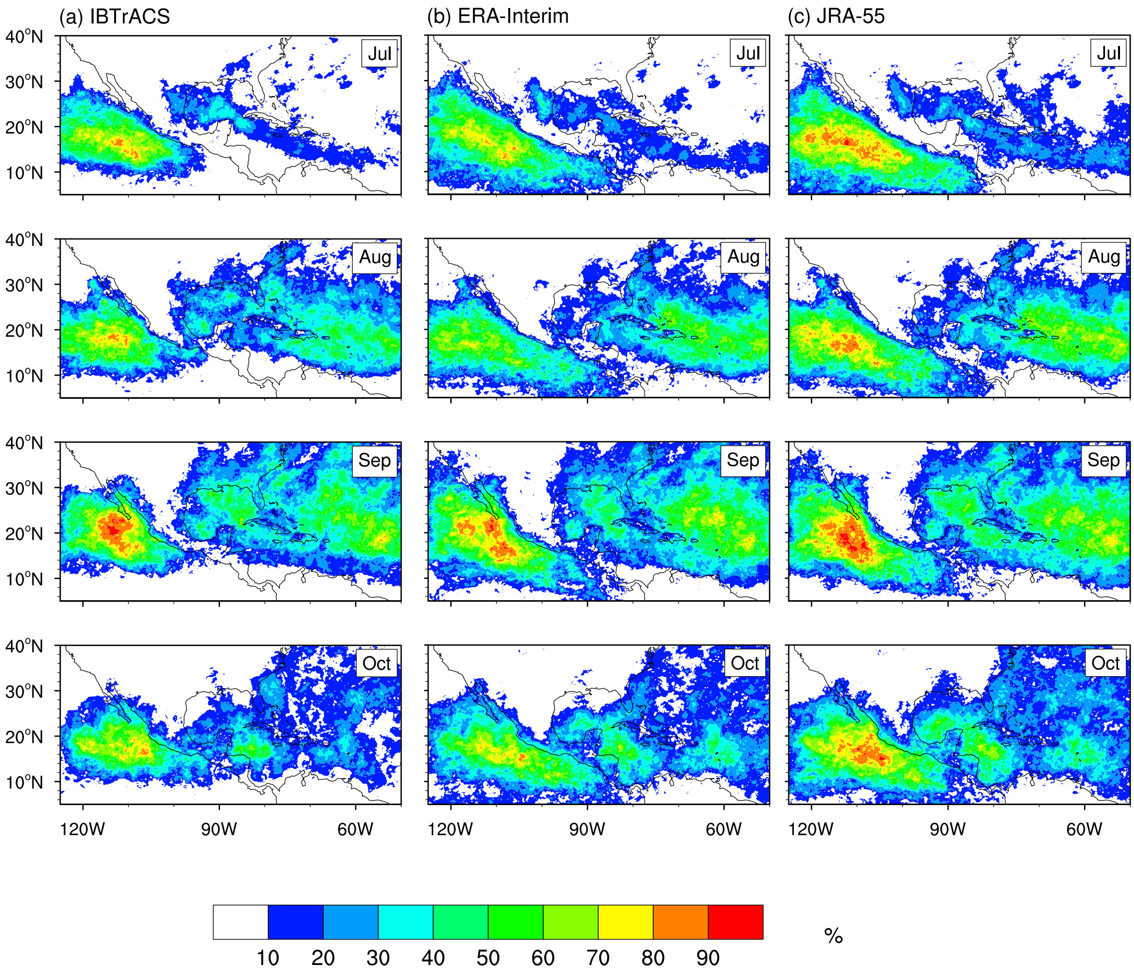

Figure 4.6: Monthly contributions of TCs to the extreme rainfall frequency (%) from July to October, employing TCs tracks from (a) IBTrACS, (b) ERA-Interim, and (c) JRA-55. Climatology for 1998-2016.

4.4.3 Contribution of Tropical Cyclones to moisture transport over Middle America

The hydrological cycle includes processes of evaporation, condensation, precipitation, and moisture advection, which represent the means whereby water is added to or removed from the atmospheric branch. The atmospheric water vapour availability and transport play an important role in determining the climate over the continents, and are strongly linked with radiative processes (e.g. Trenberth and Fasullo, 2009), with convection and the generation of rainfall (Grabowski and Moncrieff, 2004). Of particular interest to this study is the spatial distribution of the TC-related moisture transport and its contribution to the climatological moisture transport relative to the contribution from the mean circulation over Middle America. Figure 4.7 represents the spatial distribution of the monthly-accumulated VIMF (arrows) and VIMF divergence (shading) by the mean circulation ($\nabla \cdot (\bar{v}\bar{q})$) from (a) ERA-Interim and (b) JRA-55 for 1979-2016. During the TC season, strong convergence is observed over most of the Eastern Pacific, while over the North Atlantic it is confined to a band between 5°and 10°N; in both basins the region of maximum VIMF convergence is associated with the Inter Tropical Convergence Zone (ITCZ) (Peixoto and Oort, 1992) and the seasonal migration of the edges of the Hadley Cell. Divergence prevails and is less intense over the North Atlantic, especially in the north of the basin. Both reanalyses show that some portions of the Atlantic Ocean, as well as the Caribbean Sea and the Gulf of Mexico, are important moisture sources during the boreal summer. Over the Gulf of Mexico and the Caribbean, mean VIMF divergence prevails during May to August, and turns to convergence during September and October.

An analysis of the magnitude and sign of TC-related VIMF convergence shows regions where the influence of TCs becomes more relevant to the total monthly moisture transport over the domain. The contribution of TCs to moisture transport, quantified with ERA-Interim and JRA-55 (Figs. 4.8 a and 4.8 b, respectively), shows that monthly TC-related VIMF convergence is about an order of magnitude smaller than the VIMF divergence by the mean circulation.

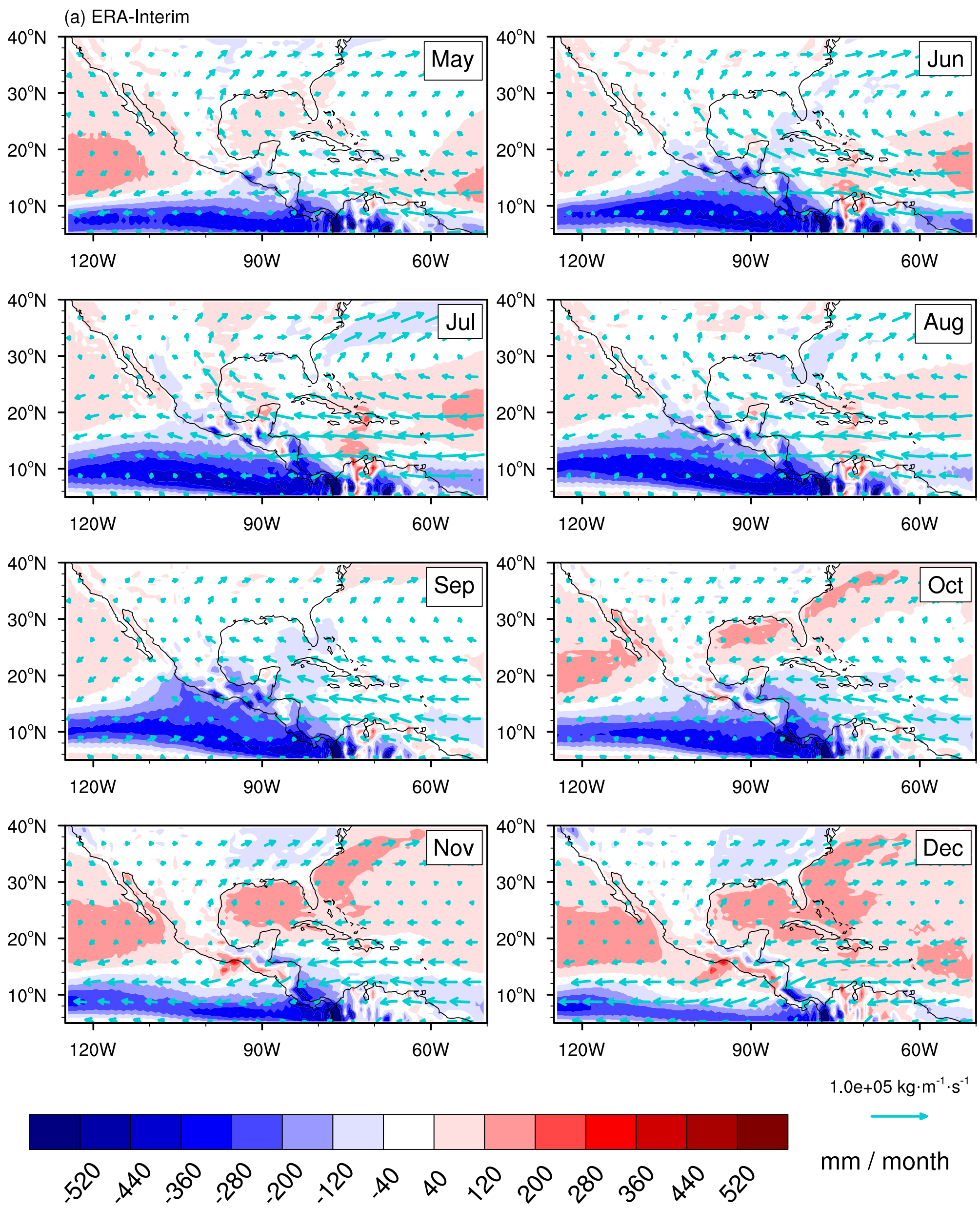

Figure 4.7: Monthly-accumulated vertically integrated moisture flux (arrows; units: $kg{\cdot}m^{-1}{\cdot}s^{-1}$) and vertically integrated moisture flux divergence (shading; units: $mm{\cdot}month^{-1}$) by the mean circulation from (a) ERA-Interim and (b) JRA-55 reanalyses. Climatology for 1979-2016 *(continued on next page)*.

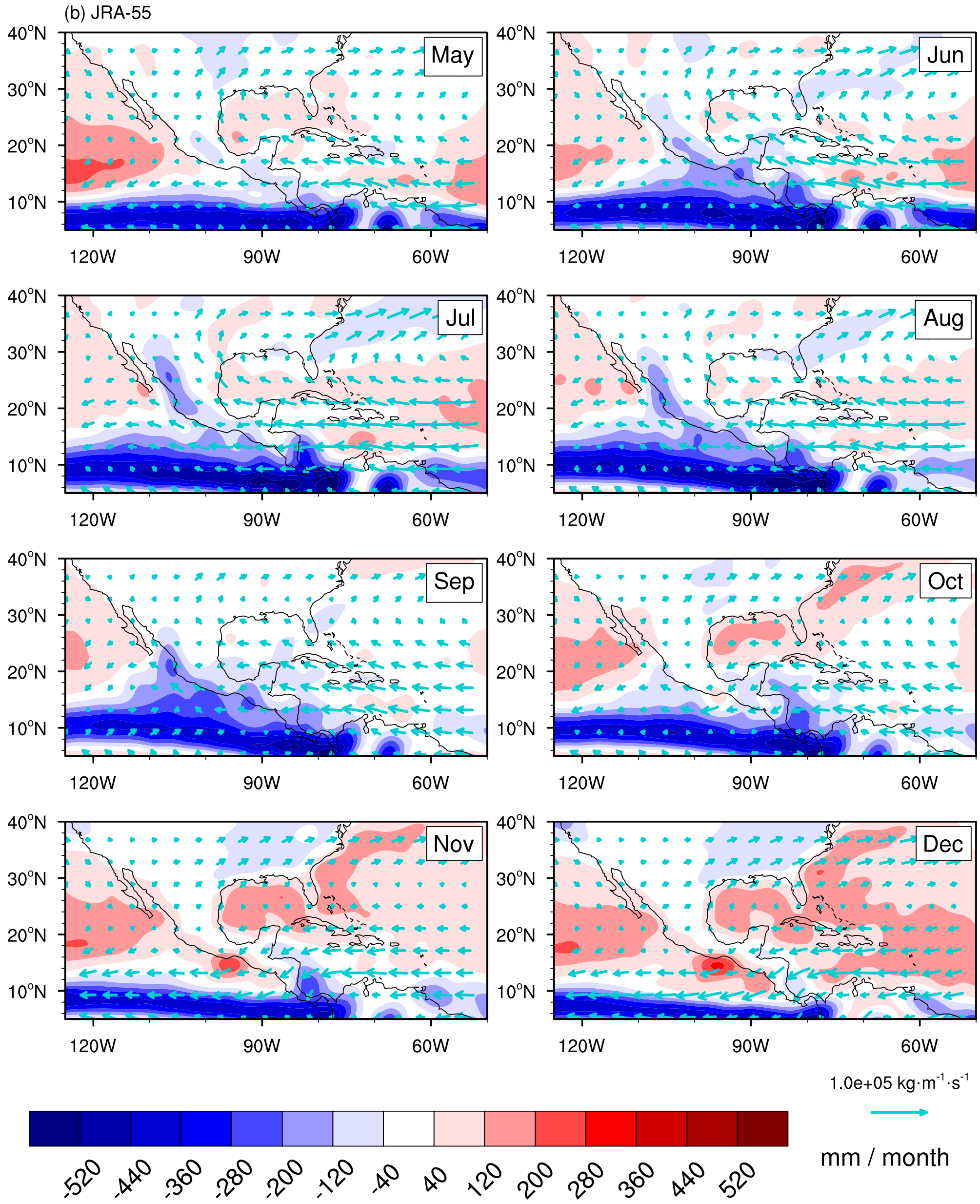

Figure 4.7: *(continued)*.

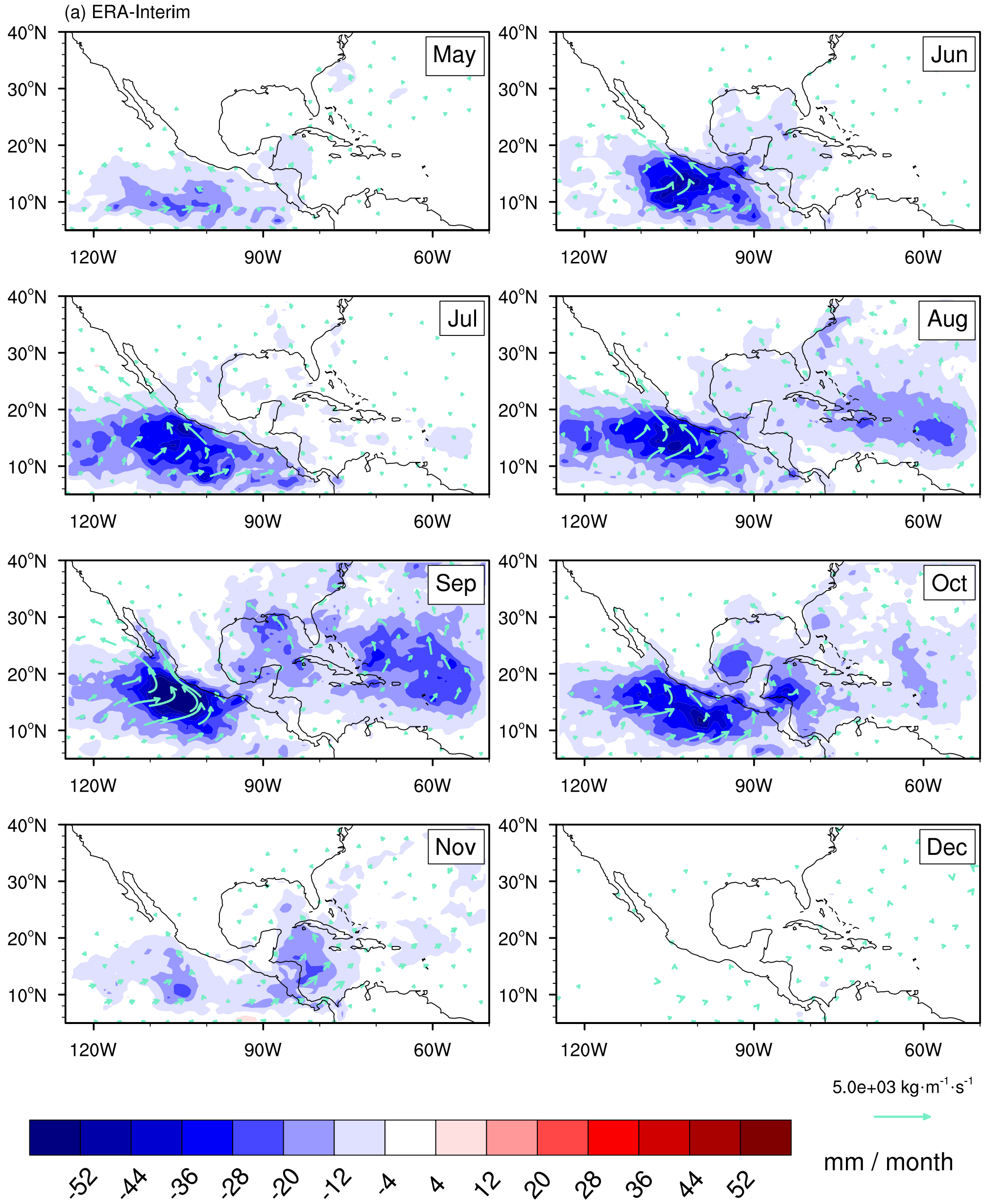

Figure 4.8: Monthly-accumulated vertically integrated moisture flux (arrows; units: $kg{\cdot}m^{-1}{\cdot}s^{-1}$) and its divergence (shading; units: $mm{\cdot}\ month^{-1}$) for TC eddies quantified by using fields and TCs tracks derived from (a) ERA-Interim and (b) JRA-55 reanalyses. Climatology for 1979-2016 *(continued on next page)*.

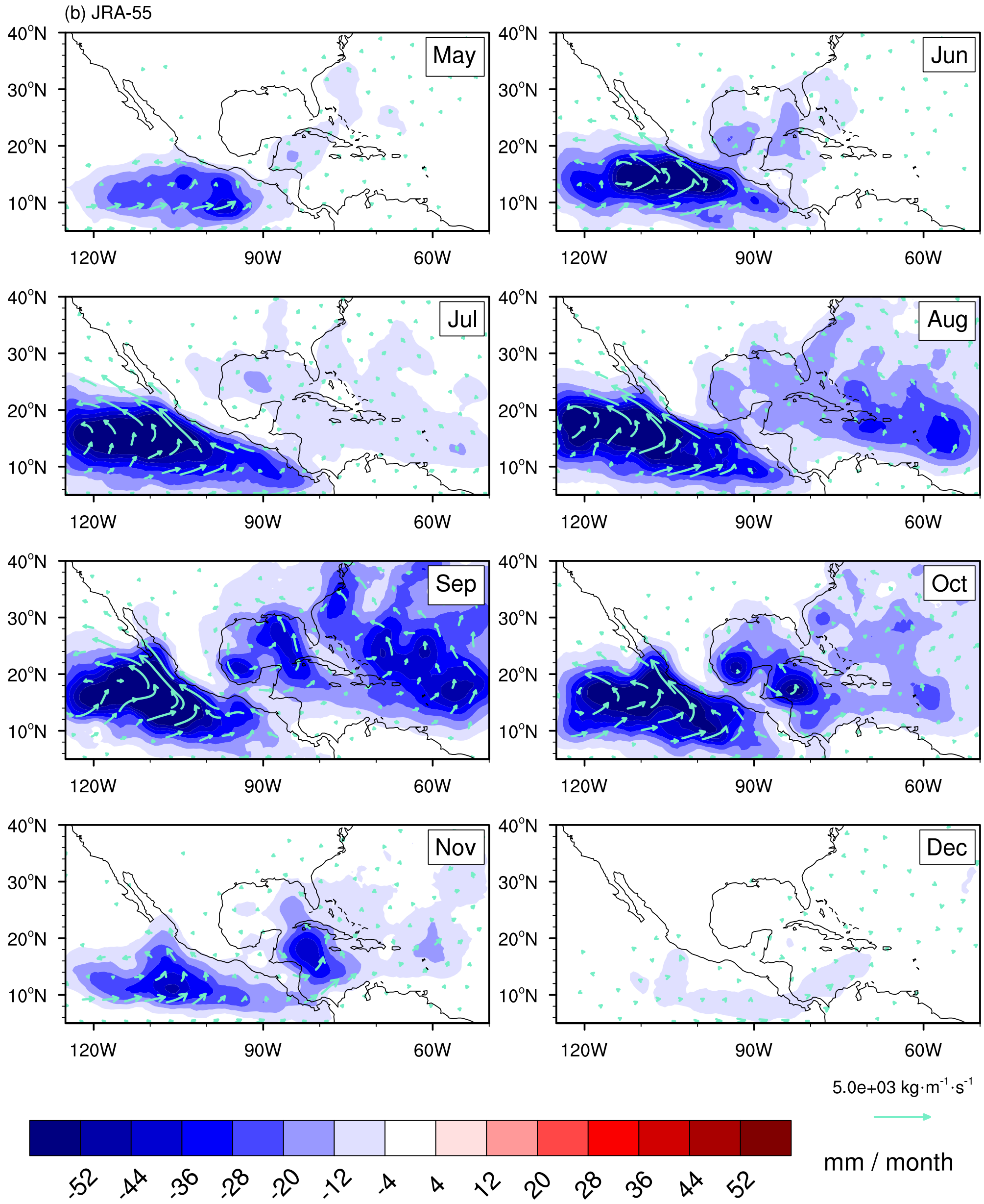

Figure 4.8: *(continued)*.

In general, the TC contribution to moisture transport over the Eastern Pacific basin is larger than that over the North Atlantic basin throughout the TC season, and it has a broader spatial extent inland relative to rainfall, suggesting that TCs can affect precipitation further downstream than the 5 geodesic degree radius we specified for the quantification. Added to this, the contribution in JRA-55 is larger than in ERA-Interim possibly due to higher resolution of JRA-55 and assimilation of TC winds, sustaining stronger storms (Hodges et al., 2017). The contribution of TCs to moisture transport is highly relevant to the summer moisture availability over the domain: the Atlantic shows a predominant VIMF divergence during the year (Fig. 4.7) with some exceptions throughout the TC season (Fig. 4.8). Figure 4.9 shows in red (blue) areas where TC VIMF convergence reinforces (weakens) the moisture convergence (divergence) by the mean circulation, quantified with (a) ERA-Interim and (b) JRA-55. TCs activity widely influences the available moisture over both oceans and continent, particularly over southern and northeast Mexico, the west coast of Mexico, and the Gulf Coast of the U.S. Even more, both reanalyses show that TC-related moisture convergence has the capability to reverse the sign of the moisture divergence by the mean circulation on a monthly basis, particularly over a wide area of the Atlantic Ocean during September and October (shaded yellow areas of Fig. 4.9) when the monthly vertically integrated divergence of moisture by the mean circulation is weak.

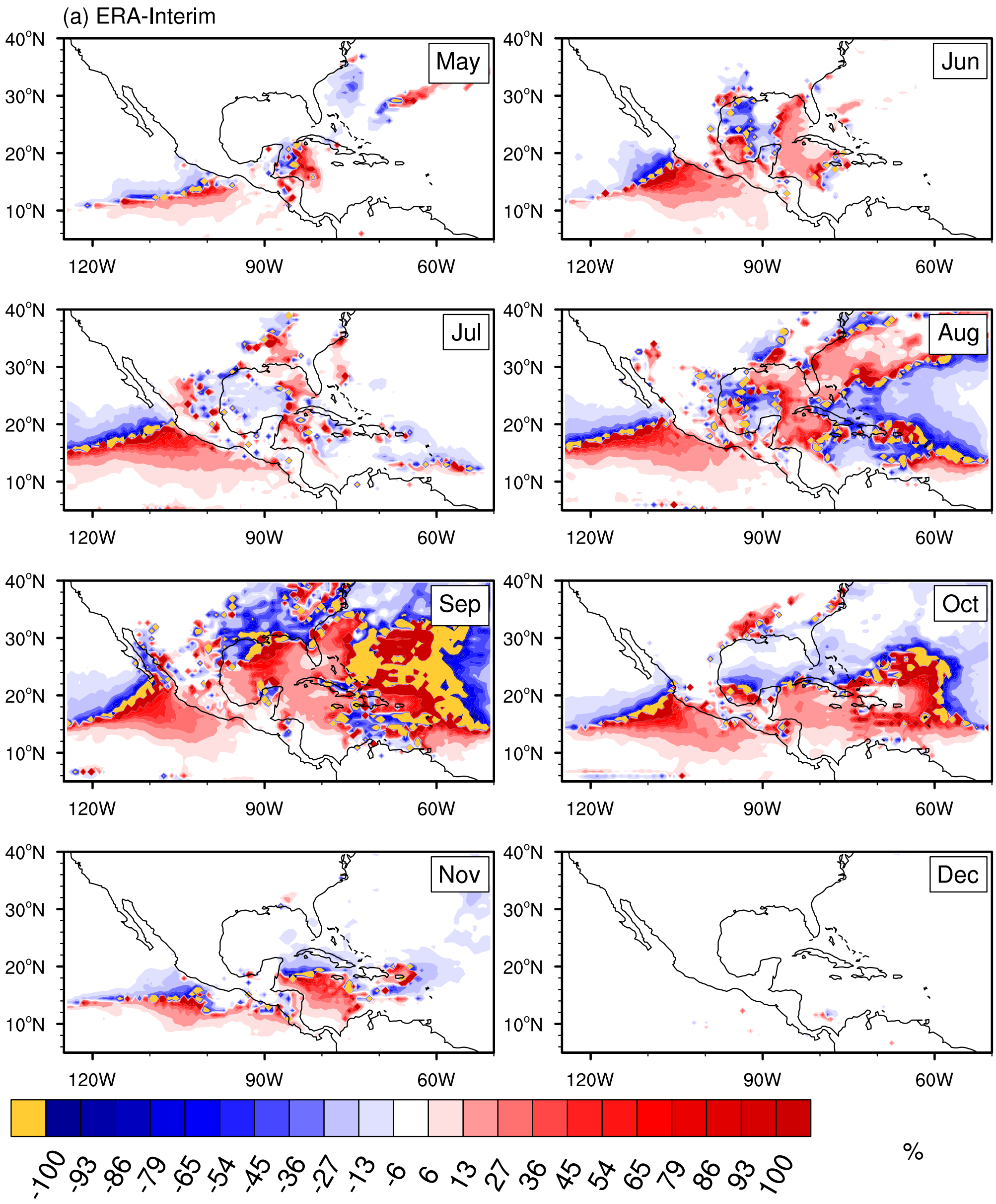

Figure 4.9: Strength of the TC-associated VIMF convergence relative to the strength of the VIMF divergence by the mean flow (%), estimated by using TC tracks from (a) ERA-Interim and (b) JRA-55 reanalysis. Shaded yellow areas indicate where TC reverses the sign of the divergence by the mean circulation. Climatology for 1979-2016 *(continued on next page)*.

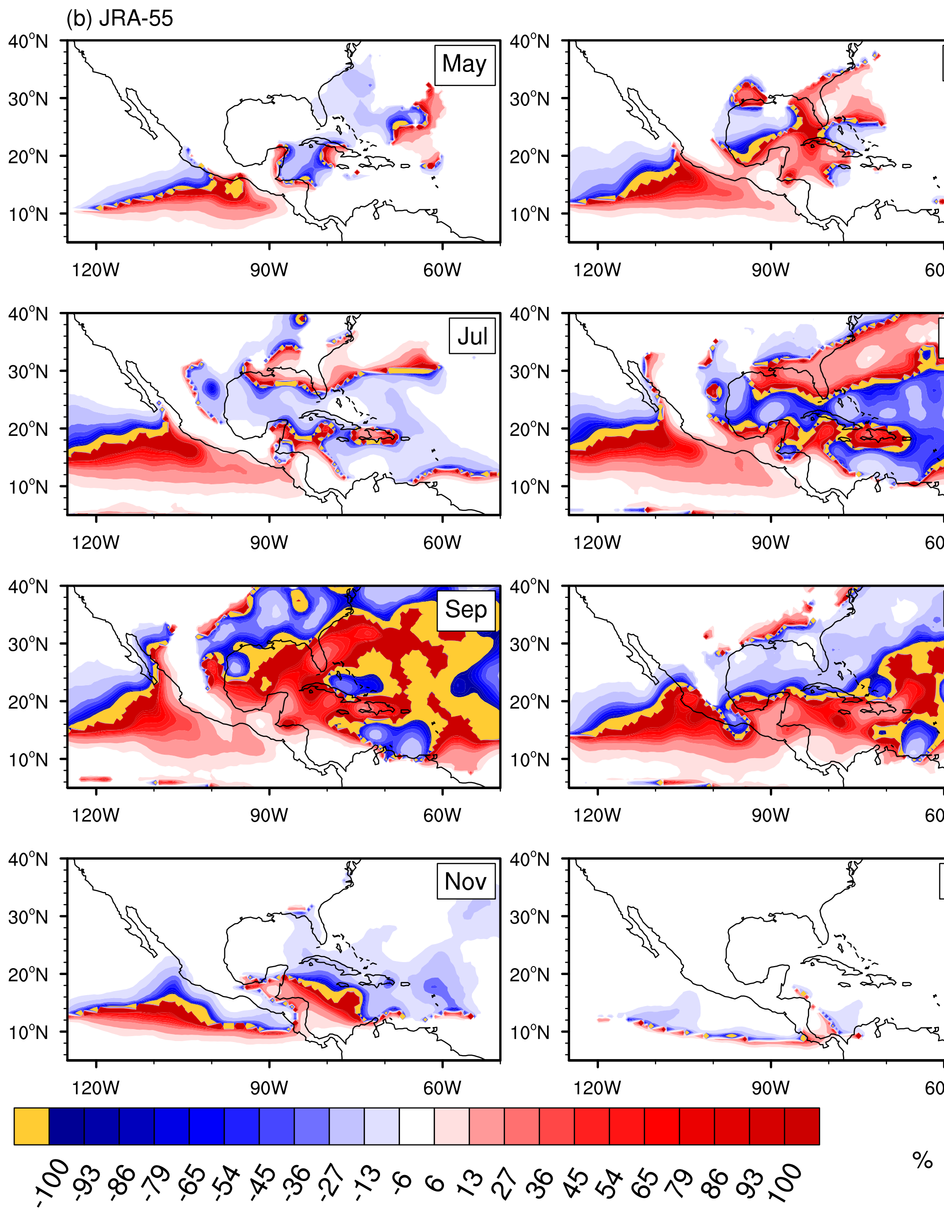

Figure 4.9: *(continued).*

4.5 Discussion

The motivation for this work comes from the need to quantify the climatological contribution of TCs to the atmospheric branch of the hydrological cycle over Middle America. It is important to understand the regional impact that TCs have on the seasonal water availability and in terms of extreme episodes of rainfall over Middle America, often linked with damages and losses of life. This study also contributes to a better understanding of the role of TCs in the global hydrological cycle. An analysis of TCs contribution to monthly-accumulated rainfall and to extreme rainfall over Middle America is presented, based on TC tracks derived from observations (IBTrACS) and from TC tracks identified by an objective feature tracking method for ERA-Interim and the JRA-55 reanalyses, using TMPA 3B42 rainfall datasets for 1998-2016. Objective tracking methods allow identifying a more complete life cycle of the TCs, including the precursor and post-extratropical transition stages (Jones et al., 2003). This extends the observed record, assuming the reanalyses are accurate. Distinct spatial distributions of quantified TC-related rainfall from observations and reanalyses were found: most of the discrepancies (agreements) occur over the Eastern Pacific and Central America (North Atlantic). TC contributions to rainfall quantified by reanalysis tracks over the Eastern Pacific (equatorward of 15°N) show a larger monthly contribution compared with IBTrACS. This analysis indicates that TC tracks derived from reanalysis are able to capture the activity of precursors of TCs over the Eastern Pacific basin, and area of active generation of easterly waves (Ferreira and Schubert, 1997; Serra et al., 2008; Toma and Webster, 2010a,b) that are important precursors of TCs in the Eastern Pacific and North Atlantic basins (Belanger et al., 2016; Agudelo et al., 2011). The differences found over continental Mexico are mainly attributed to discrepancies in TC tracks in proximity to the coast (corresponding to post-TC stages). Using the extended TC lifecycle criterion for the reanalyses increases the TC contribution over most of Central America, including in regions where IBTrACS has few or no TCs. In these areas, there are substantial differences in estimated TC rainfall between using IBTrACS and reanalysis tracks. The annual number of TCs detected in reanalyses over the Atlantic and Eastern Pacific basins are in good agreement with IBTrACS (Hodges et al., 2017). However, there are differences in the paths of the TCs identified in the reanalyses and IBTrACS, particularly for TCs that make landfall over continental Middle America (Fig. 4.10). In some cases, TC tracks derived from reanalysis are not tracked in the proximity to the coastline, and consequently the effect of the TCs on rainfall near the continent is less than when using IBTrACS. There is a strong similarity between the spatial patterns of the differences from reanalyses and IBTrACS in TC track density (Fig. 4.10) and TC related rainfall (Fig. 4.3). The differences in the quantification of TC-related rainfall are more noticeable over Mexico during September (Fig. 4.3). According to previous studies (e.g. Xu et al., 2017; Hodges et al., 2017), a significant source of error could come from the representation of the TC wind field in reanalyses, affecting the frequency and lifetime of TCs. Xu et al. (2017) argue that the combined effects of underestimated wind speed and overestimating the radial extent of TCs likely result in an underestimated TC-related moisture transport. However, the observed tracks are also subject to uncertainties in the identification of weaker TCs, due the different criteria employed by the various agencies to reporting an identified TC, resulting in the exclusion of some TCs from the Best Track, as well as the fact that some tropical depressions are excluded due to a lack of wind information (Hodges et al., 2017). Chen et al. (2013) have found that TMPA 3B42 rainfall estimations related to TCs are better represented over ocean than over land, being particularly less accurate to capture orographic features during landfalling TC episodes. The retrieval method in TMPA 3B42 is based on the Goddard Profiling Algorithm (GPROF; Kummerow et al., 2001), which uses the contrast of the emissivity of the raindrops and the underlying surfaces to estimate rainfall rates (for further details consult Huffman et al. (2007)). Over the ocean, the contrast of emissivity is better captured due to the well-defined difference between the rain and surface temperatures. As emissivity is heterogeneous over complex surfaces (such as the land), the contrasts between the emission of the rain drops and the surface are more difficult to capture, which reduces the accuracy of rain estimates (e.g. Chen et al., 2013). These uncertainties mean that our estimations of heavy rain frequency (>50 mm) of TC-related rainfall are uncertain over coastal and inland mountainous areas of Middle America.

Similar patterns and rates of TC-related extreme rainfall, quantified by using observations and reanalyses, are found. The agreement could be attributed to the fact that tracks calculated by using the objective TC identification scheme from reanalyses identify the strongest storms more accurately (e.g. Saffir-Simpson categories 4 and 5; Hodges et al., 2017). Moreover, observed tracks of strongest storms are more certain than those of weaker storms (e.g. tropical depressions, Saffir-Simpson categories 1-3), which increases our confidence in TC-extreme rainfall computed from observed and reanalysis tracks, as extreme episodes of rainfall are more likely to be related to the strongest storms.

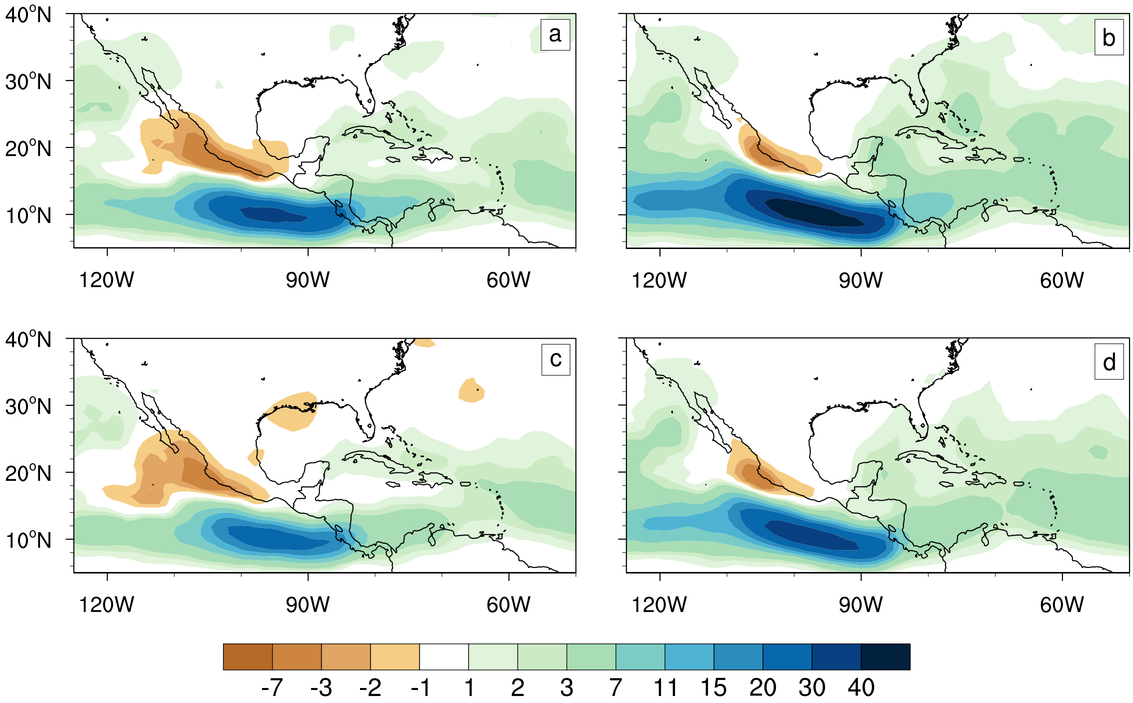

Figure 4.10: Differences between TC track densities based on ERA-Interim reanalysis and IBTrACS (a) per year and (c) during JASO, and on JRA-55 reanalysis and IBTrACS (b) per year and (d) during JASO. Units: number of TCs per unit area ($\sim 10^6$ km^2). Period 1998-2016.

TCs are important sources of moisture over the region, mainly during June to October. TC-related moisture convergence often extends further inland than TC-related precipitation, suggesting that TCs have a longer reach than their rainfall fields. Particularly, the Gulf of California, its continental surroundings and the North of Mexico receive moisture from TCs, which is comparable in magnitude to the amount of moisture extracted from the region by the mean circulation. More notably, the TC-associated VIMF convergence can reverse the sign of the VIMF divergence by the mean flow when the latter is weak, mainly over a big portion of the Atlantic Ocean and some continental regions during September and October.

Even though Central America experiences strong VIMF convergence during most of the year, the contribution of TCs is a non-negligible source of this moisture transport when a TC extended lifecycle criterion is considered. Added to this, the mean moisture transport over Central America is also likely related to the location and intensity of the ITCZ. TC contributions to moisture transport analyses suggest that a correct quantification relies heavily on the representation of TC tracks, and is strongly linked with the representation of the moisture flux in the reanalyses.

4.6 Conclusions

TCs are important sources of rainfall and moisture transport over Middle America, and make a substantial contribution to the amount of mean rainfall and the amount and frequency of extreme rainfall during the TC season. In this paper, a quantification of the climatology of TC-related rainfall and moisture transport over Middle America has been made, employing TC tracks from observations (IBTrACS) and two-state-of-the-art reanalyses: ERA-Interim and JRA-55. Our results show that the climatological mean rainfall contribution of TCs mainly occurs during September and October, when TCs in both the North Atlantic and Eastern Pacific are more active: TCs contribute about 10-20% of the monthly-accumulated rainfall over the west coast of Mexico and centre of Mexico. The largest percentage of the monthly contribution over the entire Middle America domain was found in the southern Baja California Peninsula, with rates up to 60%. Our analysis suggests that a shift in East Pacific TC tracks towards the western Mexican coast from September onwards is a main factor for the high TC contribution to the accumulated rainfall over the western continental portion of Mexico. The spatial distribution of TC rainfall over Northwestern Mexico might be related with static factors such as the orography. TCs are also important sources of extreme rainfall over Mexico and the North of Central America, in some cases contributing more than 50% of the monthly extreme rainfall amount, mainly during September and October when TCs tend to make landfall more often. Most of the agreements of spatial distributions of TC-related rainfall from observations and reanalyses are found in the North Atlantic basin, and in the contributions of TCs to extreme rainfall.

Most of the contribution of TCs to moisture transport occurs over coastal and Central Mexico, and the Eastern Pacific from June to October. TCs are likely to reverse the sign of the VIMF divergence when the VIMF divergence by the mean circulation is weak, occurring mainly in a wide area of the North Atlantic, and to a lesser extent, the Eastern Pacific, the Gulf of California and Northwestern Mexico. In this study, the robustness of the analysis of the regional contribution of TCs to the hydrological cycle heavily relies on the accuracy of the representation (location and lifetime) of the TC tracks, either based on observed TC-tracks or calculated from an objective tracking method applied to reanalysis datasets, as well as on the quality of the meteorological fields (e.g. estimations of rainfall and moisture flux from reanalysis). To improve our ability to quantify TCs contribution to rainfall and moisture, an accurate representation of the pre- and post-stage of the life cycle of the cyclones is required, including inland trajectories, no matter the stage of the TC lifecycle. This quantification of TCs contribution on the atmospheric branch of the hydrological cycle over Middle America will be useful to future studies on the understanding the sub-seasonal and inter-annual variability of the regional hydrological cycle, as well as process studies that investigate the role of TCs in the hydrological cycle.

Acknowledgments AFD was supported by The National Council of Science and Technology (CONACYT) Mexico as part of the Sectoral Fund CONACYT-Secretariat of Energy-Energy Sustainability, through a scholarship for PhD studies at the University of Reading. NPK was supported by the Natural Environment Research Council (NE/L010976/1). PLV, LG and MED were supported by the National Centre for Atmospheric Science, a collaborative centre of the Natural Environment Research Council, under contract R8/H12/83/001. We thank Dr. Kevin Hodges for helpful discussions regarding the objective TC tracking method and for providing us with the TC tracks from ERA-Interim and JRA-55 reanalyses. We also thank the Editor and anonymous reviewers for their valuable comments.

Chapter 5:

Interannual Variability of Rainfall Attributed to Tropical Cyclones in Middle America

5.1 The purpose of the present study

Chapter 3 demonstrated that Middle America's rainfall variability at interannual time scales responds to large-scale modes of climate variability such as ENSO, AMM, and NAO. That study also showed that the interannual variability of rainfall depends on the changes in seasonal TC activity in the eastern Pacific, the Caribbean Sea, and the Gulf of Mexico. Chapter 4 demonstrated that TCs significantly contribute to the atmospheric branch of the hydrological cycle in Middle America and the IAS, including to mean accumulated rainfall, moisture transport, and extreme rainfall, varying in space and time. This chapter explores the variability of rainfall attributed to TCs in Middle America and their relationship with large-scale modes of climate variability. This study addresses the final objectives and questions stated in 1.3, aiming to determine the drivers of the interannual variability of TC-related rainfall in Middle America, connected to variability of TC genesis and tracks in the East Pacific and the North Atlantic basins.

Several studies have shown that ENSO influences the variability of TC activity (genesis, trajectories, life-time, and intensity) in the North Atlantic and the East Pacific. During El Niño years (e.g., 1982-1983, 1986-1987, 1991-1992, 1997-1998, 2002-2003, 2004-2005; Camargo et al., 2007) there is reduced Atlantic TC genesis through induced changes in tropospheric vertical wind shear, reduction of relative humidity, and subsidence (Gray, 1984; Goldenberg and Shapiro, 1996; Chu, 2004; Camargo et al., 2007); the latter inhibits

Atlantic TC activity through warm upper tropospheric temperature anomalies that increase stability (Tang and Neelin, 2004). The opposite occurs during La Niña, when the Atlantic TC activity is enhanced.

Larson et al. (2005) showed that La Niña promotes TC activity in the Atlantic MDR during the positive phase of the Artic Oscillation (AO; Thompson and Wallace, 1998), while during El Niño and the negative phase of the AO there is a considerable reduction of TC activity in the MDR. In the same study, it is shown that La Niña leads to an average 15% increase in the number of Atlantic TCs, while El Niño leads to a 10% reduction (respect to the mean of the period 1950–98).

It has been suggested that the ENSO-North Atlantic teleconnection and TC activity vary according to the location of the Pacific SSTs anomalies, categorised as canonical or 'Modoki' ENSO types (e.g., Ashok et al., 2007; Taschetto et al., 2010). Kim et al. (2009) found that TC frequency in the Gulf of Mexico is larger during El Niño Modoki than canonical El Niño.

Quan et al. (2020) suggested that the effects of ENSO on the North Atlantic TC activity depend on the sequence of ENSO events: enhanced TC activity and landfall in the Gulf of Mexico and the Caribbean when El Niño summer is preceded by an El Niño winter, rather than El Niño summer preceded by La Niña winter.

Some modes of Atlantic climate variability also influence the Atlantic TC activity: the AMM modulates interannual TC activity through changes in the meridional gradient of tropical Atlantic SSTs (e.g., Vimont and Kossin, 2007; Kossin et al., 2010; Patricola et al., 2014; Lim et al., 2016). The Atlantic MDR TC activity is favoured during the positive phase of the AMM, which is characterised by anomalously warmer SSTs near the equatorial Atlantic and the northward shift of the Atlantic ITCZ (Chiang and Lintner, 2005). Added to these conditions, Smirnov and Vimont (2011) found that during the positive phase of the AMM there is significantly reduced vertical wind shear in the subtropical North Atlantic, which also favours TC genesis.

The AMO has been related to the decadal variability of Atlantic TC activity at decadal time-scales (Goldenberg et al., 2001); more intense Atlantic TCs occur during AMO positive phases, which are characterised by warmer Atlantic SSTs. The AMO can also excite the AMM on decadal scales, so that the AMO consequently influences interannual TC activity in the Atlantic (Vimont and Kossin, 2007).

Lim et al. (2016) found that ENSO impacts on TC Atlantic activity can be significantly modified and even reversed by the AMM and the NAO: in 2005, anomalously warmer SSTs linked to a positive AMM enhanced Atlantic TC activity, despite the existing weak El Niño conditions in that year. In 2013, a strong positive NAO (characterised by an enhanced NASH and an enhanced Icelandic low), produced stronger vertical wind shear and a drier lower troposphere, which inhibited Atlantic TC genesis, despite the weak La Niña experienced in that year. The combined influence of La Niña, the positive AMM, and the negative NAO favour cyclogenesis in the Atlantic basin through a westward extended, weak NASH, and a wider area of positive SST anomalies in the Atlantic basin (Lim et al., 2016).

Developing El Niño favours TC activity in the eastern North Pacific mainly through weakened vertical wind shear and increased vorticity (Laing and Evans, 2016). It also causes a westward shift of TC genesis (Irwin III and Davis, 1999; Camargo et al., 2008) and promotes an extended TC lifetime (Chu, 2004). El Niño modulates Central eastern Pacific TC activity through changes in the location of active regions and TC tracks towards the dateline (Bell et al., 2014; Chu, 2004; Camargo et al., 2008). Fu et al. (2017) found that El Niño enhances TC frequency in the western development region of the East Pacific, and reduces TC frequency in the eastern development region (next to Middle America's coast). In all those cases La Niña typically brings opposite conditions.

Intraseasonal modes of variability also affect TC activity in the IAS: Maloney and Hartmann (2000a) found that the enhanced phases of the MJO in the East Pacific are more likely to create favourable conditions for eastern Pacific TC genesis (next to coastal Middle America), such as low-level convergence and cyclonic vorticity anomalies, and low vertical wind shear. In the Gulf of Mexico and the western Caribbean hurricane genesis is up to four times greater during the enhanced phases of the MJO than during the suppressed phases (Maloney and Hartmann, 2000b).

Aiyyer and Molinari (2008) found that, during the enhanced phases of the MJO, TCs develop north of the ITCZ, near the Gulf of Tehuantepec and the Gulf of Mexico, despite the enhanced wind shear in this regions. The authors also suggested that, during suppressed phases of the MJO, TCs tend to form mainly within the ITCZ.

Although some of the aforementioned studies have focused on the influence of interannual modes of variability on TC activity, only a few have examined their effect on TC rainfall in Middle America. For example, Larson et al. (2005) explored the causes of the variability of TC-related rainfall, linked to large scale-modes of variability. The authors suggested that East Pacific TC-related rainfall increases further north in Middle America during El Niño than during La Niña events.

Most of the TC-related losses and damages over continental Middle America affect the most populated and poorest states of central and southern Mexico, protected natural areas, large cropped regions, and archeological and touristic areas (INEGI, 2019; CONAPO, 2016). For example, Category 4, Hurricane Pauline (5-10 October 1997) is considered one of the deadliest and damaging Pacific hurricanes to make landfall in Mexico: Oaxaca and Guerrero reported together a death toll at 228 people and 165 missing people and left approximately 54,000 families homeless. The damages associated with Hurricane Pauline corresponded to 180 ha of cropped areas, amounting to a loss of nearly MXN80 billion (around 1997 USD10.1 billion) (CENAPRED, 2001). During this event, the highest accumulated rainfall registered was 686 mm in San Luis Acatlán, followed by Acapulco with 411 mm (Lawrence, 1997).

On the other hand, TC-related rainfall may also be beneficial for inland regions with scarce fresh-water resources. For example, the East Pacific, category 4 Hurricane Nora (16-28 September 1997) made landfall twice in Baja California Peninsula, and its remnants moved along the Colorado River Valley, bringing heavy rainfall and strong winds over the northwestern Middle America (Farfán and Zehnder, 2001). Despite the damages caused, Hurricane-Nora-related rainfall aided to reverse the anomalously low SON 1997 rainfall conditions at some northern Middle America inland areas associated with a substantially weakened monsoon trough and a southward displacement of the ITCZ during the 1997-98 El Niño. Despite the generalised negative rainfall anomalies in Middle America, the Baja California peninsula and some portions of southern Middle America recorded above-normal precipitation, mainly during the late 1997 TC season (Bell et al., 1999), in response to six East Pacific TCs tracking close to Middle-American coasts or making landfall, including TC Andres (1-7 June), TC Blanca (9-12 June), TC Olaf (26 September-12 October), and Hurricane Rick (7-10 November).

Understanding the causes of TC-related rainfall from TC variability making landfall and/or tracking close to continental Middle America is a matter of social, economic, and scientific interest. This knowledge provides actionable information for human safety and wellbeing, water-resources management, agricultural and industrial activities, the preservation of wildlife, and for further climate-system and hydrological-cycle research.

This chapter aims to determine the patterns of rainfall that represent most of the interannual variability of TC-related rainfall over Middle America, and the corresponding large-scale phenomena, meteorological systems, and environmental conditions associated with the interannual variability of TC-related regional rainfall.

5.2 Datasets and methods

5.2.1 Data

For the period 1979–2011, daily gridded rainfall data across Middle America with a horizontal resolution of 10 km×10 km (López-Bravo, 2015; López-Bravo et al., 2018), were used to calculate seasonal TC-related rainfall. A complete description of this dataset is available in López-Bravo et al. (2018). The selected period of analysis (1979-2011) is the one that had a larger and more continuous number of available rainfall observations in situ, and that were used to create the daily gridded rainfall dataset. Therefore, the use of this dataset for the selected period gives more robustness and accuracy to the quantification of TC-related rainfall in this study.

This gridded gauge rainfall dataset has advantages over the TMPA 3B42 satellite estimates of rainfall used in chapter 4, such as a more extended period of observational record and higher horizontal resolution, compared with the satellite estimates of rainfall (1998-2016 and $0.25° \times 0.25°$, respectively). Since the TMPA 3B42 product is particularly inaccurate to capture orographic features during landfalling TC episodes (Chen et al., 2013), it is expected to have more accurate representations of TC rainfall over Middle America when using gauge observations.

Six-hourly data of winds on pressure levels, atmospheric surface pressure, and vertically integrated moisture fluxes (VIMF) from the Japanese 55-year reanalysis (JRA-55; Kobayashi et al., 2015, all at the original resolution of TL319, $\sim$ 55 km) are used in this study. The divergence of JRA-55 vertically integrated moisture flux fields is computed using spherical harmonics with truncation T64, employing the windspharm Python package (Dawson, 2016).

In this chapter, we use TC tracks from the objective TC tracking method based on Hodges (1994, 1995, 1999), applied to the JRA-55 reanalysis dataset. The methodology employed for the calculation of this dataset is fully described in Hodges et al. (2017), and in the chapter 4 of this thesis (see Sec. 4.3), where the methodology has been used to calculate the seasonal statistics of TC track densities and TC genesis densities. Overall the TC tracks tested in chapter 4, TC tracks based on JRA-55 reanalysis were chosen to calculate the TC rainfall in this study. The advantage of using TC tracks based on reanalysis comes from using the extended TC lifecycle criterion (pre- and post- TC stages; see sec. 4.3.3), compared with observations. The steering flow winds are computed as the mass-weighted, vertically-averaged horizontal wind fields from 850 to 200 hPa. Wind shear is defined as the magnitude of the vector difference between the horizontal wind fields at 850 and 200 hPa, which has been widely used for empirical studies of TC activity (Camargo et al., 2007; Wang et al., 2011). Seasonal statistics of TC track densities and TC genesis densities are used, computed with the objective TC tracking method based on Hodges (1994, 1995, 1999), applied to the JRA-55 reanalysis dataset (see Section 4.3.3 for a full description of the dataset).

Similar to Chapter 3, in this chapter is employed the NOAA Optimum Interpolation Monthly SST (OISST) Analysis dataset at resolution $1° \times 1°$ to compute seasonal SST means. Monthly mean indices corresponding to the regions Niño 3.4 and Trans-Niño index are retrieved from `https://climatedataguide.ucar.edu/climate-data/` (Trenberth, 2020). Using the definition of Patricola et al. (2016), for the period of 1979-2011 the following ENSO years are included in the period of analysis: El Niño years are 1982, 1986, 1987, 1991, 1994, 1997, 2001, 2002, 2004. La Niña years are 1988, 1998, 2010. canonical/East Pacific El Niño years are 1982, 1987, 1997. Non-canonical/Modoki El Niño years are 1986, 1991, 1994, 2001, 2002, 2004.

The monthly mean AMM index is provided by `http://www.aos.wisc.edu/~dvimont/MModes/Data.html`. The monthly mean NAO index is retrieved from `https://www.cpc.ncep.noaa.gov/products/precip/CWlink/pna/nao.shtml`. The monthly mean CLLJ index is provided by `https://iridl.ldeo.columbia.edu/maproom/ACToday/Colombia/CLLJI.html`.

5.2.2 Calculation of the rainfall associated with TCs

A total of 33 TC seasons (from 1979 to 2011) of the East Pacific and the North Atlantic basins have been analysed to quantify the contribution of TCs to Middle America's rainfall. To study the spatial distribution of the rainfall attributed to TCs, the TC season (June-November) is subdivided into two seasons: June-July-August (JJA) and September-October-November (SON). To investigate the contribution of TCs to rainfall over Middle America, the daily gridded observation data across the domain within a circle of 5 geodesic degrees, centred over the TC location, is identified as TC associated rainfall (e.g., Larson et al., 2005; Jiang and Zipser, 2010; Guo et al., 2017); the rest of the rainfall is masked. It is important to note that employing this methodology when using daily rainfall (rather than sub-daily satellite rainfall estimates) causes the loss of temporal resolution in the identification of TC rainfall. This is because the identification of TC rainfall is made using a daily gridded gauge rainfall dataset, while the TC tracks have 6-h temporal resolution. The 5 geodesic degrees criteria matches the 6-h resolution TC tracks with 0.25% of daily rainfall. The difference of temporal resolution between rainfall and TC tracks add some uncertainty to the identification of TC-related rainfall.

5.2.3 Empirical Orthogonal Teleconnections analysis for tropical-cyclone-related rainfall

The modified version of the original EOT analysis (van den Dool et al., 2000), proposed by Smith (2004, fully described in Chapter 3, section 3.2.2) is implemented to determine spatial patterns that represent coherent interannual variance of TC rainfall. The EOT analysis is applied to 1979–2011 high-resolution precipitation observations over Middle America (López-Bravo, 2015; López-Bravo et al., 2018) in JJA and SON.

To identify the large-scale climate phenomena and environmental conditions associated with interannual TC-related rainfall variability over Middle America, the EOT time series of seasonal TC-related rainfall are subjected to regression analysis and compositing analysis. In this chapter, regression patterns are expressed as units of the regressed variable per 5° spherical cap per standard deviation of seasonal rainfall of the corresponding EOT time series analysed (mm).

Spearman's rank correlation coefficients between individual EOT time series and large-scale modes of variability indexes are calculated. Spearman's rank correlation is a suitable option for this analysis as it measures monotonic relationships between the two aforementioned variables, which tend to change together, but not necessarily at a constant rate, such as TC-related rainfall and the atmospheric and oceanic variables analysed here.

5.3 Drivers of the inter-annual variability of TC-related rainfall over Middle America

In this section, the three leading TC-related rainfall EOTs for JJA, and the three leading TC-related rainfall EOTs for SON are analysed. Table 5.1 summarises the three leading EOTS for JJA and SON and their Spearman correlation coefficient with the most significant interannual climate indices, related with candidate modes of variability of the interannual variability of TC-related rainfall in Middle America. For these correlations, monthly mean indices were used to calculate the seasonal Niño SST, CLLJ , AMM, NAO, AMO indices.

EOT	Expl. variance (%)	σ_{bp} (mm)	Niño 3.4	3-mo lag Niño 3.4	CLLJ	AMM SST	AMM wind	NAO	AMO
JJA									
EOT1	79.86	30.11	**-0.49*** **	**-0.45*** **	**-0.46*** **	0.23	**0.35*** **	-0.11	0.15
EOT2	10.25	5.69	0.049	0.25	-0.05	0.192	0.11	-0.26	0.23
EOT3	4.52	14.66	-0.09	-0.07	-0.20	0.25	-0.00	0.025	0.22
SON									
EOT1	83.75	55.06	**-0.31** **	**-0.31** **	**-0.32** **	0.26*	0.07	-0.08	0.17
EOT2	3.86	6.58	-0.10	-0.10	0.14	-0.20	0.04	-0.28*	-0.07
EOT3	3.79	19.01	-0.17	-0.17	-0.16	**0.28** **	0.17	0.19	**0.34** **

Table 5.1: For the three leading EOTs of seasonal Middle America's rainfall: the percentage of variance of the area-averaged rainfall explained; the 5°-spherical-cap seasonal standard deviation of rainfall of the EOT base point (σ_{bp}, mm); the correlation between the EOT time series and Niño 3.4, the 3-month lagged Niño 3.4, the Caribbean Low-Level Jet index, the SST Atlantic Meridional Mode index, the wind Atlantic Meridional Mode index, the North Atlantic Oscillation index, and the Atlantic Multidecadal Oscillation. A *, ** , and *** indicate correlations that are statistically significant at the 12%, 6%, and 2% level, respectively.

It should be highlighted that the Spearman correlation assesses monotonic relationships between two variables, whether linear or not. Therefore, the calculation of the Spearman rank correlation coefficient is suitable for this analysis, considering the limited nature of TC-associated rainfall per year occurring in a determined region.

To understand the drivers of the interannual variability of TC-related rainfall in Middle America, composite and regressions analyses of climate variables that influence the IAS TC activity are calculated for each EOT. Table 5.2 summarises the results of this EOT analysis, for the reader's reference throughout this section.

EOT	Expl. variance (%)	Region affected	Likely driving mechanism
JJA			
EOT1	79.86	Southern/central and southeastern Middle America	Developing canonical La Niña, positive phase of the AMM
EOT2	10.25	Southern and northeastern Middle America	Atlantic warming due to ENSO
EOT3	4.52	Northwestern Middle America	Unclear, but associations with cyclogenesis in the Gulf of Tehuantepec
SON			
EOT1	83.75	Central and eastern Middle America	Developing canonical La Niña, Caribbean warming
EOT2	3.86	central/eastern Middle America	Negative phase of the AMM
EOT3	3.79	Southern/southwestern Middle America	Positive phases of the AMM & the AMO

Table 5.2: Summary of the EOT analysis, showing each EOT percentage of variance explained in area-average seasonal rainfall, the region of Middle America encompassed by the pattern, and the likely driving mechanism.

5.3.1 Summer

5.3.1.1 JJA EOT1

JJA EOT1 is located in central Middle America and explains 79.8% of the variance of the area-averaged TC-related rainfall. JJA EOT1 has a significant correlation with TC-related rainfall in central-west and east coasts, and northeastern Middle America (Fig. 5.1a).

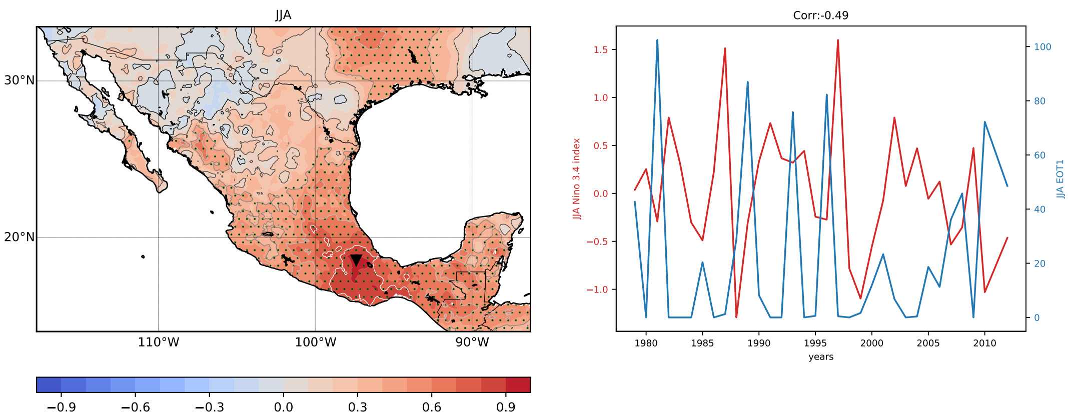

(a) (b)

Figure 5.1: a) Correlation of JJA EOT1 base point with the JJA rainfall at each point of the domain; the EOT base point is marked with a black inverted triangle (stippling indicates correlations that are significant at the 5% level). (b) Seasonal time-series of JJA EOT1 rainfall (blue line) and the JJA Niño 3.4 (red line), with a correlation coefficient of -0.49 for the period 1979-2011.

JJA EOT1 is anticorrelated with Niño 3.4 ($r = -0.49$, Fig. 5.1b). This EOT is also anticorrelated with the previous MAM SST anomalies and with simultaneous JJA SST anomalies over the East Pacific, which together resemble a developing canonical La Niña (Fig. 5.2). JJA EOT1 is also correlated with positive SST anomalies in the Caribbean Sea and the equatorial Atlantic, which resemble some features of the Atlantic warming response to the previous year's El Niño and the positive phase of the AMM (Fig. 5.2b).

JJA EOT1 has a positive correlation with SST AMM index with a correlation coefficient of 0.23.

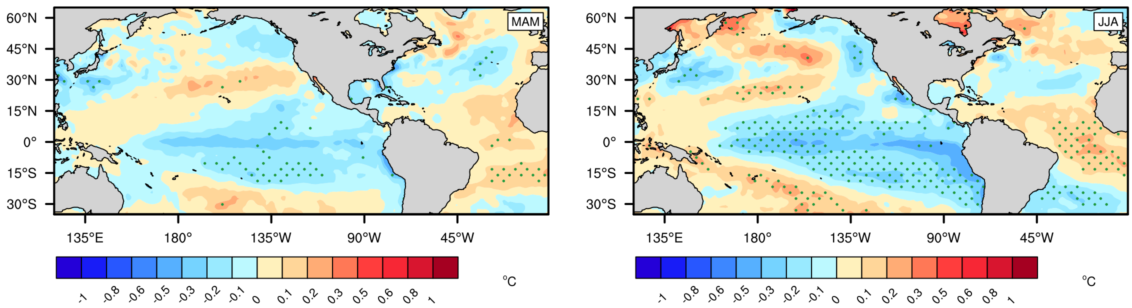

(a) (b)

Figure 5.2: Regression coefficient of (a) previous MAM and (b) simultaneous JJA SSTs, onto the normalised JJA EOT1. Shading shows the regression slopes in $°C$ per 5° spherical cap per standard deviation of seasonal rainfall (mm). Stippling indicates correlations that are significant at the 10% level.

Regression analysis shows that JJA EOT1 is significantly correlated with positive anomalies of TC track densities in the eastern development region of the East Pacific, the Gulf of Mexico, and the Caribbean, whereas it is negatively correlated with TC track densities in the western development region of the East Pacific (Fig. 5.3a). JJA EOT1 is also significantly correlated with positive anomalies of TC genesis density in the Gulf of Tehuantepec, the Gulf of Mexico, and with a fraction of the Caribbean Sea close to the coast of Guatemala and Belize, while it is negatively correlated with TC genesis density in the Gulf of Papagayo (Fig. 5.3b). These shifts in the ENP are similar to those associated with ENSO.

Regression analysis shows anomalous VIMF convergence in the IAS significantly correlated with JJA EOT1 (Fig. 5.4a). This can be explained by the relationship between La Niña and an anomalous northward displacement of the East Pacific ITCZ, which is accompanied by anomalous VIMF convergence in the East Pacific and the Caribbean Sea. These results suggest the anomalous ITCZ as a potential trigger of convection (Fig. 5.4a), favouring TC genesis in the IAS during JJA EOT1 (Fig. 5.3b).

Figure 5.4a shows regressed VIMF anomalies that resemble the path followed by the steering flow anomalies during JJA EOT1 (Fig. 5.4b). The anomalous easterly moisture flux from the East Pacific reaches the Caribbean and the tropical Atlantic, while a secondary branch of additional moisture flux follows a regional cyclonic circulation,

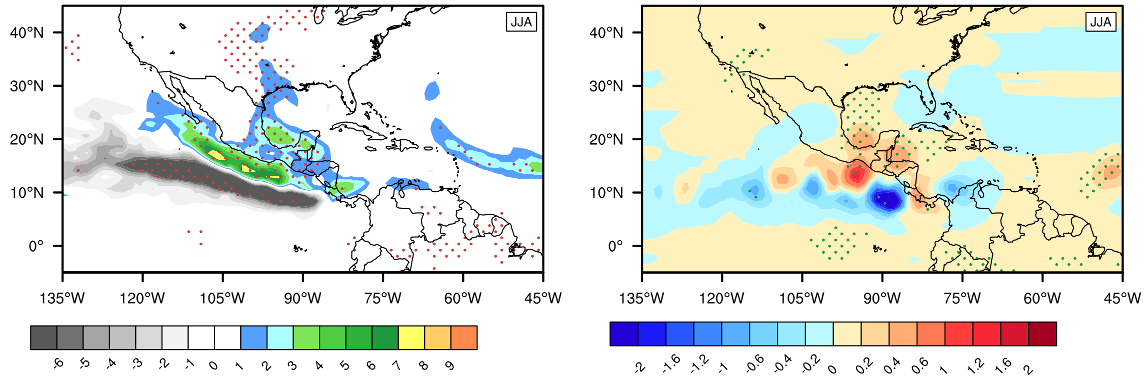

(a) (b)

Figure 5.3: (a) Regression coefficient of TC track density scaled to number density per unit area ($\sim 10^6\ km^2$) per season (JJA), onto the normalised JJA EOT1, per 5° spherical cap per standard deviation of seasonal rainfall (mm). (b) Regressed TC genesis density per unit area ($\sim 10^6\ km^2$) per season (JJA), onto the normalised JJA EOT1, per 5° spherical cap per standard deviation of seasonal rainfall (mm). Stippling indicates correlations that are significant at the 10% level.

which extends towards the Gulf of Mexico and the Gulf coastal Plain (Fig. 5.4a).

There is a significant correlation between JJA EOT1 and anomalous cyclonic steering flow over the eastern Pacific and southern/central Middle America (Fig. 5.4b), which opposes the climatological steering flow and so slows it (Fig. 5.4d). On the other hand, in the Gulf of Mexico, the northeast flank of the aforementioned cyclonic circulation converges with an anomalous anticyclonic circulation in northeastern Middle America, which together reinforce the climatological steering flow. Thus, the steering flow anomalies favour TC landfalls along the western Middle American coasts and in the Gulf coastal plain. These anomalous circulations are part of the enhanced Walker circulation typical of La Niña events, with a downward branch over the western side of the anomalously cold East Pacific. The zonally enhanced Walker circulation is coupled with a secondary reinforced zonal circulation over the IAS, which include anomalous westerlies in the East Pacific.

JJA EOT1 is anticorrelated with the CLLJ index ($r = -0.46$). Westerly wind anomalies prevailing in the Caribbean during La Niña reduce vertical wind shear, favouring conditions for TC activity in the western side of the Caribbean Sea (Fig. 5.4c). These results agree with other studies that have found that the combined effect of La Niña and positive AMM increase North Atlantic TC activity (e.g., Patricola et al., 2014; Lim et al., 2016).

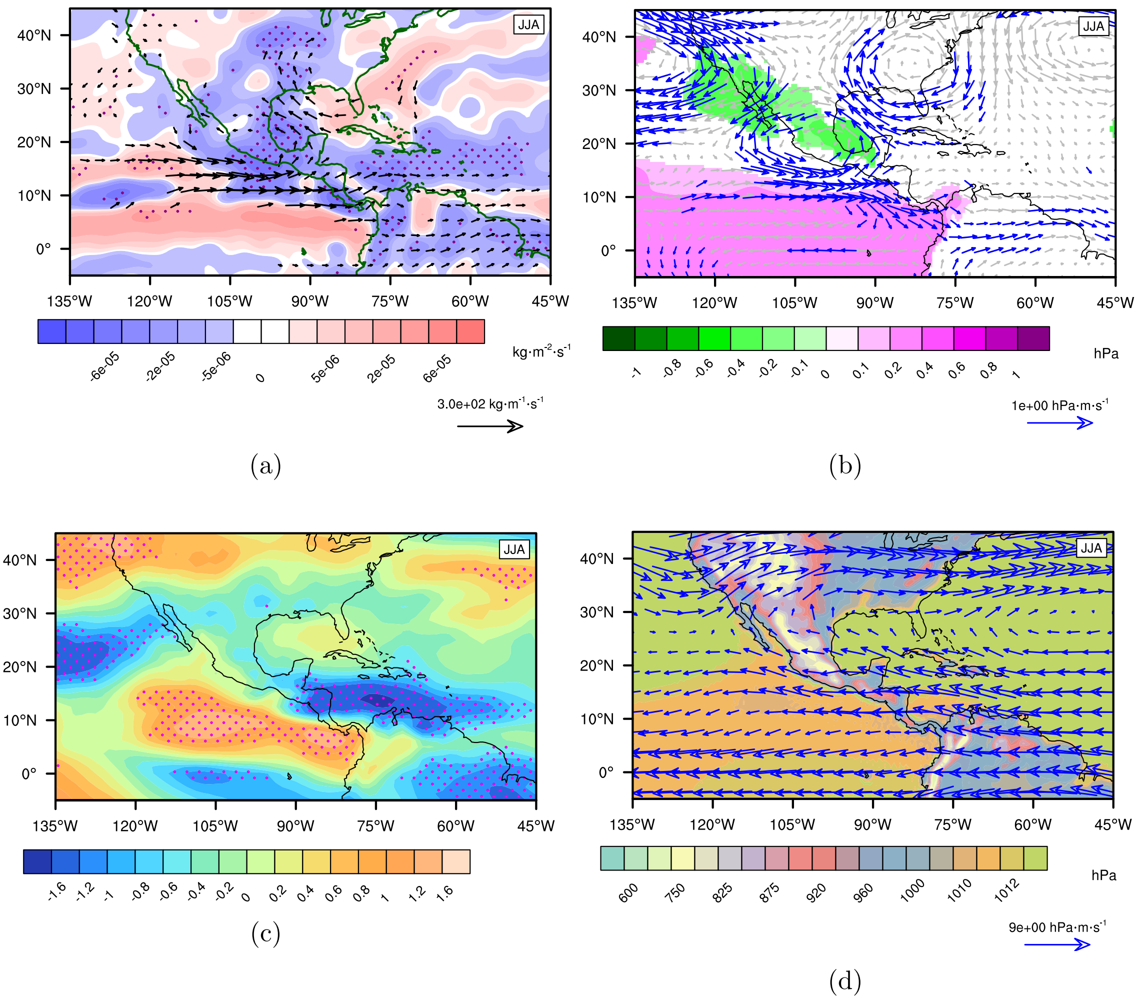

Figure 5.4: (a) Regression coefficient of JJA VIMF (arrows, $kg{\cdot}m^{-1}{\cdot}s^{-1}$) and VIMF divergence (shaded, $kg{\cdot}m^{-2}{\cdot}s^{-1}$), onto the normalised JJA EOT1 per 5° spherical cap per standard deviation of seasonal rainfall (mm); black arrows and stippling indicate VIMF and VIMF divergence significant at the 10% level, respectively. (b) Regressed JJA surface pressure (shaded, hPa) and steering flow (arrows, $hPa{\cdot}m{\cdot}s^{-1}$) onto the normalised JJA EOT1, per 5° spherical cap per standard deviation of seasonal rainfall (mm); shading and blue arrows indicate surface pressure and steering flow significant at the 10% level, respectively. (c) Regressed vertical wind shear ($m{\cdot}s^{-1}$) onto the normalised JJA EOT1, per 5° spherical cap per standard deviation of seasonal rainfall (mm); stippling indicates significance at the 10% level. (d) Climatology (1979-2011) of JJA surface pressure (shaded, hPa) and steering flow (arrows, $hPa{\cdot}m{\cdot}s^{-1}$).

5.3.1.2 JJA EOT2

Located in southern Middle America, JJA EOT2 explains 10.2% of the variance of the area-averaged TC-related rainfall for the domain of analysis (Fig. 5.5a). This EOT is positively correlated with the southernmost portion of Middle America and with a large area of northwestern Middle America. JJA EOT2 is negatively correlated with central Middle America.

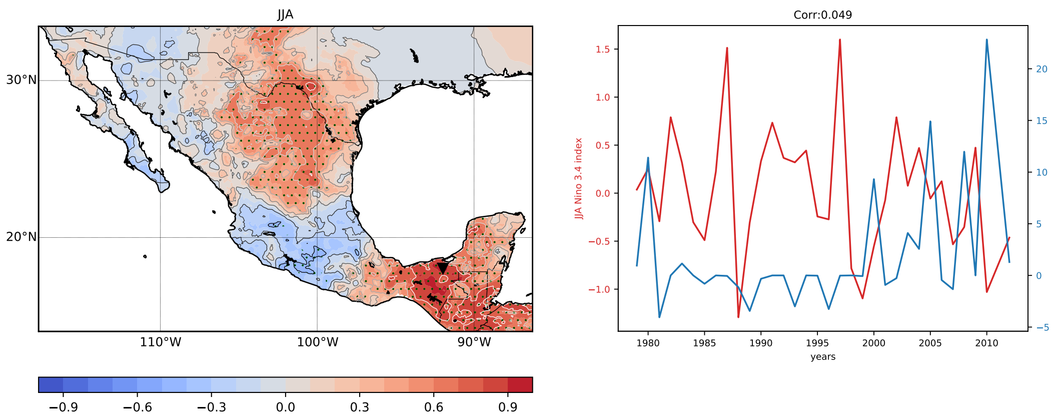

(a) (b)

Figure 5.5: (a) Correlation of JJA EOT2 base point with the JJA rainfall at each point of the domain; the EOT base point is marked with a black inverted triangle (stippling indicates correlations that are significant at the 5% level). (b) Seasonal time-series of JJA EOT2 rainfall (blue line) and the JJA Niño 3.4 (red line), with correlation coefficient 0.049 for the period 1979-2011.

Regressed TC track densities show a significant positive correlation with JJA EOT2, mainly in the Yucatan Peninsula, the southernmost Mexico, Central America, and the western development region of the East Pacific (Fig. 5.6a). TC genesis density shows positive correlations with two active cyclogenesis areas of the North Atlantic basin, one located along western coast of Africa and the other in the western Caribbean Sea (Fig. 5.6b).

Regressed wind shear shows significant large negative anomalies in the Caribbean Sea and the northeastern Mexico (Fig. 5.6c), which favour cyclogenesis and promotes TCs tracking farther inland during JJA EOT2, respectively.

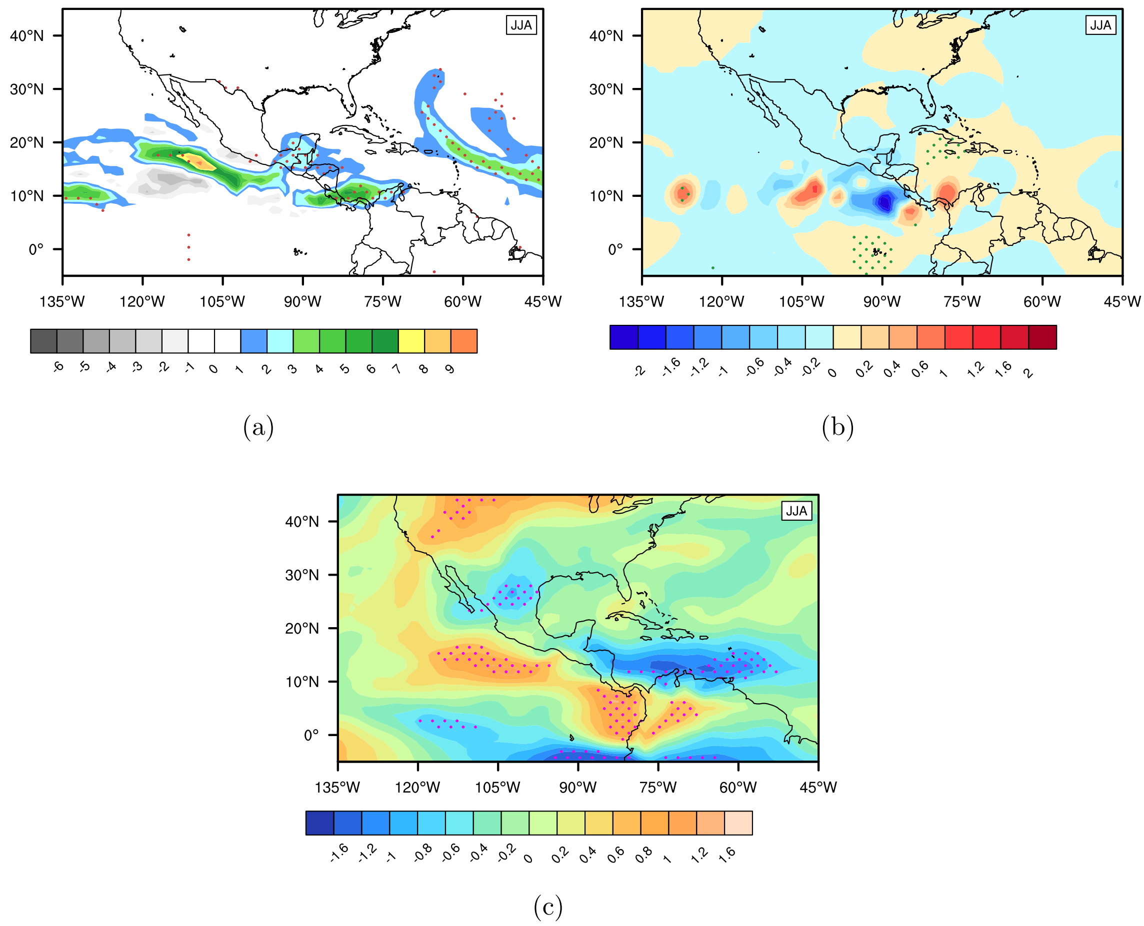

Figure 5.6: (a) Regression coefficient of TC track density scaled to number density per unit area ($\sim 10^6\ km^2$) per season (JJA), onto the normalised JJA EOT2, per 5° spherical cap per standard deviation of seasonal rainfall (mm). (b) Regression coefficient of TC genesis density per unit area ($\sim 10^6\ km^2$) per season (JJA), onto the normalised JJA EOT2, per 5° spherical cap per standard deviation of seasonal rainfall (mm). (c) Regression coefficient of vertical wind shear ($m \cdot s^{-1}$) onto the normalised JJA EOT2, per 5° spherical cap per standard deviation of seasonal rainfall (mm). Stippling indicates correlations that are significant at the 10% level.

The strongest correlation between JJA EOT2 and oceanic modes of variability comes from anomalously warm SSTs over the Tropical Atlantic Ocean. Regression maps of SSTs show positive anomalies that extend throughout the MDR, which resemble the warm phase of the AMM and the AMO. JJA EOT2 time series are correlated with the simultaneous seasonal SST AMM ($r = 0.19$) and the AMO Index ($r = 0.23$), though there are not statistically significant. JJA EOT2 is also correlated with SSTs over the central Pacific Ocean with features that resemble a weakened Pacific La Niña (Fig. 5.7b).

Regressions of VIMF show significant convergence anomalies in southern Middle America (Fig. 5.8a). VIMF convergence anomalies are also strong in a region of the East Pacific around $10° - 15°N.$, which is an anomalous positive cyclogenesis area despite the significant positive anomalies of wind shear that prevail during JJA EOT2.

Regression analysis shows that enhanced JJA EOT2 is associated with anomalously negative surface pressure in the tropical Atlantic and the Gulf of Mexico, and with anomalous cyclonic steering flow over a large area in the tropical Atlantic (Fig. 5.8b), which indicate a considerable weakening and an eastward displacement of the NASH. These results agree with Lim et al. (2016), who found that simultaneous episodes of neutral or weak ENSO and a weakened NASH are linked to enhanced Atlantic TC genesis (Fig. 5.6b).

Other studies have found that anomalies in the strength and/or location of the NASH can determine Atlantic TCs variability and TC-associated rainfall. Negative anomalies of surface pressure in central Atlantic and an anomalously extended warm tropical Atlantic are closely linked with TC landfall episodes in the North American continent, since a weakened NASH favours Atlantic TCs recurving farther west (Colbert and Soden, 2012). Bregy et al. (2020) found that TC-related precipitation in the most eastern U.S. tends to be suppressed when western flank of the NASH is displaced westwards.

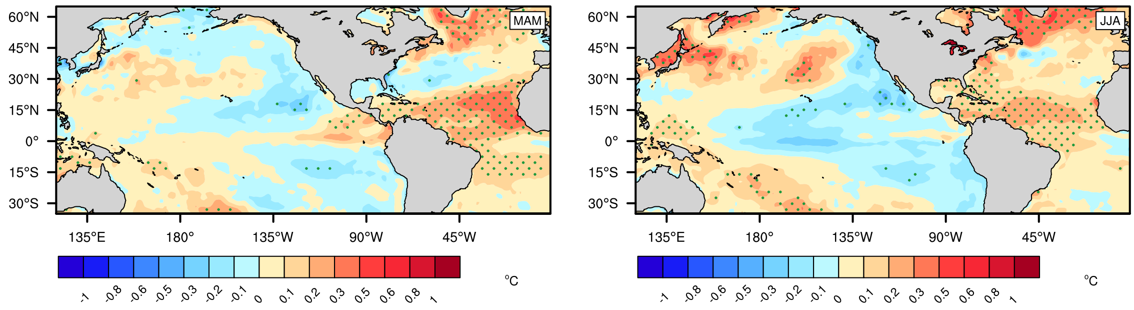

(a) (b)

Figure 5.7: Regressed (a) previous MAM and (b) simultaneous JJA SSTs, onto the normalised JJA EOT1. Shading shows the regression slopes in $^{\circ}C$ per 5° spherical cap per standard deviation of seasonal rainfall (mm). Stippling indicates correlations that are significant at the 10% level.

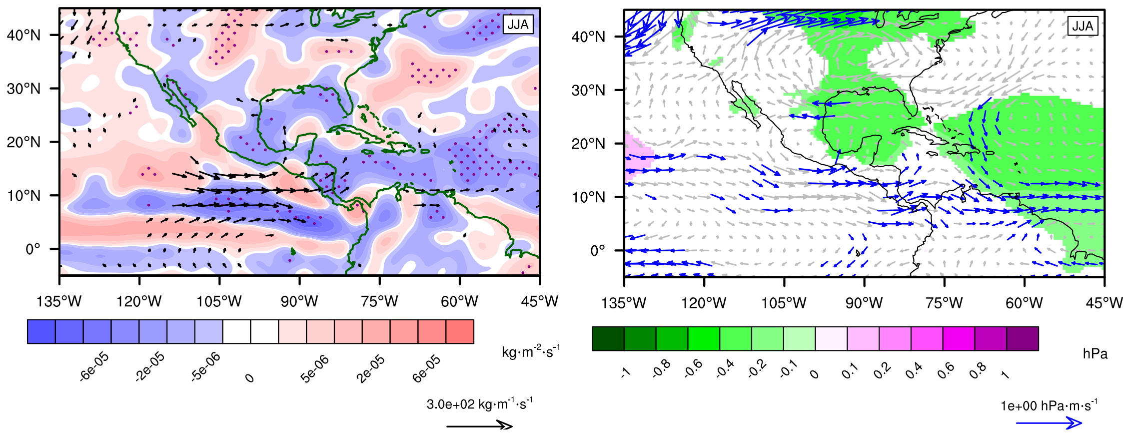

(a) (b)

Figure 5.8: (a) Regression coefficient of JJA VIMF (arrows, $kg{\cdot}m^{-1}{\cdot}s^{-1}$) and VIMF divergence (shaded, $kg{\cdot}m^{-2}{\cdot}s^{-1}$), onto the normalised JJA EOT2 per 5° spherical cap per standard deviation of seasonal rainfall (mm); black arrows and stippling indicate VIMF and VIMF divergence significant at the 10% level, respectively. (b) Regression coefficient of JJA surface pressure (shaded, hPa) and steering flow (arrows, $hPa{\cdot}m{\cdot}s^{-1}$) onto the normalised JJA EOT2, per 5° spherical cap per standard deviation of seasonal rainfall (mm); shading and blue arrows indicate surface pressure and steering flow significant at the 10% level, respectively.

5.3.1.3 JJA EOT3

JJA EOT3 represents 4.5% of the temporal variance of the area-averaged rainfall associated with TCs; it is correlated with a well-defined area on the west coast of Middle America (Fig. 5.9a).

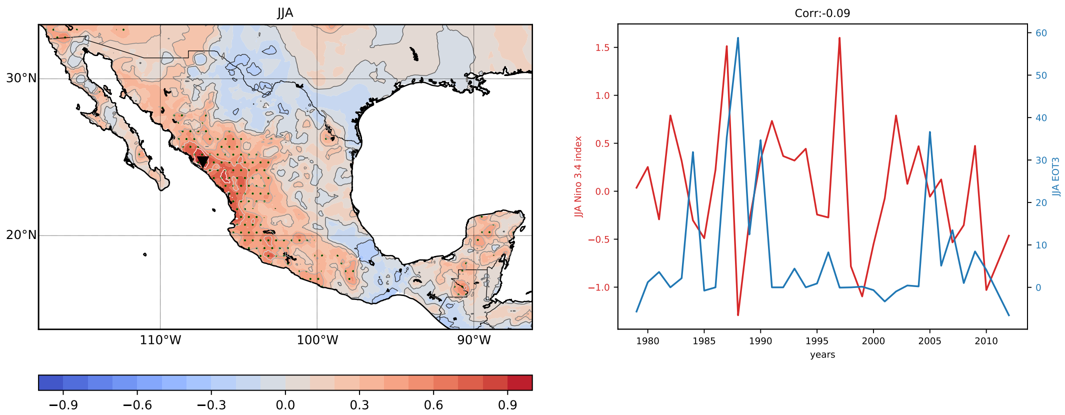

(a) (b)

Figure 5.9: (a) Correlation of JJA EOT3 base point with the JJA rainfall at each point of the domain; the EOT base point is marked with a black inverted triangle (stippling indicates correlations that are significant at the 5% level). (b) Seasonal time-series of JJA EOT3 rainfall (blue line) and the JJA Niño 3.4 (red line), with a correlation coefficient -0.09 for the period 1979-2011.

JJA EOT3 is positively correlated with anomalies of TC genesis density in the East Pacific Ocean, close to the Gulf of Tehuantepec (Fig. 5.10b). This EOT is also positively correlated with anomalies of TC track density located along the North eastern Pacific, next to Middle America's west coast (Fig. 5.10a). During periods of enhanced JJA EOT3, East Pacific TC tracks show anomalous northeastwards displacement, which allows TCs to leave more rainfall in western Middle America through their passage.

Regressed steering flow shows significant westerly anomalies in the Gulf of Papagayo and Middle America's west coast, associated with enhanced JJA EOT3 (Fig. 5.11b), which oppose the climatological steering flow (Fig. 5.4c) and favour TCs tracking closer to Middle America. Anomalous VIMF convergence in the East Pacific enhances TC genesis over the Gulf of Tehuantepec (Fig. 5.11a).

JJA EOT3 is positively correlated with wind shear anomalies in a region southwards to the eastern East Pacific development region (Fig. 5.10c).

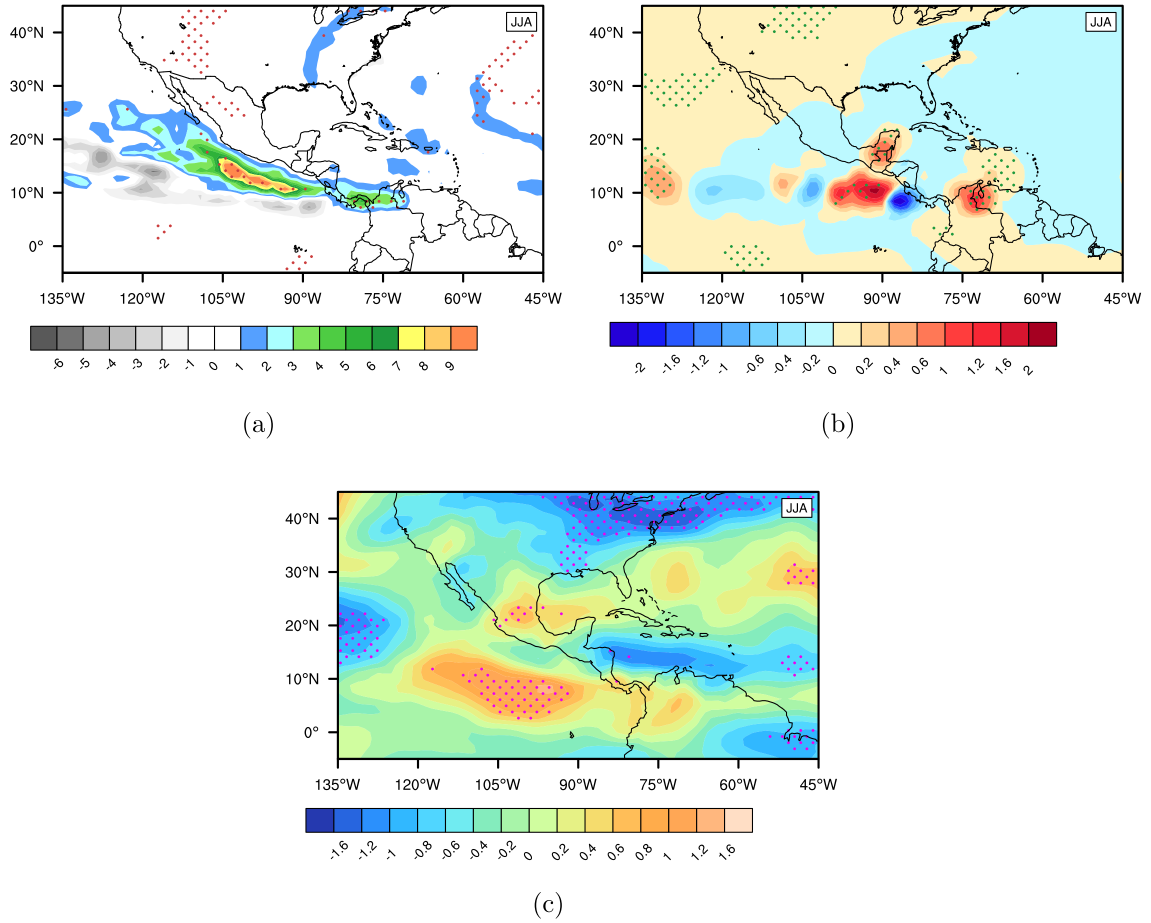

Figure 5.10: (a) Regression coefficient of TC track density scaled to number density per unit area ($\sim 10^6 km^2$) per season (JJA), onto the normalised JJA EOT3, per 5° spherical cap per standard deviation of seasonal rainfall (mm). (b) Regression coefficient of TC genesis density per unit area ($\sim 10^6 km^2$) per season (JJA), onto the normalised JJA EOT3, per 5° spherical cap per standard deviation of seasonal rainfall (mm). Stippling indicates correlations that are significant at the 10% level. (c) Regression coefficient of vertical wind shear ($m{\cdot}s^{-1}$) onto the normalised JJA EOT3, per 5° spherical cap per standard deviation of seasonal rainfall (mm).

None of the large-scale phenomena considered show a significant correlation with JJA EOT3. However, the regression analyses show a strong relationship between JJA EOT3 and TC genesis in the Gulf of Tehuantepec.

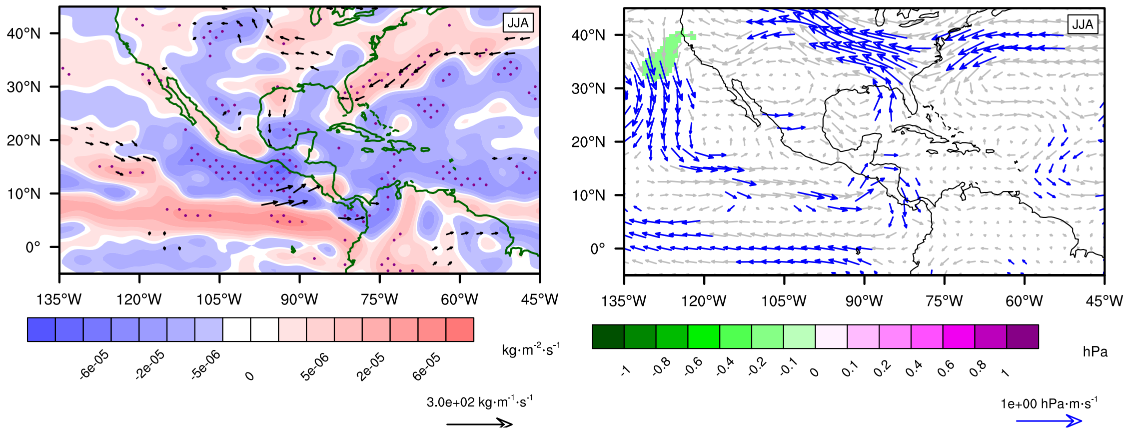

(a) (b)

Figure 5.11: (a) Regression coefficient of JJA VIMF (arrows, $kg{\cdot}m^{-1}{\cdot}s^{-1}$) and VIMF divergence (shaded, $kg{\cdot}m^{-2}{\cdot}s^{-1}$), onto the normalised JJA EOT3, per 5° spherical cap per standard deviation of seasonal rainfall (mm); black arrows and stippling indicate VIMF and VIMF divergence significant at the 10% level, respectively. (b) Regression coefficient of JJA surface pressure (shaded, hPa) and steering flow (arrows, $hPa{\cdot}m{\cdot}s^{-1}$) onto the normalised JJA EOT3, per 5° spherical cap per standard deviation of seasonal rainfall (mm); shading and blue arrows indicate surface pressure and steering flow significant at the 10% level, respectively.

5.3.2 Autumn

5.3.2.1 SON EOT1

SON EOT1, located in the Yucatan Peninsula, explains 83.75% of the variance of the area-averaged TC-related rainfall over the domain of study (Fig. 5.12a). This EOT represents variability in TC rainfall over central Middle America and a large portion of the Gulf Coastal Plain.

This EOT is negatively correlated with Niño 3.4 ($r = -0.31$, Fig. 5.12b). A regression analysis of previous JJA and simultaneous SON SSTs onto SON EOT1 shows significant negative anomalies extending along the central and eastern Pacific Ocean for enhanced SON EOT1, indicating La Niña (Figs. 5.13a and 5.13b, respectively).

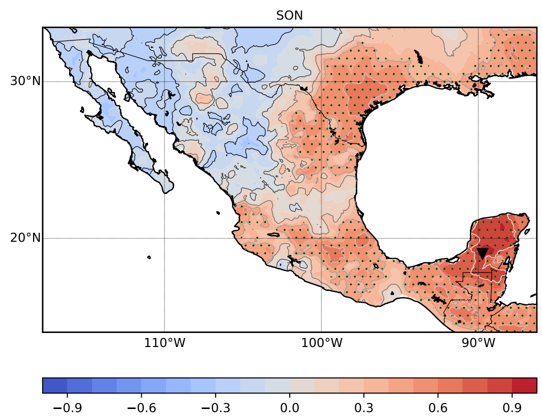

(a)

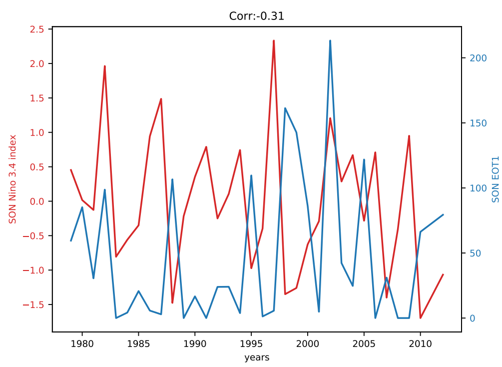

(b)

Figure 5.12: (a) Correlation of SON EOT1 base point with the SON rainfall at each point of the domain; the EOT base point is marked with a black inverted triangle (stippling indicates correlations that are significant at the 5% level). (b) Seasonal time-series of SON EOT1 rainfall (blue line) and the SON Niño 3.4 (red line), with a correlation coefficient of -0.31 for the period 1979-2011.

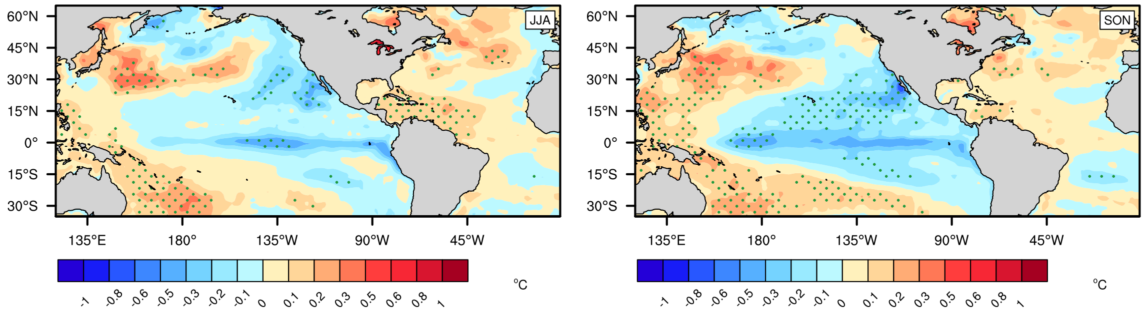

(a) (b)

Figure 5.13: Regression coefficient of (a) previous JJA and (b) simultaneous SON SSTs, onto the normalised SON EOT1. Shading shows the regression slopes in $^{\circ}C$ per 5° spherical cap per standard deviation of seasonal rainfall (mm). Stippling indicates correlations that are significant at the 10% level.

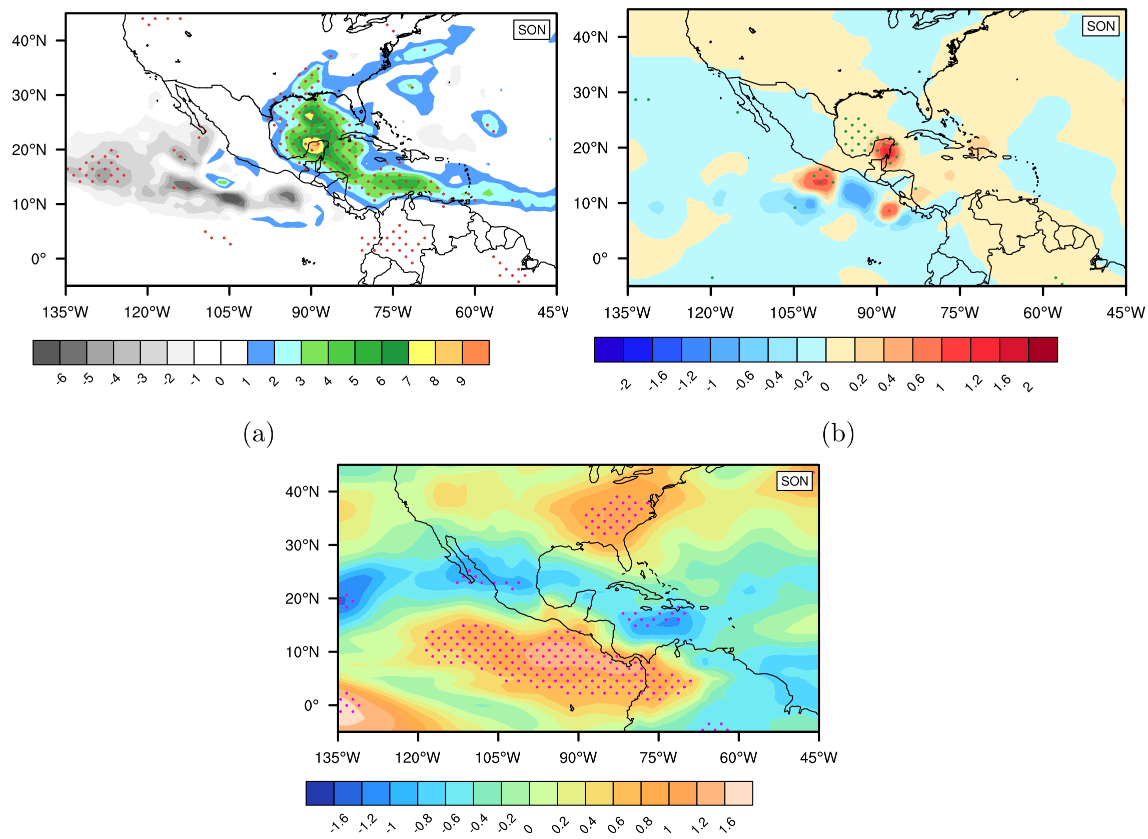

(a) (b)

(c)

Figure 5.14: (a) Regression coefficient of TC track density scaled to number density per unit area ($\sim 10^6 km^2$) per season (SON), onto the normalised SON EOT1, per 5° spherical cap per standard deviation of seasonal rainfall (mm). (b) Regression coefficient of TC genesis density per unit area ($\sim 10^6 km^2$) per season (SON), onto the normalised SON EOT1, per 5° spherical cap per standard deviation of seasonal rainfall (mm). Stippling indicates correlations that are significant at the 10% level. (c) Regression coefficient of vertical wind shear ($m{\cdot}s^{-1}$) onto the normalised SON EOT1, per 5° spherical cap per standard deviation of seasonal rainfall (mm).

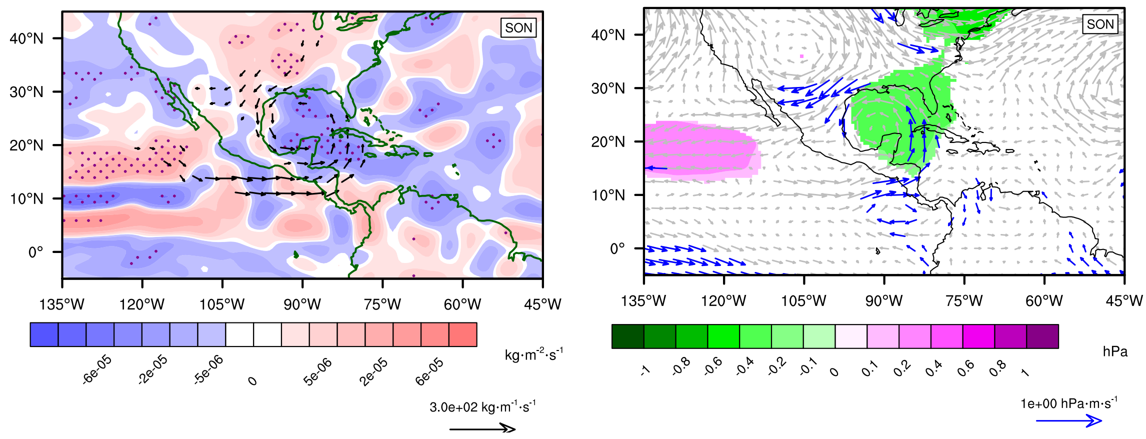

(a) (b)

Figure 5.15: (a) Regression coefficient of SON VIMF (arrows, $kg{\cdot}m^{-1}{\cdot}s^{-1}$) and VIMF divergence (shaded, $kg{\cdot}m^{-2}{\cdot}s^{-1}$), onto the normalised SON EOT1, per 5° spherical cap per standard deviation of seasonal rainfall (mm); black arrows and stippling indicate VIMF and VIMF divergence significant at the 10% level, respectively. (b) Regression coefficient of SON surface pressure (shaded, hPa) and steering flow (arrows, $hPa{\cdot}m{\cdot}s^{-1}$) onto the normalised SON EOT1, per 5° spherical cap per standard deviation of seasonal rainfall (mm); shading and blue arrows indicate surface pressure and steering flow significant at the 10% level, respectively.

Reduced wind shear prevails over the Caribbean Sea, the Gulf of Mexico, and the North of continental Mexico (Fig. 5.14c). The anomalous wind shear in the Caribbean Sea is strongly linked with La Niña events.

High SON EOT1 is associated with two areas of enhanced cyclogenesis located in the west Caribbean and the Atlantic MDR (Fig. 5.14b). Regression analysis shows positive SST anomalies over a large portion of the Caribbean Sea (Fig. 5.14b), which is an essential environmental factor linked to the increase of TC activity in the Caribbean Sea and the Gulf of Mexico during SON EOT1.

SON EOT1 is significantly correlated with anomalous VIMF convergence in the Caribbean Sea, near the eastern Middle American coasts, Cuba, and the Gulf of Mexico (Fig. 5.15a). During positive SON EOT1, anomalous moisture from the East Pacific is transported to the Caribbean Sea and the Gulf of Mexico following an anomalous cyclonic circulation (Fig. 5.15a), which is consistent with cyclonic anomalies of steering flow in over the Gulf of Mexico, which opposes the climatological flow (Fig. 5.15b). Simultaneously, high SON EOT1 is associated with decreased surface pressure over the Gulf of Mexico and the eastern Middle America (Fig. 5.15b).

5.3.2.2 SON EOT2

Located in Texas, SON EOT2 explains 3.86% of the variance of the area-averaged TC-related rainfall in the domain of study (Fig. 5.16a). This EOT is positively correlated with TC-related rainfall over northeastern Middle America, and a very localised area of the western coast of Middle America. SON EOT2 is also anticorrelated with the NAO index ($r = -0.28$, Fig. 5.16b).

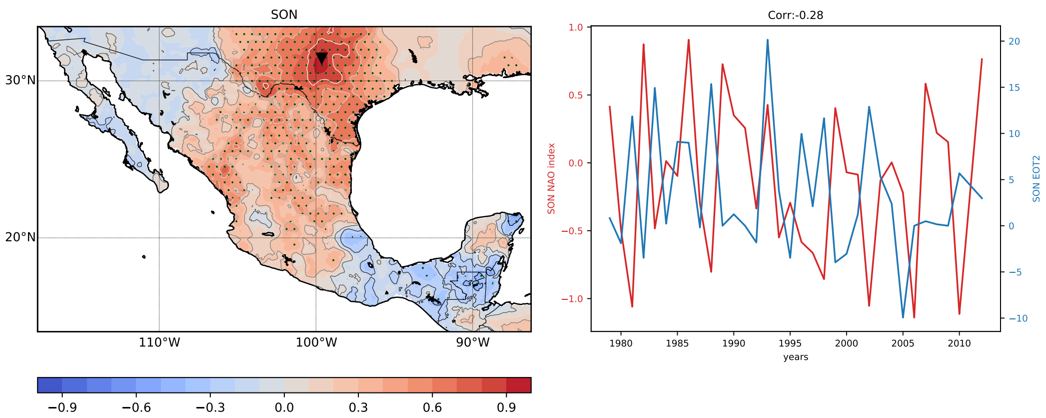

(a) (b)

Figure 5.16: (a) Correlation of SON EOT2 base point with the SON rainfall at each point of the domain; the EOT base point is marked with a black inverted triangle (stippling indicates correlations that are significant at the 5% level). (b) Seasonal time-series of SON EOT2 rainfall (blue line) and the SON NAO index (red line), with a correlation coefficient of -0.28 for the period 1979-2011.

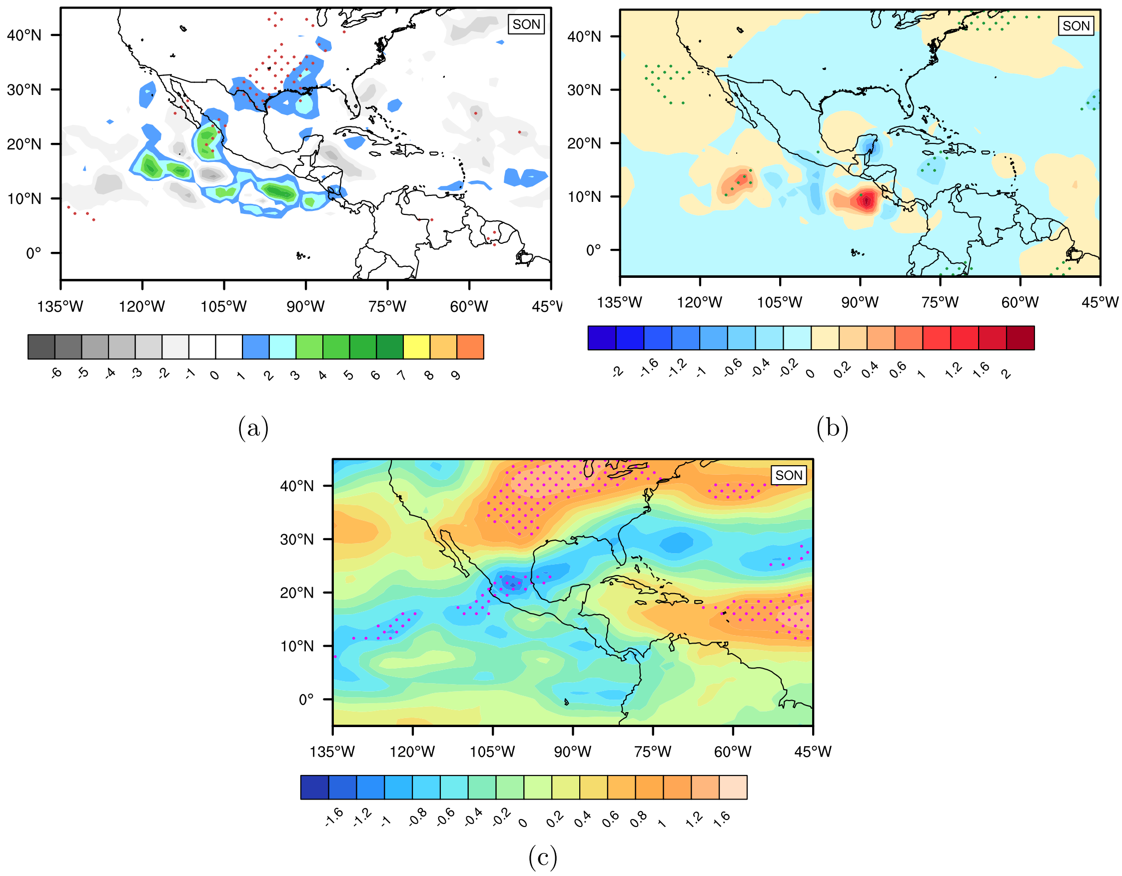

Figure 5.17: (a) Regression coefficient of TC track density scaled to number density per unit area ($\sim 10^6 km^2$) per season (SON), onto the normalised SON EOT2, per 5° spherical cap per standard deviation of seasonal rainfall (mm). (b) Regression coefficient of TC genesis density per unit area ($\sim 10^6 km^2$) per season (SON), onto the normalised SON EOT2, per 5° spherical cap per standard deviation of seasonal rainfall (mm). Stippling indicates correlations that are significant at the 10% level. (c) Regression coefficient of vertical wind shear ($m{\cdot}s^{-1}$) onto the normalised SON EOT2, per 5° spherical cap per standard deviation of seasonal rainfall (mm).

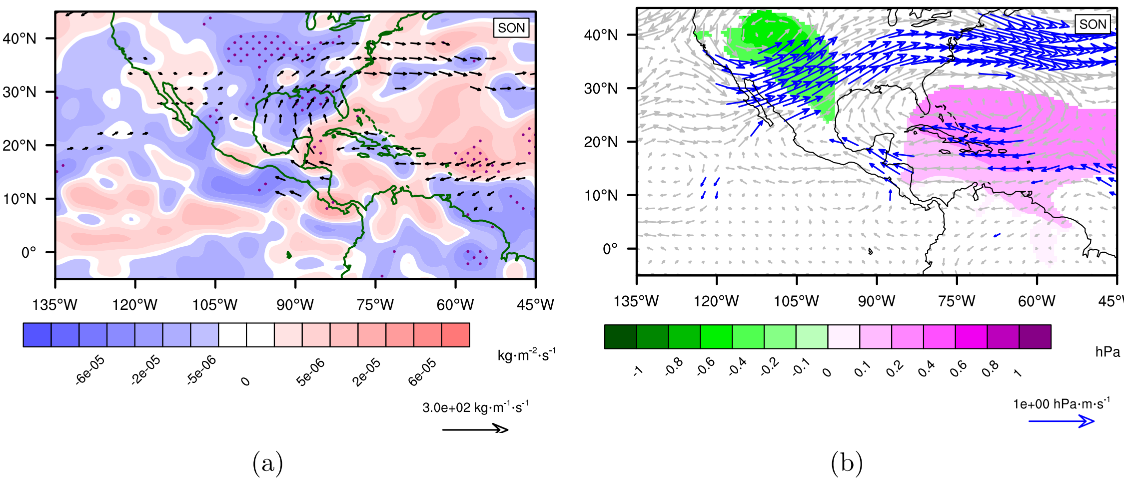

Figure 5.18: (a) Regression coefficient of SON VIMF (arrows, $kg{\cdot}m^{-1}{\cdot}s^{-1}$) and VIMF divergence (shaded, $kg{\cdot}m^{-2}{\cdot}s^{-1}$), onto the normalised SON EOT2, per 5° spherical cap per standard deviation of seasonal rainfall (mm); black arrows and stippling indicate VIMF and VIMF divergence significant at the 10% level, respectively. (b) Regression coefficient of SON surface pressure (shaded, hPa) and steering flow (arrows, $hPa{\cdot}m{\cdot}s^{-1}$) onto the normalised SON EOT2, per 5° spherical cap per standard deviation of seasonal rainfall (mm); shading and blue arrows indicate surface pressure and steering flow significant at the 10% level, respectively.

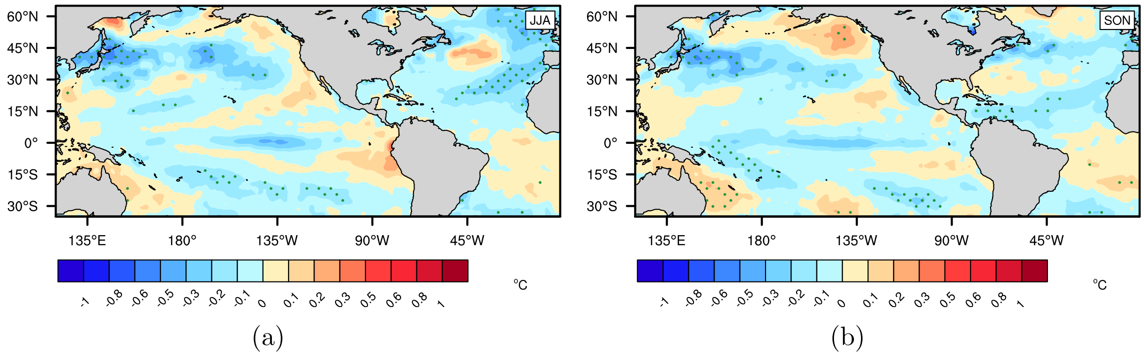

Figure 5.19: Regression coefficient of (a) previous JJA and (b) simultaneous SON SSTs, onto the normalised SON EOT2. Shading shows the regression slopes in $°C$ per 5° spherical cap per standard deviation of seasonal rainfall (mm). Stippling indicates correlations that are significant at the 10% level.

Figure 5.18b shows negative anomalies of surface pressure in the high latitudes of the North Atlantic, and positive anomalies over the central North Atlantic and the Caribbean. Regressions of steering flow show that enhanced SON EOT2 is associated with an enhanced anticyclonic circulation over the tropical North Atlantic, which is characteristic of an enhanced NASH. The strengthening of the NASH steers Atlantic TCs into an enhanced easterly flow, which corresponds to the equatorward edge of the NASH (Fig. 5.18b). Colbert and Soden (2012) found that when the NASH is farther west and the North Atlantic surface pressure is stronger, TCs tend to either recurve before making landfall or to take a straight-line track, the latter of which favour landfalls in northeastern Middle America.

Regression analysis shows reduced vertical wind shear that prevails in the Caribbean during positive SON EOT2 (Fig. 5.17c). Regressed SSTs fields onto SON EOT2 show cold anomalies in the tropical Atlantic, which resemble the negative phase of the AMM (Fig. 5.19b); SON EOT2 is correlated with the AMM index ($r = -0.20$). These conditions inhibit TC genesis in the Caribbean and Atlantic (Fig. 5.17b). These results agree with Smirnov and Vimont (2011), who found that the negative phase of the AMM, associated with negative anomalies of SSTs and positive anomalies of wind shear in the eastern tropical Atlantic, decrease TC genesis in the Atlantic MDR.

5.3.2.3 SON EOT3

Located in Guatemala, SON EOT3 explains 3.7% of the variance of the area-averaged TC-related rainfall in Middle America (Fig. 5.20a). SON EOT3 is positively correlated with a very localised area in southern Middle America; it is anticorrelated with the north-eastern Middle America and the Yucatan Peninsula.

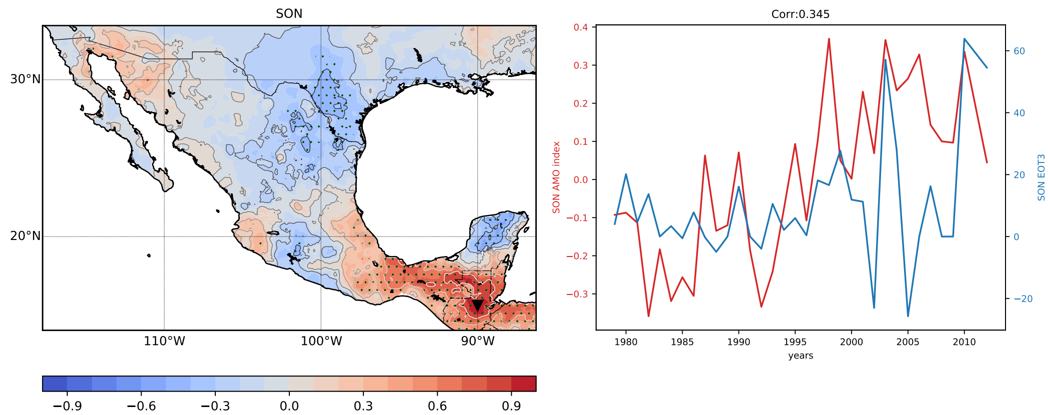

(a) (b)

Figure 5.20: (a) Correlation of SON EOT3 base point with the SON rainfall at each point of the domain; the EOT base point is marked with a black inverted triangle (stippling indicates correlations that are significant at the 5% level). (b) Seasonal time-series of SON EOT3 rainfall (blue line) and the SON AMO (red line), with a correlation coefficient of 0.34 for the period 1979-2011.

Regression analysis shows significant negative anomalies of TC track densities extended along the western development region of the East Pacific, while there are significantly more TC tracks in the Gulf of Tehuantepec (Fig. 5.21a). This EOT is strongly linked with negative anomalies of TCs genesis density in the Gulf of Papagayo (Fig. 5.21b).

Regression analyses show warmer tropical Atlantic JJA SSTs and colder central East Pacific SSTs during enhanced SON EOT3 (Fig. 5.22b). This EOT is positively correlated with the JJA AMO ($r = 0.34$, Fig. 5.20b) and AMM ($r = 0.28$) indices. Enhanced SON EOT3 is related with negative anomalies of surface pressure and anomalous cyclonic steering flow that extend along the equatorial Atlantic (Fig. 5.23b), which indicated a weakened NASH. In agreement with Colbert and Soden (2012), the weakening of the NASH favours early recurving TCs out to sea without making landfall in the U.S..

Regressed wind shear onto SON EOT3 show positive anomalies in the Caribbean Sea, which favour TC activity in the Caribbean Sea (Fig. 5.21c).

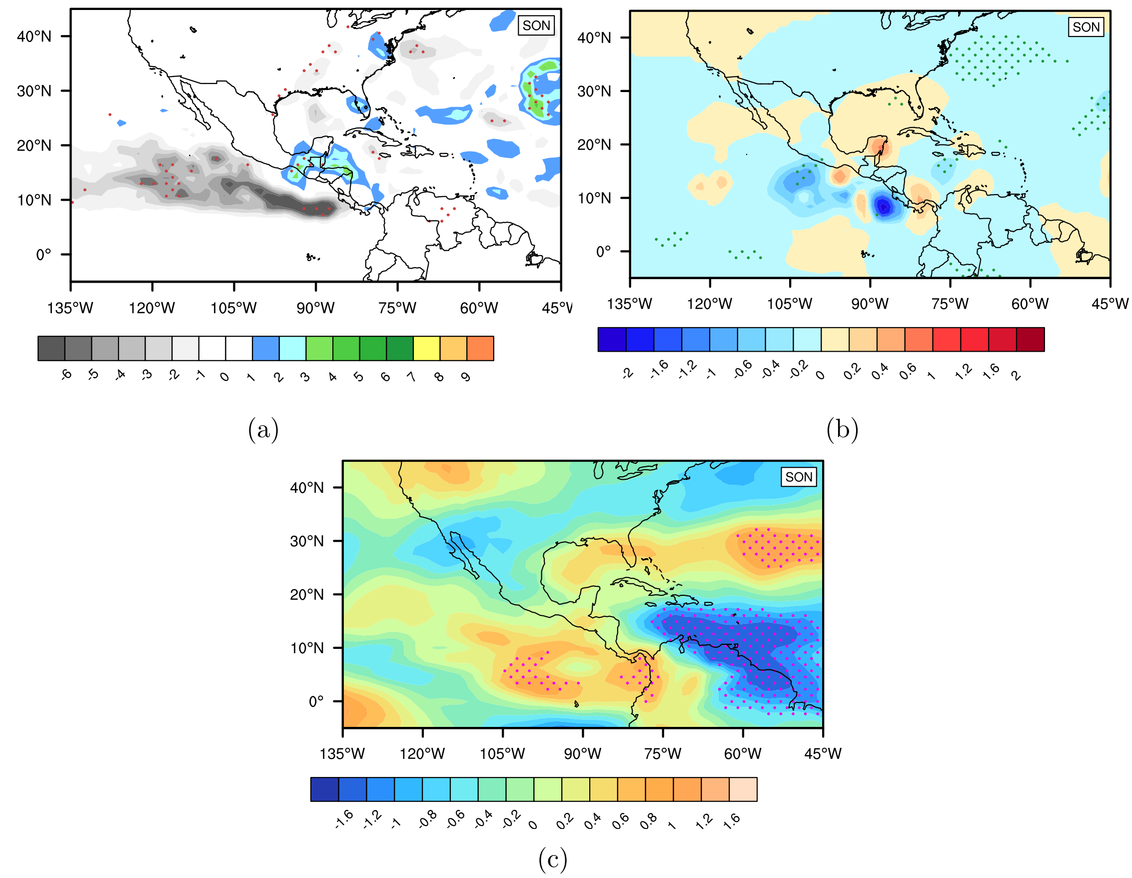

Figure 5.21: (a) Regression coefficient of TC track density scaled to number density per unit area ($\sim 10^6 km^2$) per season (SON), onto the normalised SON EOT3, per 5° spherical cap per standard deviation of seasonal rainfall (mm). (b) Regression coefficient of TC genesis density per unit area ($\sim 10^6 km^2$) per season (SON), onto the normalised SON EOT3, per 5° spherical cap per standard deviation of seasonal rainfall (mm). Stippling indicates correlations that are significant at the 10% level. (c) Regression coefficient of vertical wind shear ($m{\cdot}s^{-1}$) onto the normalised SON EOT3, per 5° spherical cap per standard deviation of seasonal rainfall (mm).

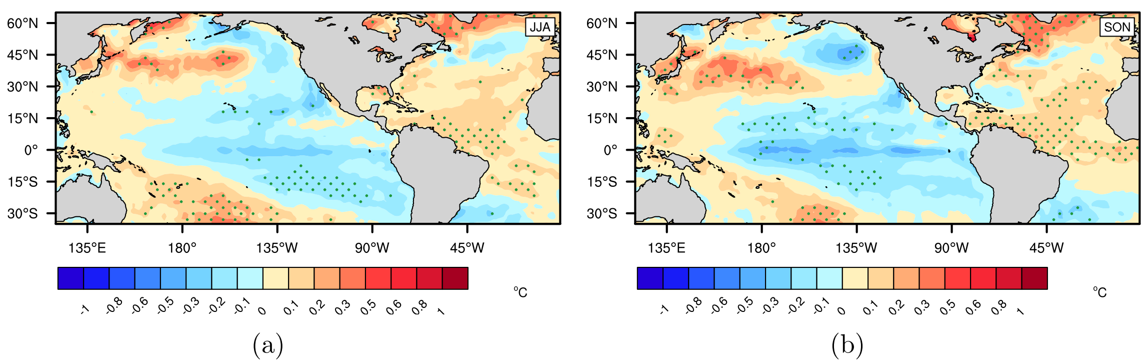

Figure 5.22: Regression coefficient of (a) previous JJA and (b) simultaneous SON SSTs, onto the normalised SON EOT3. Shading shows the regression slopes in $^{\circ}C$ per 5° spherical cap per standard deviation of seasonal rainfall (mm). Stippling indicates correlations that are significant at the 10% level.

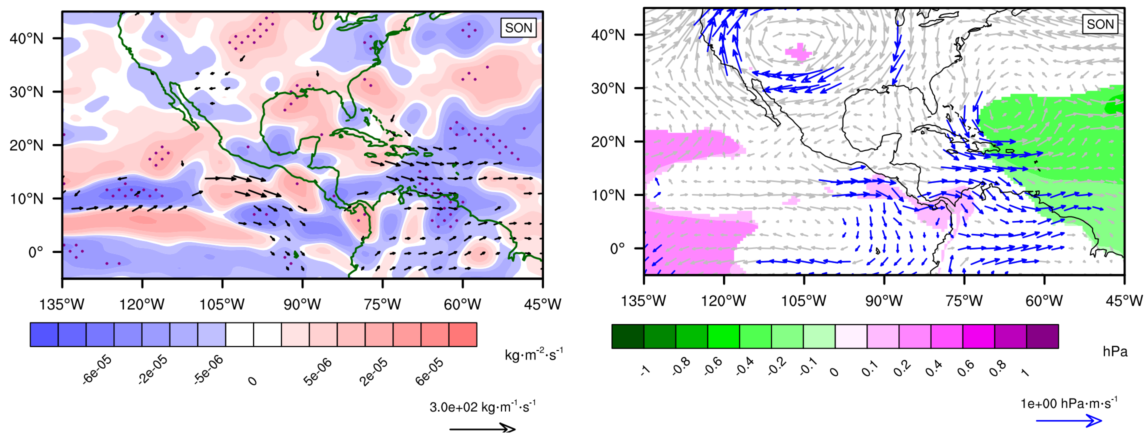

(a) (b)

Figure 5.23: (a) Regression coefficient of SON VIMF (arrows, $kg{\cdot}m^{-1}{\cdot}s^{-1}$) and VIMF divergence (shaded, $kg{\cdot}m^{-2}{\cdot}s^{-1}$), onto the normalised SON EOT3, per 5° spherical cap per standard deviation of seasonal rainfall (mm); black arrows and stippling indicate VIMF and VIMF divergence significant at the 10% level, respectively. (b) Regression coefficient of SON surface pressure (shaded, hPa) and steering flow (arrows, $hPa{\cdot}m{\cdot}s^{-1}$) onto the normalised SON EOT3, per 5° spherical cap per standard deviation of seasonal rainfall (mm); shading and blue arrows indicate surface pressure and steering flow significant at the 10% level, respectively.

5.4 Discussion

Rainfall attributed to TCs was quantified using a high-resolution daily precipitation dataset for Middle America (López-Bravo, 2015; López-Bravo et al., 2018) and TC tracks from an objective tracking method (Hodges, 1999) applied to JRA-55 reanalysis datasets. As discussed in chapter 4, this TC tracks dataset includes the pre- and post- stages of the North Atlantic and East Pacific TCs for the period 1979-2011, which offer a broader characterisation of the TC lifecycle and for the quantification of the rainfall attributed to TCs.

Coherent patterns of JJA (summer) and SON (autumn) TC-related rainfall over Middle America were found using the modified version of the EOT method, following Smith (2004). For each season, the leading EOT (EOT1) explains more than 79% of the variance of TC-related rainfall. The leading EOTs are significantly correlated with across large areas in Middle America, meaning that the region experiences a coherent interannual variability of TC rainfall.

The present analysis identifies ENSO as the most important mode of interannual variability of TC-related rainfall of Middle America for the two seasons analysed. The ENSO results are consistent with previous studies that have found that canonical La Niña increases TC activity over the North Atlantic basin (e.g., Gray, 1984; Gray and Sheaffer, 1991; Camargo et al., 2007; Kossin et al., 2010). This study suggests the enhanced Walker circulation typical of canonical La Niña plays a crucial role in the variability of the IAS TC genesis and TC tracks, which favours TC-related rainfall in central and southern Middle America. During La Niña, enhanced VIMF convergence associated with an anomalous northward shift of the ITCZ is linked to regions of active cyclogenesis in the East Pacific and Caribbean Sea (Figs. 5.3b and 5.14b). Anomalous La Niña westerly winds create reductions of vertical wind shear in the Caribbean Sea, favouring TC activity in the region (Figs. 5.4c and 5.14c).

Strong relationships between the variability of TC-related rainfall in Middle America and a secondary mode of interannual climate variability, the AMM, were found. In agreement with Smirnov and Vimont (2011), this study shows an important relationship between reduced wind shear over the subtropical North Atlantic and with the positive AMM. Both reduced wind shear and warmer SSTs have been identified as modulators of the shift in TC activity (e.g., Shapiro, 1987; Tang and Neelin, 2004), increasing the chances of cyclogenesis over the Atlantic ocean. Even more, the AMM drives variability in the strength and location of the NASH and, in consequence, influences the trajectories of the TCs in the the Caribbean Sea and the Gulf of Mexico.

During SON EOT1, the combined effect of La Niña and the positive phase of the AMM create anomalies in steering flow (Fig. 5.15) that strongly favour TC activity in the Gulf of Mexico and the Caribbean, which resemble the ones found by Maloney and Hartmann (2000b) and Aiyyer and Molinari (2008) during the active phase of the MJO, and the Chapter 3 SON EOT3 for total rainfall (Fig. 3.37a).

This study shows an important relationship between TC rainfall and anomalies of TC genesis and wind shear in the Caribbean Sea. JJA EOT1 and SON EOT1 are related with TC activity in the Caribbean Sea and the Gulf of Mexico, which is favoured by reduced vertical wind shear and warmer Atlantic SSTs (e.g., Elsner, 2003) during simultaneous developing La Niña episodes and the positive AMM. This study agrees with Camargo et al. (2007), who found that vertical wind shear plays an important role in cyclogenesis in the North Atlantic basin, being as important as thermodynamic impacts in ENSO years.

Middle America's TC-related rainfall variability is highly sensitive to anomalous TC genesis and TC tracks in the East Pacific. The Gulf of Tehuantepec and the Gulf of Papagayo are two active regions of TC genesis that are particularly correlated with TC-rainfall in Middle America. TC-related rainfall in Middle America is favoured by more TCs tracking closer to the eastern development region of the East Pacific and positive anomalies of TC genesis in the Gulf of Tehuantepec (Figs. 5.10b, 5.17b). This study shows a strong anticorrelation between anomalies of TC-related rainfall in Mexico and anomalies of TC genesis in the Gulf and Papagayo. TC genesis in the Gulf of Papagayo is positively correlated with TC tracks in the western development region of the East Pacific (Fig. 5.21a).

TC-related rainfall in the region of study is strongly correlated with changes in the location and strength of the NASH, particularly during SON, which corresponds to the second half of the TC season in the IAS. SON EOT2 are consistent with the ones found by Wang et al. (2011), which argue that a weakened NASH, as a consequence of an extended Atlantic Warm Pool (AWP, which comprises the Gulf of Mexico, the Caribbean Sea, and the western tropical North Atlantic), induces the northward and northeastward steering flow anomalies that steer TCs away from the U.S. East coast (Fig. 5.18b).

SON EOT3 has a strong correlation with simultaneous AMM ($r = 0.28$) and AMO ($r = 0.34$). This can be explained by the fact that the warm (cool) phases of the AMO are characterised by repeated large (small) AWPs (Wang et al., 2008), directly related with the AMM.

As often happens with decomposition techniques, it was not possible to link all of the EOTs analysed with a particular driver: the causes of JJA EOT3 TC-associated rainfall variability in central-western Middle America remain unclear. However, this EOT is correlated with enhanced TC genesis in the eastern development region of the East Pacific.

The TC-related rainfall in Middle America is a sparse field; for this reason, the leading EOT time-series showed no-TC rainfall in some years. This characteristic makes it more challenging to identify the drivers of TC rainfall variability through linear regressions. A possible way to overcome this limitation would be to make an EOT analysis for the entire TC season (e.g., May-November), reducing the number of no-TC rainfall years in the leading EOT time series.

TC tracks based on JRA-55 reanalysis are used in this study overall the TC tracks tested in chapter 4 is that they are based in the same reanalysis used for the regression analysis; therefore, the regressions capture the anomalous dynamic and thermodynamic conditions linked to the variability of TC activity in the IAS for the period of analysis. TC tracks densities based on JRA-55 reanalysis are in good agreement with IBTrACS, mostly in the North Atlantic and to a lesser extent in the East Pacific and continental Middle America (see sec. 4.10). In this sense, most of the uncertainties in the TC rainfall identified in this chapter are expected to occur in central-western Middle America.

5.5 Conclusions

The EOT analysis has been used to decompose the interannual variability of seasonal TC-related rainfall over Middle America, identifying regions that vary coherently in time. In both JJA and SON, the leading EOT explains more than 79% of the variance of the area-averaged rainfall associated with TCs.

This study suggests that ENSO phenomenon is the largest mode of variability influencing interannual TC-related variability for JJA and SON in Middle America. These results are consistent with other studies that found ENSO as the primary factor influencing interannual variability of tropical cyclone activity in the IAS (e.g., Camargo et al., 2007; Kossin et al., 2010; Lim et al., 2016). The results in Chapter 5 are consistent with results in Chapter 4 of this thesis: La Niña is linked to reduced vertical wind shear in the Caribbean, and enhances VIMF in the East Pacific and southern Middle America though the northward shift of the ITCZ, favouring TC activity in the IAS and TC-related rainfall in Middle America.

Atlantic modes of variability influence interannual variability of TC-related rainfall over Middle America. This study shows that the positive (negative) phase of the AMM lead to an enhanced (reduced) TC activity in the North Atlantic basin and TC genesis in the Caribbean Sea, influencing rainfall associated with TCs in Middle America.

The positive AMM weakens the NASH, and influences the anomalous southeastward shift of the NASH, favouring Caribbean TCs propagating towards southern Middle America. During these episodes, more Atlantic TCs make landfall in central/eastern Middle America, favoured by warmer SSTs and reducing the wind shear in the Caribbean.

Chapter 6:

Conclusions

The present thesis aimed to understand the causes of interannual variability of seasonal rainfall in Middle America, the role of TCs in the hydrological cycle in Middle America, and the causes of interannual variability of seasonal TC-rainfall in the region.

This thesis presented a detailed study of the mechanisms of interannual variability of Middle America's seasonal rainfall, identifying the atmospheric and coupled atmosphere-ocean drivers responsible for that variability (chapter 3). The monthly contribution of TCs to the atmospheric branch of Middle America's hydrological cycle was identified and explained (chapter 4). This thesis also provided a detailed study of the interannual variability of TC-related rainfall in Middle America, identifying the large-scale drivers of that variability (chapter 5). Section 6.1 reviews the overall conclusions of this thesis concerning the objectives presented in section 1.3. Known limitations and caveats of this thesis are presented in section 6.2, with particular focus on the methods used to identify regions of coherent interannual variability of rainfall and to associate rainfall with TCs. Future research pathways for continuing this study are suggested in section 6.3.

6.1 Summary of key findings

Key findings in chapter 3 are that interannual variability of seasonal rainfall in Middle America is mainly driven by canonical ENSO and the AMM, followed by ENSO Modoki and regional land-atmosphere interactions. Chapter 4 key findings include that TCs contribute 40-60% of extreme rainfall in Middle American coasts, and TC VIMF convergence can be larger than VIMF divergence by the mean circulation in boreal summer. Chapter 5 key finding is that interannual variability of TC rainfall in Middle America is mainly driven by canonical ENSO and the AMM.

6.1.1 The large-scale and local drivers of interannual variability of rainfall in Middle America

As stated in 1.3, the first aims of this thesis were (1) to objectively identify regions in Middle America that show coherent interannual variability of rainfall for each season, and (2) to associate these regions with their principal and secondary modes of variability, describing plausible physical mechanisms that create conditions for anomalous seasonal rainfall. These objectives are accomplished in chapter 3 by applying the EOT method to the study of seasonally accumulated rainfall from the UEA-CRU Global monthly precipitation dataset, for the period 1982-2016.

Analysis in chapter 3 identifies the ENSO as the phenomenon responsible for the largest fraction of interannual rainfall variability in Middle America in boreal summer, winter, and spring. This confirms previously reported relationships between ENSO and regional rainfall (e.g. Ropelewski and Halpert, 1987; Curtis, 2002; Magaña et al., 2003; Maloney et al., 2014).

New findings of this study include physical understanding of the response of Middle America's rainfall to distinct "flavours" of ENSO. In chapter 3, regression analysis identified Middle America's rainfall response to variations in the location and intensity of the Pacific SST anomalies. Canonical ENSO events drive most of the interannual rainfall variability; ENSO Modoki events play an important secondary role.

Results in chapter 3 show that, during winter, Middle America's rainfall variability responds to ENSO teleconnections through anomalous extra-tropical synoptic patterns. Changes in the location of the convection in the eastern (central) equatorial Pacific during peak canonical (Modoki) El Niño events influence the positions of the North Pacific subtropical jet and the winter storm track that passes over northern (central) Middle America.

Results in chapter 3 also show that, during summer, the spatial pattern of coherent rainfall variability peaks in southernmost Middle America, which corresponds to areas with the highest climatological JJA rainfall. Middle America's rainfall variability responds to the anomalous latitudinal shift of the eastern Pacific ITCZ, forced by canonical ENSO. Notably, during La Niña, most Middle America experiences enhanced rainfall due to the ITCZ's anomalous northward shift, which brings additional atmospheric convection. This shift favours TC activity in the eastern Pacific and rainfall in Middle America's central/west coast. The regional rainfall variability in summer also responds to the North Atlantic warming due to the ENSO atmospheric bridge between the Pacific and the Atlantic, triggered when a canonical El Niño precedes a canonical La Niña (e.g. Alexander and Scott, 2002). Chapter 3 results show that, in late spring and early summer, anomalously warm SSTs in the Caribbean Sea, accompanied by lower MSLP, and an enhanced Atlantic ITCZ, favour moisture convergence and rainfall in the Caribbean Sea and southern Middle America. Simultaneously, the strengthening of the Walker circulation in the Caribbean Sea during canonical La Niña decreases the local vertical wind shear and promotes Caribbean TC genesis.

Another key finding of this study is that the AMM is a secondary mode of interannual variability of rainfall in Middle America during spring, summer, and autumn. The positive phase of the AMM enhances VIMF divergence and precipitation in southern Middle America through a northward shift of the Atlantic ITCZ and anomalously warm SSTs in the equatorial Atlantic. On the other hand, the AMM's negative phase slows the climatological northward movement of the Atlantic ITCZ in spring, and enhances the NASH, and shift it southwestward. This configuration strongly inhibits convection in central-eastern Middle America and the Caribbean, while it enhances convection in easternmost Middle America.

The EOT decomposition technique allows identifying secondary regional patterns of rainfall in Middle America that vary coherently in summer: (1) northeastern Middle America and (2) the NAMS region. The variability of rainfall in northeastern Middle America is associated with enhanced deep convection, driven by local land-atmosphere processes, not significantly associated with any large-scale driver considered here. On the other hand, the NAMS rainfall increases in response to anomalous dry and warm conditions in northwestern Middle America, linked to peak and decaying canonical La Niña events in the previous winter and spring, respectively.

Chapter 3 identifies the drivers of coherent rainfall variability during the transitional seasons of MAM and SON. The EOT analysis shows that the ENSO influence on rainfall variability in Middle America depends on the ENSO phenomenon life-cycle stage. Specifically, 58% and 20% of the MAM area-averaged rainfall variance is explained by developing canonical El Niño and decaying canonical La Niña, respectively.

Chapter 3 also shows that SON is the only one of the seasons analysed in which ENSO is not the main driver of the interannual variability; instead, it plays a secondary role. The NASH and the CLLJ (driven by the AMM, the NAO, and ENSO) are two crucial mechanisms for SON rainfall and moisture variability in Middle America and the IAS, and regional TC activity. This study offers an updated view on the role of the NASH and the CLLJ in the interannual variability of Middle America's rainfall, suggesting how their variations in strength and location influence regional TC activity and atmospheric moisture availability.

6.1.2 The TC's contribution to Middle Americas' hydrological cycle

The second objective of this thesis was to determine the climatological contribution of TCs to the atmospheric branch of the hydrological cycle in Middle America (chapter 4). The quantifications of rainfall were made by identifying TC-related rainfall from the 3-h satellite estimations of rainfall of the TMPA 3B42 product (1998-2016) within a circle of 5° geodesic radius centred over the TC location. This study presents a novel approach since different sources of TC tracks are used to quantify TC rainfall: (a) observed TC-tracks from the IBTrACS dataset, and (b) TC tracks from an objective TC identification scheme (Hodges, 1994, 1995, 1999) based on JRA-55 and ERA-Interim reanalyses. Using the latter sets of TC tracks added value to the quantification since the pre-stage and post-stage of the TC lifecycle are included in the tracks.

Results in chapter 4 show that TCs are important sources of annual rainfall in Middle America, particularly in the west and east coasts, and its central region. TC contribution to monthly accumulated rainfall in those regions is $\sim$ 10–30%, with the most substantial contribution in the (climatological drier) Baja California Peninsula of up to 90% in September. Most of the TC contribution occurs during June-October, the peak season for TC activity in both the North Atlantic and East Pacific basins. TCs can make important contributions to rainfall in Middle American coasts and further inland.

TCs contribute 40–60% of extreme daily rainfall (above the 95th percentile) over the west and east coasts of Middle America, although their contribution is not limited to those regions. A substantial percentage of the extreme events of rainfall associated with TCs is also observed further inland, particularly in eastern Middle America during July, in the Gulf coastal plain and Baja California peninsula during September, and in southern Middle America during October.

The TC contribution to VIMF and VIMF convergence occurs mainly from June to October over the coasts and central region of Middle America, and in the East Pacific and the Caribbean basin. In contrast with TC-associated rainfall in Middle America, TC-associated moisture transport goes further inland, suggesting that TCs play a more critical role in supplying atmospheric moisture inland. An outstanding result of this study is that TC VIMF convergence can be larger than VIMF divergence by the mean circulation in boreal summer. This reversal occurs mainly in a wide area of the subtropical North Atlantic, and to a lesser extent in the East Pacific, the Gulf of California, and northwestern Middle America. This conclusion could only be obtained by using TC tracks and VIMF from reanalysis, simultaneously.

Chapter 4 results suggest that TCs play a crucial role in the regional hydrological cycle; their influence varies by basin depending on the stage of the TC season. For both oceanic basins, TC track densities based on JRA-55 reanalysis show more agreement with IBTrACS than those based on ERA-Interim reanalysis.

6.1.3 Main and secondary drivers of interannual variability of TC-related rainfall in Middle America

Chapter 5 aims (a) to identify regions in Middle America that have coherent interannual variability of seasonal TC-related rainfall, and (b) to identify large-scale climate phenomena that drive the interannual variability of TC-related rainfall in the region. To address these aims, the EOT decomposition technique was applied to seasonal TC rainfall calculated with a high-resolution dataset for Middle America, with daily temporal resolution and $10 \times 10km$ horizontal resolution (López-Bravo, 2015; López-Bravo et al., 2018), and by using TC tracks based on JRA-55 reanalysis.

Results in Chapter 5 show that, during both JJA and SON, the interannual variability of Middle America TC-related rainfall is mainly driven by ENSO, identifying the AMM as the secondary driver of this variability. Key findings of this study include that ENSO plays a critical role in the TC-related rainfall variability in Middle America, depending on anomalous TC activity in the IAS. During JJA, ENSO determines TC activity in both the East Pacific and the North Atlantic through variations of atmospheric moisture, wind shear, and SSTs, influencing anomalies of TC genesis and TC activity.

TC-related rainfall variability in western Middle America is linked to the variability of two important TC genesis regions in the eastern Pacific, referred here as the western development region and eastern development region, which mainly respond to ENSO through variations of SSTs, atmospheric moisture, and vertical wind shear. SSTs and wind shear also play a critical role in the Caribbean TC activity and genesis during ENSO events.

During JJA, developing canonical La Niña enhances TC genesis in the Gulf of Tehuantepec (corresponding to the eastern development region), promoting more East Pacific TCs tracking closer to Middle America's west coast. Conversely, during these events, positive anomalies of vertical wind shear in the western development region reduce TC activity in the East Pacific westernmost side.

A second key finding of this chapter is that the AMM is a driver of interannual variability of TC-related rainfall in Middle America. The AMM influences anomalous trajectories of Atlantic TCs through changes in the location and strength of the NASH. The NASH circulation defines the North Atlantic TC steering flow. The AMM also influences both TC genesis and activity in the North Atlantic through anomalies of SSTs, atmospheric moisture, and wind shear.

In JJA, the positive phase of the AMM (defined by anomalously warm SSTs, the northward migration of the Atlantic ITCZ, and decreased wind shear in the MDR) is associated with an enhanced TC activity in the North Atlantic basin and TC genesis in the Caribbean Sea.

In SON, the positive AMM weakens and promotes a southeastward shift of the NASH, favouring Caribbean TCs propagating towards southern Middle America. More Atlantic TCs make landfall in central/eastern Middle America during these episodes, favoured by warmer SSTs and reduced wind shear in the Caribbean. In SON, the negative phase of the AMM and an enhanced and anomalously extended westward NASH, are conditions that lead to TCs tracking closer to northeastern Middle America, leaving rainfall in easternmost Middle America.

The objectives of this chapter and the ones for chapter 3 (see Sec. 1.3) were connected by the hypothesis that interannual variability of seasonal TC-related rainfall and total rainfall are driven by different mechanisms. This thesis shows that during JJA, TC-related rainfall and total rainfall are both mainly driven by ENSO. However, the SON EOT analysis suggests that TC-related rainfall and total rainfall are driven by different mechanisms. SON TC-related rainfall is mainly driven by ENSO, whereas SON total rainfall is mainly driven by regional mechanisms in the Caribbean Sea (associated with the CLLJ variability).

6.2 Limitations and caveats

In chapter 3 and 5, the EOT method is applied to identify regions of coherent interannual variability of rainfall in Middle America. The resultant EOT patterns of precipitation are linearly orthogonal in time. However, the linear regressions used to identify the mechanisms of variability associated with each EOT do not determine the relative weight of each driver for the seasonal anomalies of rainfall, representing a limitation of the technique. This limitation is more evident when more than two large-scale interannual variability modes are significantly correlated with the same EOT. For example, JJA EOT1 (Fig. 3.1a, chapter 3) is associated with ENSO, the AMM, and the Atlantic response to canonical El Niño, but it is not possible to isolate the influence of each driver on the EOT. This is particularly an issue in the Atlantic basin, where anomalously warm SSTs characterise both the positive phase of the AMM and the Atlantic warming to ENSO in the tropical Atlantic. It is important to note that even when the EOTs are orthogonal by construction, the drivers of rainfall are not orthogonal themselves.

The EOT analysis assumes that the relationship between drivers and rainfall variability are stationary. However, since the climate is non-stationary, future changes in the response of the regional rainfall to their respective drivers might be expected.

A major limitation of the EOT analysis made in chapter 3 and 5 is that there are only presented correlations and regression. Since correlations may not necessarily show causal relationship, the identified "drivers" and plausible mechanisms might not be a cause of rainfall variability.

In this study, TC tracks from observations (IBTrACS) and those based on JRA-55 and ERA-Interim reanalyses were used to quantify TC contribution to rainfall and moisture over Middle America. As discussed in chapter 4, these quantifications depend strongly on the TC track dataset used and as all sources of TC track data involve uncertainties. For TC tracks based on reanalysis the uncertainty comes from the GCM used, the data assimilation technique, and the data assimilated. For observed TC-tracks the uncertainty comes from differences between agencies in TC identification. In all the cases, the uncertainty added to the quantification of TC-related rainfall and moisture over Middle America is greatest for the weakest storms, and for the pre-TC and post-TC stages for all storms.

Chapters 4 and 5 present TC contributions to rainfall by using satellite estimations of rainfall and rainfall observations, respectively, and employing TC tracks based on reanalysis. One might argue that identifying TC-related rainfall using these estimates of rainfall is likely to be spatially less accurate than those from reanalysis rainfall, since the source of the rainfall datasets is not the same as the one used to build the TC tracks. However, most evaluation studies that have compared reanalysis data with observations for continental-scale areas have found the largest errors in tropical oceanic regions (Bosilovich et al., 2008). The poor performance of rainfall in reanalysis might occur because precipitation is mostly dependent on the model physics and physical parameterisations, leading to uncertainty in the rainfall data products (Kim and Alexander, 2013). For all the reasons mentioned above, rainfall estimates from observations were used in each chapter of this thesis.

6.3 Future work

This thesis provides several future research pathways, particularly on the study of the modes of variability influencing both Middle America's seasonal rainfall and TC contributions to the hydrological cycle, which can be applied for improved predictions under current and future climates.

The present study offers an extensive EOT analysis of the potential causes of interannual anomalies of regional and seasonal rainfall in response to anomalous SST, atmospheric circulations, moisture transport and moisture convergence. This EOT analysis can be used as the basis to assess the performance of GCMs to simulate circulation features that are key for interannual variability of seasonal rainfall in Middle America, in sensitivity experiments with atmosphere-only (e.g. response to prescribed SSTs) and coupled models (e.g., Rotstayn et al., 2010; Stephan et al., 2018c). The assessment of GCMs performance in Middle America would allow to investigate the sources of systematic errors in GCM processes, such as biases in mean seasonal rainfall, atmospheric moisture, and intensity and location of atmospheric circulations. These investigations will lead to the identification of physical processes that must be captured to reliably simulate Middle America's climate and its interannual variability. This would be useful for the improvement of GCMs used for seasonal forecasting of rainfall that could also support decision making (e.g., population welfare and ecosystems health, agriculture, hydroelectric, water management, and insurance sectors).

Results in chapter 3 suggest that land-atmosphere interactions in northern Middle America (particularly in the Great Plains and the NAMS region) are very important for the occurrence of summer rainfall (Cotton et al., 2010). Koster et al. (2004) have suggested that soil moisture anomalies substantially impact precipitation in northeastern Middle America during JJA. The authors suggested that this region is a transition zone between wet and dry climates, where the atmosphere can trigger moist convection through boundary-layer moisture and regional evaporation is sensitive to soil moisture. Therefore soil moisture can influence rainfall in this region. GCM simulations would help to understand the influence of regional land-atmosphere interactions and variables such as soil moisture and evaporation, on the interannual variability of rainfall in northeastern Middle America.

Further studies could refer the results of this thesis to analyse of the impact of interannual variability of seasonal rainfall and TC rainfall on human population wellbeing and ecosystems health, regional river network discharge, water storage, and spread of tropical diseases, considering the regions of coherent variability identified with the EOT method. In this respect, it would be required to explore variables such as atmospheric temperature, soil moisture, and evaporation that also influence the spread of the aforementioned diseases (e.g. Lozano-Fuentes et al., 2012) and wildfires (e.g. Westerling et al., 2006).

Notably, this thesis has contributed to the research on the role of TCs in the hydrological cycle of Middle America and the IAS, which provides the basis for future studies on the regional hydrological cycle variability at different temporal scales. Further studies could refer to this study to address the role of TCs in the terrestrial branch of the hydrological cycle in Middle America and other regions affected by TCs, and their influences on surface runoff, subterranean runoff, evaporation rate, and rate of storage of water.

One of the most significant contributions of this thesis is the suggestion that TC VIMF convergence can reverse the VIMF divergence by the mean circulation in certain portions of Middle America and the IAS. These results could guide the assessment of GCMs simulating seasonal TC-associated rainfall and moisture transport in Middle America and the IAS. These assessments are important to detect systematic errors in GCMs to simulate TCs and its associated atmospheric variables. Improved numerical simulations would help to understand how TC dynamics, TC rainfall and moisture transport influence regional atmospheric, oceanic and air-sea coupled processes.

Further studies could refer to the EOT analysis for interannual variability of TC-related rainfall presented in this thesis, to be applied to different TC basins and seasons (e.g. extended TC season). The EOT analysis could be also applied to the analysis of TC-related rainfall over continent and ocean, simmultaneously. The applicability of the EOT analysis for TC-rainfall could aid to assess GCMs on the simulation of the variability of seasonal TC rainfall.

There is ample scope for expansion upon this research in studies of rainfall variability in Middle America at intraseasonal temporal scales, concerning the variability of TCs and the NAMS. As reviewed in chapter 2, IAS TCs and the NAMS are subject to the influence of different modes of intraseasonal variability such as the 10-30 day mode in the eastern Pacific (east-west mode and west-east mode; Jiang and Waliser, 2008; Wen et al., 2011), and the 30-90-day modes (Jiang and Waliser, 2009), such as the MJO (Higgins and Shi, 2001). However, the mechanisms that influence the intraseasonal variability of rainfall in Middle America are still a matter of study. EOT analysis represents a potential method for investigating the causes of Middle America's intraseasonal variability of rainfalll (as in Stephan et al., 2018b, for East Asia). It is expected that results from EOT analysis at intraseasonal scales are different from the EOT analysis at interannual scales, since modes of variability that vary on timescales of multiple years (such as ENSO) are not expected to have a strong influence on rainfall variability over periods of a few days (e.g., Stephan et al., 2018b). The methodology proposed in this thesis to quantify TC-related rainfall could be employed to investigate the causes of the intraseasonal variability of TC-related rainfall in Middle America. High-resolution datasets would be required to study the sources of intraseasonal rainfall variability in Middle America through EOT analysis.

Daily, high-spatial-resolution, gridded gauge rainfall dataset, such as López-Bravo et al. (2018), are good candidates to address future studies on intraseasonal variability of rainfall in Middle America proposed here, since these studies require the analysis of sets of averaged days of rainfall (e.g., Stephan et al., 2018b).

References

Agudelo, P. A., C. D. Hoyos, J. A. Curry, and P. J. Webster, 2011: Probabilistic discrimination between large-scale environments of intensifying and decaying African easterly waves. *Clim. Dyn.*, **36**, 1379–1401, doi:10.1007/s00382-010-0851-x.

Aiyyer, A. and J. Molinari, 2008: MJO and tropical cyclogenesis in the Gulf of Mexico and Eastern Pacific: Case study and idealized numerical modeling. *J. Atmos. Sci.*, **65**, 2691–2704, doi:10.1175/2007JAS2348.1.

Aiyyer, A. and C. Thorncroft, 2011: Interannual-to-multidecadal variability of vertical shear and tropical cyclone activity. *J. Clim.*, **24**, 2949 – 2962, doi:10.1175/2010JCLI3698.1.

Alexander, M., 2010: Extratropical Air-Sea Interaction, Sea Surface Temperature Variability, and the Pacific Decadal Oscillation. *Washington DC American Geophysical Union Geophysical Monograph Series*, **189**, doi:10.1029/2008GM000794.

Alexander, M. and J. Scott, 2002: The influence of ENSO on air-sea interaction in the Atlantic. *Geophys. Res. Lett.*, **29**, 46–1–46–4, doi:10.1029/2001GL014347.

Amador, J., 2009: The Intra-Americas Sea low-level jet. *Ann. N. Y. Acad. Sci.*, **1146**, 153–88, doi:10.1196/annals.1446.012.

Amador, J. A., 2008: The Intra-Americas Sea Low-level Jet. *Ann. N. Y. Acad. Sci.*, **1146**, 153–188, doi:10.1196/annals.1446.012.

Amaya, D. J., M. J. DeFlorio, A. J. Miller, and S.-P. Xie, 2017: Wes feedback and the atlantic meridional mode: observations and cmip5 comparisons. *J. Clim.*, **49**, 1665–1679, doi:10.1007/s00382-016-3411-1.

An, S.-I., 2008: Interannual variations of the tropical ocean instability wave and ENSO. *J. Clim.*, **21**, 3680–3686, doi:10.1175/2008JCLI1701.1.

Anderson, B. T., J. O. Roads, and S.-C. Chen, 2000a: Large-scale forcing of summertime monsoon surges over the Gulf of California and the southwestern United States. *J. Geophys. Res. Atmos.*, **105**, 24455–24467, doi:10.1029/2000JD900337.

Anderson, B. T., J. O. Roads, S.-C. Chen, and H.-M. H. Juang, 2000b: Regional simulation of the low-level monsoon winds over the Gulf of California and southwestern United States. *J. Geophys. Res. Atmos.*, **105**, 17955–17969, doi:10.1029/2000JD900161.

Anthes, R. A., 1974: The dynamics and energetics of mature tropical cyclones. *Reviews of Geophysics*, **12**, 495–522, doi:10.1029/RG012i003p00495.

Antinao, J. L. and L. M. Farfán, 2016: Occurrence of landslides during the approach of tropical cyclone Juliette (2001) to Baja California Sur, Mexico. *Atmos.*, **26**, 183–208, doi:10.1016/S0187-6236(13)71071-3.

Arias, P., A. Martinez, and S. Vieira, 2015: Moisture sources to the 2010–2012 anomalous wet season in northern South America. *Clim. Dyn.*, **45**, 2861–2884, doi:10.1007/s00382-015-2511-7.

Ashok, K., S. K. Behera, S. A. Rao, H. Weng, and T. Yamagata, 2007: El Niño Modoki and its possible teleconnection. *J. Geophys. Res. Oceans*, **112**, doi:10.1029/2006JC003798.

Barlow, M., 2011: Influence of hurricane-related activity on North American extreme precipitation. *Geophys. Res. Lett.*, **38**, doi:https://doi.org/10.1029/2010GL046258.

Barnston, A. G. and R. E. Livezey, 1987: Classification, seasonality and persistence of low-frequency atmospheric circulation patterns. *Mon. Weather Rev.*, **115**, 1083–1126, doi:10.1175/1520-0493(1987)115¡1083:CSAPOL¿2.0.CO;2.

Barnston, A. G., R. E. Livezey, and M. S. Halpert, 1991: Modulation of Southern Oscillation-Northern Hemisphere Mid-Winter Climate Relationships by the QBO. *J. Clim.*, **4**, 203–217, doi:10.1175/1520-0442(1991)004¡0203:MOSONH¿2.0.CO;2.

Battisti, D. S. and A. C. Hirst, 1989: Interannual variability in a tropical atmosphere–ocean model: Influence of the basic state, ocean geometry and nonlinearity. *J. Atmos. Sci.*, **46**, 1687–1712, doi:10.1175/1520-0469(1989)046¡1687:IVIATA¿2.0.CO;2.

Bayr, T., M. Latif, D. Dommenget, C. Wengel, J. Harlaß, and W. Park, 2018: Mean-state dependence of ENSO atmospheric feedbacks in climate models. *Clim. Dyn.*, **50**, 3171–3194, doi:10.1007/s00382-017-3799-2.

Belanger, J. I., M. T. Jelinek, and J. A. Curry, 2016: A climatology of easterly waves in the tropical Western Hemisphere. *Geosci. Data J.*, **3**, 40–49, doi:10.1002/gdj3.40.

Bell, G. D., M. S. Halpert, C. F. Ropelewski, V. E. Kousky, A. V. Douglas, R. C. Schnell, and M. E. Gelman, 1999: Climate Assessment for 1998. *Bull. Am. Meteorol. Soc*, **80**, S1–S48, doi:10.1175/1520-0477-80.5s.S1.

Bell, R., K. Hodges, P. L. Vidale, J. Strachan, and M. Roberts, 2014: Simulation of the global ENSO–tropical cyclone teleconnection by a high-resolution coupled general circulation model. *J. Clim.*, **27**, doi:10.1175/JCLI-D-13-00559.1.

Beven II, J. L. . N. H. C. S. E., 2014: National Hurricane Center tropical cyclone report: Hurricane Ingrid. `https://www.nhc.noaa.gov/data/tcr/AL102013-Ingrid.pdf`.

Bjerknes, J., 1969: Atmospheric teleconnections from the equatorial Pacific. *Mon. Weather Rev.*, **97**, 163–172, doi:10.1175/1520-0493(1969)097¡0163:ATFTEP¿2.3.CO;2.

Bosilovich, M. G., J. Chen, F. R. Robertson, and R. F. Adler, 2008: Evaluation of Global Precipitation in Reanalyses. *J. Appl. Meteor.*, **47**, 2279–2299, doi:10.1175/2008JAMC1921.1.

Bregy, J. C., J. T. Maxwell, S. M. Robeson, J. T. Ortegren, P. T. Soulé, and P. A. Knapp, 2020: Spatiotemporal variability of tropical cyclone precipitation using a high-resolution, gridded (0.25° × 0.25°) dataset for the eastern United States, 1948–2015. *J. Clim.*, **33**, 1803–1819, doi:10.1175/JCLI-D-18-0885.1.

Brun, J. and A. P. Barros, 2014: Mapping the role of tropical cyclones on the hydroclimate of the southeast United States: 2002–2011. *Int. J. Climatol.*, **34**, 494–517, doi:10.1002/joc.3703.

Burpee, R. W., 1972: The origin and structure of Easterly Waves in the lower troposphere of North Africa. *J. Atmos. Sci.*, **29**, 77–90, doi:10.1175/1520-0469(1972)029¡0077:TOASOE¿2.0.CO;2.

Byerle, L. A. and J. Paegle, 2003: Modulation of the Great Plains low-level jet and moisture transports by orography and large-scale circulations. *J. Geophys. Res. Atmos.*, **108**, doi:10.1029/2002JD003005.

Camargo, S. J., K. A. Emanuel, and A. H. Sobel, 2007: Use of a genesis potential index to diagnose ENSO effects on tropical cyclone genesis. *J. Clim.*, **20**, 4819–4834, doi:10.1175/JCLI4282.1.

Camargo, S. J., A. W. Robertson, A. G. Barnston, and M. Ghil, 2008: Clustering of eastern North Pacific tropical cyclone tracks: ENSO and MJO effects. *Geochem. Geophys.*, **9**, doi:https://doi.org/10.1029/2007GC001861.

Camargo, S. J., M. C. Wheeler, and A. H. Sobel, 2009: Diagnosis of the MJO modulation of tropical cyclogenesis using an empirical index. *J. Atmos. Sci*, **66**, 3061–3074, doi:10.1175/2009JAS3101.1.

Cavazos, T., 1999: Large-scale circulation anomalies conducive to extreme precipitation events and derivation of daily rainfall in northeastern Mexico and southeastern Texas. *J. Clim.*, **12**, 1506–1523, doi:10.1175/1520-0442(1999)012¡1506:LSCACT¿2.0.CO;2.

CENAPRED, 2001: Características del impacto socioenconómico de los principales desastres ocurridos en méxico en el periodo 1980-99. `http://www.proteccioncivil.gob.mx/work/models/ProteccionCivil/Resource/375/1/images/no_1.pdf`.

— 2015: Impacto socioenconómico de los principales desastres ocurridos en la República Mexicana en 2013. `http://www.cenapred.gob.mx/es/Publicaciones/archivos/324-NO.15-IMPACTOSOCIOECONMICODELOSPRINCIPALESDESASTRESOCURRIDOSENMXICOENELAO2013.PDF`.

Cerveny, R. S. and L. E. Newman, 2000: Climatological Relationships between Tropical Cyclones and Rainfall. *Mon. Weather Rev.*, **128**, 3329–3336, doi:10.1175/1520-0493(2000)128¡3329:CRBTCA¿2.0.CO;2.

Chan, J. C. L., 1985: Tropical cyclone activity in the Northwest Pacific in relation to the El Niño/Southern Oscillation phenomenon. *Mon. Weather Rev.*, **113**, 599 – 606, doi:10.1175/1520-0493(1985)113¡0599:TCAITN¿2.0.CO;2.

Chan, J. C. L. and C. K. M. Yip, 2003: Interannual variations of tropical cyclone size over the western North Pacific. *Geophys. Res. Lett.*, **30**, doi:https://doi.org/10.1029/2003GL018522.

Chen, T.-C., 2003: Maintenance of Summer Monsoon Circulations: A Planetary-Scale Perspective. *J. Clim.*, **16**, 2022–2037.

Chen, Y., E. E. Ebert, K. J. Walsh, and N. E. Davidson, 2013: Evaluation of TRMM 3B42 precipitation estimates of tropical cyclone rainfall using PACRAIN data. *J. Geophys. Res. Atmos.*, **118**, 2184–2196, doi:10.1002/jgrd.50250.

Chiang, J. C. H. and B. R. Lintner, 2005: Mechanisms of remote tropical surface warming during El Niño. *J. Clim.*, **18**, 4130–4149, doi:10.1175/JCLI3529.1.

Chiang, J. C. H. and D. J. Vimont, 2004: Analogous Pacific and Atlantic Meridional Modes of tropical atmosphere–ocean variability. *J. Clim.*, **17**, 4143–4158, doi:10.1175/JCLI4953.1.

Chu, P.-S., 2004: ENSO and tropical cyclone activity. *Hurricanes and Typhoons, Past, Present and Future*, R. J. Murnane and K.-B. Liu, eds., Columbia University Press, New York, chapter 11, 297–332.

Clement, A., K. Bellomo, L. N. Murphy, M. A. Cane, T. Mauritsen, G. Rädel, and B. Stevens, 2015: The Atlantic Multidecadal Oscillation without a role for ocean circulation. *Science*, **350**, 320–324, doi:10.1126/science.aab3980.

Clement, A., M. A. Cane, L. N. Murphy, K. Bellomo, T. Mauritsen, and B. Stevens, 2016: Response to comment on "the atlantic multidecadal oscillation without a role for ocean circulation". *Science*, **352**, 1527–1527, doi:10.1126/science.aaf2575.

Colbert, A. J. and B. J. Soden, 2012: Climatological variations in North Atlantic tropical cyclone tracks. *J. Clim.*, **25**, 657–673, doi:10.1175/JCLI-D-11-00034.1.

CONAGUA, 2018: Estadísticas del Agua en méxico, edición 2018. `http://sina.conagua.gob.mx/publicaciones/EAM_2018.pdf`.

CONANP, 2019: Áreas Naturales Protegidas decretadas. `http://sig.conanp.gob.mx/website/pagsig/datos_anp.htm`, accessed: 2019-04-30.

CONAPO, 2016: Indice de marginacion por entidad federativa y municipio 2015. `https://www.gob.mx/conapo/documentos/indice-de-marginacion-por-entidad-federativa-y-municipio-2015`, publised: 2016-10-26.

Cook, K. H. and E. K. Vizy, 2010: Hydrodynamics of the Caribbean Low-Level Jet and Its Relationship to Precipitation. *J. Clim.*, **23**, 1477–1494, doi:10.1175/2009JCLI3210.1.

Corbosiero, K. L., M. J. Dickinson, and L. F. Bosart, 2009: The contribution of Eastern North Pacific tropical cyclones to the rainfall climatology of the Southwest United States. *Mon. Weather Rev.*, **137**, 2415–2435, doi:10.1175/2009MWR2768.1.

Cotton, W., G. Bryan, and S. van den Heever, 2010: *Storm and Cloud Dynamics*. ISSN, Elsevier Science.

Cotton, W. R., M.-S. Lin, R. L. McAnelly, and C. J. Tremback, 1989: A Composite Model of Mesoscale Convective Complexes. *Mon. Weather Rev.*, **117**, 765–783, doi:10.1175/1520-0493(1989)117¡0765:ACMOMC¿2.0.CO;2.

Covey, D. L. and S. Hastenrath, 1978: The Pacific El Niño phenomenon and the Atlantic circulation. *Mon. Weather Rev.*, **106**, 1280–1287, doi:10.1175/1520-0493(1978)106¡1280:TPENPA¿2.0.CO;2.

CPC, 2005: The ENSO cycle. `https://www.cpc.ncep.noaa.gov/products/analysis_monitoring/ensocycle/enso_cycle.shtml`, accessed: 2020-05-03.

Curtis, S., 2002: Interannual variability of the bimodal distribution of summertime rainfall over Central America and tropical storm activity in the far-eastern Pacific. *Climate Res.*, **22**, 141–146, doi:10.3354/cr022141.

Dare, R. A., N. E. Davidson, and J. L. McBride, 2012: Tropical Cyclone Contribution to Rainfall over Australia. *Mon. Weather Rev.*, **140**, 3606–3619, doi:10.1175/MWR-D-11-00340.1.

Dare, R. A. and J. L. McBride, 2011: The threshold sea surface temperature condition for tropical cyclogenesis. *Journal of Climate*, **24**, 4570 – 4576, doi:10.1175/JCLI-D-10-05006.1.

Davis, R. E., B. P. Hayden, D. A. Gay, W. L. Phillips, and G. V. Jones, 1997: The North Atlantic Subtropical Anticyclone. *J. Clim.*, **10**, 728–744, doi:10.1175/1520-0442(1997)010¡0728:TNASA¿2.0.CO;2.

Dawson, A., 2016: Windspharm: A high-level library for global wind field computations using spherical harmonics. *J. Open Res. Software*, **4**, 1–5, doi:10.2151/jmsj.2015-001.

Dee, D. P., S. M. Uppala, A. J. Simmons, P. Berrisford, P. Poli, S. Kobayashi, U. Andrae, M. A. Balmaseda, G. Balsamo, P. Bauer, P. Bechtold, A. C. M. Beljaars, L. van de Berg, J. Bidlot, N. Bormann, C. Delsol, R. Dragani, M. Fuentes, A. J. Geer, L. Haimberger, S. B. Healy, H. Hersbach, E. V. Hólm, L. Isaksen, P. Kållberg, M. Köhler, M. Matricardi, A. P. McNally, B. M. Monge-Sanz, J.-J. Morcrette, B.-K. Park, C. Peubey, P. de Rosnay, C. Tavolato, J.-N. Thépaut, and F. Vitart, 2011: The ERA-Interim reanalysis: configuration and performance of the data assimilation system. *Q. J. Royal Meteorol. Soc.*, **137**, 553–597, doi:10.1002/qj.828.

Defforge, C. L. and T. M. Merlis, 2017: Evaluating the evidence of a global sea surface temperature threshold for tropical cyclone genesis. *J. Clim.*, **30**, 9133 – 9145, doi:10.1175/JCLI-D-16-0737.1.

Delworth, T., S. Manabe, and R. J. Stouffer, 1993: Interdecadal variations of the Thermohaline Circulation in a coupled ocean-atmosphere model. *J. Clim.*, **6**, 1993 – 2011, doi:10.1175/1520-0442(1993)006¡1993:IVOTTC¿2.0.CO;2.

Deser, C., M. A. Alexander, S.-P. Xie, and A. S. Phillips, 2010: Sea surface temperature variability: Patterns and mechanisms. *Annu. Rev. Mar. Sci.*, **2**, 115–143, doi:10.1146/annurev-marine-120408-151453.

Deser, C., A. S. Phillips, and J. W. Hurrell, 2004: Pacific Interdecadal Climate Variability: Linkages between the Tropics and the North Pacific during Boreal Winter since 1900. *J. Clim.*, **17**, 3109–3124, doi:10.1175/1520-0442(2004)017¡3109:PICVLB¿2.0.CO;2.

Domínguez, C. and V. Magaña, 2018: The role of tropical cyclones in precipitation over the tropical and subtropical North America. *Front. Earth Sci.*, **6**, 19, doi:10.3389/feart.2018.00019.

Dunkerton, T. J., M. T. Montgomery, and Z. Wang, 2009: Tropical cyclogenesis in a tropical wave critical layer: easterly waves. *Atmos. Chem. Phys.*, **9**, 5587–5646, doi:10.5194/acp-9-5587-2009.

Durán-Quesada, A., M. Reboita, and L. Gimeno, 2012: Precipitation in tropical America and the associated sources of moisture: a short review. *Hydrolog. Sci. J.*, **57**, 612–624, doi:10.1080/02626667.2012.673723.

Durán-Quesada, A. M., L. Gimeno, J. A. Amador, and R. Nieto, 2010: Moisture sources for Central America: Identification of moisture sources using a lagrangian analysis technique. *J. Geophys. Res. Atmos.*, **115**, doi:10.1029/2009JD012455.

Elsner, J. B., 2003: Tracking hurricanes. *Bull. Am. Meteorol. Soc.*, **84**, 353–356, doi:10.1175/BAMS-84-3-353.

Emanuel, K., 2005: Increasing destructiveness of tropical cyclones over the past 30 years. *Nature*, **436**, 686–688, doi:10.1038/nature03906.

Emanuel, K., F. Fondriest, and J. Kossin, 2012: Potential Economic Value of Seasonal Hurricane Forecasts. *Weather Clim. Soc.*, **4**, 110–117, doi:10.1175/WCAS-D-11-00017.1.

Emanuel, K. A., 1995: Sensitivity of tropical cyclones to surface exchange coefficients and a revised steady-state model incorporating eye dynamics. *J. Atmos. Sci.*, **52**, 3969 – 3976, doi:10.1175/1520-0469(1995)052¡3969:SOTCTS¿2.0.CO;2.

Endfield, G. H. and I. Tejedo-Fernández, 2006: Decades of Drought, Years of Hunger: Archival Investigations of Multiple Year Droughts in Late Colonial Chihuahua. *Clim. Change*, **75**, 391–419, doi:10.1007/s10584-006-3492-7.

Enfield, D. B. and D. A. Mayer, 1997: Tropical Atlantic sea surface temperature variability and its relation to El Niño-Southern Oscillation. *J. Geophys. Res. Oceans*, **102**, 929–945, doi:10.1029/96JC03296.

Enfield, D. B., A. M. Mestas-Nuñez, and P. J. Trimble, 2001: The Atlantic Multidecadal Oscillation and its relation to rainfall and river flows in the continental U.S. *Geophys. Res. Lett.*, **28**, 2077–2080, doi:10.1029/2000GL012745.

Fang, J. and F. Zhang, 2016: Contribution of Tropical Waves to the Formation of Supertyphoon Megi (2010). *J. Atmos. Sci.*, **73**, 4387–4405, doi:10.1175/JAS-D-15-0179.1.

Farfán, L. M. and J. A. Zehnder, 2001: An analysis of the landfall of Hurricane Nora (1997). *Mon. Weather Rev.*, **129**, 2073–2088, doi:10.1175/1520-0493(2001)129¡2073:AAOTLO¿2.0.CO;2.

Ferreira, R. N. and W. H. Schubert, 1997: Barotropic aspects of ITCZ breakdown. *J. Atmos. Sci.*, **54**, 261–285, doi:10.1175/1520-0469(1997)054¡0261:BAOIB¿2.0.CO;2.

Franco-Díaz, A., N. P. Klingaman, P. L. Vidale, L. Guo, and M.-E. Demory, 2019: The contribution of tropical cyclones to the atmospheric branch of Middle America's hydrological cycle using observed and reanalysis tracks. *Clim. Dyn.*, **53**, 6145–6158, doi:10.1007/s00382-019-04920-z.

Frank, N. L., 1970: Atlantic tropical systems of 1969. *Mon. Weather Rev.*, **98**, 307–314, doi:10.1175/1520-0493(1970)098¡0307:ATSO¿2.3.CO;2.

Frank, W. M., 1977: The structure and energetics of the tropical cyclone i. Storm structure. *Mon. Weather Rev.*, **105**, 1119–1135, doi:10.1175/1520-0493(1977)105¡1119:TSAEOT¿2.0.CO;2.

Fu, D., P. Chang, and C. M. Patricola, 2017: Intrabasin variability of east Pacific tropical cyclones during ENSO regulated by Central American gap winds. *Sci. Rep.*, **7**, 1–8, doi:10.1038/s41598-017-01962-3.

Giannini, A., J. C. H. Chiang, M. A. Cane, Y. Kushnir, and R. Seager, 2001: The ENSO teleconnection to the tropical Atlantic Ocean: Contributions of the remote and local SSTs to rainfall variability in the Tropical Americas. *J. Clim.*, **14**, 4530–4544, doi:10.1175/1520-0442(2001)014¡4530:TETTTT¿2.0.CO;2.

Gilford, D. M., S. Solomon, and K. A. Emanuel, 2017: On the seasonal cycles of tropical cyclone potential intensity. *J. Clim.*, **30**, 6085–6096, doi:10.1175/JCLI-D-16-0827.1.

Gill, A. E., 1980: Some simple solutions for heat-induced tropical circulation. *Q. J. Royal Meteorol. Soc.*, **106**, 447–462, doi:10.1002/qj.49710644905.

Goldenberg, S. B., C. W. Landsea, A. M. Mestas-Nuñez, and W. M. Gray, 2001: The recent increase in Atlantic hurricane activity: Causes and implications. *Science*, **293**, 474–479, doi:10.1126/science.1060040.

Goldenberg, S. B. and L. J. Shapiro, 1996: Physical mechanisms for the association of el Niño and West African rainfall with Atlantic major hurricane activity. *J. Clim.*, **9**, 1169–1187, doi:10.1175/1520-0442(1996)009¡1169:PMFTAO¿2.0.CO;2.

Grabowski, W. W. and M. W. Moncrieff, 2004: Moisture-convection feedback in the tropics. *Q. J. Royal Meteorol. Soc.*, **130**, 3081–3104, doi:10.1256/qj.03.135.

Gray, W. M., 1968: Global view of the origin of tropical disturbances and storms. *Mon. Weather Rev.*, **96**, 669–700, doi:10.1175/1520-0493(1968)096¡0669:GVOTOO¿2.0.CO;2.

— 1984: Atlantic seasonal hurricane frequency. Part I: El Niño and 30 mb Quasi-Biennial Oscillation influences. *Mon. Weather Rev.*, **112**, 1649–1668, doi:10.1175/1520-0493(1984)112¡1649:ASHFPI¿2.0.CO;2.

Gray, W. M. and J. D. Sheaffer, 1991: El Niño and QBO influences on tropical cyclone activity. *Teleconnections Linking Worldwide Anomalies*, M. H. Glantz, R. W. Katz, and N. Nicholls, eds., Cambridge University Press, Cambridge, chapter 10, 257–284.

Guilyardi, E., A. Wittenberg, A. Fedorov, M. Collins, C. Wang, A. Capotondi, G. J. van Oldenborgh, and T. Stockdale, 2009: Understanding El Niño in Ocean–Atmosphere General Circulation Models: Progress and Challenges. *Bull. Am. Meteorol. Soc.*, **90**, 325–340, doi:10.1175/2008BAMS2387.1.

Guo, L., N. P. Klingaman, P. L. Vidale, A. G. Turner, M.-E. Demory, and A. Cobb, 2017: Contribution of tropical cyclones to atmospheric moisture transport and rainfall over East Asia. *J. Clim.*, **30**, 3853–3865, doi:10.1175/JCLI-D-16-0308.1.

Gutzler, D. S., K. M. Wood, E. A. Ritchie, A. V. Douglas, and M. D. Lewis, 2013: Interannual variability of tropical cyclone activity along the Pacific coast of North America. *Atmosfera*, **26**, 149–162, doi:https://doi.org/10.1016/S0187-6236(13)71069-5.

Hall, T. and M. K. Tippett, 2017: Pacific hurricane landfalls on Mexico and SST. *J. Appl. Meteorol. Climatol.*, **56**, 667–676, doi:10.1175/JAMC-D-16-0194.1.

Harada, Y., H. Kamahori, C. Kobayashi, H. Endo, S. Kobayashi, Y. Ota, H. Onoda, K. Onogi, K. Miyaoka, and K. Takahashi, 2016: The JRA-55 reanalysis: Representation of atmospheric circulation and climate variability. *J. Meteorol. Soc. Jpn.*, **94**, 269–302, doi:10.2151/jmsj.2016-015.

Hartmann, D. L. and E. D. Maloney, 2001: The Madden–Julian Oscillation, Barotropic Dynamics, and North Pacific Tropical Cyclone Formation. Part II: Stochastic Barotropic Modeling. *J. Atmos. Sci.*, **58**, 2559–2570, doi:10.1175/1520-0469(2001)058¡2559:TMJOBD¿2.0.CO;2.

Hastenrath, S., 1978: On modes of tropical circulation and climate anomalies. *J. Atmos. Sci.*, **35**, 2222–2231, doi:10.1175/1520-0469(1978)035¡2222:OMOTCA¿2.0.CO;2.

— 1988: *Climate and circulation of the tropics*. Springer, 1 edition, 464 pp.

Hatsushika, H., J. Tsutsui, M. Fiorino, and K. Onogi, 2006: Impact of wind profile retrievals on the analysis of tropical cyclones in the JRA-25 Reanalysis. *J. Meteor. Soc. Japan. Ser. II*, **84**, 891–905, doi:10.2151/jmsj.84.891.

Henry, W. K., 1979: Some aspects of the fate of cold fronts in the Gulf of Mexico. *Mon. Weather Rev.*, **107**, 1078–1082, doi:10.1175/1520-0493(1979)107¡1078:SAOTFO¿2.0.CO;2.

Herrera, E., V. Magaña, and E. Caetano, 2015: Air–sea interactions and dynamical processes associated with the midsummer drought. *Int. J. Climatol.*, **35**, 1569–1578, doi:10.1002/joc.4077.

Higgins, R. W., Y. Chen, and A. V. Douglas, 1999: Interannual variability of the North American warm season precipitation regime. *J. Clim.*, **12**, 653–680, doi:10.1175/1520-0442(1999)012¡0653:IVOTNA¿2.0.CO;2.

Higgins, R. W., K. C. Mo, and Y. Yao, 1998: Interannual variability of the U.S. summer precipitation regime with emphasis on the southwestern monsoon. *J. Clim.*, **11**, 2582–2606, doi:10.1175/1520-0442(1998)011¡2582:IVOTUS¿2.0.CO;2.

Higgins, R. W. and W. Shi, 2001: Intercomparison of the principal modes of interannual and intraseasonal variability of the North American Monsoon System. *J. Clim.*, **14**, 403–417, doi:10.1175/1520-0442(2001)014¡0403:IOTPMO¿2.0.CO;2.

Hodges, K., 1994: A general method for tracking analysis and its application to meteorological data. *Mon. Weather Rev.*, **122**, 2573–2586, doi:10.1175/1520-0493(1994)122¡2573:AGMFTA¿2.0.CO;2.

— 1995: Feature tracking on the unit sphere. *Mon. Weather Rev.*, **123**, 3458–3465, doi:10.1175/1520-0493(1995)123¡3458:FTOTUS¿2.0.CO;2.

— 1999: Adaptive constraints for feature tracking. *Mon. Weather Rev.*, **127**, 1362–1373, doi:10.1175/1520-0493(1999)127¡1362:ACFFT¿2.0.CO;2.

Hodges, K., A. Cobb, and P. Vidale, 2017: How well are tropical cyclones represented in reanalysis datasets? *J. Clim.*, **30**, 5243–5264, doi:10.1175/JCLI-D-16-0557.1.

Hodges, K. and R. Emerton, 2015: The prediction of Northern Hemisphere tropical cyclone extended lifecycles by the ECMWF Ensemble and Deterministic Prediction Systems. Part 1: Tropical cyclone stage. *Mon. Weather Rev.*, **143**, 5091–5114 (Open Access), doi:10.1175/MWR-D-13-00385.1.

Hoskins, B. J. and D. J. Karoly, 1981: The Steady Linear Response of a Spherical Atmosphere to Thermal and Orographic Forcing. *J. Atmos. Sci.*, **38**, 1179–1196, doi:10.1175/1520-0469(1981)038¡1179:TSLROA¿2.0.CO;2.

Huffman, G. J. and D. T. Bolvin, 2015: TRMM and other data precipitation data set documentation. `https://pmm.nasa.gov/sites/default/files/document_files/3B42_3B43_doc_V7.pdf`, accessed: 2018-05-01.

Huffman, G. J., D. T. Bolvin, E. J. Nelkin, D. B. Wolff, R. F. Adler, G. Gu, Y. Hong, K. P. Bowman, and E. F. Stocker, 2007: The TRMM Multisatellite Precipitation Analysis (TMPA): Quasi-global, multiyear, combined-sensor precipitation estimates at fine scales. *J. Hydrometeorol.*, **8**, 38–55, doi:10.1175/JHM560.1.

Hunter, L. M., S. Murray, and F. Riosmena, 2013: Rainfall patterns and U.S. migration from Rural Mexico. *Int. Migr. Rev.*, **47**, 874–909, doi:10.1111/imre.12051.

INEGI, 2019: México en cifras: indicadores sociodemográficos y económicos por área geográfica. `https://www.inegi.org.mx/datos/default.html#Areas_geograficas`, accessed: 2019-10-30.

INEGI, 2020: PIB y cuentas nacionales. https://www.inegi.org.mx/temas/pib.

IPCC, 2013: Annex I: Atlas of Global and Regional Climate Projections. In: Climate Change 2013: The Physical Science Basis. Contribution of Working Group I to the Fifth Assessment Report of the Intergovernmental Panel on Climate Change. `https://www.ipcc.ch/report/ar5/wg1/atlas-of-global-and-regional-climate-projections/`.

Irwin III, R. P. and R. E. Davis, 1999: The relationship between the Southern Oscillation Index and tropical cyclone tracks in the eastern North Pacific. *Geophys. Res. Lett.*, **26**, 2251–2254, doi:10.1029/1999GL900533.

Jadhav, J., S. Panickal, S. Marathe, and K. Ashok, 2015: On the possible cause of distinct El niño types in the recent decades. *Sci. Rep.*, **5**, 1–13, doi:10.1038/srep17009.

Jakubowski, S., A. Podlaha, A. Krovvidi, and S. Bowen, 2014: September 2013 Global Catastrophe Recap. `http://thoughtleadership.aonbenfield.com/Documents/20131007_if_september_global_recap.pdf`.

Jiang, H. and E. J. Zipser, 2010: Contribution of tropical cyclones to the global precipitation from eight seasons of TRMM data: Regional, seasonal, and interannual variations. *J. Clim.*, **23**, 1526–1543, doi:10.1175/2009JCLI3303.1.

Jiang, X. and N.-C. Lau, 2008: Intraseasonal Teleconnection between North American and Western North Pacific Monsoons with 20-Day Time Scale. *J. Clim.*, **21**, 2664–2679, doi:10.1175/2007JCLI2024.1.

Jiang, X., N.-C. Lau, I. M. Held, and J. J. Ploshay, 2007: Mechanisms of the Great Plains Low-Level Jet as Simulated in an AGCM. *J. Atmos. Sci.*, **64**, 532–547, doi:10.1175/JAS3847.1.

Jiang, X. and D. E. Waliser, 2008: Northward propagation of the subseasonal variability over the eastern Pacific warm pool. *Geophys. Res. Lett.*, **35**, doi:10.1029/2008GL033723.

— 2009: Two dominant subseasonal variability modes of the eastern Pacific ITCZ. *Geophys. Res. Lett.*, **36**, doi:10.1029/2008GL036820.

Jin, F.-F., 1997: An Equatorial Ocean Recharge Paradigm for ENSO. Part I: Conceptual Model. *J. Atmos. Sci.*, **54**, 811–829, doi:10.1175/1520-0469(1997)054¡0811:AEORPF¿2.0.CO;2.

Jin, F.-F., J. Boucharel, and I.-I. Lin, 2014: Eastern Pacific tropical cyclones intensified by El Niño delivery of subsurface ocean heat. *Nature*, **516**, 82 – 85, doi:10.1038/nature13958.

Johnson, N. C., 2013: How many ENSO flavors can we distinguish? *J. Clim.*, **26**, 4816–4827, doi:10.1175/JCLI-D-12-00649.1.

Jones, S. C., P. A. Harr, J. Abraham, L. F. Bosart, P. J. Bowyer, J. L. Evans, D. E. Hanley, B. N. Hanstrum, R. E. Hart, F. Lalaurette, M. R. Sinclair, R. K. Smith, and C. Thorncroft, 2003: The extratropical transition of tropical cyclones: Forecast challenges, current understanding, and future directions. *Wea. Forecasting*, **18**, 1052–1092, doi:10.1175/1520-0434(2003)018¡1052:TETOTC¿2.0.CO;2.

Khouakhi, A., G. Villarini, and G. A. Vecchi, 2017: Contribution of Tropical Cyclones to Rainfall at the Global Scale. *J. Clim.*, **30**, 359–372, doi:10.1175/JCLI-D-16-0298.1.

Kim, H.-M. and M. A. Alexander, 2015: ENSOs modulation of water vapor transport over the Pacific–North American Region. *J. Clim.*, **28**, 3846–3856, doi:10.1175/JCLI-D-14-00725.1.

Kim, H.-M., P. J. Webster, and J. A. Curry, 2009: Impact of shifting patterns of Pacific Ocean warming on North Atlantic tropical cyclones. *Science*, **325**, 77–80, doi:10.1126/science.1174062.

— 2012: Seasonal prediction skill of ECMWF System 4 and NCEP CFSv2 retrospective forecast for the Northern Hemisphere Winter. *Clim. Dyn.*, **39**, 2957–2973, doi:10.1007/s00382-012-1364-6.

Kim, J.-E. and M. J. Alexander, 2013: Tropical Precipitation Variability and Convectively Coupled Equatorial Waves on Submonthly Time Scales in Reanalyses and TRMM. *J. Clim.*, **26**, 3013–3030, doi:10.1175/JCLI-D-12-00353.1.

Klingaman, N. P., S. J. Woolnough, and J. Syktus, 2013: On the drivers of inter-annual and decadal rainfall variability in Queensland, Australia. *Int. J. Climatol.*, **33**, 2413–2430, doi:10.1002/joc.3593.

Klotzbach, P. J., 2014: The Madden–Julian Oscillation's impacts on worldwide tropical cyclone activity. *J. Clim.*, **27**, 2317 – 2330, doi:10.1175/JCLI-D-13-00483.1.

Klotzbach, P. J. and E. C. J. Oliver, 2014: Modulation of Atlantic Basin Tropical Cyclone Activity by the Madden–Julian Oscillation (MJO) from 1905 to 2011. *J. Clim.*, **28**, 204–217, doi:10.1175/JCLI-D-14-00509.1.

Knaff, J. A., 1997: Implications of Summertime Sea Level Pressure Anomalies in the Tropical Atlantic Region. *J. Clim.*, **10**, 789–804, doi:10.1175/1520-0442(1997)010¡0789:IOSSLP¿2.0.CO;2.

Knapp, K. R., M. C. Kruk, D. H. Levinson, H. J. Diamond, and C. J. Neumann, 2010: The International Best Track Archive for Climate Stewardship (IBTrACS). *Bull. Am. Meteorol. Soc.*, **91**, 363–376, doi:10.1175/2009BAMS2755.1.

Knapp, P. A., J. T. Maxwell, and P. T. Soulé, 2016: Tropical cyclone rainfall variability in coastal North Carolina derived from longleaf pine (Pinus palustris Mill.): AD 1771–2014. *Clim. Change*, **135**, 311–325, doi:10.1007/s10584-015-1560-6.

Knight, J. R., R. J. Allan, C. K. Folland, M. Vellinga, and M. E. Mann, 2005: A signature of persistent natural thermohaline circulation cycles in observed climate. *Geophys. Res. Lett.*, **32**, doi:https://doi.org/10.1029/2005GL024233.

Kobayashi, S., Y. Ota, Y. Harada, A. Ebita, M. Moriya, H. Onoda, K. Onogi, H. Kamahori, C. Kobayashi, H. Endo, K. Miyaoka, and K. Takahashi, 2015: The JRA-55 Reanalysis: General specifications and basic characteristics. *J. Meteor. Soc. Japan. Ser. II*, **93**, 5–48, doi:10.2151/jmsj.2015-001.

Kossin, J. P., 2018: A global slowdown of tropical-cyclone translation speed. *Nature*, **558**, 104–107, doi:10.1038/s41586-018-0158-3.

Kossin, J. P., S. J. Camargo, and M. Sitkowski, 2010: Climate modulation of North Atlantic hurricane tracks. *J. Clim.*, **23**, 3057–3076, doi:10.1175/2010JCLI3497.1.

Kossin, J. P. and D. J. Vimont, 2007: A more general framework for understanding Atlantic hurricane variability and trends. *Bull. Am. Meteorol. Soc.*, **88**, 1767–1782, doi:10.1175/BAMS-88-11-1767.

Koster, R. D., P. A. Dirmeyer, Z. Guo, G. Bonan, E. Chan, P. Cox, C. T. Gordon, S. Kanae, E. Kowalczyk, D. Lawrence, P. Liu, C.-H. Lu, S. Malyshev, B. McAvaney, K. Mitchell, D. Mocko, T. Oki, K. Oleson, A. Pitman, Y. C. Sud,

C. M. Taylor, D. Verseghy, R. Vasic, Y. Xue, and T. Yamada, 2004: Regions of strong coupling between soil moisture and precipitation. *Science*, **305**, 1138–1140, doi:10.1126/science.1100217.

Krishnamurti, T. N., 1961: The subtropical jet stream of winter. *J. Meteorol.*, **18**, 172–191, doi:10.1175/1520-0469(1961)018¡0172:TSJSOW¿2.0.CO;2.

Kummerow, C., Y. Hong, W. S. Olson, S. Yang, R. F. Adler, J. McCollum, R. Ferraro, G. Petty, D.-B. Shin, and T. T. Wilheit, 2001: The evolution of the Goddard Profiling Algorithm (GPROF) for rainfall estimation from passive microwave sensors. *J. Appl. Meteor.*, **40**, 1801–1820, doi:10.1175/1520-0450(2001)040¡1801:TEOTGP¿2.0.CO;2.

Kunkel, K. E., D. R. Easterling, D. A. Kristovich, B. Gleason, L. Stoecker, and R. Smith, 2010: Recent increases in U.S. heavy precipitation associated with tropical cyclones. *Geophys. Res. Lett.*, **37**, doi:https://doi.org/10.1029/2010GL045164.

Laing, A. and J.-L. Evans, 2016: *Introduction to Tropical Meteorology*, University Corporation for Atmospheric Research. 2nd edition.

Landsea, C. W. and J. L. Franklin, 2013: Atlantic hurricane database uncertainty and presentation of a new database format. *Mon. Weather Rev.*, **141**, 3576–3592, doi:10.1175/MWR-D-12-00254.1.

Landsea, C. W., R. A. Pielke, A. M. Mestas-Nuñez, and J. A. Knaff, 1999: Atlantic basin hurricanes: Indices of climatic changes. *Clim. Change*, **42**, 89–129, doi:10.1023/A:1005416332322.

Larkin, N. K. and D. E. Harrison, 2002: ENSO Warm (El Niño) and Cold (La Niña) event life cycles: Ocean surface anomaly patterns, their symmetries, asymmetries, and implications. *J. Clim.*, **15**, 1118–1140, doi:10.1175/1520-0442(2002)015¡1118:EWENOA¿2.0.CO;2.

Larson, J., Y. Zhou, and R. W. Higgins, 2005: Characteristics of landfalling tropical cyclones in the United States and Mexico: Climatology and interannual variability. *J. Clim.*, **18**, 1247–1262, doi:10.1175/JCLI3317.1.

Lau, W. K. M. and Y. P. Zhou, 2012: Observed recent trends in tropical cyclone rainfall over the North Atlantic and the North Pacific. *J. Geophys. Res. Atmos.*, **117**, doi:https://doi.org/10.1029/2011JD016510.

Lawrence, M. . N. H. C. S. E., 1997: Preliminare Report Hurricane Pauline.

LeComte, D., 2014: "International Weather Highlights 2013: Super typhoon Haiyan, super heat in Australia and China, a long winter in Europe". *Weatherwise*, **67**, 20–27, doi:10.1080/00431672.2014.899800.

Lee, H. K., P. S. Chu, C. H. Sui, and K. M. Lau, 1998: On the annual cycle of latent heat fluxes over the equatorial Pacific using TAO buoy observations. *J. Meteorol. Soc. Jpn. Ser. II*, **76**, 909–923, doi:10.2151/jmsj1965.76.6.909.

Liebmann, B. and C. A. Smith, 1996: Description of a complete (interpolated) Outgoing Longwave Radiation dataset. *Bull. Am. Meteorol. Soc.*, **77**, 1275–1277.

Lim, Y.-K., S. D. Schubert, O. Reale, A. M. Molod, M. J. Suarez, and B. M. Auer, 2016: Large-scale controls on Atlantic tropical cyclone activity on seasonal time scales. *J. Clim.*, **29**, 6727–6749, doi:10.1175/JCLI-D-16-0098.1.

Liverman, D. M., 1999: Vulnerability and Adaptation to Drought in Mexico. *Nat. Resour. J.*, **39**, 99–115.

López-Bravo, C., E. Caetano, and V. Magaña, 2018: Forecasting summertime surface temperature and precipitation in the Mexico City metropolitan area: Sensitivity of the WRF Model to land cover changes. *Front. Earth Sci.*, **6**, 6, doi:10.3389/feart.2018.00006.

López-Bravo, L. C., 2015: *Evaluación de la predictibilidad del tiempo atmosférico en el Valle de México*, National Autonomous University of Mexico/PCT. 109, available online at http://132.248.9.195/ptd2015/noviembre/0738778/Index.html (in Spanish).

Lorenz, D. J. and D. L. Hartmann, 2006: The effect of the MJO on the North American Monsoon. *J. Clim.*, **19**, 333–343, doi:10.1175/JCLI3684.1.

Lozano-Fuentes, S., M. H. Hayden, C. Welsh-Rodriguez, C. Ochoa-Martinez, B. Tapia-Santos, K. C. Kobylinski, C. K. Uejio, E. Zielinski-Gutierrez, L. D. Monache, A. J. Monaghan, D. F. Steinhoff, and L. Eisen, 2012: The Dengue Virus Mosquito Vector Aedes aegypti at High Elevation in Mexico. *Am. J. Trop. Med. Hyg.*, **87**, 902–909, doi:https://doi.org/10.4269/ajtmh.2012.12-0244.

Madden, R. A. and P. R. Julian, 1971: Detection of a 40–50 day oscillation in the zonal wind in the tropical Pacific. *J. Atmos. Sci.*, **28**, 702–708, doi:10.1175/1520-0469(1971)028¡0702:DOADOI¿2.0.CO;2.

— 1972: Description of global-scale circulation cells in the tropics with a 40–50 day period. *J. Atmos. Sci*, **29**, 1109–1123, doi:10.1175/1520-0469(1972)029¡1109:DOGSCC¿2.0.CO;2.

Magaña, V., J. A. Amador, and S. Medina, 1999: The midsummer drought over Mexico and Central America. *J. Clim.*, **12**, 1577–1588, doi:10.1175/1520-0442(1999)012¡1577:TMDOMA¿2.0.CO;2.

Magaña, V., J. Vázquez, J. Pérez, and J. Pérez, 2003: Impact of el niño on precipitation in mexico. *Geofis. Int.*, **42**, 313–330.

Maher, P., M. E. Kelleher, P. G. Sansom, and J. Methven, 2020: Is the subtropical jet shifting poleward? *Clim. Dym.*, **54**, 203–217, doi:10.1007/s00382-019-05084-6.

Maldonado, T., A. Rutgersson, R. Caballero, F. S. R. Pausata, E. Alfaro, and J. Amador, 2017: The role of the meridional sea surface temperature gradient in controlling the Caribbean low-level jet. *J. Geophys. Res. Atmos.*, **122**, 5903–5916, doi:10.1002/2016JD026025.

Maloney, E. D., S. J. Camargo, E. Chang, B. Colle, R. Fu, K. L. Geil, Q. Hu, X. Jiang, N. Johnson, K. B. Karnauskas, J. Kinter, B. Kirtman, S. Kumar, B. Langenbrunner, K. Lombardo, L. N. Long, A. Mariotti, J. E. Meyerson, K. C. Mo, J. D. Neelin, Z. Pan, R. Seager, Y. Serra, A. Seth, J. Sheffield, J. Stroeve, J. Thibeault, S.-P. Xie, C. Wang, B. Wyman, and M. Zhao, 2014: North American Climate in CMIP5 Experiments: Part III: Assessment of Twenty-First-Century Projections*. *J. Clim.*, **27**, 2230–2270, doi:10.1175/JCLI-D-13-00273.1.

Maloney, E. D. and D. L. Hartmann, 2000a: Modulation of eastern North Pacific hurricanes by the Madden–Julian Oscillation. *J. Clim.*, **13**, 1451–1460, doi:10.1175/1520-0442(2000)013¡1451:MOENPH¿2.0.CO;2.

— 2000b: Modulation of hurricane activity in the Gulf of Mexico by the Madden-Julian Oscillation. *Science*, **287**, 2002–2004, doi:10.1126/science.287.5460.2002.

Mann, M. E. and K. A. Emanuel, 2006: Atlantic hurricane trends linked to climate change. *EOS Trans. Amer. Geophys. Union.*, **87**, 233–244, doi:10.1126/science.288.5473.1984.

Martinez, C., L. Goddard, Y. Kushnir, and M. Ting, 2019: Seasonal climatology and dynamical mechanisms of rainfall in the Caribbean. *Clim. Dyn.*, **53**, 825–846, doi:10.1007/s00382-019-04616-4.

Matsuno, T., 1966: Quasi-geostrophic motions in the equatorial area. *J. Meteorol. Soc. Jpn.*, **44**, 25–43, doi:10.2151/jmsj1965.44.1.25.

Matyas, C., 2007: Quantifying the Shapes of U.S. Landfalling Tropical Cyclone Rain Shields. *The Professional Geographer*, **59**, 158–172, doi:10.1111/j.1467-9272.2007.00604.x.

Mayorga, P., 2020: Chihuahua: sube la intensidad de la guerra por el agua (In Spanish). `https://www.proceso.com.mx/640620/chihuahua-guerra-por-el-agua-protestas`, accessed: 2020-07-26.

McPhaden, M. J., 2003: El Niño and La Niña: Causes and global consequences. *Encyclopedia of Global Environmental Change, The Earth System: Physical and Chemical Dimensions of Global Environmental Change*, M. MacCracken, J. Perry, and T. Munn, eds., Wiley, Cambridge, volume 1, chapter 2, 353–370.

McPhaden, M. J., S. E. Zebiak, and M. H. Glantz, 2006: ENSO as an integrating concept in Earth science. *Science*, **314**, 1740–1745, doi:10.1126/science.1132588.

Mechoso, C., A. Robertson, C. Ropelewski, and A. Grimm, 2004: The American Monsoon Systems. Third International Workshop on Monsoons, World Meteorological Organization.

Méndez, M. and V. Magaña, 2010: Regional aspects of prolonged meteorological droughts over Mexico and Central America. *J. Clim.*, **23**, 1175–1188, doi:10.1175/2009JCLI3080.1.

Miao, H., D. Dong, G. Huang, K. Hu, Q. Tian, and Y. Gong, 2020: Evaluation of Northern Hemisphere surface wind speed and wind power density in multiple reanalysis datasets. *Energy*, doi:10.1016/j.energy.2020.117382.

Misra, V., D. Groenen, A. Bhardwaj, and A. Mishra, 2016: The warm pool variability of the tropical northeast Pacific. *Int. J. Climatol.*, **36**, 4625–4637, doi:10.1002/joc.4658.

Mitchell, T. D. and P. D. Jones, 2005: An improved method of constructing a database of monthly climate observations and associated high-resolution grids. *Int. J. Climatol.*, **25**, 693–712, doi:10.1002/joc.1181.

Mitchell, T. P. and J. M. Wallace, 1992: The annual cycle in equatorial convection and sea surface temperature. *J. Clim.*, **5**, 1140–1156, doi:10.1175/1520-0442(1992)005¡1140:TACIEC¿2.0.CO;2.

Mo, K. C., 2000: Intraseasonal Modulation of Summer Precipitation over North America. *Mon. Weather Rev.*, **128**, 1490–1505, doi:10.1175/1520-0493(2000)128¡1490:IMOSPO¿2.0.CO;2.

— 2010: Interdecadal modulation of the impact of ENSO on precipitation and temperature over the United States. *J. Clim.*, **23**, 3639–3656, doi:10.1175/2010JCLI3553.1.

Mo, K. C. and E. H. Berbery, 2004: Low-level jets and the summer precipitation regimes over North America. *J. Geophys. Res. Atmos.*, **109**, doi:10.1029/2003JD004106.

Molinari, J., D. Knight, M. Dickinson, D. Vollaro, and S. Skubis, 1997: Potential vorticity, easterly waves, and eastern Pacific tropical cyclogenesis. *Mon. Weather Rev.*, **125**, 2699–2708, doi:10.1175/1520-0493(1997)125¡2699:PVEWAE¿2.0.CO;2.

Molinari, J., D. Vollaro, S. Skubis, and M. Dickinson, 2000: Origins and mechanisms of Eastern Pacific tropical cyclogenesis: A case study. *Mon. Weather Rev.*, **128**, 125–139, doi:10.1175/1520-0493(2000)128¡0125:OAMOEP¿2.0.CO;2.

Molinari, R. L. and A. M. Mestas-Nuñez, 2003: North Atlantic decadal variability and the formation of tropical storms and hurricanes. *Geophys. Res. Lett.*, **30**, doi:https://doi.org/10.1029/2002GL016462.

Montgomery, M. T., L. L. Lussier III, R. W. Moore, and Z. Wang, 2010: The genesis of Typhoon Nuri as observed during the tropical cyclone structure 2008 (TCS-08) field experiment – part 1: The role of the easterly wave critical layer. *Atmos. Chem. Phys.*, **10**, 9879–9900, doi:10.5194/acp-10-9879-2010.

Moore, A. M. and R. Kleeman, 1999: Stochastic forcing of ENSO by the intraseasonal oscillation. *J. Clim.*, **12**, 1199–1220, doi:10.1175/1520-0442(1999)012¡1199:SFOEBT¿2.0.CO;2.

Moore, R. W., O. Martius, and T. Spengler, 2010: The modulation of the subtropical and extratropical atmosphere in the Pacific basin in response to the Madden–Julian Oscillation. *Mon. Weather Rev.*, **138**, 2761–2779, doi:10.1175/2010MWR3194.1.

Muñoz, E., A. J. Busalacchi, S. Nigam, and A. Ruiz-Barradas, 2008: Winter and Summer Structure of the Caribbean Low-Level Jet. *J. Clim.*, **21**, 1260–1276, doi:10.1175/2007JCLI1855.1.

Murakami, H., G. A. Vecchi, T. L. Delworth, A. T. Wittenberg, S. Underwood, R. Gudgel, X. Yang, L. Jia, F. Zeng, K. Paffendorf, and W. Zhang, 2017: Dominant role of subtropical Pacific warming in extreme eastern Pacific hurricane seasons: 2015 and the future. *J. Clim.*, **30**, 243 – 264, doi:10.1175/JCLI-D-16-0424.1.

Murphy, L. N., K. Bellomo, M. Cane, and A. Clement, 2017: The role of historical forcings in simulating the observed Atlantic Multidecadal Oscillation. *Geophys. Res. Lett.*, **44**, 2472–2480, doi:https://doi.org/10.1002/2016GL071337.

Neumann, C. J., 2017: Global Guide to Tropical Cyclone Forecasting Overview. *Global Guide to Tropical Cyclone Forecasting*, World Meteorological Organization WMO, Geneva, chapter 1, 25–60, available online at https://library.wmo.int/index.php?lvl=notice$_{d}isplayid = 16963.Xupjyp4zZTY$.

NGDC, 1995: TerrainBase, Global 5 Arc-minute Ocean Depth and Land Elevation from the US National Geophysical Data Center (NGDC). `https://doi.org/10.5065/E08M-4482`.

NHC, 2018: Tropical cyclone climatology. `https://www.nhc.noaa.gov/climo/`, accessed: 2018-06-30.

Nigam, S. and B. Guan, 2011: Atlantic tropical cyclones in the twentieth century: natural variability and secular change in cyclone count. *Clim. Dyn.*, **36**, 2279–2293, doi:10.1007/s00382-010-0908-x.

Nigam, S., B. Guan, and A. Ruiz-Barradas, 2011: Key role of the Atlantic Multidecadal Oscillation in 20th century drought and wet periods over the Great Plains. *Geophys. Res. Lett.*, **38**, doi:10.1029/2011GL048650.

NOAA, 2004: The North American monsoon: Reports to the nation on our changing planet. `https://www.cpc.ncep.noaa.gov/products/outreach/Report-to-the-Nation-Monsoon_aug04.pdf`, accessed: 2018-05-01.

Onogi, K., J. Tsutsui, H. Koide, M. Sakamoto, S. Kobayashi, H. Hatsushika, T. Matsumoto, N. Yamazaki, H. Kamahori, K. Takahashi, S. Kadokura, K. Wada, K. Kato, R. Oyama, T. Ose, N. Mannoji, and R. Taira, 2007: The JRA-25 Reanalysis. *J. Meteorol. Soc. Jpn.*, **85**, 369–432, doi:10.2151/jmsj.85.369.

O'Reilly, C. H., M. Huber, T. Woollings, and L. Zanna, 2016: The signature of low-frequency oceanic forcing in the Atlantic Multidecadal Oscillation. *Geophys. Res. Lett.*, **43**, 2810–2818, doi:https://doi.org/10.1002/2016GL067925.

Ortega-Gaucin, D., J. Cruz, and H. Castellano Bahena, 2018: Drought vulnerability indices in mexico. *Water*, **10**, 1671, doi:10.3390/w10111671.

Pasch, R. J., D. A. Zelinsky, and National Hurricane Center Staff (Eds), 2014: National Hurricane Center tropical cyclone report: Hurricane Manuel. `https://www.nhc.noaa.gov/data/tcr/EP132013-Manuel.pdf`.

Patricola, C., R. Saravanan, and P. P. Chang, 2014: The impact of the El Niño–Southern Oscillation and Atlantic Meridional Mode on seasonal Atlantic tropical cyclone activity. *J. Clim.*, 5311–5328, doi:10.1175/JCLI-D-13-00687.1.

Patricola, C. M., P. Chang, and R. Saravanan, 2016: Degree of simulated suppression of Atlantic tropical cyclones modulated by flavour of El Niño. *Nature*, **9**, 155–160, doi:10.1038/ngeo2624.

Patricola, C. M., R. Saravanan, and P. Chang, 2018: The response of Atlantic tropical cyclones to suppression of African easterly waves. *Geophys. Res. Lett.*, **45**, 471–479, doi:10.1002/2017GL076081.

Peixoto, J. P. and A. H. Oort, 1992: *Physics of Climate*. AIP-Press, American Institute of Physics, 1 edition, 520 pp.

Penland, C. and P. D. Sardeshmukh, 1995: The optimal growth of tropical sea surface temperature anomalies. *J. Clim.*, **8**, 1999–2024, doi:10.1175/1520-0442(1995)008¡1999:TOGOTS¿2.0.CO;2.

Picaut, J., F. Masia, and Y. du Penhoat, 1997: An advective-reflective conceptual model for the oscillatory nature of the ENSO. *Science*, **277**, 663–666, doi:10.1126/science.277.5326.663.

Poveda, G. and O. J. Mesa, 1999: The westerly low-level Chocó jet and two other atmospheric jets over Colombia: Climatology and variability during ENSO phases (in spanish). *Rev. Acad. Colomb. Cienc.*, **23**, 517–528.

Prat, O. P. and B. R. Nelson, 2013a: Mapping the world's tropical cyclone rainfall contribution over land using the TRMM Multi-satellite Precipitation Analysis. *Water Resour. Res.*, **49**, 7236–7254, doi:10.1002/wrcr.20527.

— 2013b: Precipitation contribution of tropical cyclones in the Southeastern United States from 1998 to 2009 using TRMM Satellite Data. *J. Clim.*, **26**, 1047–1062, doi:10.1175/JCLI-D-11-00736.1.

— 2016: On the link between tropical cyclones and daily rainfall extremes derived from global satellite observations. *J. Clim.*, **29**, 6127–6135, doi:10.1175/JCLI-D-16-0289.1.

Quan, M., X. Wang, G. Zhou, K. Fan, and Z. He, 2020: Effect of winter-to-summer El niño transitions on tropical cyclone activity in the North Atlantic. *Clim. Dyn.*, **54**, 1683,1698, doi:10.1007/s00382-019-05081-9.

Raymond, D. J., C. S. Bretherton, and J. Molinari, 2006: Dynamics of the Intertropical Convergence Zone of the east Pacific. *J. Atmos. Sci.*, **63**, 582–597, doi:10.1175/JAS3642.1.

Reed, R. J., D. C. Norquist, and E. E. Recker, 1977: The structure and properties of African wave disturbances as observed during phase III of GATE. *Mon. Weather Rev.*, **105**, 317–333, doi:10.1175/1520-0493(1977)105¡0317:TSAPOA¿2.0.CO;2.

Ren, F., Y. Wang, X. Wang, and W. Li, 2007: Estimating tropical cyclone precipitation from station observations. *Advances in Atmospheric Sciences*, **24**, 700–711, doi:10.1007/s00376-007-0700-y.

Reynolds, R. W., N. A. Rayner, T. M. Smith, D. C. Stokes, and W. Wang, 2002: An improved in situ and satellite SST analysis for climate. *J. Clim.*, **15**, 1609–1625, doi:10.1175/1520-0442(2002)015¡1609:AIISAS¿2.0.CO;2.

Ritchie, E. A., K. M. Wood, D. S. Gutzler, and S. R. White, 2011: The influence of eastern Pacific tropical cyclone remnants on the southwestern United States. *Mon. Weather Rev.*, **139**, 192 – 210, doi:10.1175/2010MWR3389.1.

Rodwell, M. J. and B. J. Hoskins, 2001: Subtropical anticyclones and summer monsoons. *J. Clim.*, **14**, 3192–3211, doi:10.1175/1520-0442(2001)014¡3192:SAASM¿2.0.CO;2.

Ropelewski, C. F. and M. S. Halpert, 1987: Global and regional scale precipitation patterns associated with the El Niño/Southern Oscillation. *Mon. Weather Rev.*, **115**, 1606–1626, doi:10.1175/1520-0493(1987)115¡1606:GARSPP¿2.0.CO;2.

Rotstayn, L. D., M. A. Collier, M. R. Dix, Y. Feng, H. B. Gordon, S. P. O'Farrell, I. N. Smith, and J. Syktus, 2010: Improved simulation of Australian climate and ENSO-related rainfall variability in a global climate model with an interactive aerosol treatment. *Int. J. Climatol.*, **30**, 1067–1088, doi:10.1002/joc.1952.

Roundy, P. E. and G. N. Kiladis, 2006: Observed relationships between oceanic Kelvin waves and atmospheric forcing. *J. Clim.*, **19**, 5253–5272, doi:10.1175/JCLI3893.1.

Rydbeck, A. V., E. D. Maloney, S.-P. Xie, J. Hafner, and J. Shaman, 2013: Remote Forcing versus Local Feedback of East Pacific Intraseasonal Variability during Boreal Summer. *J. Clim.*, **26**, 3575–3596, doi:10.1175/JCLI-D-12-00499.1.

Santiago-García, M. W., A. F. Parés-Sierra, and A. Trasviña, 2019: Dipole-wind interactions under gap wind jet conditions in the Gulf of Tehuantepec, Mexico: A surface drifter and satellite database analysis. *PLoS One*, **14**, e0226366, doi:10.1371/journal.pone.0226366.

Sardeshmukh, P. D. and B. I. Hoskins, 1984: Spatial smoothing on the sphere. *Mon. Weather Rev.*, **112**, 2524–2529, doi:10.1175/1520-0493(1984)112¡2524:SSOTS¿2.0.CO;2.

Schmitz, J. T. and S. L. Mullen, 1996: Water vapor transport associated with the summertime north american monsoon as depicted by ecmwf analyses. *Journal of Climate*, **9**, 1621–1634, doi:10.1175/1520-0442(1996)009¡1621:WVTAWT¿2.0.CO;2.

Serra, Y., J. Braun, and D. Adams, 2016: Observing the Intra-Americas Sea climate: Existing and emerging technologies. *US CLIVAR Variations*, **14**, 1–9.

Serra, Y. L., G. N. Kiladis, and M. F. Cronin, 2008: Horizontal and vertical structure of easterly waves in the Pacific ITCZ. *J. Atmos. Sci.*, **65**, 1266–1284, doi:10.1175/2007JAS2341.1.

Shapiro, L. J., 1987: Month-to-month variability of the Atlantic tropical circulation and its relationship to tropical storm formation. *Mon. Weather Rev.*, **115**, 2598–2614, doi:10.1175/1520-0493(1987)115¡2598:MTMVOT¿2.0.CO;2.

Shapiro, L. J. and S. B. Goldenberg, 1998: Atlantic sea surface temperatures and tropical cyclone formation. *J. Clim.*, **11**, 578–590, doi:10.1175/1520-0442(1998)011¡0578:ASSTAT¿2.0.CO;2.

Smirnov, D. and D. J. Vimont, 2011: Variability of the Atlantic Meridional Mode during the Atlantic hurricane season. *J. Clim.*, **24**, 1409–1424, doi:10.1175/2010JCLI3549.1.

Smith, I., 2004: An assessment of recent trends in Australian rainfall. *Aust. Meteorol. Mag.*, **53**, 163–173.

Stensrud, D. J., R. L. Gall, S. L. Mullen, and K. W. Howard, 1995: Model climatology of the Mexican monsoon. *J. Clim.*, **8**, 1775–1794, doi:10.1175/1520-0442(1995)008¡1775:MCOTMM¿2.0.CO;2.

Stephan, C. C., N. P. Klingaman, P. L. Vidale, A. G. Turner, M.-E. Demory, and L. Guo, 2018a: A comprehensive analysis of coherent rainfall patterns in China and potential drivers. Part i: Interannual variability. *Clim. Dyn.*, **50**, 4405–4424, doi:10.1007/s00382-017-3882-8.

— 2018b: A comprehensive analysis of coherent rainfall patterns in china and potential drivers. part ii: intraseasonal variability. *Clim. Dyn.*, **51**, 17–33, doi:10.1007/s00382-017-3904-6.

— 2018c: Interannual rainfall variability over China in the MetUM GA6 and GC2 configurations. *Geosci. Model Dev.*, **11**, 1823–1847, doi:10.5194/gmd-11-1823-2018.

Suarez, M. J. and P. S. Schopf, 1988: A delayed action oscillator for ENSO. *J. Atmos. Sci.*, **45**, 3283–3287, doi:10.1175/1520-0469(1988)045¡3283:ADAOFE¿2.0.CO;2.

Sutton, R. T., G. D. McCarthy, J. Robson, B. Sinha, A. T. Archibald, and L. J. Gray, 2018: Atlantic multidecadal variability and the U.K. ACSIS Program. *Bull. Am. Meteorol. Soc.*, **99**, 415 – 425, doi:10.1175/BAMS-D-16-0266.1.

Tang, B. H. and J. D. Neelin, 2004: ENSO Influence on Atlantic hurricanes via tropospheric warming. *Geophys. Res. Lett.*, **31**, doi:10.1029/2004GL021072.

Taschetto, A. S., R. J. Haarsma, A. S. Gupta, C. C. Ummenhofer, K. J. Hill, and M. H. England, 2010: Australian monsoon variability driven by a Gill–Matsuno-type response to central west Pacific warming. *J. Clim.*, **23**, 4717–4736, doi:10.1175/2010JCLI3474.1.

Taylor, M. A., D. B. Enfield, and A. A. Chen, 2002: Influence of the tropical Atlantic versus the tropical Pacific on Caribbean rainfall. *J. Geophys. Res. Atmos*, **107**, 10–1–10–14, doi:10.1029/2001JC001097.

Thompson, D. W. J. and J. M. Wallace, 1998: The Arctic Oscillation signature in the wintertime geopotential height and temperature fields. *Geophys. Res. Lett.*, **25**, 1297–1300, doi:10.1029/98GL00950.

Thorncroft, C. and K. Hodges, 2001: African easterly wave variability and its relationship to Atlantic tropical cyclone activity. *J. Clim.*, **14**, 1166–1179, doi:10.1175/1520-0442(2001)014¡1166:AEWVAI¿2.0.CO;2.

Thorncroft, C. D., N. M. J. Hall, and G. N. Kiladis, 2008: Three-dimensional structure and dynamics of African easterly waves. Part III: Genesis. *J. Atmos. Sci.*, **65**, 3596–3607, doi:10.1175/2008JAS2575.1.

Thorncroft, C. D. and B. J. Hoskins, 1994: An idealized study of African easterly waves. I: A linear view. *Q. J. Royal Meteorol. Soc.*, **120**, 953–982, doi:10.1002/qj.49712051809.

Ting, M., Y. Kushnir, and C. Li, 2014: North Atlantic Multidecadal SST Oscillation: External forcing versus internal variability. *J. Mar. Syst.*, **133**, 27–38, doi:https://doi.org/10.1016/j.jmarsys.2013.07.006.

Ting, M., Y. Kushnir, R. Seager, and C. Li, 2009: Forced and internal twentieth-century SST trends in the North Atlantic. *J. Clim.*, **22**, 1469 – 1481, doi:10.1175/2008JCLI2561.1.

Toma, V. E. and P. J. Webster, 2010a: Oscillations of the Intertropical Convergence Zone and the genesis of easterly waves. Part I: diagnostics and theory. *Clim. Dyn.*, **34**, 587–604, doi:10.1007/s00382-009-0584-x.

— 2010b: Oscillations of the Intertropical Convergence Zone and the genesis of easterly waves Part II: numerical verification. *Clim. Dyn.*, **34**, 605–613, doi:10.1007/s00382-009-0585-9.

Tory, K. J. and R. A. Dare, 2015: Sea surface temperature thresholds for tropical cyclone formation. *J. Clim.*, **28**, 8171 – 8183, doi:10.1175/JCLI-D-14-00637.1.

Touma, D., S. Stevenson, S. J. Camargo, D. E. Horton, and N. S. Diffenbaugh, 2019: Variations in the intensity and spatial extent of tropical cyclone precipitation. *Geophys. Res. Lett.*, **46**, 13992–14002, doi:https://doi.org/10.1029/2019GL083452.

Trenberth, K., R. Zhang, and N. C. for Atmospheric Research Staff (Eds), 2019: The climate data guide: Atlantic Multi-decadal Oscillation (AMO). `https://climatedataguide.ucar.edu/climate-data/atlantic-multi-decadal-oscillation-amo`, accessed: 2020-06-07.

Trenberth, K. . N. C. f. A. R. S. E., 2020: The Climate Data Guide: Nino SST Indices (Nino 1+2, 3, 3.4, 4; ONI and TNI). https://climatedataguide.ucar.edu/climate-data/nino-sst-indices-nino-12-3-34-4-oni-and-tni, accessed: 2020-05-10.

Trenberth, K. E. and J. T. Fasullo, 2009: Global warming due to increasing absorbed solar radiation. *Geophys. Res. Lett.*, **36**, doi:10.1029/2009GL037527.

Trenberth, K. E. and D. J. Shea, 2006: Atlantic hurricanes and natural variability in 2005. *Geophys. Res. Lett.*, **33**, doi:https://doi.org/10.1029/2006GL026894.

Trenberth, K. E. and D. P. Stepaniak, 2001: Indices of El Niño Evolution. *J. Clim.*, **14**, 1697–1701, doi:10.1175/1520-0442(2001)014¡1697:LIOENO¿2.0.CO;2.

van den Dool, H. M., S. Saha, and A. Johansson, 2000: Empirical orthogonal teleconnections. *J. Clim.*, **13**, 1421–1435, doi:10.1175/1520-0442(2000)013¡1421:EOT¿2.0.CO;2.

Ventrice, M. J., C. D. Thorncroft, and M. A. Janiga, 2012: Atlantic Tropical Cyclogenesis: A Three-Way Interaction between an African Easterly Wave, Diurnally Varying Convection, and a Convectively Coupled Atmospheric Kelvin Wave. *Mon. Weather Rev.*, **140**, 1108–1124, doi:10.1175/MWR-D-11-00122.1.

Vigaud, N. and A. Robertson, 2017: Convection regimes and tropical-midlatitude interactions over the Intra-American Seas from May to November. *Int. J. Climatol.*, **37**, 987–1000, doi:10.1002/joc.5051.

Vimont, D. J. and J. P. Kossin, 2007: The Atlantic Meridional Mode and hurricane activity. *Geophys. Res. Lett.*, **34**, doi:10.1029/2007GL029683.

Waliser, D. E. and C. Gautier, 1993: A satellite-derived climatology of the ITCZ. *J. Clim.*, **6**, 2162–2174.

Wang, C., 2004: *ENSO, Atlantic Climate Variability, and the Walker and Hadley Circulations*, Springer Netherlands, Dordrecht. 173–202.

— 2007: Variability of the Caribbean low-level jet and its relations to climate. *Clim. Dyn.*, **29**, 411–422, doi:10.1007/s00382-007-0243-z.

— 2018: A review of ENSO theories. *Natl. Sci. Rev.*, **5**, 813–825.

Wang, C. and D. B. Enfield, 2001: The Tropical Western Hemisphere Warm Pool. *Geophys. Res. Lett.*, **28**, 1635–1638, doi:10.1029/2000GL011763.

— 2003: A Further Study of the Tropical Western Hemisphere Warm Pool. *J. Clim.*, **16**, 1476–1493, doi:10.1175/1520-0442(2003)016¡1476:AFSOTT¿2.0.CO;2.

Wang, C., S.-K. Lee, and D. B. Enfield, 2008: Atlantic Warm Pool acting as a link between Atlantic Multidecadal Oscillation and Atlantic tropical cyclone activity. *Geochem. Geophy. Geosy.*, **9**, doi:10.1029/2007GC001809.

Wang, C., S.-K. Lee, and C. R. Mechoso, 2010: Interhemispheric influence of the Atlantic warm pool on the southeastern Pacific. *J. Clim.*, **23**, 404–418, doi:10.1175/2009JCLI3127.1.

Wang, C., H. Liu, S.-K. Lee, and R. Atlas, 2011: Impact of the Atlantic warm pool on United States landfalling hurricanes. *Geophys. Res. Lett.*, **38**, doi:10.1029/2011GL049265.

Weaver, E. A. and K. N. Kolivras, 2018: Investigating the Relationship Between Climate and Valley Fever (Coccidioidomycosis. *EcoHealth*, **15**, 840–852, doi:10.1007/s10393-018-1375-9.

Webster, P. J., 1995: The annual cycle and the predictability of the tropical coupled ocean-atmosphere system. *Meteorol. Atmos. Phys.*, **56**, 33–55, doi:10.1007/BF01022520.

Webster, P. J. and S. Yang, 1992: Monsoon and ENSO: Selectively interactive systems. *Q. J. Royal Meteorol. Soc.*, **118**, 877–926, doi:10.1002/qj.49711850705.

Weisberg, R. H. and C. Wang, 1997: A Western Pacific Oscillator paradigm for the El Niño-Southern Oscillation. *Geophys. Res. Lett.*, **24**, 779–782, doi:10.1029/97GL00689.

Wen, M., S. Yang, W. Higgins, and R. Zhang, 2011: Characteristics of the Dominant Modes of Atmospheric Quasi-Biweekly Oscillation over Tropical–Subtropical Americas. *J. Clim.*, **24**, 3956–3970, doi:10.1175/2011JCLI3916.1.

Weng, H., K. Ashok, S. K. Behera, S. A. Rao, and T. Yamagata, 2007: Impacts of recent el niño Modoki on dry/wet conditions in the Pacific rim during boreal summer. *Clim. Dyn.*, **29**, 113–129, doi:10.1007/s00382-007-0234-0.

Weng, H., S. K. Behera, and T. Yamagata, 2009: Anomalous winter climate conditions in the Pacific rim during recent El Niño Modoki and El Niño events. *Clim. Dyn.*, **32**, 663–674, doi:10.1007/s00382-008-0394-6.

Westerling, A. L., H. G. Hidalgo, D. R. Cayan, and T. W. Swetnam, 2006: Warming and Earlier Spring Increase Western U.S. Forest Wildfire Activity. *Science*, **313**, 940–943, doi:10.1126/science.1128834.

Wheeler, M. C. and H. H. Hendon, 2004: An all-season real-time multivariate MJO index: Development of an index for monitoring and prediction. *Mon. Weather Rev.*, **132**, 1917–1keywords = Atlantic Multidecadal Oscillation, Great Plains hydroclimate, decadal SST variability, droughts,932, doi:10.1175/1520-0493(2004)132¡1917:AARMMI¿2.0.CO;2.

Wilder, M., G. Garfin, P. Ganster, H. Eakin, P. Romero-Lankao, P. Lara-Valencia, A. Cortez-Lara, S. Mumme, C. Neri, and F. Muñoz Arriola, 2013: Climate Change and U.S.-Mexico Border communities. *Assessment of Climate Change in the Southwest United States: A Report Prepared for the National Climate Assessment*, G. Garfin, R. A. Jardine, and M. Merideth, eds., Southwest Climate Alliance,Island Press, Washington, D.C., chapter 16, 340–384.

WMO, 2007: Use of seasonal forecasts and climate prediction in operational agriculture. `http://www.wamis.org/agm/pubs/CAGMRep/CAGM102.pdf`, accessed: 2020-08-04.

Wood, K. M. and E. A. Ritchie, 2013: An updated climatology of tropical cyclone impacts on the southwestern United States. *Mon. Weather Rev*, **141**, 4322 – 4336, doi:10.1175/MWR-D-13-00078.1.

Wu, P. and P.-S. Chu, 2007: Characteristics of tropical cyclone activity over the eastern North Pacific: the extremely active 1992 and the inactive 1977. *Tellus A*, **59**, 444–454, doi:https://doi.org/10.1111/j.1600-0870.2007.00248.x.

Xie, S.-P. and S. G. H. Philander, 1994: A coupled ocean-atmosphere model of relevance to the ITCZ in the eastern Pacific. *Tellus A*, **46**, 340–350, doi:10.1034/j.1600-0870.1994.t01-1-00001.x.

Xie, S.-P., H. Xu, W. S. Kessler, and M. Nonaka, 2005: Air–sea interaction over the eastern Pacific warm pool: Gap winds, thermocline dome, and atmospheric convection. *J. Clim.*, **18**, 5–20, doi:10.1175/JCLI-3249.1.

Xu, G., T. J. Osborn, and A. J. Matthews, 2017: Moisture transport by Atlantic tropical cyclones onto the North American continent. *Clim. Dyn.*, **48**, 3161–3182, doi:10.1007/s00382-016-3257-6.

Yang, G.-Y. and J. Slingo, 2001: The Diurnal Cycle in the Tropics. *Mon. Weather Rev.*, **129**, 784–801, doi:10.1175/1520-0493(2001)129¡0784:TDCITT¿2.0.CO;2.

Yepes, J., G. Poveda, J. F. Mejía, L. Moreno, and C. Rueda, 2019: CHOCO-JEX: A research experiment focused on the Chocó low-level jet over the far eastern Pacific and western Colombia. *Bull. Am. Meteorol. Soc.*, **100**, 779–796, doi:10.1175/BAMS-D-18-0045.1.

Yu, W., W. Han, E. D. Maloney, D. Gochis, and S.-P. Xie, 2011: Observations of eastward propagation of atmospheric intraseasonal oscillations from the Pacific to the Atlantic. *J. Geophys. Res. Atmos.*, **116**, doi:10.1029/2010JD014336.

Yu, Z. and Y. Wang, 2018: Rainfall Distribution in Landfalling Tropical Cyclones. *Extreme weather*, P. S. Sallis, ed., IntechOpen, volume 1, chapter 4, 49–84.

Zebiak, S. E., 1993: Air–Sea interaction in the equatorial Atlantic region. *J. Clim.*, **6**, 1567–1586, doi:10.1175/1520-0442(1993)006¡1567:AIITEA¿2.0.CO;2.

Zehnder, J. A., D. M. Powell, and D. L. Ropp, 1999: The interaction of easterly waves, orography, and the Intertropical Convergence Zone in the genesis of Eastern Pacific tropical cyclones. *Mon. Weather Rev.*, **127**, 1566–1585, doi:10.1175/1520-0493(1999)127¡1566:TIOEWO¿2.0.CO;2.

Zehnder, J. A. and M. J. Reeder, 1997: A numerical study of barotropic vortex motion near a large-scale mountain range with application to the motion of tropical cyclones approaching the Sierra Madre. *Meteorol. Atmos. Phys.*, **64**, 1–19, doi:10.1007/BF01044127.

Zehr, R. M., 1992: Tropical cyclogenesis in the western North Pacific. NOAA Technical Report, U.S. Dept. of Commerce, Washington, D.C.

Zhang, R., R. Sutton, G. Danabasoglu, T. L. Delworth, W. M. Kim, J. Robson, and S. G. Yeager, 2016: Comment on “the atlantic multidecadal oscillation without a role for ocean circulation”. *Science*, **352**, 1527–1527, doi:10.1126/science.aaf1660.

Zhang, R., R. Sutton, G. Danabasoglu, Y.-O. Kwon, R. Marsh, S. G. Yeager, D. E. Amrhein, and C. M. Little, 2019: A review of the role of the Atlantic Meridional Overturning Circulation in Atlantic multidecadal variability and associated climate impacts. *Rev. Geophys.*, **57**, 316–375, doi:https://doi.org/10.1029/2019RG000644.

Zheng, Z.-W., I.-I. Lin, B. Wang, H.-C. Huang, and C.-H. Chen, 2015: A long neglected damper in the El Niño—Typhoon relationship: a ‘Gaia-Like’ process. *Sci. Rep.*, **5**, 1–7, doi:10.1038/srep11103.